Modeling Excited States and Charge Transport with Density Functional Theory

Modeling Excited States and Charge Transport with Density Functional Theory

by

Zachary J. Knepp

Presented to the Graduate and Research Committee

of Lehigh University

in Candidacy for the Degree of

Doctor of Philosophy

in

Chemistry

Lehigh University

April 2025

Dissertation is accepted and approved in partial fulfillment of the requirements for the degree of Doctor of Philosophy in Chemistry.

Zachary J. Knepp

Date Approved:

_____
Date

List of Committee Members:

_____
Lisa A. Fredin

_____
Elizabeth R. Young

_____
Kai Landskron

_____
Srinivas Rangarajan

Acknowledgments

This dissertation would not have been possible without the support of my family, friends, mentors, and collaborators. I am deeply grateful to my wife, Kayla Knepp, for her unwavering support, patience, and love – everything she does for our family is beyond measure. I am beyond thankful for my daughter, Marcilene Knepp, whose presence fills even the darkest days with light and joy. I deeply appreciate my parents, Patrice and Dennis Knepp Jr., for their endless encouragement, as well as our visits and frequent calls. I am grateful to my sister, Madison Carson, for putting up with my antics, and my brother-in-law, Austyn Carson, for our much-needed sports conversations. I am grateful to my in-laws, Kim and Tommy Schriner, for their constant support, and to my gram-in-law, Shawnee Petchel, for always bringing our family together. I owe a special debt of gratitude to my lab mate and best friend, Gil Repa. This Ph.D. would not have been possible without you. I am thankful to the Photochemistry Group, including Prof. Elizabeth Young, Gisselle Rojas, Robert Hamburger, Domenica Fertal, Christian Guzman, Andrea Dorsa, Isabelle Herlinger, and Christabella Fortna, for the insightful discussions, continuous support, and collaborative efforts that have strengthened this work. I am especially grateful to my Ph.D. advisor, Prof. Lisa Fredin, for the freedom to explore challenging projects, which have shaped me into the chemist I am today. In addition, I acknowledge support from the National Science Foundation under Grant No. CHE-2310205 and the Pittsburgh Foundation (UN2020-114823). Resources were provided by Lehigh Research Computing partially supported by the NSF CC* Compute program through Grant No. OAC-2019035 and allocation TG-CHE190011 from the Advanced Cyberinfrastructure Coordination Ecosystem: Services & Support (ACCESS) program, which is supported by National Science Foundation grants #2138259, #2138286, #2138307, #2137603, and #2138296.

Contents

List of Tables

List of Figures

Abstract

Kohn-Sham density functional theory (DFT) and its periodic extension are widely used to investigate the electronic structure, energetics, and geometries of molecules and materials. While DFT reliably predicts ground-state properties, it struggles to accurately describe vibrational and electronic excited states as well as charge transport. Perturbative extensions, such as coupled-perturbed Kohn-Sham (CPKS) for infrared and Raman spectra and linear-response time-dependent DFT (LR-TDDFT) for UV-Vis spectra, attempt to address these limitations but remain constrained by system size and are typically restricted to vertical excitations. This thesis first introduces ground- and excited-state electronic structure methods (Chapter 1) and evaluates the accuracy of excited-state methods (Chapter 2). Ground-state isomer difference spectra were used to characterize small populations of pyridine-based azo dyes with DFT and LR-TDDFT (Chapter 3). A new approach is developed for predicting excited-state absorption spectra and interpreting transient absorption spectra by applying the linear-response Tamm-Dancoff approximation to non-Aufbau configurations (Chapter 4). To study charge transport, a finite-displacement method is introduced to quantify the impact of vibrational modes on carrier mobility in organic crystals (Chapter 5). Anisotropic carrier mobilities in organic crystals are subsequently predicted using Boltzmann transport theory (BTE, Chapter 6), and this framework is extended by incorporating the finite-displacement method to evaluate the detrimental effects of vibrational modes on charge transport in tetracene (Chapter 7). The methods developed in this work provide new insights into the photophysics of molecular chromophores and the role of vibrational disorder in charge transport and will continue to advance the theoretical understanding of these processes.

Part I

Theoretical Background

Chapter 1

Ground- and Excited-State Electronic Structure Theory[†]

1.1 Introduction

The theoretical treatment of atomic and molecular energy levels is essential to our understanding of the quantum world. Even the pioneering works of Planck and Einstein, which established the existence of quantized energy levels, were driven by the need to explain experimental absorption and emission phenomena. Today, advances in computational infrastructure and the development of improved methods for solving the Schrödinger equation enable researchers to routinely calculate the ground- and excited-state properties of molecules and materials. These advancements not only provide deeper insights into experimental results but also facilitate the rational design of new molecules and materials with tailored photophysical characteristics, ultimately enhancing our understanding of the chemical physics of matter.

Two formalisms are possible for solving the electronic Schrödinger equation, each differing in their mathematical descriptions of the quantum states. Wavefunctions (ψ) represent the natural choice for solving the Schrödinger equation and provide all the observable information about a many-body Fermionic system. They are directly derived from the solution of a Hamiltonian eigenvalue problem for the total energy of a system. Alternatively, density functional theory (DFT) replaces the wavefunction with the three-dimensional electronic density (ψ^2) to simplify the prob-

[†]Accepted at *Chem. Phys. Rev.* **2025**.

lem. Each of these methods are made possible by the Born-Oppenheimer (BO) approximation, which separates nuclear and electronic spatial coordinates, treating the former as classical point-like particles that propagate according to the non-adiabatic potential energy surface. This condition allows for the use of gradient descent algorithms to locate energetically minimized nuclear configurations for ground and excited states. This simplification can limit the accuracy of both ground- and excited-state properties.

An additional challenge for electronic structure theory is a reliable and simultaneously affordable treatment of the interaction between electrons in a quantum system, termed electron correlation. Electron correlation can be categorized as static or dynamic. Static electron correlation arises from the superposition of electron configurations represented by multiple Slater determinants. Errors arise from the use of a single determinant to describe the ground state of molecules in most commonly used electronic structure methods, such as Hartree-Fock (HF) theory and DFT. Dynamic electron correlation arises from the instantaneous electron-electron interaction, which cannot be captured by mean-field approximations.

The current challenges in accurately describing the ground and excited states of molecules stem from a need to balance accuracy and computational cost. For example, even when very accurate methods are available, they tend to lack widespread adoption because they are too computationally expensive to be applied to many experimentally interesting systems. Therefore, common practice has been to select black-box methods that are affordable but may or may not agree with experiment. Critically, agreement may occur fortuitously from an unphysical electronic structure. For example, it is common practice to select a density functional for a linear-response (LR) time-dependent (TD) DFT calculation that reproduces experimental excitation energies without considering the underlying physics. This has also given rise to practices like density functional tuning, which can shift excitation energies to better agreement but can also dramatically change other physical properties like oscillator strengths and geometries. Even when higher levels of theory are computationally accessible for a system, they are often overlooked because of the potentially large learning curve and computational cost. Furthermore, navigating the vast number of excited-state approximations can be confusing and selecting an appropriate method for a new system is non-intuitive. Therefore, excited-state descriptions beyond DFT-based approaches have been largely restricted to simple molecules intended to test the theoretical performance of a method, as opposed to obtaining new

chemical insights into experimentally relevant systems. This chapter aims to make *ab initio* electronic structure theory methods more accessible to non-experts by providing a brief introduction to widely used ground- and excited-state methods. The next chapter evaluates the performance of various excited-state methods.

1.2 Ground-State Methods

Before describing how excited-states can be modeled, it is important to have a general understanding of the underlying ground-state theories. The simplest approach to describing the quantum mechanics of a many-body system is to construct a single Slater determinant that describes the lowest-energy electronic configuration of a system. With this, one can determine the quantum mechanical observables of the system with either wavefunction-based or density functional-based methods. First, we discuss the simplest wavefunction method, HF theory (Section 1.2.1) followed by a discussion of DFT (Section 1.2.2). Next, we present corrections to HF (post-HF) including Møller–Plesset (MP) perturbation theory (Section 1.2.3), configuration interaction (CI, Section 1.2.4), and coupled cluster (CC) theory (Section 1.2.5). Multiconfigurational (MC) self-consistent field (SCF) theories (Section 1.2.6) that does not assume that a single Slater determinant is representative of a system and numerical spin scaling approximations (Section 1.2.7) which reduce computational cost are explained.

1.2.1 Hartree-Fock

HF theory is the simplest way to solve the time-independent electronic Schrödinger equation for a many-body system. The HF eigenvalue equation is

$$\hat{f}(\mathbf{x}_1)\chi_i(\mathbf{x}_1) = \epsilon_i\chi_i(\mathbf{x}_1) \tag{1.1}$$

where $\hat{f}$ is the Fock operator, χ_i is a i^{th} spin orbital with an energy eigenvalue ϵ_i, and $\mathbf{x}_1$ is the set of space ($\mathbf{r}$) and spin coordinates ($\omega = \alpha$ or β) for electron 1. The Fock operator in atomic units

$$\hat{f}(\mathbf{x}_1) = \hat{h}(\mathbf{x}_1) + \sum_j \hat{J}_j(\mathbf{x}_1) - \hat{K}_j(\mathbf{x}_1) \tag{1.2}$$

is composed of a one-electron operator

$$\hat{h}_i = -\frac{1}{2}\nabla_i^2 - \sum_A \frac{Z_A}{r_{iA}} \tag{1.3}$$

with kinetic energy ($-\frac{1}{2}\nabla_i^2$) and electron-nuclear Coulombic attraction ($\frac{Z_A}{r_{iA}}$, Z_A is the charge of nucleus A and r_{iA} is the distance between electron i and nucleus A) terms and two electron operators, *i.e.,* the Coulomb and exchange operators, which are

$$\hat{J}_j(\mathbf{x}_1) = \int \chi_j^*(\mathbf{x}_2)\frac{1}{r_{12}}\chi_j(\mathbf{x}_2)d\mathbf{x}_2 \tag{1.4}$$

and

$$\hat{K}_j(\mathbf{x}_1)\chi_i(\mathbf{x}_1) = \left[\int \chi_j^*(\mathbf{x}_2)\frac{1}{r_{12}}\chi_i(\mathbf{x}_2)d\mathbf{x}_2\right]\chi_j(\mathbf{x}_1), \tag{1.5}$$

respectively, and r_{12} is the distance between electrons 1 and 2.[1,2] The total HF energy is the energy expectation value of the electronic Hamiltonian ($\hat{H}_{el}$) for one Slater determinant which is given by

$$E_{HF} = \sum_i \langle i|\hat{h}|i\rangle + \frac{1}{2}\sum_{ij}[ii|jj] - [ij|ji] \tag{1.6}$$

with one- and two-electron matrix elements

$$\langle i|\hat{h}|i\rangle = \int \chi_i^*(\mathbf{x}_1)\hat{h}(\mathbf{x}_1)\chi_i(\mathbf{x}_1)d\mathbf{x}_1 \tag{1.7}$$

and

$$[ij|kl] = \int \chi_i^*(\mathbf{x}_1)\chi_j(\mathbf{x}_1)\frac{1}{r_{12}}\chi_k^*(\mathbf{x}_2)\chi_l(\mathbf{x}_2)d\mathbf{x}_1 d\mathbf{x}_2, \tag{1.8}$$

respectively.[1,2]

The development of HF theory was not only a significant advancement for electronic structure theory, but also pioneered understanding of chemistry and chemical physics through the introduction of molecular orbital (MO) theory. HF treats electrons as independent particles that interact within an effective mean-field potential generated by both the nuclei and other electrons. In the BO approximation, HF approximates the electronic structure of atoms, molecules, and materials by reducing the complexity of the many-body system into a series of coupled one-body problems.

This allows the problem to be mathematically tractable on computer hardware. Another key to the success of HF theory is through the use of Slater determinants, which satisfy the Pauli exclusion principle. Because there is no analytical solution to the HF equations, they must be solved variationally and self-consistently. The eigenfunction solution of the HF Hamiltonian produces a set of spin orbitals that each have a unique energy eigenvalue, or energy level. Orbitals provide chemical intuition and direct correlation to measurable properties, as in Koopmans' theorem.[3]

In practice for closed-shell molecules, the restricted formalism (RHF), which enforces that all electrons be spin-paired to allow for a single set of doubly-occupied spatial orbitals, is used to simplify the complexity of the problem. Unrestricted (UHF) implementations require two sets of orbitals for spin-up and spin-down electrons, accommodating a wider range of systems including radicals and transition metals. However, because of the mean-field approximation of electron-electron interactions, UHF is susceptible to the artificial mixing of different electronic spin-states (*i.e.*, spin contamination), making accurate predictions challenging. Both RHF and UHF neglect effects of static and dynamic electron correlation, which play a crucial role in chemical bonding and excited states. This has led to a substantial number of post-HF methods (Sections 1.2.3–1.2.5) that have been used to build on the pioneering work of HF theory to describe the properties of ground and excited states for countless molecules and materials.

1.2.2 Density Functional Theory

Exchanging the fundamental variable ψ for ψ^2 provides attractive computational simplification of a multielectron wavefunction to a probabilistic electronic density that maintains the chemical intuition of the positions of the electrons. In DFT, a system of interacting electrons is represented by a fictitious system of non-interacting electrons with a ground-state density identical to the many-body system.[4] The energy of such a system can be broken into components such as

$$E[\rho(\mathbf{r})] = T_{ni}[\rho(\mathbf{r})] + V_{ne}[\rho(\mathbf{r})] + V_{ee}[\rho(\mathbf{r})] + \Delta T[\rho(\mathbf{r})] + \Delta V_{ee}[\rho(\mathbf{r})] \tag{1.9}$$

where the terms refer to the kinetic energy of the non-interacting electrons (T_{ni}), the nuclear-electron interaction (V_{ne}), the classical electron-electron interaction (V_{ee}), the correction to the kinetic energy (ΔT) deriving from the interacting nature of the electrons, and all non-classical

corrections to the electron-electron interaction energy (ΔV_{ee}), respectively.

The foundation of this approach is provided by the Hohenberg-Kohn theorems,[5] which provide assurance that the Hamiltonian can be determined by the ground-state density when an external potential, *i.e.*, atomic coordinates and their charges are defined, and that DFT calculations must be performed self-consistently using a variational theorem, just like HF and some other wavefunction methods.[6] It is critical to note that the Hohenberg-Kohn existence theorem is only applicable to the lowest energy spin configuration.[7] The efforts to extend the DFT formalism to accurately describe arbitrary excited states are a critical focus of later sections of this review (Sections 1.3.1–1.3.3).

In the DFT Hamiltonian, the nuclear-electron and electron-electron potentials are classically approximated by Coulombic pairwise interactions. The errors introduced by these approximations are incorporated into the so-called exchange-correlation term (E_{xc}). Provided that a functional form is known for E_{xc}, DFT is exact. However, this is unfortunately not the case and E_{xc} necessarily must be approximated. The set orbitals that minimize the energy of a given density functional are typically found by solving the one-electron Kohn-Sham (KS) equations

$$\hat{h}_i^{ks}\chi_i = \epsilon_i\chi_i. \tag{1.10}$$

Here, the KS one-electron operator is defined as

$$\hat{h}_i^{ks} = -\frac{1}{2}\nabla_i^2 - \sum_A \frac{Z_A}{|\mathbf{r}_i - \mathbf{r}_A|} + \int \frac{\rho(\mathbf{r}')}{|\mathbf{r}_i - \mathbf{r}'|}d\mathbf{r}' + V_{xc} \tag{1.11}$$

with terms including the kinetic energy operator (∇_i^2), electron-nuclear Coulombic attraction, electron-electron Coulomb repulsion, and the exchange-correlation potential (V_{xc}), which is the functional derivative of the exchange-correlation energy functional. This reduces solving for the total system density to determining the orbital coefficients using a set of basis functions, similar to the approach taken in HF. Because DFT was developed after HF, implementations often draw from similar conventions, including basis functions, variational solvers, and restricted (RDFT) and unrestricted (UDFT) formalisms.

The largest issue with DFT is that an exact form of the exchange-correlation term is unknown, and thus all current functionals are approximations of the true solution.[8] Initially, local density

approximations (LDA) were derived by assuming a uniform electron gas with constant density.[4] Using a Dirac expression of the exchange energy gives fairly accurate structures but tends to overbind molecules, limiting its usefulness.[9] Instead, general gradient approximations (GGA) are more widely used.[10] GGAs assume a constant electron density and the exchange correlation depends on the electron density and its gradient at each point. A functional that includes correlation and exchange at the GGA level yields a complete picture of localized exchange, left-right correlation, and dynamic correlation.[11] This results in reasonable local geometry and electronic structure, reproducing atomization energies, ionization potentials, and proton affinities, but underestimating reaction barriers, nuclear magnetic resonance (NMR) shielding, and non-localized excited states.

A natural expansion to a GGA functional would be to introduce the higher-order derivatives of the density. Meta-GGAs do just this and include both the Laplacian of the density and the gradient of the kinetic energy density, whose integral over space is the non-interacting kinetic energy.[12] Although meta-GGAs provide improved descriptions across a range of systems, they do not offer a significant improvement over GGAs for most molecules. Instead, hybrid functionals mix a percentage (α) of HF exchange with the DFT exchange to calculate E_{xc}. These functionals provide improved energetics leading to both better predictions of local properties and slight improvements in non-local properties. Hybrid functionals successfully describe many short-range electron-electron interactions; however, they can have large errors for long-range interactions like charge transfer, large delocalization of aromaticity, or intermolecular forces. Coulomb attenuation or range separation increases the amount of exact exchange as the interaction becomes longer-ranged.

To solve some of the issues with functionals that have incorrect $1/r$ behavior, range-separated (RS) hybrid functionals were developed.[13] Using a error function or parametrization, the amount of short-range and long-range interactions is controlled at different interaction distances. Many of these functionals are widely used because they provide accurate structures and energetics, particularly of systems that have long-range electronic interactions. Combined with dispersion corrections, RS functionals provide very accurate results for non-bonding and bonding interactions.[14] However, prediction of some properties are highly sensitive to the value of the range-separation parameter.[13] In contrast, double-hybrid (DH) functionals correct for the some of the lack of long-range correlation by adding dispersion forces directly from MP2 (Section 1.2.3) into the functional resulting in

an exchange correlation energy

$$E_{xc} = E_{xc}^{HGGA} + a_c E_{corr}^{MP2} \tag{1.12}$$

that is a combination of a hybrid GGA functional (E_{xc}^{HGGA}) and the MP2 second-order correction (E_{corr}^{MP2} or $E_0^{(2)}$ in Section 1.2.3), where a_c is the perturbative correlation fraction, analogous to the HF exchange fraction.[15] Dispersion corrections when added to DH functionals provide some of the most accurate adiabatic energies.[16] The implications of these long-range corrections for excited states are discussed in Section 1.3.3.

DFT has enabled widespread electronic structure calculations and remains the workhorse in computational quantum chemistry. Its affordability allows it to be used for large systems with hundreds of atoms, providing insight into many technologically relevant systems today, including metal-centered complexes, nanoparticles, and materials. However, in general, further improvement is needed in the description of E_{xc}. One of the largest issues is that the predicted energies are highly dependent on functional choice and more complex functionals do not always provide a better description of the electronic structure.

1.2.3 Møller-Plesset Perturbation Theory

Møller-Plesset perturbation theory (MP or MPn) improves the HF wavefunction and energy by including electronic correlation effects through perturbation theory.[1,17–19] By assuming that the true wavefunction and energy are reasonably close to what is predicted with HF theory, a Hamiltonian can be constructed as the sum of the HF Hamiltonian and a perturbation (V) with a variable parameter (λ). Solving the Schrödinger equation produces the ground-state energy

$$E_0 = E_0^{(0)} + \lambda E_0^{(1)} + \lambda^2 E_0^{(2)} + \lambda^3 E_0^{(3)} + ... \tag{1.13}$$

in terms of the nth-order MP energies ($E_0^{(n)}$). Here, the zeroth order energy ($E_0^{(0)}$) is simply the sum of the HF orbital energies, which double counts the electron-electron interactions. The addition of $E_0^{(1)}$ corrects this error, and the resulting energy is equal to E_{HF}. The first correction to the HF energy comes in at 2$^{\text{nd}}$ order, and therefore is referred to as MP2.[20] All perturbation corrections

above first-order serve to better approximate the electron correlation

$$E_{corr} = E_0^{(2)} + E_0^{(3)} + E_0^{(4)} + ... \tag{1.14}$$

In the literature, MP2 is the common truncation length for routine calculations, but it is possible to append higher order corrections for additional cost, *e.g.* MP3 and MP4.[21] However, as MP4 scales as $O(N^7)$, alternative higher-level methods such as CCSD(T) (Section 1.2.5) that provide more accurate descriptions at similar scaling are often used instead. It is now common to use scaled versions (see Section 1.2.7) of the MP2 correlation energy, which corrects for the MP2 overestimation of same-spin correlation energy.

MP theory systematically describes both electron-correlation and dispersion interactions. Perturbation theory ensures that higher-level corrections systematically improve energy. However, because MP theory assumes that a single reference HF wavefunction is a good representation of the electronic structure, it can still produce rather large errors for systems of large multi-reference character. In addition, convergence of MP theory can actually be slow, oscillatory, erratic, or even non-existent at higher orders.[22]

1.2.4 Configuration Interaction

Configuration Interaction (CI) corrects the HF energies by recovering the missing electron correlation energy.[1,23,24] By definition, the correlation energy is defined as the difference between the exact energy and the HF energy for a system described with an infinite basis

$$E_{\text{corr}} = E_{\text{exact}} - E_{\text{HF}}. \tag{1.15}$$

A portion of the correlation energy is recovered by constructing a superposition of ground and excited-state Slater determinants. Excited electron configurations are generated by exchanging electrons from occupied to unoccupied reference orbitals. In the linear expansion, each electronic configuration is assigned a unique coefficient. Subsequently, the coefficients are optimized to minimize the total energy of the system. Magnitudes of these coefficients can be thought of as the contributions of each determinant to the total wavefunction describing the ground state of the

system.

Full CI (FCI) uses all possible excited electron configurations, including single excitations ($|_i^a\rangle$), double excitations ($|_{ij}^{ab}\rangle$), and all other higher-order excitations, along with the reference configuration (ψ_0, usually HF) to represent the wavefunction. The FCI wavefunction

$$|\Psi\rangle = C_0|\psi_0\rangle + \sum_{i,a} C_i^a|_i^a\rangle + \sum_{i<j,a<b} C_{ij}^{ab}|_{ij}^{ab}\rangle + ... \tag{1.16}$$

provides an exact solution to the time-independent Schrödinger equation for a given basis set. Practically, the higher-energy configurations are less likely to contribute to the ground state, so full CI is often truncated to include configurations up to a certain excitation level, *e.g.* singles (S, CIS), doubles (D, CISD), triples (T, CISDT), and so forth. Truncated CI provides a way to approximate the electronic structure of molecules with substantially better scaling than FCI.

Although computationally cheaper, truncated CI falls short in maintaining both size consistency and size extensivity. Size consistency is the ability to properly describe the entire potential energy surface of a system, both at equilibrium geometries and when in the non-interacting limit, where most methods break down. Mathematically, a size-consistent method predicts that the energy of two non-interacting systems separated by a large distance is equal to the sum of the individual energies. Generally, size-extensive properties depend on the size of the system. In quantum systems, size extensivity describes the fact that the total energy should grow linearly with the number of electrons. In particular, for calculations of H_2 molecules, CISD fails at both size consistency and extensivity.

To grasp the significance of size consistency, consider the scenario of two infinitely separated H_2 molecules with a minimal basis set. A CISD calculation reproduces the FCI energy for two isolated H_2 molecules. However, the CISD of two non-interacting H_2 molecules does not reproduce this energy due to the absence of quadruple excitations, *i.e.,* local double excitations on each H_2 simultaneously. Consequently, this yields inconsistent energies between the sum of two isolated monomers and an infinitely separated dimer.[1] Similarly, in terms of size extensivity, imagine constructing a chain of N H_2 molecules and performing a CID (or CISD) calculation. Rather than showing the anticipated linear scaling of $O(N)$, the resulting energy scales as $O(N^{1/2})$, defying the physical expectation that the energy per H_2 molecule remains finite as $N \to \infty$.[1]

1.2.5 Coupled Cluster Theory

Because FCI is only computationally tractable for the smallest molecules and truncated CI is neither size consistent (with the exception of CIS) nor size extensive, an alternative electronic structure theory known as coupled cluster (CC) theory was developed to overcome these limitations.[25–27] Similarly to CI, CC theory recovers missing correlation energy by producing a superposition with excited electron configurations and the ground-state configuration. In contrast to CI, the series of excited determinants is constructed using the exponential cluster operator ($e^{\hat{T}}$) on a reference wavefunction, usually from HF molecular orbitals. This series of operators ($\hat{T}$)

$$\hat{T} = \hat{T}_1 + \hat{T}_2 + \hat{T}_3 + ... \tag{1.17}$$

act by exchanging a finite number (the subscript) of occupied orbitals ($\{ijk...\}$) with virtual orbitals ($\{abc...\}$) to produce excited configurations as Slater determinants

$$\hat{T}_n = \frac{1}{(n!)^2} \sum_{ij...} \sum_{ab...} t_{ij...}^{ab...} \hat{a}_a^\dagger \hat{a}_b^\dagger ... \hat{a}_j \hat{a}_i. \tag{1.18}$$

This works because $e^{\hat{T}}$ can be represented by its power series expansion

$$e^{\hat{T}} = (1 + \hat{T} + \frac{\hat{T}^2}{2!} + \frac{\hat{T}^3}{3!} + ...) = \sum_{m=0}^{N} \frac{\hat{T}^m}{m!}. \tag{1.19}$$

In the limit where all possible excited determinants for N electrons are included in the sum, the CC wavefunction is equivalent to the FCI wavefunction. Unfortunately, full CC does not avoid the exponential scaling of FCI. However, in truncated CC theory, the excitation order, *i.e.* how many electrons are excited, is restricted. By truncating the set of determinants to a smaller order, exponential scaling can be mitigated while simultaneously retaining size consistency and size extensivity. It is common to truncate the excitations up to second order (CCSD)[28] and to use perturbation theory to approximate the third-order excitations (CCSD(T)).[29]

In fact, CCSD(T) is often considered the gold standard for computing ground-state properties of molecules. By considering only first and second order excitations ($\hat{T} \approx \hat{T}_1 + \hat{T}_2$) the exponential

operator "simplifies" to

$$\begin{aligned} e^{\hat{T}} \approx e^{\hat{T}_1+\hat{T}_2} &= 1 + (\hat{T}_1 + \hat{T}_2) + \frac{1}{2}(\hat{T}_1 + \hat{T}_2)^2 + \frac{1}{6}(\hat{T}_1 + \hat{T}_2)^3 + ... \\ &= 1 + (\hat{T}_1) + (\hat{T}_2 + \frac{1}{2}\hat{T}_1^2) + (\frac{1}{6}\hat{T}_1^3 + \hat{T}_1\hat{T}_2) + ... \end{aligned} \tag{1.20}$$

Thus, even though the excitation operator is restricted to the truncated singles and doubles, approximations of triple- and higher-order excitations are provided by the disconnected excitations. For example, triple excitations can be approximated by applying the single excitation ($\hat{T}_1$) operation thrice (*i.e.* $\hat{T}_1^3$) or by applying the $\hat{T}_1$ operator followed by the double-excitation ($\hat{T}_2$) operator (*i.e.* $\hat{T}_1\hat{T}_2$). An identical process is used to approximate the higher-order excitations, which results in a size-consistent and size-extensive solution to the time-independent Schrödinger equation.

Unfortunately, most molecules of interest are too large for geometric optimization with CC theory, so optimized geometries are often obtained from DFT or MP2. This means that the electronic structure is only as accurate as the underlying nuclear coordinates. In other words, if the geometry is wrong, so are the CC energies. Accurate CC methods such as CCSD(T) scale as $O(N^7)$, which limits their applicability to small and medium-sized molecules.

1.2.6 Multiconfigurational Self-Consistent Field

Perturbation, CI, and CC theories work to systematically improve the description of dynamic correlation that arises from assuming that the electrons are non-interacting in the mean-field assumption. Another source of missing correlation, static correlation, arises from the assumption that the ground state is well described by a single Slater determinate. For some systems, the ground state is really a combination of multiple low-lying states. In particular, when modeling systems that involve the breaking and formation of bonds, transition metals, or radicals, the single-electron configuration of DFT or HF is often insufficient. Although unrestricted wavefunctions or densities offer a qualitative depiction of bond breaking via potential energy surfaces, they lead to quantitative inaccuracies.[30] The UHF wavefunction is not an eigenfunction of the spin operator ($\hat{S}^2$), therefore, to satisfy the spin operator and correctly describe bond breaking, a minimum of two determinants must be included in the wavefunction expansion. This is because at non-interacting distances, two degenerate electronic configurations are necessary.

In multiconfigurational self-consistent field (MCSCF) theory, the wavefunction of a particular state is constructed as a linear combination of a reference state and higher-order excited-state determinants.[31–33] Unlike CI, the reference configuration does not need to be the HF Slater determinant. This is because in MCSCF, both the linear CI coefficients and the orbitals are variationally optimized. Due to the complexity of this problem, the CI space is restricted to a set of hand-picked orbitals to form an active space.

Different methods of selecting the orbital subspace include hand selection (general MCSCF), complete-active-space selection (CASSCF),[33,34] or restricted-active-space selection (RASSCF).[35,36] Of these methods, CASSCF only requires the user to select the number of electrons and the subset of chemically relevant orbitals on which to perform a FCI expansion. RASSCF requires more user input to subdivide the orbital space into three regions. The first and third regions are restricted to include only a finite number of holes or electrons, respectively, with the middle subspace being equivalent to the CAS subspace.

Active space selection often relies on chemical intuition and can differ greatly depending on the systems considered. This can introduce a significant bias in the result. The combination of a steep learning curve and highly variable results has prevented these methods from supplanting other *ab initio* methods with more "black-box" tools such as TDDFT. Furthermore, CASSCF and RASSCF do not properly consider dynamic electron correlation, which has necessitated perturbative corrections, such as multiconfigurational second-order perturbation theory (*e.g.,* CASPT2) or multireference CI, to reliably produce ground- and excited-state energies and properties.[37,38] There have also been multireference[39] or multiconfigurational methods developed from density functional references for both ground and excited states. These methods[40,41] should be benchmarked for more systems as they are very promising, in particular for large radical or transition metal systems. In addition, although beyond the scope of this review, multireference methods are critical for reaction mechanisms where descriptions of conical intersections are important.[39,41]

1.2.7 Separate Spin Scaling

Calculating the correlation energy (E_{corr}) in most post-HF methods is computational expensive. In these methods E_{corr} is often the sum of all of the doubly excited determinant energies. Spin scaling starts from the idea that this sum can be split into two sums over the two spin cases, same spin

(SS) and opposite spin (OS) pairs.[42] As double amplitudes describe antiparallel (OS) and parallel (SS) spin pairs differently, they can be scaled separately[42,43] to generate a scaled correlation energy

$$E_{corr}^{scaled} = c_{SS}E^{SS} + c_{OS}E^{OS} \tag{1.21}$$

where the SS and OS energy scaling factors (c) for MP2 were set as 1/3 and 6/5 by Grimme.[43] This resulting "spin-component scaled" (SCS) version of a correlation energy provides a more accurate correlation energy for a large system. In order to reduce the computational complexity associated with the SS exchange contribution and because the same-spin correlation is already described at the HF level, a scaled opposite-spin (SOS) version that sets the $c_{SS} = 0$ and solves for an optimized OS component, 1.3 for MP2,[44] was developed. Because the correlation energy is ubiquitous in all ground and excitation methods, these corrections can be applied to many wavefunction and density based calculations.

1.3 Excited-State Methods

Similar to ground-state methods, excited states can be derived using either a density-based or wavefunction formalism. This section reviews common excited-state methods, providing a reference for Sections 2 and 2.6. The description begins with the re-purposing of ground-state optimizers for excited states (ΔSCF, Section 1.3.1) and extensions based on solving the time-dependent (TD) Schrödinger equation in either wavefunction (Section 1.3.2) or electron density form (Section 1.3.3), including the Tamm-Dancoff approximation. Among these, LR-TDDFT (Section 1.3.3) has become widely adopted due to its favorable scaling ($O(N^4)$) and its ability to reproduce spectral features for a broad range of medium to large systems. This section also covers promising functionals and formalisms that address specific limitations of standard LR-TDDFT theory, including the implementation of DH and RS functions for excited states (Section 1.3.3). Additionally, spin-flip (SF, Section 1.3.3) and real-time (RT, Section 1.3.3) TDDFT theories are summarized. The focus then shifts to CC-based methods for predicting excited states, concluding with a discussion of the algebraic diagrammatic construction (ADC, Section 1.3.5).

1.3.1 ΔSCF methods

The framework and algorithms developed to understand the ground-state properties of systems can also provide insight into electronic excited states. A basic technique for this involves manually creating a specific excitation by simply creating a hole in an occupied orbital, placing an electron in a virtual orbital, and then allowing the orbitals to relax around this constraint using a normal SCF procedure. By comparing the calculated energy of this non-Aufbau system with the calculated energy of the ground state, one can obtain an excitation energy. Such approaches have been appropriately referred to as ΔSCF methods and historically represent some of the first attempts of excited-state calculations.[45–47]

Several practical considerations are necessary when repurposing traditional orbital relaxation techniques for the calculation of excited states. In particular, traditional descent optimizers that minimize the total energy are prone to returning local minima or predicting non-orthogonal excited states in an effect known as *variational collapse*. Popular approaches to mitigate these issues include optimization with respect to different properties[48–50] or enforcing SCF constraints that result in maximum overlap between guess and optimized orbitals.[51] Furthermore, the multireference character of singlet excitations in closed-shell systems can be approximately restored by separately optimizing the triplet excited states as a correction factor for the singlet excitation energy.[52,53]

In the density form, when the above approaches successfully result in excited-state orbitals that have not collapsed, ΔSCF can predict excitation energies that are competitive with or better than alternative TDDFT methods (Section 1.3.3). Indeed, ΔSCF has proven quite useful for high-energy excited states, such as those involving core electrons, which is a regime that LR-TDDFT has typically failed to describe well.[54] Thus, the main application of the ΔSCF methods has been in the prediction and assignment of X-ray spectra.[55] However, an important limitation of ΔSCF that significantly prevents its widespread application is the need to manually specify which orbitals are involved in the target transition. This necessitates either a large number of independent SCF calculations to probe every possible transition or prior knowledge of the system. This makes it cumbersome or nearly impossible to predict the properties of new molecular frameworks *a priori*.

In wavefunction algorithms, SCF optimization of the orbitals of a core electron excitation are most often done using a core-valence separation (CVS) scheme.[56] This decouples the excitations

involving core electrons from the rest of the configurational space, reducing computational cost and the possibility of orbital collapse. These methods provide very accurate X-ray spectra predictions[57] and descriptions of excited properties when combined with equation of motion (like in Section 1.3.4) methods.[58] Indeed, density-based CVS methods are also gaining popularity for core excitations.[59]

1.3.2 Hartree-Fock-Based Excited States

Linear-Response Time-Dependent HF

Time-dependent Hartree-Fock (LR-TDHF or TDHF) theory is a linear-response extension of ground-state HF derived from first-order time-dependent perturbation theory. In the literature, these equations are often referenced as random-phase approximations (RPA)[60] to the time-dependent HF equation

$$\hat{f}(\mathbf{r},t)\psi(\mathbf{r},t) = i\frac{\partial}{\partial t}\psi(\mathbf{r},t), \tag{1.22}$$

and are composed of the product of the time-dependent Fock operator ($\hat{f}(\mathbf{r},t)$)

$$\hat{f}(\mathbf{r},t) = \sum_{i}^{N} \hat{h}_i(\mathbf{r},t) + \hat{J}_i(\mathbf{r},t) - \hat{K}_i(\mathbf{r},t) + \hat{v}_i(\mathbf{r},t). \tag{1.23}$$

and a Slater determinant derived from the ground-state HF. This is equal to the product of the imaginary number (i) and the partial derivative of $\psi(\mathbf{r},t)$ with respect to time. $\hat{f}(\mathbf{r},t)$ differs from ground-state HF theory because it includes a single particle time-dependent potential ($\hat{v}_i$), usually a time-dependent electric field. $\hat{J}$ and $\hat{K}$ are also time-dependent in TD-HF because of the time dependence on the wavefunction.[60]

Starting from the ground state, *i.e.*, the Slater determinant from the time-independent HF equations, the time-dependent change to the orbitals can be assumed to be small after some small time step. From this assumption, first-order time-dependent perturbation theory, neglecting higher order terms, should provide a reasonable approximation to solve for the wavefunction. In other words, only the linear-response effects from the time-dependent Fock operator on the time-dependent single particle wavefunctions are included.[60]

Derivation from the density matrix formulation (see references 61, 60, 62, and 63 for more

details) leads to a non-Hermitian eigenvalue equation

$$\begin{bmatrix} \mathbf{A} & \mathbf{B} \\ \mathbf{B^*} & \mathbf{A^*} \end{bmatrix} \begin{bmatrix} \vec{X} \\ \vec{Y} \end{bmatrix} = \omega \begin{bmatrix} 1 & 0 \\ 0 & -1 \end{bmatrix} \begin{bmatrix} \vec{X} \\ \vec{Y} \end{bmatrix}. \tag{1.24}$$

Here, **A** and **B** are orbital rotation Hessian matrices where

$$A_{ia,jb} = (\epsilon_a - \epsilon_i)\delta_{ij}\delta_{ab} + (ia||jb) \tag{1.25}$$

and

$$B_{ia,jb} = (ia||bj). \tag{1.26}$$

where ϵ_a and ϵ_i are the energies of the orbitals ϕ_a and ϕ_i, respectively, and $(ia||jb)$ are anti-symmetrized two-electron integrals. $\vec{X}$ and $\vec{Y}$ are eigenvectors with amplitudes involving the excitation and de-excitation of electron-hole pairs with excitation frequencies ω.

CIS and CIS(D)

Configuration interaction (CI) methods provide a natural extension of single reference HF theory for accessing excited states. As described above (Section 1.2.4), excited-state electron configurations are generated through the exchange of occupied and unoccupied orbitals. Of the CI methods, CI singles (CIS) offers an inexpensive way to predict excitation energies and other excited-state properties by limiting the type of excitations in the CI expansion to include Slater determinants where one electron is excited. The wavefunctions in CIS are

$$\psi_{CIS} = \sum_{ia} c_i^a \phi_i^a(\mathbf{r}) \tag{1.27}$$

where c_i^a are the linear CIS coefficients and $\phi_i^a(\mathbf{r})$ are excited Slater determinates generated from the HF reference state.[60] Through left multiplying by $\langle\phi_j^b|$ and subtracting the HF ground-state energy, CIS excitation energies can be obtained by solving

$$\sum_{ia} c_i^a \left\{(\epsilon_a - \epsilon_i)\delta_{ij}\delta_{ab} + (ia||jb)\right\} = \omega_{CIS} \sum_{ia} c_i^a \delta_{ij}\delta_{ab} \tag{1.28}$$

where ϵ_a and ϵ_i are the energies of the orbitals ϕ_a and ϕ_i, respectively, $(ia||jb)$ are the anti-symmetrized two-electron integrals, and $\omega_{CIS} = E_{CIS} - E_{HF}$ are the CIS excitation energies. In matrix form, these equations can be cast into an eigenvalue problem and solved through the diagonalization of matrix $\mathbf{A}$

$$(\mathbf{A} - \omega)\vec{X} = 0 \tag{1.29}$$

where $\mathbf{A}$ is

$$A_{ia,jb} = (\epsilon_a - \epsilon_i)\delta_{ij}\delta_{ab} + (ia||jb) \tag{1.30}$$

and $\vec{X}$ is an eigenvector of CIS coefficients. Diagonalization of $\mathbf{A}$ produces eigenvalues that correspond to the excitation energies ω and eigenvectors that correspond to the CIS expansion coefficients involved in each of the excited states.[60] CIS wavefunctions are size consistent with singly excited determinants that are orthogonal to the ground state. This allows both pure singlet and triplet states of closed-shell systems to be obtained. Importantly, the CIS total energy is analytically differentiable, meaning that excited-state geometries and vibrational frequencies are obtainable.[60] Often, CIS excitation energies are too large by 0.5 to 3 eV because the excited-state energies are the upper bounds to their exact values.[60] Additionally, the transition dipole moments and oscillator strengths are only semi-quantitative, because they do not obey the Thomas-Reiche-Kuhn dipole sum rule.[60,64]

CIS(D) introduces some correlation energy by including a perturbative doubles correction to the CIS energies and an MP2 corrected ground state.[65] CIS(D) is a second-order approximation to the CCSD eigenvalue equation which results in excitation energies

$$\omega_{CIS(D)} = E_{CIS(D)} - E_{MP2}. \tag{1.31}$$

In other words, CIS(D) is essentially an excited-state analog of MP2 theory. Unlike CIS, which scales as $O(N^4)$, CIS(D) scales as $O(N^5)$, similar to MP2.[65] Importantly, CIS(D) is size consistent, size extensive, and the energies are generally closer to experimental values than CIS energies.

1.3.3 Time-Dependent Density Functional Theory

TDDFT is a computationally tractable way to investigate the dynamic and excited-state properties of molecules and materials.[66–69] The Runge-Gross theorem provides a one-to-one mapping between the time-dependent external potential (v_{ext}) and the time-dependent electron density (ρ)

$$v_{ext} \overset{1-1}{\Longleftrightarrow} \rho, \tag{1.32}$$

for a given initial state.[66] This allows all of the excited states and their properties to be calculated using standard functionals of the electron density, just as is done in ground-state DFT.

The time-dependent KS equations[69]

$$i\frac{\partial}{\partial t}\psi_j(\mathbf{r},t) = \left[-\frac{\nabla^2}{2} + v_{KS}[\rho](\mathbf{r},t)\right]\psi_j(\mathbf{r},t), \tag{1.33}$$

depend on the effective KS potential

$$v_{KS}[\rho](\mathbf{r},t) = v_{ext}[\rho](\mathbf{r},t) + v_H[\rho](\mathbf{r},t) + v_{xc}[\rho](\mathbf{r},t), \tag{1.34}$$

which includes the external potential $v_{ext}[\rho]$, the Hartree potential ($v_H[\rho]$), and the exchange correlation potential ($v_{xc}[\rho]$). The time-dependent exchange-correlation potential attempts to encapsulate all of static and time-dependent many-body effects. Several approximations for $v_{xc}[\rho]$ have been developed over the years, ranging from the simplest adiabatic local density approximation (ALDA) to memory-dependent and non-adiabatic functionals.[70]

Linear-Response TDDFT

LR-TDDFT is the most common method for determining excitation energies and oscillator strengths for most molecules within the TDDFT framework. The theory assumes that the response to a small or weak time-dependent change can be approximated by a first-order perturbation to the ground-state density. In this assumption, the linear density response ($\delta\rho(\mathbf{r},\omega)$) is computed in the presence

of a small time- or frequency-dependent perturbation ($\delta v_{ext}(\mathbf{r},\omega)$):[60,69]

$$\delta\rho(\mathbf{r},\omega) = \int \chi(\mathbf{r},\mathbf{r'},\omega)\delta v_{ext}(\mathbf{r},\omega)d\mathbf{r'} \tag{1.35}$$

where $\chi(\mathbf{r},\mathbf{r'},\omega)$ is the density response function. It is common to represent the response function in the spectral representation

$$\chi(\mathbf{r},\mathbf{r}',\omega) = \lim_{\eta\to 0}\sum_n \left[\frac{\langle\psi_0|\hat{\rho}(\mathbf{r})|\psi_n\rangle\langle\psi_n|\hat{\rho}(\mathbf{r}')|\psi_0\rangle}{\omega-(E_n-E_0)+i\eta} - \frac{\langle\psi_0|\hat{\rho}(\mathbf{r}')|\psi_n\rangle\langle\psi_n|\hat{\rho}(\mathbf{r})|\psi_0\rangle}{\omega+(E_n-E_0)+i\eta}\right] \tag{1.36}$$

which reveals poles when $\omega = (E_n - E_0)$. Poles are the excitation energies for a given system in the LR approximation. Typically, these equations are cast into a matrix form known as Casida's equation (eqn. 1.24).[61] The matrix elements of **A** and **B** differ from LR-TDHF as they contain a response to the exchange potential called the exchange kernel (f_{xc})

$$A_{ia,jb} = (\epsilon_a - \epsilon_i)\delta_{ij}\delta_{ab} + (ia|jb) + (ia|f_{xc}|jb) \tag{1.37}$$

and

$$B_{ia,jb} = (ia|bj) + (ia|f_{xc}|bj). \tag{1.38}$$

More details regarding these equations and their derivation can be found elsewhere.[60,63,69] Solutions to this pseudo-eigenvalue problem give both the excitation energies (ω) and the transition vectors ($(\vec{X}\&\vec{Y})$) which are used to determine state-to-state transition dipole moments and oscillator strengths.

LR-TDDFT has been tremendously successful in describing valence excitations for a wide range of molecular systems and is often comparable in accuracy to wavefunction-based methods. While LR-TDDFT is an exact theory, the combination of approximations leads to problems with many functionals, resulting in the common sentiment that LR-TDDFT does not describe charge-transfer states, Rydberg states, and double excitations well.[71–76] In particular, the adiabatic approximation of the frequency-independent exchange-correlation kernel leads to predicted transition energies and properties that are highly dependent on the selected functional.[72,73,75] TDDFT is known for predicting spurious low energy excitations, sometimes called the ghost state problem. These low

energy states are a larger issue when predicting triplet excitations, where the energies are highly dependent on the amount of exact exchange in the functional.[77] Known as the triplet instability problem, erroneous triplet excitation energies arise from a ground-state triplet instability in functionals incorporating exact exchange.[77] These instabilities manifest as negative eigenvalues in the electronic Hessian and should be diagnosed using a HF stability analysis (*e.g.* with "Stable" in Gaussian 16[78]) when employing such functionals.[77]

Many research groups are attempting to develop new exchange-correlation, RS hybrids, and DH functionals[15,79–83] to improve predictions for these systems. In particular, DH functionals do not just provide a more accurate LR-TDDFT functional but are actually a mixture of TDDFT and CIS(D) (Section 1.3.2).[15] CIS(D) provides a perturbative correction to CIS excitation energies (like eqn. 1.31) that can be written as

$$\omega_{CIS(D)} = \omega + \Delta_{(D)} \tag{1.39}$$

where ω refers to the singles-only excitation energies that come from solving the Casida equations (eqn. 1.24) in the TDDFT or TDA (Section 1.3.3) form and $\Delta_{(D)}$ is the second-order perturbation theory doubles correction.[65] Thus $\Delta_{(D)}$ can be treated in the same way as the MP2 ground-state correlation energy in DH functionals (Section 1.2.2) and therefore DH-TDDFT also scales as $O(N^5)$. This provides a noniterative method that is applicable to large systems when applying the resolution of the identity approximation.[15] In particular, when DH functionals have HF exchange on the order of 50% they have reduced self-interaction error compared to local GGAs and normal hybrid functionals (typically 20% HF exchange) resulting in improved predictions of excitation properties. These methods can be improved by employing SCS (Section 1.2.7) schemes.[83,84,85]

Despite promising performance, DH-TDDFT still struggles to describe long-range excitations, like charge transfer. Combining promising DH and RS functionals provides a promising strategy for predicting accurate excitations with long-range corrections. Using DH functionals that have been implemented for excited states as described above and splitting their exchange terms into short- and long-range components provides a RS excitation method with the accuracy of a DH local density. Initial implementations have done this by splitting the HF exchange into short-range adjusted GGA and Fock exchange and unscaled long-range Fock exchange. The correlation energy

is the same as in underlying DH functionals, a combination of a scaled local correlation functional and scaled nonlocal correlation from MP2 for a ground state or CIS(D) for excited states.[83,86] Additionally, there have been efforts to scale the CIS(D) correlation.[82]

Also, going beyond the LR regime through quadratic or high-order response theories is an active area of research for predicting non-linear spectroscopic phenomena.[87] For example, a quadratic response function can be used to predict two-photon absorption amplitudes and transition properties between excited states without the need of an explicit wavefunction.[87]

Linear-Response Tamm-Dancoff Approximation

Starting from the Casida equations introduced in the LR-TDHF or LR-TDDFT sections (eqns. 1.24 and 1.37-1.38), the Tamm-Dancoff approximation (TDA) sets the **B** matrix to zero, *i.e.*, neglects it, which reduces the complexity of the equation to a Hermitian eigenvalue problem of the form

$$\mathbf{A}\vec{X} = \omega\vec{X} \tag{1.40}$$

with eigenvalues ω. The TDA of the LR-TDHF equation (TDA/TDHF) is equivalent to the CIS eigenvalue equation presented above (eqn. 1.29).[60] However, the TDA of the LR-TDDFT equation (TDA/TDDFT) is not equivalent to CIS because the matrix **A** includes the exchange potential (v_{xc}) and the exchange kernel (f_{xc}). Generally, TDA/TDDFT is a good approximation of TDDFT, which is not necessarily the case for TDA/TD-HF, possibly because the amplitudes of the **Y** matrix are smaller for TDA/TDDFT than TDA/TD-HF because TDDFT includes some electron correlation in the ground state and TD-HF does not.[60] TDA/TDDFT generally produces a blue shift in excitation energies compared to full TDDFT.[15,88] Depending on the system, this shift can be advantageous. In particular, for the triplet instability problem discussed above, TDA/TDDFT applied to various density functionals yields more accurate triplet excitation energies while preserving proper state ordering.[77]

Many of the extensions and corrections for TDDFT can be implemented within the TDA. In particular, TDA RSDH methods provide accurate calculation of excitation energies of molecules that is simple and cost effective. Long-range corrections are applied using a two-parameter decomposition of the Coulomb potential[89] for which both the exchange and correlation contributions are

range separated. Expanding this to DH excitations[82] leads to splitting the excitation energies (ω in eqn. 1.39) into short- and long-range components. This method differs from the ground-state version (Section 1.3.3) in that the range separation appears in both the exchange and the correlation contributions, as compared to just the exchange. Thus, this method requires the evaluation of the second-order corrections, which comes with computational cost. However, the more general implementation with arbitrary long-range and exchange parameters allows for any combination of exchange and correlation functionals.[82] Generally, both RS and DH methods show very promising results for important classes of molecules (discussed more in Section 2).

Spin-flip TDDFT

SF-TDDFT was developed to address some of the limitations of conventional LR-TDDFT to describe, for example, multiconfigurational and open-shell systems.[90] SF-TDDFT considers electronic transitions that involve both an electronic promotion and a spin flip. This is achieved by using a high spin reference state ($M_S = S$) and then generating the target-spin ground state, whose total spin ($M_S = S - 1$) is one unit smaller than the reference state. Generally, using a triplet reference state, a ground-state singlet is formed by a single spin flip combined with a single excitation or de-excitation. Excited states are typically generated as single and double excitations in an orbital subspace of closed- to open-shell excitations (c-v), open-shell to virtual excitations (o-v), and closed-shell to virtual excitations (c-v).[91] Usually, SF-TDDFT equations are cast in a matrix form that resembles Casida's equation

$$(\mathbf{A} - \mathbf{B})(\mathbf{A} + \mathbf{B})(\vec{X} + \vec{Y}) = \omega^2(\vec{X} + \vec{Y}), \tag{1.41}$$

where the $\mathbf{A} \pm \mathbf{B}$ are orbital Hessians and $\vec{X}$ and $\vec{Y}$ are eigenvectors with amplitudes involving the excitation and de-excitation of electron-hole pairs with excitation frequencies ω.

SF-TDDFT has been highly successful in describing homolytic bond breaking, diradicals, and even conical intersections.[90,92] The theory is particularly useful for studying photochemical processes with significant multireference character.[90] Unfortunately, SF-TDDFT can suffer from spin contamination after spin flipping because of the unrestricted high-spin reference state[90] or it can be difficult to converge to a solution away from the Franck-Condon region, as $\mathbf{A} + \mathbf{B}$ starts to have

negative eigenvalues.[93]

To overcome most of these limitations, mixed reference (MR) SF-TDDFT was recently developed.[94] MRSF-TDDFT has been shown to simultaneously describe the topology of conical intersections and eliminate spin contamination of SF-TDDFT. It can also produce doubly excited configurations that are critical for describing bond breaking, excited states, and conical intersections. MRSF-TDDFT can also be used to predict accurate X-ray absorption spectra by ensuring core-hole relaxation. What is particularly exciting about this method is that it formally scales as $O(N^4)$ so all of these benefits come at a fraction of the cost of more computationally demanding wavefunction methods, *e.g.*, CASSCF or CASPT2, that are generally used to describe these scenarios.

Real-time TDDFT

In traditional LR-TDDFT methods, the excitation energies of a system are obtained in the frequency domain for a system subject to a small perturbation. An alternate approach to obtain excited-state properties is real-time TDDFT, which explicitly propagates the one-particle KS wavefunctions in the time domain (via equation 1.33).[95] The properties of such a system are governed by the single-particle reduced density matrix

$$P_{\mu\nu}(t) = \sum_{i}^{N_{MO}} f_i C^*_{\mu i}(t) C_{\nu i}(t), \tag{1.42}$$

where $C(t)$ are the time-dependent orbital coefficients and f_i is the occupation of orbital i. The time evolution of the density matrix is governed by the Liouville-Von Neumann equations to yield

$$i\frac{\partial P'(t)}{\partial t} = [H'(t), P'(t)] \tag{1.43}$$

where $H'(t)$ is the time-dependent Hamiltonian matrix. Propagating the system in time reduces to computing the Hamiltonian at each time step using numerical integration. In practice, the relative intensities for excitations can then be computed directly from a fast Fourier transform of the dipole moment.[95]

The scaling of RT-TDDFT is better than that of LR-TDDFT, and therefore, RT-TDDFT is

an appealing alternative for capturing interactions of molecules and materials in weak and strong external fields in real time.[95] It can also be used to capture broad spectral regions with a high density of states. A key challenge of RT approaches is that the time dependence of $H'(t)$ arises not only from time propagation, but also from time dependence in the electron-electron potential (V_{ee}) term, creating inaccuracies in the calculated properties, such as unphysical peak shifting or incorrect charge transfer dynamics.[95] This problem has been somewhat alleviated by modifying traditional exchange-correlation functionals. Specifically, the most common approximation is to eliminate the memory dependence of the electron density, instead using the instantaneous electron density parameterized from the ground state.[95]

1.3.4 Coupled Cluster Based Excited States

Equation-of-Motion

Equation-of-Motion Coupled Cluster (EOM-CC) theory is a highly accurate single-reference wavefunction method that is used to describe excited states in a black-box fashion, similar to truncated CI. Excited states are constructed through a series of excited Slater determinate configurations from the ground-state coupled-cluster reference wavefunction (Ψ_{CC}).[96–99] The EOM-CC ansatz solves a modified Schrödinger equation

$$\hat{H}_N|\psi_k\rangle = \Delta E_k|\psi_k\rangle \tag{1.44}$$

using a normal ordered Hamiltonian ($\hat{H}_N$) to solve for k excited states,[100] where $|\psi_k\rangle$ is the k^{th} excited-state wavefunction and ΔE_k is the energy difference between a k^{th} excited-state and the reference CC ground state.

Excited-state wavefunctions are constructed by applying a linear, CI-like, excitation operator ($\hat{\mathcal{R}}$)

$$\hat{\mathcal{R}}_k = r_0(k) + \sum_{n=1}^{N} \frac{1}{(n!)^2} \sum_{ij\ldots} \sum_{ab\ldots} r_{ij\ldots}^{ab\ldots}(k) \hat{a}_a^\dagger \hat{a}_b^\dagger \ldots \hat{a}_j \hat{a}_i \tag{1.45}$$

to a coupled-cluster ground-state wavefunction (Ψ_{CC})

$$|\Psi_k\rangle = \hat{\mathcal{R}}_k|\Psi_{CC}\rangle = \hat{\mathcal{R}}_k e^{\hat{T}}|\psi_0\rangle. \tag{1.46}$$

Here, $r_{ijk..}^{abc...}$ are the right amplitudes, $\hat{a}^\dagger$ and $\hat{a}$ are the creation and annihilation operators, respectively, $\hat{T}$ is the cluster operator (eqn. 1.17), and ψ_0 is the HF reference wavefunction. By substituting the EOM-CC ansatz into the Schrödinger equation, left multiplying by $e^{-\hat{T}}$, and taking advantage of the fact that $\hat{\mathcal{R}}$ and $\hat{T}$ commute; an eigenvalue problem for the normal-ordered similarity-transformed Hamiltonian ($\bar{H}_N$) for the k excited states emerges

$$\bar{H}_N \hat{\mathcal{R}}_k |\psi_0\rangle = e^{-\hat{T}} \hat{H}_N e^{\hat{T}} \hat{\mathcal{R}}_k |\psi_0\rangle = \omega_k \hat{\mathcal{R}}_k |\psi_0\rangle, \tag{1.47}$$

with excitation energies (ω_k) and eigenvectors ($\hat{\mathcal{R}}_k$). Because $\bar{H}_N$ is non-Hermitian, the system is bi-orthogonal, meaning that two sets of eigenvectors and their corresponding eigenvectors can be solved for. These include the left ($\hat{\mathcal{L}}$) and right ($\hat{\mathcal{R}}$) excitation operators. Like the excitation operator $\hat{\mathcal{R}}$, $\hat{\mathcal{L}}$ is a de-excitation operator that essentially reverses what $\hat{\mathcal{R}}$ does.

In practice, EOM methods are often truncated to include only single and double excitations (EOM-CCSD), but calculations up to quadruple excitations (EOM-CCSDTQ) have been performed.[101] Additionally, the excitation space of EOM-CC must be expanded one excitation level above the state of interest because the transformed Hamiltonian contains three-particle and high-ranking operators.[102]

An alternative and cheaper approach to EOM-CC is similarity-transformed (ST)EOM-CC. In STEOM-CC, a second similarity transformation is performed on the Hamiltonian to generate a new Hamiltonian $\hat{G}$.[102] By doing this for EOM-CCSD, the two-particle matrix elements that couple the singly and doubly excited determinants are zeroed.[102] In turn, this reduces the complexity of the problem to one that diagonalizes $\hat{G}$ in the single-excitation space. Costs can be reduced even further when the STEOM-CC method is combined with the domain-based local pair natural orbital (DLPNO) scheme, and large systems with up to 100 atoms can be investigated with DLPNO-STEOM-CCSD/def2-TZVP.[103]

Another way to reduce costs is by reducing scaling with the approximate CC2 and CC3 methods that are widely available.[104] CC2 and CC3 methods approximate EOM-CCSD and EOM-CCSDT, respectively, with one order of magnitude better scaling. CC2 gives MP2 quality energies but, unlike MP2, excitation energies and transition moments can be obtained as poles and residues of the linear-response function, respectively.[104] In CC2, the equations for double excitations are

approximated while the singles are retained. Similarly in CC3, the equations for triple excitations are approximated, while the singles and doubles are retained.[104] Employing spin scaling (Section 1.2.7) can also reduce computational cost and complexity. In particular, SCS-CC2 provides balanced accuracy and cost.[105]

The excitation energies predicted via EOM-CC are equivalent to those predicted by LR-CC theory, but the transition moments and polarizabilities can differ.[104] Similar to the case for truncated CI and LR-TDDFT, users are only required to specify a certain number of excited states to solve for, making the barrier-to-entry rather low for even inexperienced practitioners. In general, the hierarchy of CC methods for excited states is as follows: CC2 $O(N^5)$, CCSD $O(N^6)$, CC3 $O(N^7)$, and CCSDT $O(N^8)$. Unlike other "black-box" methods methods, CC methods with higher computational cost tend to produce more accurate energies and properties.[106]

Linear-Response CC

Linear-response coupled-cluster theory (LR-CC) was derived from the time-dependent Schrodinger equation using perturbation theory.[97,107] Starting from the CC equations, rather than the CC wavefunction,[107] LR-CC provides a non-iterative way to solve for excitation energies and properties. Extending non-iterative CCSD(T) to excited states, since it produces such accurate ground states, would provide a cost effective excitation method for accurate excited-state electronic structures.

In the EOM (Section 1.3.4) formalism only iterative approximations to CCSDT such as CCSDT-n ($n = 1 - 3$) and CC3 can be extended to excited states by solving the left and right eigenvalue problems (eqn. 1.47).[107] The scaling of these methods is typically high, *e.g.*, EOM-CCSDT and CC3 scale as $O(N^7)$ and $O(N^8)$, making approximations important to reduce computational cost. Non-iterative or perturbative excited-state CC theories are only possible in the LR regime which does not require a CC wavefunction. As LR-CC and EOM-CC result in the same excitation energies and only differ in their transition dipole moments and oscillator strengths,[97,108] accurate results are expected in the LR formulism. This has allowed non-iterative approximations to be developed and expanded these methods to larger systems.

CCSDR(T) and CCSDR(3) offer two non-iterative approximations to CC3.[107] Both overestimate the triplet corrections[107] but CCSDR(3) was found to be the superior because it allows relaxation of the ground-state amplitudes and produces results closer to CC3. Non-iterative meth-

ods like CCSDR(3)[109] can substantially reduce computational cost for excited-state predictions.

1.3.5 Algebraic Diagrammatic Construction

Algebraic diagrammatic construction (ADC) schemes are another class of black-box excited-state methods that use a single reference MP ground state to approximate excited states.[110,111] Often, ADC methods are named according to their underlying MP reference; for example, ADC(2) is often referred to as "MP2 for excited states".[112,113] Their simple mathematical structure makes it possible to use robust iterative numerical solvers like the Davidson algorithm for optimizations.[112,113] These methods scale rather well compared to other excited-state wavefunction methods such as CASSCF/CASPT2 and EOM-CC, which makes them particularly well suited for single reference photochemistry problems.[64]

ADC based on the polarization propagator for electronic excited states was initially derived from Green's function theory.[110,111] The polarization propagator describes the time-dependent ground-state density or wavefunction fluctuations of a many-electron system.[112] The elegance of the formulation of linear-response ADC made it an appealing alternative to CC based methods,[60] however, the high computational cost limited its application to fairly small molecules.[114] In addition, the so-called "Dyson-ADC" cannot be used to explicitly construct excited-state wavefunctions, so it is limited in its ability to predict excited-state properties.[113]

To address this, ADC was reformulated in terms of an intermediate state representation (ISR) basis.[115–117] In the ISR, it becomes a Hermitian eigenvalue problem that takes the form of

$$\mathbf{MY} = \mathbf{Y}\Omega; \quad \mathbf{Y}^\dagger\mathbf{Y} = 1 \tag{1.48}$$

where $\mathbf{M}$ is the shifted Hamiltonian matrix with matrix elements

$$\{\mathbf{M}\}_{IJ} = \langle\tilde{\Psi}_I|\mathbf{H} - E_0^{MP}|\tilde{\Psi}_J\rangle. \tag{1.49}$$

$\mathbf{Y}$ is the eigenvector matrix, and Ω is the diagonal matrix of excitation energies (ω_n).[113] $|\tilde{\Psi}_J\rangle$ is the so-called intermediate state (IS), which is generated in two steps. First, the excitation operators ($\hat{C}_J = \{\hat{c}_a^\dagger\hat{c}_i, \hat{c}_a^\dagger\hat{c}_b^\dagger\hat{c}_i\hat{c}_j, ...\}$) up to a particular excitation level, *i.e.* singles, doubles, etc., are applied

to a reference MP ground state

$$\bar{\Psi}_J = \hat{C}_J \Psi_0^{MP}, \tag{1.50}$$

where $\hat{c}_a^\dagger$ and $\hat{c}_i$ are one-particle creation and annihilation operators, respectively. Next, a Gram-Schmidt orthogonalization procedure is performed to ensure that the correlated excited-state wavefunctions of different excitation classes are orthogonalized with respect to lower-excitation classes and the ground state.[113] After this, the eigenvalue problem is solved by diagonalization to determine the excitation energies and ADC vectors. The resulting ADC vectors are used to construct excited-state wavefunctions of the form

$$|\Psi_n\rangle = \sum_J Y_{Jn} |\tilde{\Psi}_J\rangle. \tag{1.51}$$

With these, all physical observables can be determined as a standard expectation value problem for a given operator. Fortunately, unlike some excited-state methods, ADC is both size consistent and size extensive.[113] Many scaling methods developed for MP2 or wavefunction methods can be combined with ADC to further reduce computational cost, like spin scaling (Section 1.2.7).[118]

Chapter 2

Performance of Excited-State Methods[†]

Developing new methods that provide more accurate descriptions of excited states for a wide range of systems has proven to be difficult in practice. There is constantly a trade-off between theoretical completeness, accuracy, and computational scaling. More accurate theories tend to scale poorly for more orbitals and more electrons. Even though multireference theories can provide both accurate ground-state orbitals and orbital energies, these methods are often limited to the smallest of systems. Therefore, benchmarking against either experimental energies or higher-level methods for small systems provides insights into the accuracy of methods that can be used for larger systems of experimental interest. However, it is difficult to appropriately benchmark against experimental energies because of a number of variables, including solvent, pH, temperature, and impurities. Generally, it is acceptable to benchmark against theoretical best estimates (TBEs) rather than experiment because of these difficulties. This necessarily limits the benchmark system size due to computational scaling and TBEs can be worse for large systems.

This chapter focuses on benchmarking excited-state methods applied to larger systems, as opposed to the smaller molecule sets typically used in method development. Most benchmarking studies have concentrated on vertical excitation energies, and as such, these will be the primary focus of the discussion below. Particular attention is given when other properties are also compared across

[†]Accepted at *Chem. Phys. Rev.* **2025**.

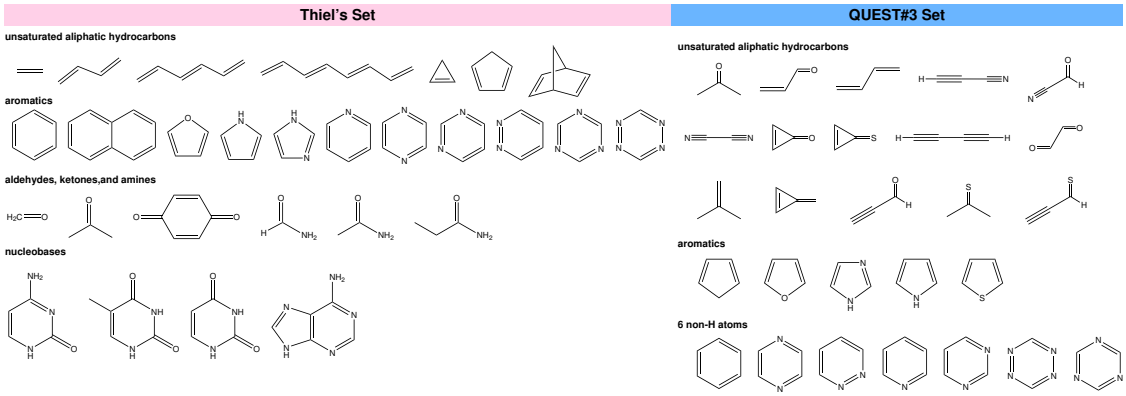

Figure 2.1: Thiel and QUEST#3 molecular test sets. Left adapted from J. Chem. Phys. 128, 13 (2008), with the permission of AIP Publishing. Right adapted with permission from J. Chem. Theory Comput. 16, 3 (2020). Copyright 2020 American Chemical Society.

larger sets of molecules. Starting with general guidelines (Section 2.1) summarized for systems of varying sizes, the chapter then covers recent results in areas where single-reference methods perform particularly poorly, including charge transfer excitations (Section 2.2), radical systems (Section 2.3), and metal-centered complexes (Section 2.4). Finally, the challenges of accurately describing common experimental dyes, such as boron dipyrromethene (BODIPY, Section 2.5), are highlighted.

2.1 General guidance

Benchmarking plays a crucial role in the advancement of new *ab initio* methods by evaluating the ability of a method to model, for example, excitations or to determine structure-function relationships for systems of interest. Many existing benchmarks focus on small molecules with fewer than a dozen atoms. This subset of structures provides abundant benchmark data as these systems are manageable in size for testing even the most costly methods. The availability of highly precise reference values from both experiment and higher-level theory enables a thorough examination of various approaches to modeling excitations and their impact on calculated properties.

The usefulness of benchmark results depends on the degree to which the test set is representative of technologically relevant molecules. Multiple benchmark sets have been developed and expanded over the years from those developed for ground-state properties[119] to those more focused on excited states like Thiel's,[120] QUEST,[121] (Figure 2.1) and other smaller sets.[122] In addition, there are many specialized sets developed for particular purposes, for example, XABOOM[123] that was developed

for X-ray absorption predictions or the SG set.[84]

One of the most widely used test sets (Figure 2.1) for organic molecular systems is Thiel's test set. This test set has evolved a bit overtime, with various TBEs adopted for different molecules in the set as discussed in detail in Ref. 120. The most robust version was proposed by Thiel *et al.* in 2008[120] consisting of 28 organic molecules designed to encompass different classes of chromophores, such as polyenes, unsaturated aliphatic compounds, aromatic hydrocarbons, heterocycles, carbonyl compounds, and nucleobases. The initially characterized valence excitations of the test set include 152 singlet and 71 triplet states.[120] The TBEs for the vertical excitation energies of these compounds were determined by calculations at the CASPT2,[120] CC3,[124] or various MR-CC/CI[125] levels of theory on either experimental or optimized structures.

An extensive number of benchmark studies utilizing Thiel's test set have revealed common trends with respect to method performance. In general, LR and EOM formalisms produce equivalent excitation energies.[97] However, the predicted properties can be quite different and differences in the predicted responses tend to increase with the number of electrons.[126] The most widely applied basis set, aug-cc-pVTZ has been shown to produce improved singlet and triplet excitation energies that are reduced by ~ 0.10 eV compared to the smaller TZVP basis sets at the CASPT2 level of theory.[127] While excitation energies are relatively insensitive to basis set, oscillator strengths and excited-state dipole moments are slower to converge with respect to basis set size.[128]

In addition, because the molecules in the test set cover a wide rage of chemistries, other studies have used the same molecules to benchmark excitations with Rydberg character.[129] In other studies that use Thiel's test set, the geometries are often optimized at MP2/6-31G* level of theory.[120,127–129] Furthermore, it has been widely shown that inclusion of diffuse functions in the basis set is critical to reasonably capture Rydberg states.[129,130] While, the majority of benchmark studies are still primarily concerned with achieving accurate vertical excitation energies, many theorists have attempted to develop better theoretical metrics beyond an adiabatic vertical excitation energy.[131,132]

One way to go beyond adiabatic excitation energies would be to calculate the $0-0$ energy (E^{0-0}), which is the energy difference between the zero-point vibrational energy of the ground and excited-state geometric minima. This provides one of the most direct comparisons between experiment and theory for gas phase molecules, where vibronic spectra are often measured with 1

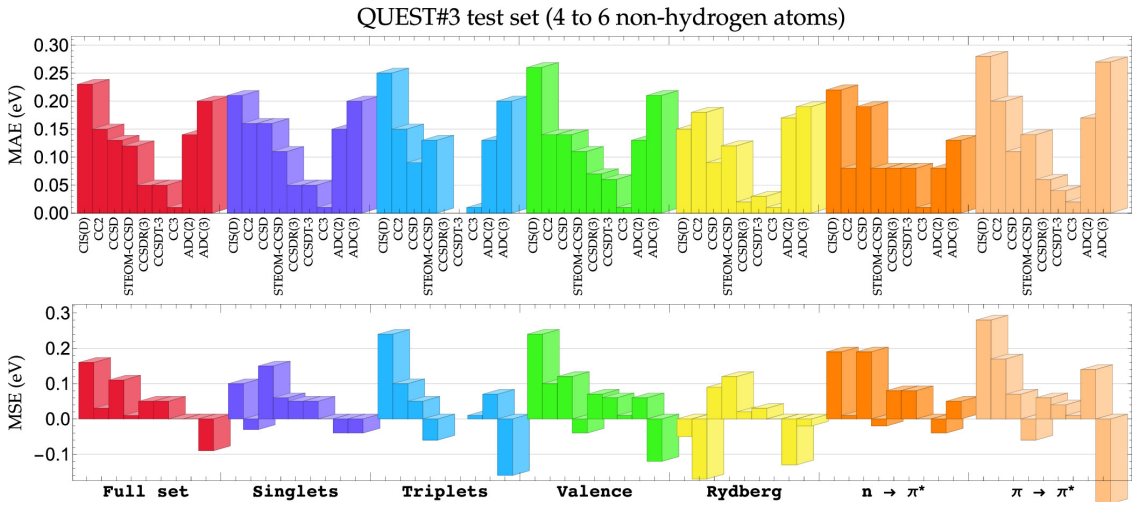

Figure 2.2: Performance of a wavefunction-based excited-state methods on the QUEST#3 molecular test set. Reprinted with permission from J. Phys. Chem. Lett. 11, 6 (2020). Copyright 2020 American Chemical Society.

cm^{-1} accuracy and for which the vibrational frequencies of the excited state are well estimated by harmonic oscillators. In solution E^{0-0} matches the crossing point between the normalized absorption and emission spectra, limiting its use for systems that have complex excited-state mechanisms or significant radiative decay. Different methods for calculating theoretical $0-0$ energies have been well reviewed in Ref. 131. Importantly, these analyses provide a rough estimate of the accuracies of given theoretical methods because of the direct comparison with experiment. In particular, hybrid functional TDDFT, ADC(2) and CC2, and CC3 increase in accuracy from $\sim$ 0.3 eV to 0.15 eV to 0.04 eV, respectively. While E^{0-0} has been well benchmarked, it is clear that it is also essential to benchmark additional properties and metrics when considering the overall quality of certain methods.[120,127–129,132]

An insightful meta-analysis of method performance as of 2020 using Thiel's test set[133] provides a good overview of wavefunction-based methods. For excitations without significant double-excitation character, CC3 energy values have mean absolute deviations less than 0.20 eV[120] with respect to CASPT2 results, which have errors of 0.11 eV from FCI.[134] For CC2 and CC3 calculations, the vertical excitation energies are nearly equivalent[128] with a correlation factor of 0.994 between the two methods. When comparing CC2 and EOM-CCSD data, CC2 is observed to outperform EOM-CCSD in certain cases, but EOM-CCSD demonstrates a more balanced performance across various types of excitations.[133] The accuracy of certain methods is influenced by the size of the systems

calculated, with CC2 showing better performance for larger molecules and poorer performance for smaller ones.[133] The size extensivity of certain methods is critical when considering dimeric systems and those characterized by large charge transfer (*Section 2.2).* The benchmark accuracy of ADC methods is highly dependent on parameters such as auxiliary basis sets, molecular grids, orbital domains, or pair natural orbitals (PNO) truncation thresholds.[101,118] Appropriate selection of these values can minimize the error below 0.1 eV. The EOM and STEOM methods exhibit similar performance and tend to outperform CC2 for both valence and Rydberg states.[133] More recent studies have focused on the SCS and SOS variants of CC2 and ADC(2) methods.[118] The vertical ionization and vertical electron affinities predicted by these methods generally show reduced errors and computational expense compared to their unscaled counterparts.[133] As a general rule, ADC(2), ADC(3), and CC2 predict errors of approximately 0.2 eV or less compared to the results of CCSDTQ and CCSDTQP.[101]

The QUEST test set (Figure 2.1) has also evolved over time[135] to include 500 vertical excitation energies of various natures, including $\pi \rightarrow \pi^*$, $n \rightarrow \pi^*$, double excitation, Rydberg, singlets, doublets, and triplets. In fact, the Thiel's and QUEST sets include some of the same molecules, resulting in similar TBEs between the two sets for many methods. Because QUEST has been more thoroughly benchmarked for density functional excitations (both TD and TDA),[121] it provides crucial insights for accurate predictions of excitations for large experimentally relevant models without fitting to experimental properties.[135]

While the reliability and accuracy of wavefunction-based methods are attractive for predicting excited-state properties (Figure 2.2),[136] their poor scaling prevents their use in modeling all but the smallest of technologically relevant systems. Even new active space approaches[137] that improve scaling, at best, scale as $O(N^5)$. Cost-effective DFT methods and TD extensions have broadened the size of molecules for which optimized structures of up to hundreds of atoms can be obtained. The development of empirical dispersion corrections has resulted in more reliable ground-state properties for larger organics, particularly aromatics.[16,138] Regularly, DFT is used to understand the band gap and absorption spectra of molecular chromophores,[139–143] polymer subunits or fragments, and crystalline organic materials[144–146] with applications from basic photophysics, photocatalysis,[147–149] energy generation,[150] or energy storage.[151]

In most fields, there is a standard set of functionals and basis sets that are widely used to

support experimental results. The standard in these fields is driven both by the computational cost and the availability of a particular functional or TDDFT method. Often, a standard in the molecular community consists of a hybrid or RS hybrid functional, with or without dispersion corrections, combined with a continuum model of a solvent, and a double or triple-ζ basis set for predicting optimized geometries and excited-state properties.[152] It is important to note that while dispersion corrections for both ground state and TDDFT predictions are widely used, these corrections were formulated for ground-state properties, and they inconsistently reduce the error of TDDFT, so they shouldn't be used as a black-box correction.[153] Depending on the choice of functional, DFT (both TD and TDA) methods generally produce results for small well-behaved systems within 0.22-0.45 eV of high level CCSDTQ and CCSDTQP methods.[101] In fact, the root-mean square error of particular hybrid functionals is around 0.27 eV that is even more accurate that CIS(D) excitations which for the same set of molecules had an error of 0.36 eV.[121] In addition, TDA has been shown to offer a good balance between accuracy and computational efficiency for many organic chromophores.[121] The computational cost for larger systems paired with the inability to optimize their electronic structure with higher level wavefunction methods, has limited the number and breadth of benchmarks for systems beyond 20 atoms or so.

When a hybrid functional is insufficient for a system of interest, it is possible to go up in theory and use DH functionals to improve the energetic descriptions of ground- and excited-state properties. In general, DH functionals tend to lead to the lowest energy differences for the main absorption feature with respect to the experimental excitation energies.[154,121] It turns out that the root-mean square (RMS) error for the best DH functionals is about one-half of that of the best hybrid functional, about 0.1 – 0.15 eV.[73,83,86,155] Thus, Jacob's ladder generally holds,[156,157] except that hybrid meta-GGAs are not universally better than hybrid GGAs.[121]

True benchmarking reveals that small computational changes can lead to large differences in accuracy: polarizable continuum model (PCM) solvents often improve energetic matches; RS hybrid functionals, such as ωB97X–D and CAM-B3LYP, improve intermolecular charge transfer accuracy;[106] DH functionals are more consistent when coupled with an augmented basis sets; and RSDHs can provide the energies for longer molecules.[154] This makes it difficult to choose a method for challenging molecules like BODIPY, where TDDFT and TDA tend to overestimate the first singlet excitation energy and underestimate the first triplet energy (Section 2.5).[158] Functionals

have been developed that correct the excitation energies for particular sets of molecules, but they tend to do this by adding or tuning adjustable parameters.[159] This takes them further from a true *ab initio* method and more toward a semi-empirical method. This frequently means that *when* these functionals fail to reproduce the excitation energy or the nature of the excitation, and it is not always clear why.

Although most benchmarking has focused on accurately predicting excitation energies or fitting to the main absorption peak, it is well understood that this only provides a narrow picture of accuracy. Fitting to the whole spectral range for organic photocatalysts reveals that DHs are the most accurate.[160,161] Specific properties such as oscillator strength and excited-state dipole moment are among several excited-state descriptors that have been suggested as convenient, yet insightful, benchmarks.[132,162] If the metrics for a "good" method are expanded to metrics that capture the types of excited states, it would be easier to prove that a method provides the right answer for the right reason. However, alternative parameters such as these can be more complex to benchmark because of how they are calculated in different methods.

Generally, hybrid TDDFT performs worse for excitations that are highly correlated or involve a charge transfer. For instance, the transition dipole moment can vary depending on the gauge used in the operator's interaction between the quantum system and the applied periodic field.[101] In the case of high-level wavefunction methods and most TDDFT functionals, this choice can be insignificant. However, variations in the excited-state dipole moment up to 15% have been reported for the M06-2X functional.[101] Metrics such as an electron-hole pair distance[132] or the excited-state dipole moment can help identify methods that correctly describe these hard-to-model types of excitations. DH functionals perform better than their HF exchange counter parts because the large Fock exchange reduces self-interaction errors and the nonlocal corrections provide better description of higher energy excitations.[163] Modern, RSDH functionals, like ω functionals, yield the most reliable excitation energies (Figure 2.3) for all kinds of singlet excitations.[83,84,86,155,164,165] Semi-empirical or parameterized RSDH provide accurate valence excitations, Rydberg excitations, and charge-transfer excitations.[82] The robustness of the second order correction for the excitations (Section 1.3.3) provides quantitative excitation energies even for double excitations.[75]

Furthermore, the cost-effectiveness of TDDFT makes it an important tool for understanding the geometries of excited states, while a full review of excited-state optimization and conical intersection

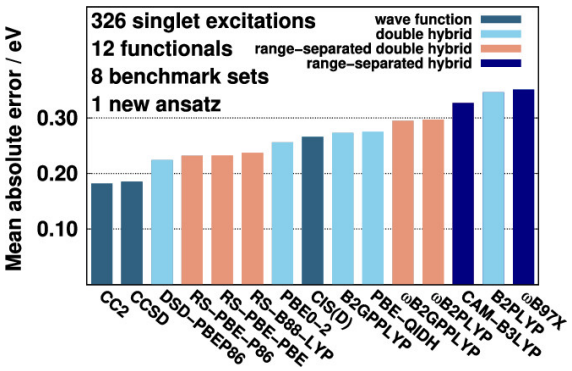

Figure 2.3: Performance of RS and DH functionals for excited states. Mester, D., Kállay, M., J. Chem. Theory Comput. 17, 2 (2021); licensed under a Creative Commons Attribution (CC BY) license. Copyright 2021 American Chemical Society.

is beyond the scope of this review a broad overview is provided here. The lowest energy singlet excited-state geometries predicted by CC2 and TDDFT have been shown to possess only minor structural differences (RMS = 0.011 Å).[166] Comparing TDDFT with CC3 or CCSDR(3) in a test set of 41 small and medium-sized organic molecules has also shown only small discrepancies in the excited-state geometries.[167] Specifically, DFT and TDDFT tend to predict bond lengths that are slightly compressed compared to CC3 and CCSDR(3). The predicted DFT bond lengths were also found to tend to increase with the amount of exact exchange included in the functional with mean absolute error (MAE) = 0.009 – 0.028 Å.[167] This effect is more pronounced for polar bonds such as C=O and C=S. In fact for systems in the QUEST set, the TDA excited states provide decent accuracy, especially for their computational cost.[121] Overall, these results suggest that DFT predicts fairly accurate geometries. And therefore, understanding excited states depends most on the quality of the transition energies and oscillator strengths.

2.2 Charge Transfer

Charge-transfer states (CTs) are particularly challenging to model for most theoretical approximations (Figure 2.4). Even when considering only the ground-state geometries, accurately describing non-covalent interactions, such as dispersion effects, has proven difficult for any method that approximates correlation through an average (or mean-field) electronic interaction. Furthermore, results are confounded by effects such as basis set superposition error.[168] Disperse electronic density errors from ground-state DFT persist in TDDFT and can introduce phenomena such as ghost

states or artificial red shifting of excitation energies.[106]

In addition to the problems inherited from ground-state DFT, the adiabatic approximation of TDDFT allows a frequency-independent kernel to be found at the expense of capturing certain excitation properties.[70] The adiabatic approximation has enabled LR-TDDFT prediction of chemically interesting systems with a wide range of approximate exchange–correlation functionals, as it is remarkably accurate for single excitations. However, errors are introduced from both the ground-state exchange-correlation potentials and the static kernel. Most corrections have focused on fixing the functionals to improve adiabatic TDDFT.[169] These functional fixes tend to focus on correcting a certain type of excitation, like CT states, but at the expense of describing other excitations well.[73,169]

Thus in most implementations of LR-TDDFT, an unequal description of local and CT excitations may lead to incorrect excitation energy ordering for these systems, leading to erroneous results.[73] Furthermore, in the ground state, dispersion interactions are typically accounted for by adding an empirical correction term to the functional. However, the fitting terms in many popular dispersion models are determined on the basis of ground-state polarizabilities. As the polarizability of excited states are inherently different from those of ground states,[170] the transferability of the ground-state dispersion to molecules in excited states is fundamentally limited. Furthermore, optimal tuning of the non-local Fock exchange term in hybrid functionals may also affect the applicability of dispersion terms, that were originally developed as ground-state corrections.[153] As excited-state systems are more polarizable, it was initially suggested that unadjusted dispersion corrections represent the lower bound for the dispersion energy of an excited-state system. Recently, the dependence of functional parameters on the dispersion correction was systematically tested and revealed that re-parameterization of the dispersion coefficients was dependent on the type of functional employed.[170] Specifically, PBE-based functionals exhibited a weak dependency on a range of dispersion values, while B88-based functionals are strongly affected by ω and predict a large systematic overbinding. It has been suggested that the key to mitigating such issues will be to develop more robust and chemically diverse functional fitting sets that allow functional parameters to be derived with more transferable parameters.[170]

Similarly to the benchmarking performed for organic molecules, there have been several attempts to benchmark the vertical excitation energies of dimeric systems.[74,105,171] In a series of

small dimers optimized in the ground state at the CC2/cc-pVDZ level of theory and with reference energies obtained at the CCSDT-3 level of theory, it was found that CCSD systematically overestimates CT excitation energies.[74] The magnitude of this overestimation increases for triple-zeta basis sets. Both CC2 and ADC(2) significantly underestimate the excitation energy of charge transfer states.[74] Compared to these, STEOM-CCSD shows some improvement and represents a cost-effective alternative.[74] Of the triple excitation methods, CC3 was the least accurate and significantly underestimates the excitation energy with respect to both CCSDT and CCSDT-3.[74]

The added degrees of freedom present in dimeric systems present additional metrics through which methods should be benchmarked. The ability to reproduce the dimer dissociation potential energy curves provides an obvious visual assessment of method performance. In these studies, STEOM-CCSD remains the most promising choice for these systems.[171] The larger error in CCSD, CC2, and ADC(2) manifests itself in potential energy curves with incorrect asymptotic behavior at infinite separation. At this limit, point charge transfer should be equal to the sum of the ionization potential and electron affinity of the respective subunits. However, recent testing of the SCS variants of CC2 and ADC(2) revealed that scaling can reduce the observed errors.[105] In some cases, these methods outperform CCS and CCSD when referenced against the CCSDT-3 energies.[105] CC2 and ADC(2) perform similarly with no clear winner.[105]

The considerations for modeling excitations in dimeric systems are also generally applicable to the cases of intramolecular charge transfer. In particular, polycyclic aromatic hydrocarbons (PAHs) are particularly challenging for hybrid functional LR-TDDFT to correctly order the lowest two singlet excited states, which are both $\pi \rightarrow \pi^*$.[172,173] DH-TD provides the most accurate predictions of the energies, ordering, and oscillator strengths for the singlet and triplet excited states in both linear and non-linear PAHs.[83,163] The DH and RSDH functionals have provided a significant improvement in excited-state predictions that does not depend on adjustment to experimental parameters. In particular, the SOS and SCS RSDH provide particularly low errors with RMSDs of SOS-PBE-QIDH and SCS-PBE-QIDH only 0.14 eV.[83]

As charge-transfer excitations are not clearly definable, several metrics have been proposed,[174,175] usually attempting to describe the distance between the hole and the electron upon excitation. Many TDDFT functionals do not provide adequate representations of intramolecular charge transfer, however some functionals, like ωB97X-D, CAM-B3LYP, and M06-2X, provide mean absolute

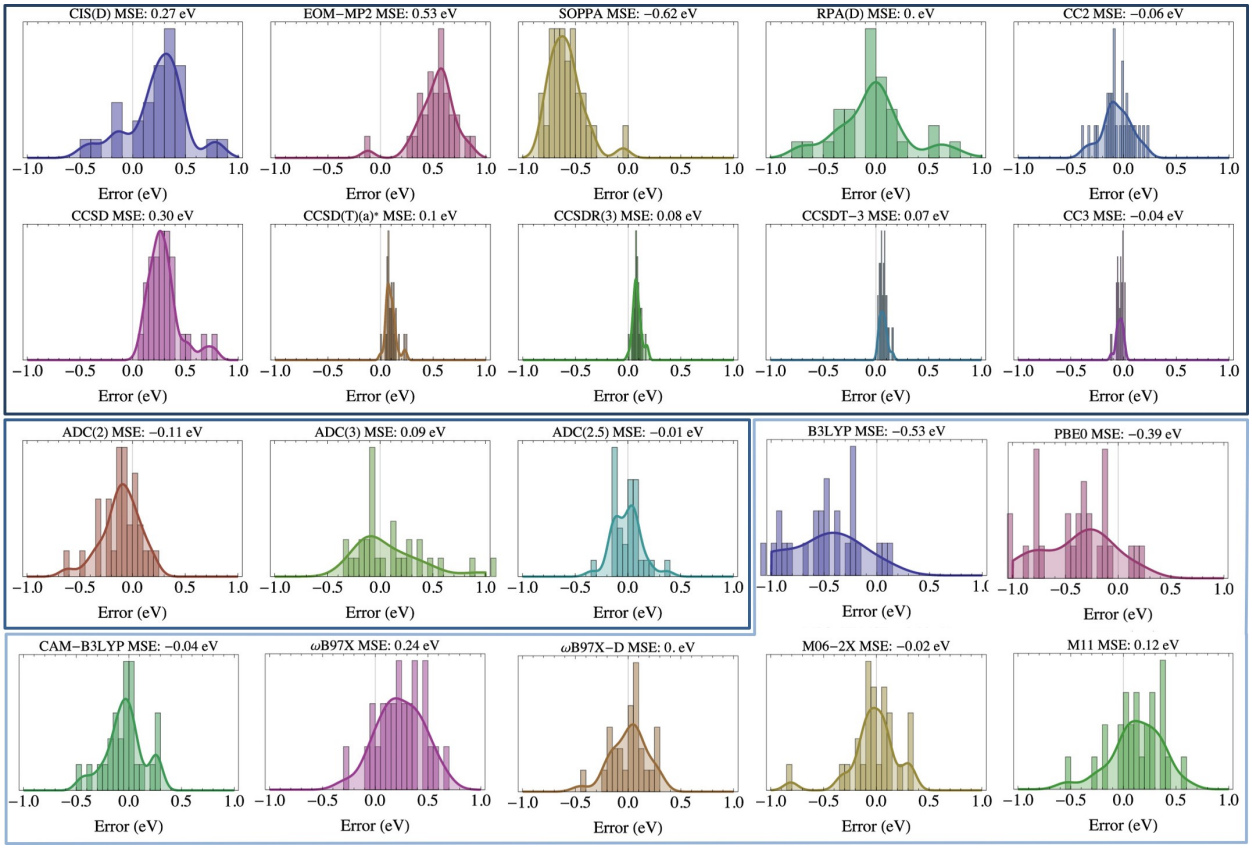

Figure 2.4: Error of charge transfer transitions. The error (eV) versus TBE/cc-pVTZ is reported for 31 transitions for wavefunction (upper dark blue box), ADC (middle blue box), and TDDFT (lower light blue box) methods. Adapted with permission from J. Chem. Theory Comput. 17, 6 (2021). Copyright 2021 American Chemical Society.

errors around 0.15 eV relative to CCSDT and higher reference values for a set of 30 transitions in 17 compounds.[71] For the same test set, CC2 was shown to yield MAE = 0.12 eV at a reasonable cost, while CC3 was the only method to produce chemically accurate results.[106] Alternatively, there are promising new density based multireference methods that must be benchmarked more thoroughly for larger CT systems.[176] The requirement of using higher level methods with large computational cost remains a significant barrier for studying these complex systems, and necessitates the development of improved methods that produce accurate results at reasonable cost.

2.3 Radicals

One area of photochemistry that is particularly challenging for computational chemistry is radicals or systems that have unpaired electrons. Most radical molecules result from an odd number of

electrons leading to a doublet ground state or from the separation of unpaired electrons on different areas of a molecule that can result in diradicals or triradicals. Diradicals have an even number of electrons, but at least two electrons are not spin-paired in the same orbital, leading to a complex electronic structure that cannot be adequately described by a restricted wavefunction or density method. Although protocols have been developed for optimizing and predicting the orbitals of radicals using both wavefunction methods and DFT, correctly calculating excited states is still difficult for most common methods.

DFT has two basic problems for representing the ground states of systems with unpaired electrons. First, like charge-transfer excitations, unpaired spins tend to be quite localized,[177] making many of the advances to better describe dispersion and other long-range effects of no use in improving the description of their excitations. Spin-flip methods provide a good way to deal with the ground-state orbitals being a bad reference by using unrestricted orbitals from a triplet guess for diradicals.[178] For small radicals, including those with Rydberg states, SF methods provide similar accuracy for doublet excitations as singlet excitations;[179,180] however, experience with larger aromatics shows that quartet guesses[181] do not necessarily provide a better reference state for doublet-doublet excitations. Second, in systems with unpaired spins, the arbitrary convention of assigning unpaired spins as spin-up seems to lead to more correlation errors due to orbital rotations.[182] In fact, using the same reference state, a canonical or a local orbital representation can have a large effect on the apparent multireference character of the system.[183]

For the ground state, it is clear that coupled-cluster methods predict more accurate orbital energies for these systems;[184] however, their scaling has limited benchmarking to very small systems, on the order of two to ten non-hydrogen atoms. Even in these fairly small systems, the error seen in cheaper wavefunction methods other than CC3 is large[71] (Figure 2.5).

Even with an accurate ground-state representation for an open-shell system, predicting excited-state properties is non-trivial. There is no obvious best functional as a starting point.[75,76] Currently, it is accepted that TD and TDA DH functionals are best for predicting excitation energies of organic molecules.[15,76] However, when comparing doublet-doublet excitation energies in 23 different small radicals, TDA causes blue shifting of the excitation energies, RS functionals result in large deviations unless spin-scaling was applied, and DH functionals do not categorically outperform hybrid functionals.[75]

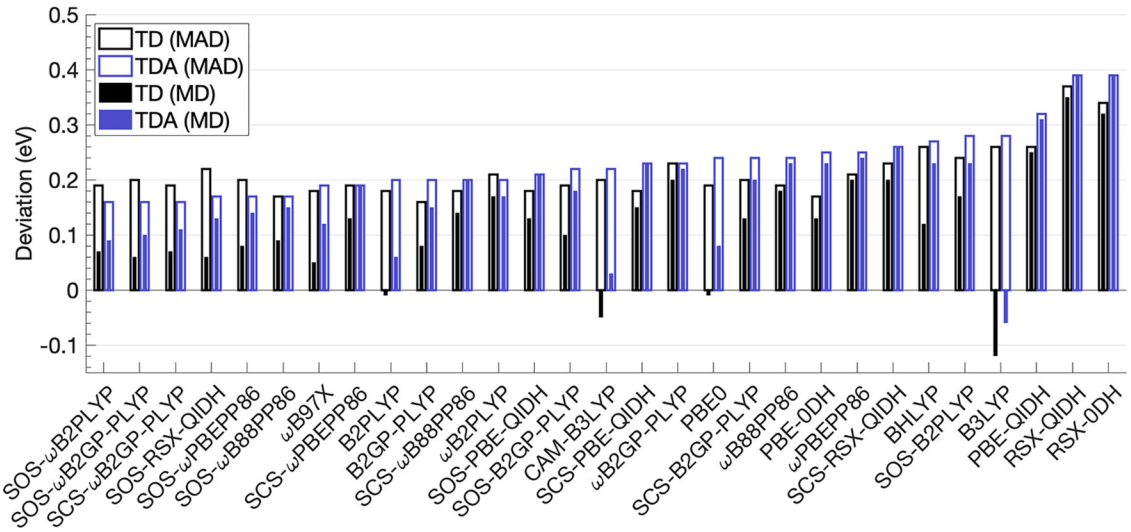

Figure 2.5: Mean deviation (MD) and mean absolute deviation (MAD) for a set of 41 of doublet–doublet excitation energies (in eV) using various TDDFT and TDA-DFT functionals. Van Dijk, J, Casanova-Páez, M., Goerigk, L., ACS Phys. Chem. Au 2, 5 (2022); licensed under a Creative Commons Attribution (CC BY) license. Copyright 2022 American Chemical Society.

It is now well established that the energy of any wavefunction method can be extrapolated to the complete basis set limit with different spin-scaling SCS or SOS components.[42,185] These corrections give rise to more accurate doublet-doublet excitations.[75] Unfortunately, optimal scaling parameters for the SCS and SOS components vary significantly between basis sets and the predicted property.[186]

2.4 Metal-Centered Complexes

One of the largest problems in quantum mechanical descriptions of metal complexes is that the frontier molecular orbitals are nearly degenerate and are frequently partially filled. This results in many electronic states that are close in energy, often of different spins, which gives rise to their interesting magnetic and optical properties. Unfortunately, this makes it difficult to calculate their energies and excited states accurately. In particular, there is a delicate balance between electron–electron exchange interactions and d-orbital splitting that requires an accurate treatment of both dynamic and static correlation.

It is well understood that CASSCF methods provide the most accurate descriptions of the orbitals in these systems. However, because of the missing dynamic correlation in CASSCF electronic

structures, multireference perturbation theory, *e.g.* CASPT2, is often required to reliably calculate properties, like energy differences, between different spin and excited states.[37,187] Despite these methods giving superior electronic structures, they come with significant computational cost and require an expert to choose an appropriate active space.[188] While there are general guidelines in the literature to choose active spaces,[189,190] along with some automated selection schemes,[191] there is still a relatively narrow set of metal-centered complexes which have been fully explored with these high level methods.[187,192–198] Furthermore, it is often difficult to retain a consistent active space when investigating multiple spin states for the same molecule. This is because an orbital that is important to describe one state or structure is not necessarily important for another, leading to different minimal active spaces for each state.[199] Some researchers have attempted to reduce the large CASSCF active spaces required for these systems by using RASSCF,[200,201] density matrix renormalization group methods,[202,203] and strongly contracted/partially contracted valence state perturbation theory.[204,205] Often, these methods lead to fairly good results for individual complexes. However, choosing an appropriate active space for these methods can be complicated.

Due to the high computational cost and the art of choosing active spaces, the DFT and TDDFT[187] methods are more commonly used to understand these systems. However, because of the approximations in DFT,[206] several functionals are reasonably reliable but *none* are universally appropriate for all systems or properties.[207,208] Of particular importance for transition metals, the hybrid density functional dependence of spin-state energetics[209] can be highly sensitive to the percent of exact HF exchange included.[210] Unfortunately, the value for mixing (α) that provides experimental agreement is difficult to know for each new system and therefore does not eliminate the need for a trained practitioner to perform even DFT level calculations. Importantly, tuning α does not correct for missing static and dynamic correlation but essentially hides the error. Despite these limitations, DFT can be accurate enough to determine the molecular structure and vibrational frequencies of these systems, allowing some of the cost of higher-level methods to be reduced by optimizing with DFT first and then performing higher-level single-point energy calculations on top.

Regardless of the level of theory, the predicted nature of each excited state is critical to understanding the photophysics and photochemistry of metal-centered complexes (Figure 2.6). The interaction between the ligands and the heavy atom gives rise to excited-state transitions centered

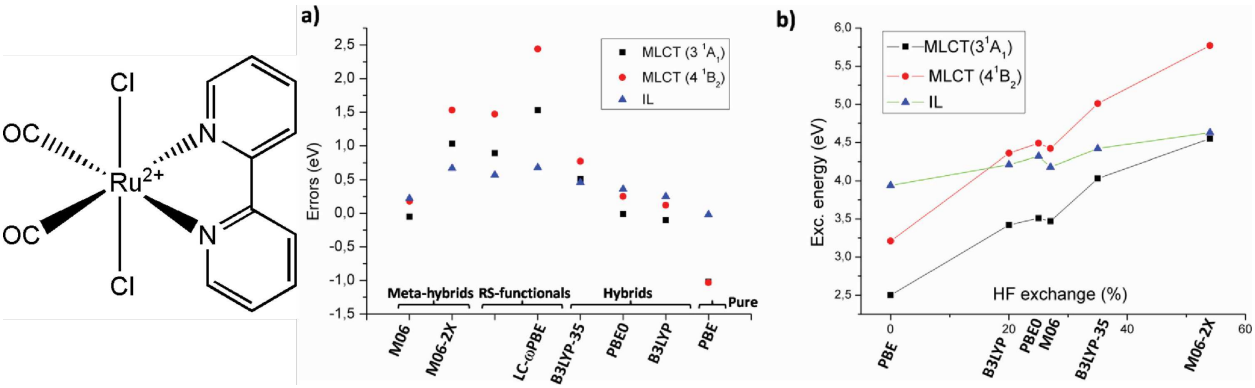

Figure 2.6: Excitation Errors for a small transition metal complex (*trans*(Cl)-Ru(bpy)$Cl_2(CO)_2$, left) for which C_2v single point CASPT2/CASSCF/ANO-rcc-VTZP and RASPT2/RASSCF/ANO-rcc-VTZP energies can be converged. (a) Errors in the vertical excitation for various types of excited states and (b) the effect of HF exchange (%). Adapted with permission from J. Chem. Theory Comput. 8, 1 (2012). Copyright 2011 American Chemical Society.

on the metal or centered on a ligand, or charge transfer excitations from metal-to-ligand, ligand-to-metal, or ligand-to-ligand. Typically, the nature of the excited state is identified by visualizing the orbital transitions or using a partitioning method to quantify the location of the orbitals.[211] Accurate prediction of the energy and nature of the excited states is a difficult and often tedious process for both general analysis and benchmarking. Experts in the field necessarily have to develop an eye for selecting a minimal set of orbitals that will converge and produce an accurate solution for a given molecule, when a high density of states will require multireference methods, and where including spin-orbit coupling[211] or thermal effects are critical.[212]

Because of the nuances of method selection, most of the benchmarks of spectral prediction focus on a particular molecular test set, like chlorophylls,[213] BODIPYs (discussed fully in Section 2.5),[152] or other transition metal complexes.[199,214,215] For non-transition metal-centered complexes, like chlorophylls and BODIPYs, most TDDFT approaches tend to overestimate excitation energies.[213] Using DH functionals, like B2PLYP for chlorophyll and DSD-BLYP or DSD-PBEP86 for BODIPY, can improve the accuracy of excitation energies over standard density functionals.[213,214] For transition metal complexes, it has become standard to use RS hybrid functionals, like CAM-B3LYP, or hybrid functionals like M06-2X, which also tend to overestimate excitation energies.[216] Notably, the newer better scaling domain-based local pair natural orbital (DLPNO) STEOM-CCSD method performed equivalently to the DH B2PLYP for predicting the excitation energies of chlorophylls.[213]

On the other hand, common functionals such as CAM-B3LYP, ωB97X-D3(BJ), BHandHLYP, and RSDH like ωB2PLYP overestimate the chlorophyll B-band energies.[213]

2.5 A case study on method performance: BODIPY

If the preceding sections are not clear on which methods to employ for a specific system, it is due to the challenge of establishing precise guidelines that are universally applicable to any molecular system. To further demonstrate the intricacies involved in selecting a method to model initial excitations, as well as to provide a more practical overview of the field, we present a case study for the widely studied BODIPY molecule. BODIPY and its derivatives are characterized by a boron diflouride group bonded to two pyrrole rings. These molecules present unique photophysical properties, such as large molar extinction coefficients in the ultra-violet visible region, high fluorescence quantum yields, tunable absorption and emission processes, and high stability. They are chemically related to cyanine dyes, and thus previous studies have considered the benchmarking data to be generally applicable to both families. By itself, the base BODIPY molecule is amenable to calculation with high-level computational methods such as CASPT2. However, there is extensive interest in substituting the BODIPY rings to tune the photophysical properties. These substitutions may involve a large number of atoms, which is accessible only with DFT methods. Therefore, understanding the quality and availability of DFT descriptions of BODIPY is also critical.

The difficulty in calculating a realistic electronic structure of BODIPY stems in part from its complicated ground state, which has non-negligible electronic correlation due to its open-shell character. In fact, the best ground state includes approximately 2.6% of doubly excited electron configurations.[158] Consequently, many methods struggle to calculate the low-lying excited states, often significantly overestimating vertical excitation energies.

Most TDDFT methods overestimate the first vertical singlet excitation TBE by 0.2 eV or more (Table 2.1). It is notable that some of the best agreement with experiments is obtained from simple GGA functionals, such as BLYP and PBE. This is likely due to error cancellation and therefore may not provide adequate insight into the underlying physics of the predicted process.[219] Furthermore, the common practice of defining the first experimental excitation based on the λ_{max} shows opposite trends in accuracy compared with the TBE (Table 2.1). In fact, worse agreement

Table 2.1: Vertical singlet excitation energies for photochemically equivalent BODIPYs. Experimentally the first excitation is found at 2.460 eV[217] and the TBE (CC3/AVTZ) is 2.77 eV.[218]

	BODIPY TD	dimethyl-BODIPY TD[158]	dimethyl-BODIPY TDA[158]
BLYP	3.006[a]		
PBE	3.020[a]	2.94	3.38
B3LYP	3.154,[a] *3.129*[b]	3.02	3.38
PBE0	3.186[a]	3.05	3.41
LC-BLYP	3.073[a]		
LC-PBE	3.084[a]		
CAM-B3LYP	3.145[a]	2.99	3.31
ωB97XD-D	3.147[a]		
LC-ωPBE	3.077[a]		
PBE50		3.08	3.41
ωPBEh		3.00	3.31
ωPBE		2.93	3.23
M11-L		3.02	3.39
M06-2X		2.99	3.32
B2PLYP			3.12
SF-PBE50			3.02
CIS	3.519[a]	3.38	
CIS(D)	2.968[a]	2.84	
ADC(2)		2.71	
SOS-ADC(2)		2.48	
ADC(2)-x		1.93	
SF-ADC(2)		2.82	
CC2		2.84	
ADC(3)		2.42	
DLPNO-STEOM-CCSD	*2.463*,[b] **2.469**[c]		
EOM-CCSD	2.973[a]	2.83	
RAS-SF		2.91	
CASPT2		2.48	
TD-HF	3.206[a]		
LCC2*	2.647,[a] 2.643[c]		
SAC-CI	2.657[a]		
CASSCF	**2.829**[a]	2.80	
CASPT2	**2.538**[a]		
CCS	**3.578**[a]		
CC2	**3.017**[a]		
CCSDR(T)	2.380[a]		
CCSDR(3)	**2.895**[a]		

Most calculations use the cc-pVTZ basis set. Those that use **cc-pVDZ** or *def2-TZVP* are indicated. [a]Ref. 219. [b]Ref. 103. [c]Ref. 220.

between the first singlet excited state and the experimental λ_{max} often coincides with an increase in the accuracy of the energy of the first triplet excited state (*ex.* Table 2.1 TDA),[158] revealing that either choice leads to an incomplete picture of the photophysics of the molecule. In addition, while a polarizable solvent is often recommended to obtain better agreement with experiment, in LR-TD methods this mostly corrects for dispersive effects. Thus is systems, like BODIPY, where the lowest energy state is brightly emissive, the coupling between the first excited state and the ground state should be large even in apolar solvents, which is not captured by these simple polarizable models. Ultimately, the misleadingly high performance of the GGA functionals and the effects of the TDA approximation underscore the shortcomings of using simple metrics, such as vertical excitation energy or comparing to λ_{max}, to assess the overall quality of a method.

TDDFT is able to capture the main spectral features of BODIPY, and can still provide qualitative trends and correct ordering of substituted BODIPYs, allowing for more quantitative ordering with a simple linear correction.[219,221] CAM-B3LYP and M06-2X predict the most accurate excitation energies, where the latter has previously been recommended for excited states of BODIPY.[222] Exploration of the potential energy surfaces of BODIPY also shows that M06 and M11 provide the best descriptions of the excited-state geometries.[221] These methods have been shown to predict improved T_1 energies that approach the accuracy of CASPT2.[158] Comparisons of the first dipole-allowed vertical singlet excitation energy, shows reduced error using SCS-DH functionals, on the order of 0.1 eV.[214,223] Thus, DH functionals are probably needed to obtain a more accurate evaluation of the relative ground-state (S_0), T_1, and S_1 energies.[224]

Wavefunction methods lead to more accurate excited states for BODIPY, and greatly reduce the overestimation of vertical excitation energies (Table 2.1). Among these, local CC singles and approximate doubles (LCC2*) and SOS-ADC(2) perform well and are attractive options for larger BODIPYs, considering their reduced cost compared to methods like CASPT2.[219,220] However, the superior performance of LCC2* can be attributed to a cancellation of errors rather than a correct description of the underlying physics.[220] EOM-CCSD appears to be a bad choice for these compounds, as CIS(D) can predict similar or more accurate results (Table 2.1). The DLPNO-STEOM-CCSD method is also notable in that it provides some of the TBEs of both the first excited-state singlet (S_1) and the first excite-state triplet (T_1) for all methods presented here at significantly reduced computational expense compared to other wavefunction methods.[103,220] Over-

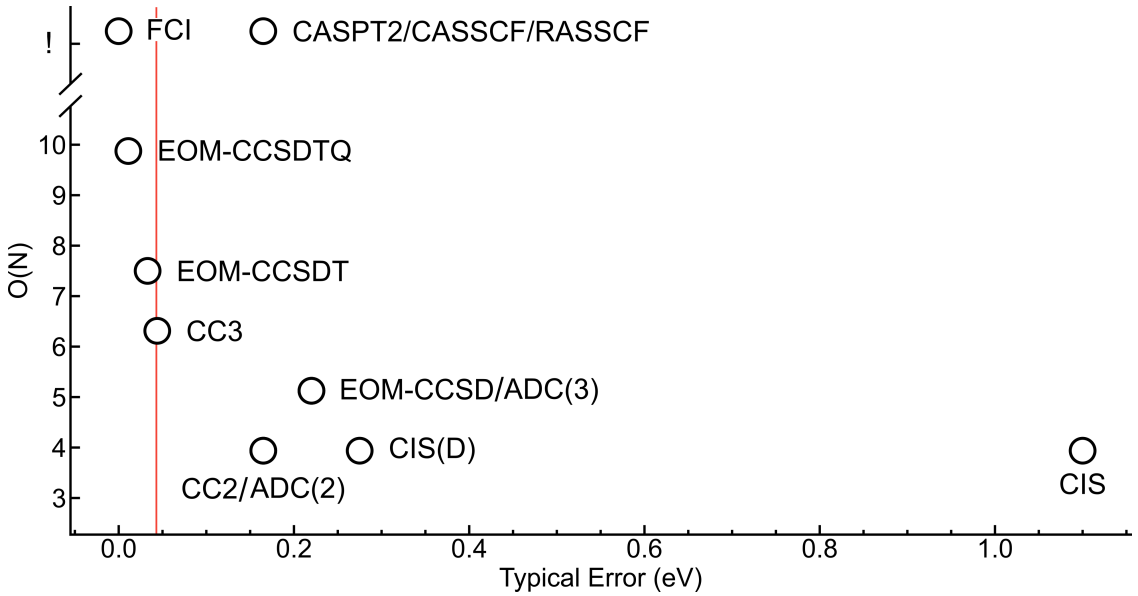

Figure 2.7: Computational scaling and typical error[136] for the methods discussed in this review. The red line is chemical accuracy.

all, these results underscore how difficult it is to study a new photochemical system and choose a computational method that balances accuracy and efficiency in capturing the correct excitation physics and properties.

2.6 Conclusion and Outlook

The discussion above demonstrates the significant advances that have been made toward accurately calculating excited-state properties for a variety of molecular chemistries and system sizes. It is clear that there is always a trade-off between accuracy (Figure 2.7) and computational effort. While methods such as CC3 and EOM-CCSDT demonstrate capabilities that exceed chemical accuracy, they are often too expensive for systems under experimental investigation. In general, the trends revealed by this review show that predictions using long-range corrected DFT functionals are often an appropriate and affordable starting point for most molecules. RSDH functionals provide the most accurate energies and properties for molecules where hybrid functionals traditionally fail. Beyond TDDFT methods, there is no universal or obvious next-best method. In general, wavefunction methods like ADC(2) and CC2 produce reasonable results at higher costs but are not necessarily better than TDDFT methods. Therefore, lower-scaling EOM-CC methods and RSDH

excitation methods that retain accuracy at a fraction of the computational cost are promising avenues for future developments. Specifically, when investigating a new class of molecules or trying to understand complex experimental data, it can be difficult to pick a computational method that gives the best balance of accuracy and effort. This is because, despite efforts to make benchmark data more accessible, the community still lacks a centralized location to compare methods for a variety of chemical systems.

In addition to the development of new accurate and affordable methods, *benchmarking should be the responsibility of the whole community.* And thus *we* need to:

(1) *Benchmark beyond vertical excitation energies.* It is critical to benchmark parameters beyond the vertical excitation energies to ensure that the methods are providing the correct results for the right reasons. A wider focus on predictions that provide an accurate understanding of excited states could help eliminate the use of methods, such as BLYP, that yield deceivingly accurate vertical excitation energies while missing other properties, like the Rydberg character of excited states.[132] In particular, the practice of fitting vertical TDDFT excitations with experimental λ_{max} is both theoretically questionable and also biases functional choice. While the onset of absorption might be a better estimate for the first calculated vertical excitation energy, comparison to experiment should be done with caution as there are many confounding factors like solvent effects. Systematically examining other excited-state properties provides opportunities to gain deeper insight into the shortcomings of specific methods. One challenge that prevents benchmarking these parameters lies in the non-standard, and often non-trivial, calculation of excited-state properties. In addition, benchmarking against what have long been seen as qualitative metrics, such as the charge-transfer character, requires quantifying these ideas in a standardized metric. However, to predict the correct excited-state properties, methods need to be benchmarked with both excitation energies and a metric of the excitation character, which could include oscillator strengths, electron-hole distance, and correct orbital decomposition.

(2) *Increase the availability and user-friendliness of new methods.* In addition to fully understanding method performance for a variety of systems, it is also critical to make newly developed methods user-friendly and widely available in existing quantum chemical software

packages. Lack of availability and user-expertise are some of the biggest hurdles for predicting excited-state properties using methods beyond TDDFT. While, most codes provide small molecule examples and tutorials to help users check that the method is running correctly, many researchers find it difficult to converge or know when a calculation has run accurately. Often researchers fall back on the "if ain't broke don't fix it" way of thinking and choose to stick with LR-TDDFT because the predictions are "good enough." In the case of calculations where an active space or orbitals need to be selected, despite recent developments to automatically select the active space,[191] untrained users often produce inaccurate results by improperly selecting too few or by missing chemically important orbitals. In order to stimulate broad adoption, beyond users trained in groups that develop the method or that attend specialized theory workshops, more tutorials on how to run methods for experimentally relevant systems are needed. In particular, example calculations that trigger known chemical inaccuracies when naive choices are made would allow novices to build intuition on how to run and troubleshoot these methods before extending them to their research questions.

(3) *Try new methods on larger systems.* Once implemented, computational researchers must take advantage of these new methods. Most researchers employ standard TDDFT methodologies as their initial approach to modeling excited states of experimental systems. Often, alternative methods are only used when TDDFT fails to confirm pre-existing notions of the chemical system or match an experimental result. In such cases, common practice is to switch or tune the functional to align more closely with experimental data or to transition to more advanced wavefunction techniques. Notably, a prevalent tendency is to favor the former over the latter. It is fairly common practice to include functional scans in supplemental information, but rarely does one see a comparison to wavefunction methods in a combined DFT and experimental paper. Indeed, I and the Fredin group notice a reluctance to explore wavefunction methods due to perceived computational costs, which are not always accurate. Furthermore, it should be more acceptable to document and share when a particular method has failed to describe a system. It is the responsibility of computationally focused groups (including our own) to model best practices when it comes to method comparison and adoption.

I believe that adopting these suggestions as a community will extend the role of computation

in obtaining useful, reliable, and robust excited-state information that is directly comparable to experiment.

In addition to the development of excited-state methods that provide a more accurate description of excited-state properties at a reasonable computational cost, I look forward to upcoming advancements that tackle some of the more complex and subtle challenges of computational modeling. One such challenge lies in capturing excited-state dynamics. With quantum dynamics methods like Tully's fewest switches surface hopping (FSSH) scheme,[225] ab initio multiple spawning (AIMS),[226] ring polymer molecular dynamics (RPMD),[227] and exact factorization,[228] it is possible to simulate non-adiabatic excited-state dynamics with great accuracy and reasonable costs, depending on the underlying excited-state method(s). For the curious reader, we point to references 229 and 230 for more details on excited-state dynamics, as a detailed discussion is beyond the scope of this review. Furthermore, the nuclear-electronic orbital (NEO) method offers the potential to go beyond the BO to treat nuclei quantum mechanically to determine various excited-state vibronic properties at various levels of theory.[231] The recent emergence of machine learning approaches in chemistry and physics may provide new avenues for affordable calculation of excited-state dynamics, either by extending the timescales that can be modeled or the number of trajectories run to more fully explore the reaction space.[232]

While affordable excited-state methods of FCI quality will likely remain out of reach for some time, the wide number of developed approximations and the progress achieved by each instill a sense of optimism for the future of quantum-mechanical modeling. This ever-evolving landscape of excited-state methods shines light on the intricate nature of molecular systems, improving our understanding of both photophysics and quantum properties. By describing molecular systems accurately with quantum mechanics, a deeper understanding of structure-function relationships in these important molecular systems is developed, potentially leading to rational molecular design.

Part II

Computational Photochemistry and Photophysics

Chapter 3

Controlling Pyridine Azo Dynamics with Protons[†,‡]

3.1 Introduction

Azo dyes (Ar−N=N−Ar) make up the majority of organic dyes used in the textile and food industries due to their vibrant colors and synthetic modularity.[233–235] Their color, governed by their absorption maximum (λ_{max}), depends on the size of the aromatic rings and the substituents on them. Because of their intricate electronic structure, their photophysical properties can also be modified by changing the pH or solvent.[236–239] In solution, the ground state of most azo dyes is the *trans*-isomer, with a few notable exceptions, such as diazocines whose strained cyclic structure stabilizes the *cis*-isomer.[240]

When photoexcited with ultraviolet (UV) or visible light, azo dyes can isomerize from the *trans*- to the *cis*-isomer through dynamics in low-lying excited states.[241,242] The meta-stable *cis*-isomer can revert back to the *trans*-isomer thermally, on the ground-state singlet surface, with a half-life ranging from microseconds to hundreds of days.[233,234,243,244] Alternatively, the *cis*-isomer can be rapidly forced back to the *trans*-isomer through a second photoexcitation, typically with a longer excitation wavelength than the λ_{max}.[233] The half-lives of thermal reversion can be modified through

[†]Reprinted with permission from Knepp, Z. J.; Hamburger, R. C.; Thongchai, I. A.; Englehart, K.; Sorto, K.; Jaffer, A.; Young, E. R.; Fredin, L. A. *J. Phys. Chem. Lett.* **2024**, 15, 38, 9593–9600. Copyright 2024 American Chemical Society.

[‡]Electronic supplementary information is available at https://doi.org/10.1021/acs.jpclett.4c02155.

clever aromatic or hetero-aryl substitutions,[245,246] allowing azo moieties to control the potency of photopharmaceuticals in a variety of therapeutic scenarios.[247–251] Long half-lives also give azo dyes the ability to store energy in the meta-stable *cis*-state as molecular solar thermal fuels.[252–254] For example, pyridine-based azo dyes have been incorporated into a range of photomaterials[255–258] and photopharmaceuticals.[245,258,259]

The subtle interplay of electronic and steric effects has led to a literature debate on the underlying mechanisms of photoisomerization and thermal reversion of azobenzene and its derivatives.[260–269] To capture these excited-state phenomena, femtosecond transient absorption spectroscopy (TAS) is required.[270] Generally, it is accepted that solvated azobenzene has three excited-state lifetimes: a sub-ps, a few ps, and 10s of ps. However, the photophysical assignments of the shortest lifetimes differ in the literature.[233,267] The sub-ps lifetime has been assigned to the relaxation to the lowest energy singlet surface (S_1) from the initially exited state, typically S_2. Alternatively, it has been assigned to vibrational cooling away from the S_1 Frank-Condon region. Because of the fast rate of excited-state to excited-state relaxation, the sub-ps lifetime is most often assigned to vibrational cooling.[239,267,271] The second lifetime has been assigned to the internal conversion from the S_1 state to a hot-S_0 state, often denoted as $S_1 \rightarrow$ hot-S_0. The third lifetime has been assigned to a non-radiative path through the S_1/S_0 conical intersection that yields both *cis*-isomer and reformation of *trans*-isomer.

The disentanglement of the TAS spectra and the assignment of mechanisms to the experimental lifetimes often relies on electronic structure theory calculations.[243,260–267,269,272] With electronic structure theory, three reaction coordinates have been proposed to describe the photoisomerization of azo dyes.[233,262,263,267] These include an in-plane inversion, a torsional rotation around the azo N=N bond, and combinations of the two. Different reaction mechanisms are observed depending on the direction of isomerization, $trans \rightarrow cis$ or $cis \rightarrow trans$, and the aryl substituents. It is generally accepted that, after photoexciting the *trans*-isomer into the S_2 or a higher energy excited-state, the dye quickly relaxes to the S_1 excited-state in the first picosecond or so.[267] After this, relaxation on the S_1 excited-state surface occurs via a dihedral rotation around the azo bond. A population of *cis*-isomer is ultimately formed by continued illumination because the S_1 excited-state surface forms a conical intersection with the S_0 surface at an azo dihedral angle of ≈ 90 deg. Photoisomerization quantum yields have been reported in the range of 0.2 to 0.5.[273] After the *cis*-isomer is formed,

thermal reversion ($cis \rightarrow trans$) occurs on the S_0 surface through a dihedral rotation, an inversion or a combination of the two, depending on the dye substituents.[233,237,267,271] Recently, highly accurate electronic structure theory calculations suggest that thermal reversion can transiently populate the lowest triplet state near the rotational transition state (TS) between the *cis*- and *trans*-isomer, which effectively solved the "entropy puzzle" by rationalizing the experimentally observed negative entropy.[269]

Protonation of the azo bond can restrict photoisomerization by blocking rotational degrees of freedom or changing excited-state energy landscapes.[237–239] Previously, the protonation of pyridine nitrogens, away from the azo bond, was demonstrated to limit the photoisomerization yields by shifting the energetic minima of the S_1 surface closer to the *trans*-isomer.[237] In addition, protonation was found to decrease the computed S_0 reversion barrier, which in turn, could reduce the *cis*-isomer lifetime by several orders of magnitude.[237] Because of these two potential factors, no appreciable amount of *cis*-isomer was observed for pyridine-azo dyes with steady-state UV-vis absorption spectroscopy. These findings left two possible *unresolved* mechanisms regarding the effect of protonation: 1) *cis*-isomer yield is limited through an accelerated reversion mechanism or 2) *cis*-isomer formation is *entirely* restricted through the modulation of ground and excited-state potential energy surfaces. Either of these mechanisms show promise for manipulating the relative populations without significant chemical modification, making these dyes of particular interest for photopharmaceuticals and molecular solar thermal fuels.

3.2 Methods

In this letter, a computational method for generating difference spectra that can be used to assign low population and fast-transient isomers measured experimentally is demonstrated. Application of this methodology enables definitive determination that protonation of the pyridine moiety results in accelerated reversion (mechanism 1) while direct protonation of the azo bond restricts formation of the *cis*-isomer altogether (mechanism 2). The effect of single ($pK_{a,1}^{MeCN} = 14.6 - 15.3$) and double protonation ($pK_{a,2}^{MeCN} = 11.3 - 13.8$) on the photophysics of three pyridine-based azo dyes, 2-(*p*-dimethylaminophenyl)azopyridine (**Pyr2**), 3-(*p*-dimethylaminophenyl)-azopyridine (**Pyr3**), and 4-(*p*-dimethylaminophenyl)azopyridine (**Pyr4**) (Figure 3.1), is elucidated using both femtosecond

Table 3.1: Excited state lifetimes from GLA fits for the dominant rotamer of each protonation state.

	trans	$\lambda_{max}^{\mathrm{MeCN}}/nm^a$	λ_{exc}/nm^b	$\tau_{1,VC}/ps$	$\tau_{2,VC}/ps$	τ_{IC}/ps	τ_{cis}/ps	τ_{anti}/ps	τ_{unk}/ps
Pyr2	*anti-* (88%)[c]	425	280, 290	—	0.6±0.1	9.0±1.3	unresolved[d]	—	—
Pyr3	*anti-* (73%)[c]	425	280, 290	—	$0.6\pm0.0_3$	7.4±0.6	unresolved[d]	—	—
Pyr4	—	435	290	—	0.6±0.1	7.5±1.0	unresolved[d]	—	
Pyr2-H	*eclipsed-* (84%)[c]	561	500, 600	$0.3\pm0.0_3$	$0.7\pm0.0_9$	10.1±0.7	208.4±8.4	unresolved[d]	—
Pyr3-H	*anti-* (62%)[c]	491	550	$0.2\pm0.0_3$	0.6±0.1	12.2±1.3	unresolved[d]	—	—
Pyr4-H	—	543	600	$0.3\pm0.0_1$	$0.8\pm0.0_8$	10.0±1.2	628.8±362.3	—	—
Pyr2-HH	*eclipsed-* (>99%)[c]	452	290	—	$0.7\pm0.0_3$	9.1±0.6	—	unresolved[d]	—
Pyr3-HH	*eclipsed-* (62%)[c]	467	290	—	1.0±0.6	8.4±1.0	—	—	unresolved[d]
Pyr4-HH	—	449	290	—	$0.6\pm0.0_5$	9.1±0.3	—	—	—

[a]maximum experimental absorption in MeCN. [b]TAS pump excitation wavelengths(SI Section 1.3). [c]Boltzmann weight at 300 K. [d]beyond the 5.5 ns detection window of the TAS.

transient absorption spectroscopy and time-dependent density functional theory (TD-DFT)[78] at the CAM-B3LYP/6-311g(d,p)/PCM(MeCN) level of theory.[159] For the TAS experiments, pump excitation wavelengths (λ_{ex} = 280 or 290 nm) are selected in order to avoid scattering with the CaF_2 optical window ($\sim$ 340 – 680 nm). For the singly protonated species, signatures from both the unprotonated and singly protonated forms are observed upon high energy excitation, so low energy excitations (λ_{ex} = 500–600 nm) are used to exclusively excite the singly protonated species, as the other protonation states do not absorb in this region (SI Section 1.3‡). Global lifetime analysis (GLA) is used to fit the TAS data and quantify the excited-state kinetics. Potential energy surfaces, S_0 transition states, and computational difference spectra are used to decipher the photoisomerization ($trans \rightarrow cis$) and reversion ($cis \rightarrow trans$) mechanisms of the dyes in various protonation states. Full details on theoretical and experimental methodologies are available in the Supporting Information‡.

3.3 Results and Discussion

In previous work, DFT calculations revealed that the *trans-* and *cis*-isomers of **Pyr2** and **Pyr3** have two meta-stable rotational isomers around the pyridine-azo NNCN single bond, which is equivalent to the NNCC in **Pyr3**, (Figure 3.1) with dihedrals of 180 (*anti*) or 0° (*eclipsed*). **Pyr4** is symmetric through the pyridine rotation so it has only one *trans-* and one *cis*-isomer. In the unprotonated S_0 ground singlet state, **Pyr2** and **Pyr3** share an energetic preference for the *anti-trans*-isomer with large > 70% Boltzmann weights at 300 K (Table 3.1). According to TD-DFT calculations, the *anti-trans-* and *eclipsed-trans*-isomer excitation features are too similar in energy to be resolved

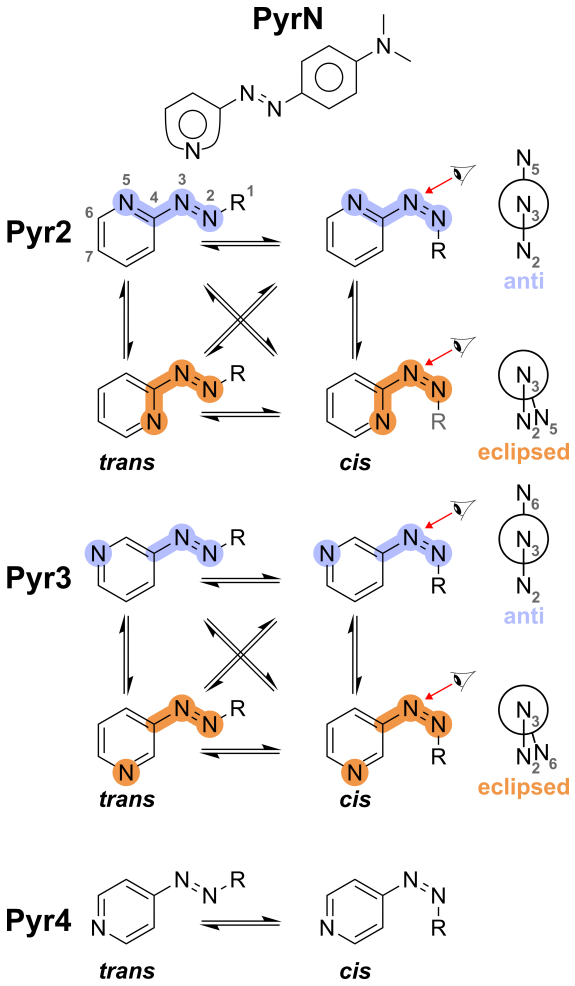

Figure 3.1: **Pyr2**, **Pyr3**, and **Pyr4** isomers. *Trans*- and *cis*-isomers are on the left and right, respectively. *Anti*- and *eclipsed*-rotamers are highlighted with lavender and orange, respectively. Atoms of interest are numbered 1 – 7. Newman projections down the N_3C_4-bond are included to highlight the rotamer nomenclature based on the pyridine dihedral angle (NNCN$\equiv D^{Pyr2}_{2345}$ or D^{Pyr3}_{2346}). For **Pyr3** $D_{2346} \simeq$ NNCC $\equiv D_{2345}$. R = Ph$-NMe_2$.

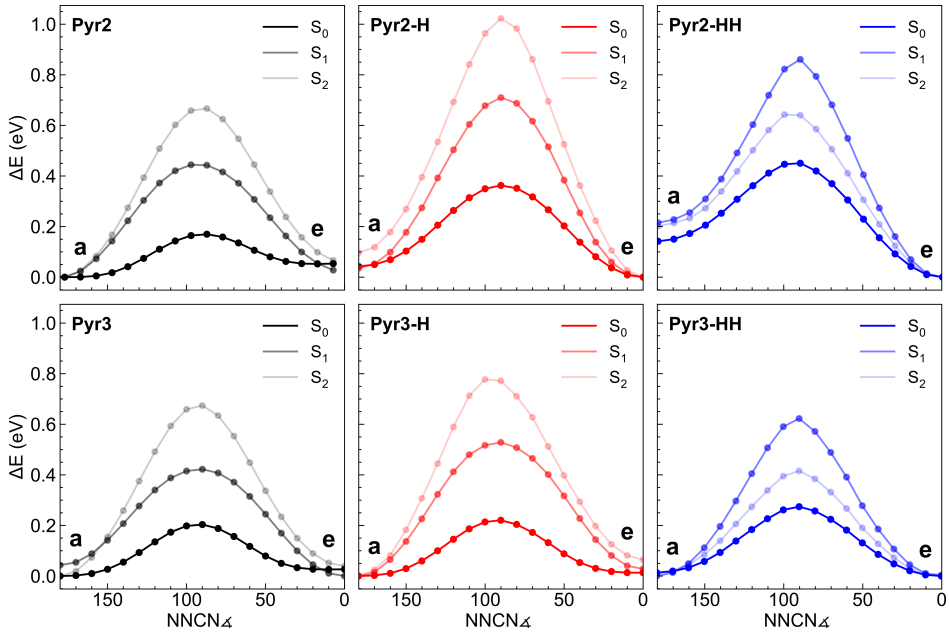

Figure 3.2: Lowest three singlet surfaces between the *anti-trans* (**a**) and *eclipsed-trans* (**e**) geometries. Pyridine dihedral angles are defined as NNCN $\equiv D^{Pyr2}_{2345}$ and D^{Pyr3}_{2346} labeled in Figure 1. All energies are relative (ΔE) to the lowest energy minimum on the surface. S_1 and S_2 are single-point TD-DFT energies above a relaxed S_0 scan.

with steady-state UV-vis spectroscopy (Figure S1‡).[237]

For all **PyrN**, the first protonation site was found to occur at the pyridine nitrogen (Table S1‡). When singly protonated, *eclipsed-trans*-**Pyr2-H** is 0.042 eV more stable than the *anti-trans*-**Pyr2-H**. This effect appears to be due to a hydrogen bond between the pyridine and azo nitrogen in *eclipsed-trans*-**Pyr2-H** (Figure S6‡ and S7‡). *Anti-trans*-**Pyr3-H** is 0.013 eV more stable than the *eclipsed-trans*. Due to the *meta*-nitrogen position of **Pyr3-H**, *anti-trans*- and *eclipsed-trans*-**Pyr3-H** cannot form a hydrogen bond (Figure S6‡ and S7‡). In addition, the orientation of *anti-trans*-**Pyr2-H** does not allow for a hydrogen bonding interaction. The second protonation site was found to occur at the nitrogen closest to the pyridine ring of the azo bond (Table S1‡). Both **Pyr2-HH** and **Pyr3-HH** were found to energetically favor the *eclipsed-trans*-isomer to avoid steric clashing between the two acidic protons. Relaxed potential energy surface scans of the *trans*-**PyrN** along the pyridine dihedral angle predict larger *anti*(**a**)→*eclipsed*(**e**) rotation barriers for the protonated species and the two lowest energy singlet excited states than for the unprotonated species (Figure 3.2). Hydrogen bonding between the pyridine nitrogen and the azo bond in **Pyr2-H** and **Pyr2-HH** is the most likely culprit for the ≈ 0.2 eV higher electronic activation energy between the

rotamers. In fact, ΔE_a is the same order of magnitude as what is expected for a hydrogen bond of this nature.[274]

Previous steady-state UV-vis absorption spectroscopy revealed that no appreciable build up of *cis*-isomer was achieved on timescales greater than a millisecond when **PyrN-H** and **PyrN-HH** were irradiated with light around their λ_{max}.[270] To confirm whether *cis*-isomer is formed on sub-millisecond time scales and to explain photophysical mechanisms, ultrafast femtosecond transient UV-vis absorption spectroscopy and global lifetime analysis were employed to measure the excited-state evolution and generate lifetimes, respectively. Decay-associated difference spectra (DADS) were produced from GLA (Figure 3.3) and compared with TD-DFT difference spectra to assign lifetimes to particular geometries (Figure 3.4). Representative spectra are available in the SI for each **PyrN** in each protonation state (Figure S12‡).

Due to the push-pull nature of the dyes, their λ_{max} are red shifted compared to azobenzene.[237] In addition, the λ_{max} were found to depend both on the position of pyridine nitrogen and on the protonation state.[237] These characteristics made it possible to visualize absorption features on either side of the ground-state bleach, making the comparison with the computational difference spectra more reliable.

The unprotonated species were best fit with three lifetimes, one of which was unresolved, *i.e.* longer than what could be fit with the data collected in the 5.5 ns TAS detection window (Table 3.1). The number and magnitudes of the lifetimes are generally consistent with what has been reported for azobenzene and other derivatives.[267,271] The first lifetime is assigned to vibrational cooling of S_1 ($\tau_{2,VC}$). The second is assigned to the internal conversion from the S_1 excited state to the hot-S_0 state (τ_{IC}), which can subsequently form either *cis*- or *trans*-isomer. No obvious pattern was observed regarding the position of pyridine nitrogen and the $\tau_{2,VC}$ and τ_{IC} lifetimes. The third unresolved lifetime is assigned to the lifetime of the meta-stable *cis*-isomer (τ_{cis}). Computational difference spectra of *cis* minus *trans* for each unprotonated dye were found to match the DADS of τ_{cis} (Figure 3.4).

Azo dyes can undergo reversion from *cis* $\rightarrow$ *trans* on the S_0 through an inversion of the pyridine ring after or simultaneously with a dihedral rotation of the pyridine ring (Figures 3.5, S8-S10‡). Transition states (TS) indicate that reversion for each **PyrN** likely proceeds through a t-shaped inversion (INV_{pyr}). A high-energy inversion TS of the DMA-substituted ring (INV_{dma}) was found

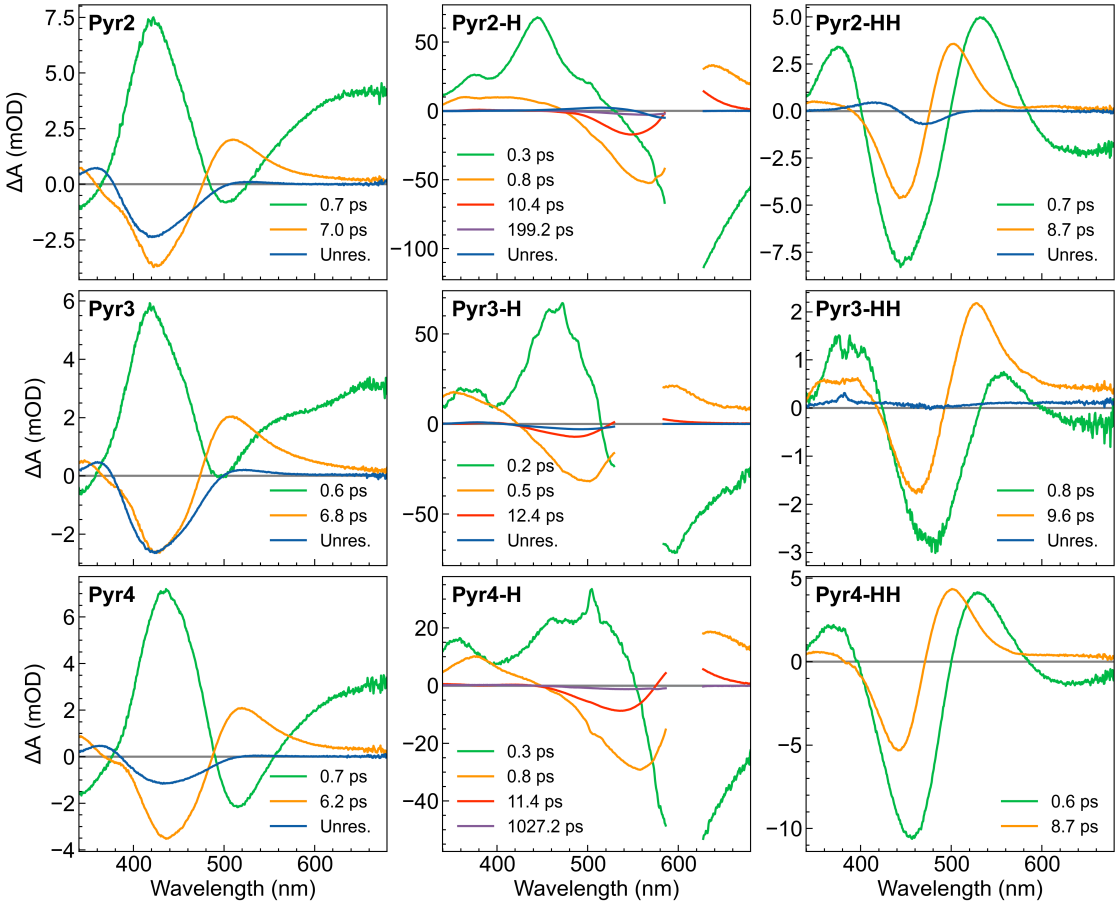

Figure 3.3: Representative decay associated difference spectra (DADS) obtained from GLA of **PyrN**, **PyrN-H**, **PyrN-HH**. Resolved lifetimes (ps) are green, orange, red, and purple. Unresolved lifetimes are blue. Representative spectra of the raw data for each fit are shown in Figure S12‡. Pump excitation wavelength of 290 nm was used for **PyrN** and **PyrN-HH**. Pump excitation wavelengths of 600 nm, 550 nm, and 600 nm were used for **Pyr2-H**, **Pyr3-H**, and **Pyr4-H**, respectively.

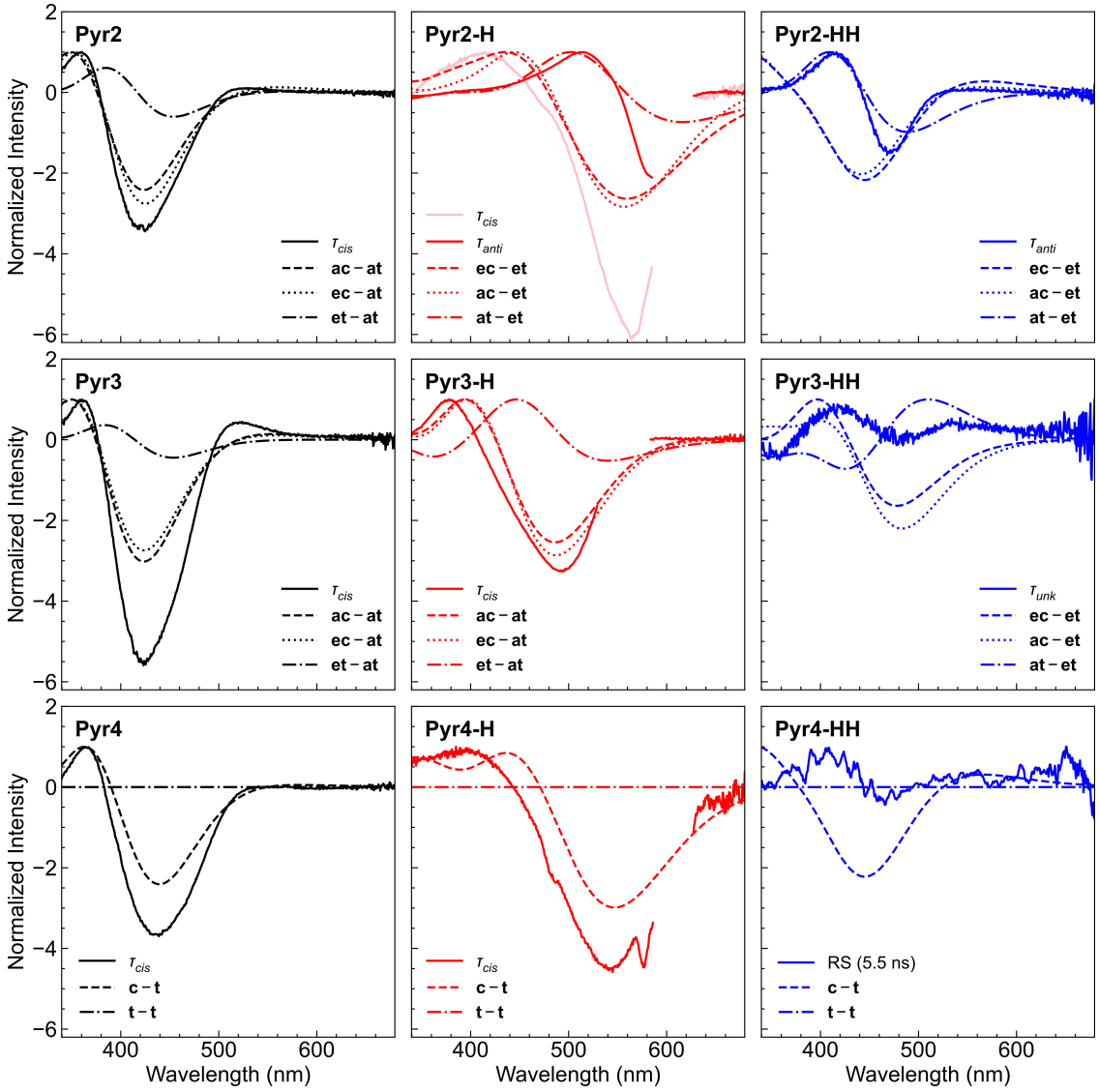

Figure 3.4: Comparison of computational difference spectra (dashed, dotted, and dashed-dotted lines) at CAM-B3LYP/6-311g(d,p)/PCM(MeCN) level of theory[159] and experimental long lived species (solid lines). The unresolved lifetimes and their decay-associated difference spectra for **PyrN**, **PyrN-H**, and **PyrN-HH**; and a representative difference spectrum at 5.5 ns for **Pyr4-HH**, which doesn't have an unresolved component, are compared to the computational differences between meta-stable isomers and the ground state. Spectral shifts of the TD-DFT energies were performed to ensure that the lowest allowed transitions (S_2) for the *trans*-isomer are aligned with the λ_{max} of the steady-state absorbance spectra for each protonation state (Figure S11[‡]). Rotamer names are abbreviated: *anti-trans* (**at**), *anti-cis* (**ac**), *eclipsed-trans* (**et**), and *eclipsed-cis* (**ec**).

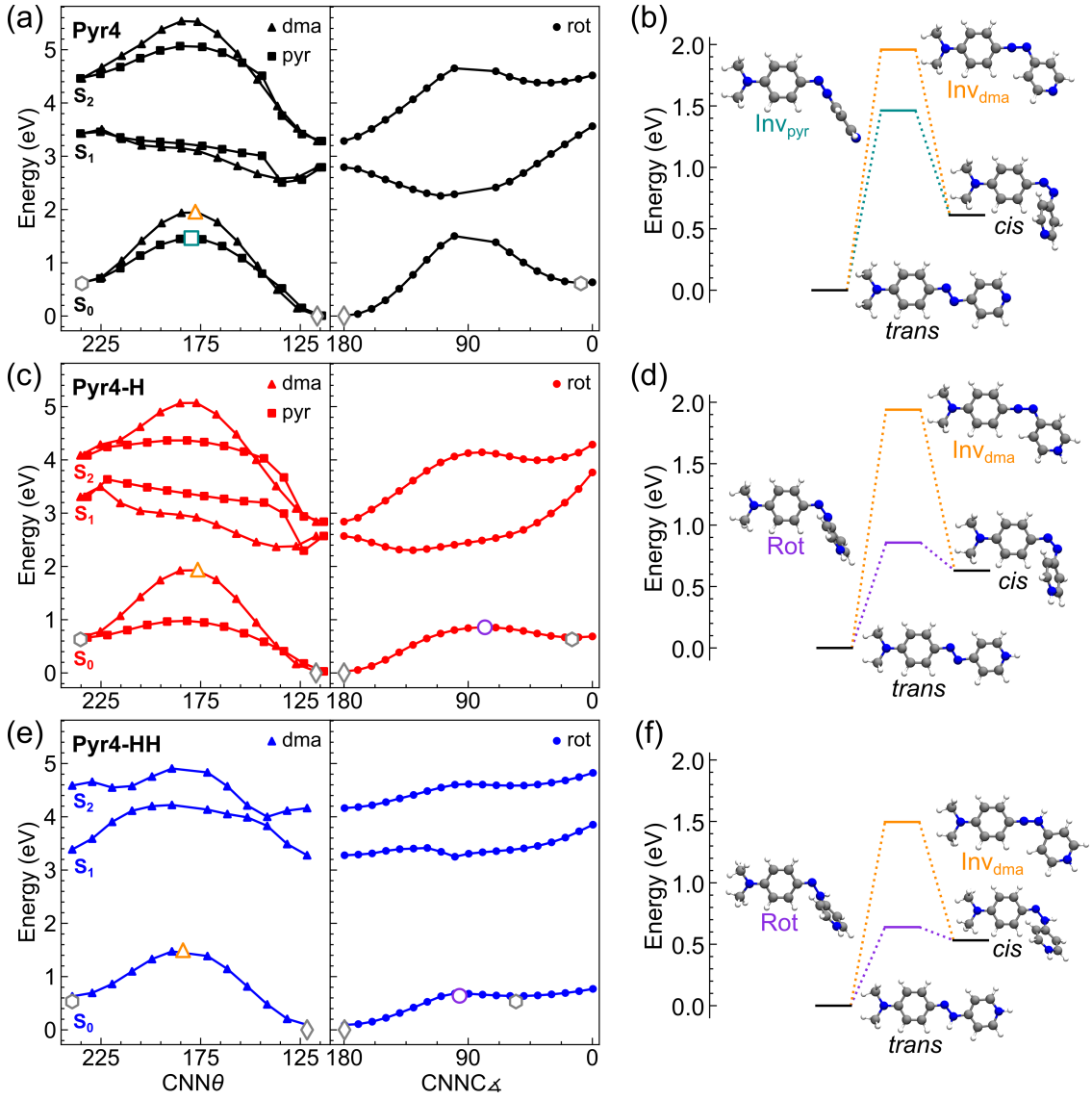

Figure 3.5: (a,c,e) The potential energy curves of the lowest three singlet surfaces of **Pyr4**, **Pyr4-H**, and **Pyr4-HH** at CAM-B3LYP/6-311g(d,p)/PCM(MeCN) level of theory[159] along the rotational (CNNC∠=D_{1234},right) coordinate along with the inversion coordinates for both the **dma** (CNNθ=A_{123}) and **pyr** (CNNθ=A_{234}) rings (left). Atom numbers are labeled in Figure 1. (b,d,f) The rotational (**Rot**) and inversion ($\mathbf{INV_{dma}}$ and $\mathbf{INV_{pyr}}$) S_0 transition states. The structures shown are marked with open shapes on the curves in the corresponding colors. The optimized *trans*- and *cis*-isomers are open diamonds and hexagons, respectively. Open purple circles, teal squares, or orange triangles are optimized rotation, **dma** and **pyr** inversion transition states, respectively.

for each **PyrN**. Rotational transition states were not found, either because the energetic barrier is even higher on the S_0 surface or because it is nearly degenerate with the S_1 state. At this point on the DFT potential energy surface, the S_0 energy spikes rather than forming a proper conical intersection because of the single reference approximation. Multiple reference determinants would be necessary to correctly describe this region. Previous higher-level *ab initio* calculations have shown that the overall PES of azo dyes is well described by TD-DFT,[264,269,275] so optimizing the S_0/S_1 conical intersection is not critical to understanding the overall dynamics of **PyrN**.

Interestingly, the singly protonated dyes (**PyrN-H**) have considerably more complex dynamics than the unprotonated dyes. Starting with the symmetrically simplest, **Pyr4-H** is fit to have four lifetimes (Table 3.1) and *no* unresolved component. **Pyr3-H** differs from **Pyr4-H** because the fourth lifetime is unresolved. **Pyr2-H** is fit to have five lifetimes, one of which is unresolved. The two shortest lifetimes of **PyrN-H** are sub-picosecond processes that are likely due to two distinct vibrational cooling (VC) events, which are denoted $\tau_{1,VC}$ and $\tau_{2,VC}$ (Table 3.1). The third lifetimes (τ_{IC}) are longer lived and on the order of $\approx$ 10 ps. These are likely due to internal conversion (IC) from the S_1 state into the hot-S_0 state. Compared to the unprotonated dyes, a considerably smaller fraction of *cis*-isomer is formed for **PyrN-H** because the S_1 minimum is shifted towards the *trans*-isomer (Figure 3.5, S8‡, and S9‡). This shift reduces the formation of *cis*-isomer as it is endothermic on the S_0 surface. The fourth lifetimes are assigned to the *cis*-state (τ_{cis}) due to its longevity and because the DADS are highly aligned with the computational difference spectra (Figure 3.4). The τ_{cis} lifetimes are different for each **PyrN-H**, but are similar for both **Pyr2-H** (208 ps) and **Pyr4-H** (629 ps), when the standard deviation is taken into account (Table 3.1). However, τ_{cis} for **Pyr3-H** is unresolved ($>$ 5500 ps) and is *at least* an order of magnitude longer than that of **Pyr2-H** and **Pyr4-H**.

To explain the discrepancy in the lifetimes among the species, transition state theory (TST) was used to approximate the reversion lifetimes from the lowest energy *cis*-isomer to the lowest energy transition state to form *trans*-isomer (Figures 3.5 and S10). Here, the calculated Gibb's free energies at 298.15 K are used to approximate the barrier heights and the rates. TST predicts that the singly protonated species should revert $\approx$ 5 to 12 orders of magnitude faster than the unprotonated species at 298.15 K (Table S2‡). Based on this fast reversion, the population of protonated *cis*-isomer is too short-lived to be detected by steady-state UV-vis absorption spectroscopy. TST also predicts

that the *cis*-isomer of **Pyr3-H** would be 8 orders of magnitude longer lived than **Pyr2-H** and **Pyr4-H**, corresponding to the longer τ_{cis} found for **Pyr3-H**.

The **Pyr2-H** is the only species best fit with five lifetimes, where the fourth is from the *cis*-isomer and the fifth is from some other process. The fifth lifetime is likely from a meta-stable S_0-state other than the ground state *trans* or *cis*. Because the preferential rotamer of **Pyr2-H** is significantly stabilized (*eclipsed* = 84% at 300 K), a change in the ratio of **e**/**a**, or an increase in the population of *anti-trans*-isomer from laser-induced heating, could explain the fifth lifetime. The formation of *anti-trans*-isomer is unlikely to proceed through an excited-state path because the excited-state scan curves have higher activation energies than the S_0 (Figure 3.2). The DADS of the fifth lifetime match the computational difference spectra between the *eclipsed-trans*-isomer and the *anti-trans*-isomer remarkably well (Figure 3.4), so it is assigned to the reversion of *anti*- to *eclipsed*-rotamer (τ_{anti}, Table 3.1). In comparison, since **Pyr3-H** only has a 62 % preference for the *anti-trans*-rotamer, no fifth lifetime is expected or necessarily improves the fit.

The doubly protonated dyes **Pyr2-HH** and **Pyr3-HH** are best fit with three lifetimes, one of which is unresolved. Their spectral features differ significantly from those of the unprotonated and singly protonated species. **Pyr4-HH**, on the other hand, is best fit with two lifetimes *only* (Table 3.1). For all doubly protonated **PyrN-HH**, the shortest 1 ps lifetime is assigned as a vibrational cooling event ($\tau_{2,VC}$). The second lifetime between 8.4 and 9.1 ps is likely from the internal conversion from the S_1 excited state to a hot-S_0 state. Interestingly, no evidence of *cis*-isomer was observed for any of the doubly protonated species.

Focusing on the longest lived **Pyr2-HH** DADS, this spectrum best matches the computational difference spectrum between the *eclipsed-trans*-isomer and the *anti-trans*-isomer (Figure 3.4), denoted τ_{anti}. Comparing τ_{cis} of **Pyr2-H** (208 ps) to the theoretical reversion time (691 ps), a difference of a few hundred picoseconds is predicted (Tables 3.1 and S2‡). The same is true for τ_{cis} of **Pyr4-H** (629 ps), where the theoretical reversion time is predicted to be 326 ps. Because the theoretical lifetimes are within the same order of magnitude of the experimental ones, it is possible to approximate the longevity of τ_{anti} for **Pyr2-HH** from the ΔE between the TS between *anti-trans* and *eclipsed-trans* and the optimized *anti-trans* structure with decent confidence. At 298.15 K, its lifetime according to TST would be on the order of 27.5 ns, beyond the detection limit of the TAS instrument, which explains why the state is unresolved. This state could not be detected

with ns-TAS because of the low signal-to-noise ratio (data not shown). In addition, the unresolved component of **Pyr3-HH** neither matches the *cis* structure nor the *anti*-rotamer. Therefore, this state is probably another hot-*trans* geometry not predicted by DFT, so it is called τ_{unk}.

3.4 Conclusion

In conclusion, unprotonated pyridine-based azo dyes form a significant population of *cis*-isomer upon photoexcitation. When singly protonated, a fraction of *cis*-isomer is formed but quickly reverts to *trans*-isomer such that no appreciable population of *cis*-isomer is built up to be detected by steady-state UV-vis spectroscopy. Slower thermal reversion of **Pyr3-H** leads to a population of *cis*-isomer that persists beyond 5 ns. Evidence of shifts in the *anti-trans-* and *eclipsed-trans*-isomer populations were predicted with theory and observed with TAS for **Pyr2-H** and **Pyr2-HH**. No convincing evidence, even on sub-ps timescales, of *cis*-isomer was observed for doubly protonated dyes.

These findings provide design rules for controlling the isomerization of azo dyes with protons. Specifically, if isomerization must be shutdown completely, like for pharmaceuticals, the first protonation location should be on the azo bond, for instance by blocking all other protonation sites. Slow release of an active *cis*-drug or control of the charging and discharging of a molecular fuel could be achieved by limiting the population of *cis*-isomer generated by designing a distant protonation site away from the azo bond. Overall, these results highlight the power of modifying the photophysical processes of azo dyes through pH modulation and the mechanism to harness the protonatable pyridine moiety for the rapid release of heat from molecular solar thermal fuels through the addition of acid.

Finally, assigning lifetimes of low population states or those that are only transiently populated has remained a significant challenge for spectroscopists when there is no quantitative way to compare computed states and the measured experimental spectra. Here, insight needed to assign many of these lifetimes arises directly from the match between the computational difference spectra and the time-resolved DADS. This successful demonstration shows the applicability of widely available TD-DFT calculations to assign low-population and fast transient isomers measured experimentally. Thus, computational difference spectra provide a direct and powerful way to validate a proposed

excited-state evolution mechanism.

Chapter 4

Predicting Excited-State Absorption Spectra from Non-Aufbau Configurations[†]

4.1 Introduction

Predicting ground-state absorption spectra (*e.g.,* $S_0 \rightarrow S_n$ and $T_0/T_1 \rightarrow T_n$) with density- or wavefunction-based methods presents several challenges due to the complex interplay of electronic structure, solvation effects, and electron correlation.[276] While methods like linear-response time-dependent density functional theory (LR-TDDFT)[61,66,68,277] have been quite successful at predicting excitation energies and oscillator strengths from a ground-state reference, their accuracy is sensitive to the choice of functional, basis set, and the treatment of electron correlation.[278,279] Additionally, since much of molecular photochemistry and photophysics occurs in solution, accurately modeling solvation effects is crucial. Implicit solvent models, such as the Conductor-like Polarizable Continuum Model (CPCM)[280] and the Solvation Model based on Density (SMD)[281] offer computational efficiency but often fail to capture important solute-solvent interactions, *e.g.,* ion-dipole and dipole-dipole.[282] Moreover, accurately describing excited states often requires accounting for multiple electron excitations (*e.g.,* double, triple, *etc.*) and multiconfigurational character, *i.e.*,

[†] *Submitted.*

cannot be described by a single Slater determinant, particularly in systems with significant electron correlation.[276] As a result, non-expert users or those studying large molecules often rely on black-box methods like LR-TDDFT and its approximations for their efficiency and ease of use.

These challenges are even more pronounced when predicting excited-state absorption spectra (*e.g.,* $S_n \rightarrow S_m$ and $T_n \rightarrow T_m$). Unlike ground-state absorption, excited-state transitions often involve higher-order excitations,[283,284] spin-state mixing,[285] and non-equilibrium excited-state geometries,[286] making them significantly more complex to model. Consequently, LR-TDDFT or LR-TDA in the expectation value formalism[287,288] may provide less accurate descriptions of these systems. To improve the accuracy of excited-state properties, quadratic response TDDFT (QR-TDDFT),[289] CASPT2,[37,290] and CC-based[291,292] (*e.g.,* CCS, CC2, CCSD, CCSDR(3), and CC3) methods are often used,[287,288,291–294] though they come with significant computational costs. Excited-state absorption spectra can also be predicted via real-time TDDFT (RT-TDDFT) propagation with an excited-state density obtained from linear-response TDDFT gradients, which calculates the linear response of the excited state rather than the quadratic response from the ground state,[295] or with second linear response theory (SLR)[296,297] at double the cost of LR-TDDFT. Unfortunately, neither of these DFT-based methods has gained widespread adoption, particularly within the photochemistry and photophysics community.

Instead, molecular orbital-level insight into structure-function-dynamics relationships in photochemical systems is often obtained from *ab initio* excited-state calculations.[276] While ground-state methods often provide a reasonable description of UV–vis absorption spectra, analysis of transient absorption spectroscopy (TAS) requires accurate prediction of excited-state absorption spectra. TAS is a powerful pump-probe technique[298] that measures changes in absorption as a function of wavelength and time. TAS has been employed to study systems ranging from photoswitches[299] to photoredox catalysts.[300] In photoredox systems, spectro-electrochemistry yields spectra of key intermediates that can be used to fit time-resolved features and support mechanistic interpretations.

Because it is difficult to generate excited-state absorption spectra for isolated states experimentally, species-associated difference spectra (SADS) cannot be used to fit TAS data that are mostly comprised of excited state absorption features. As a result, global lifetime analysis (GLA) of TAS is often employed to produce decay-associated difference spectra (DADS), separating transient signals into components with distinct lifetimes. However, despite the utility of GLA, assigning specific

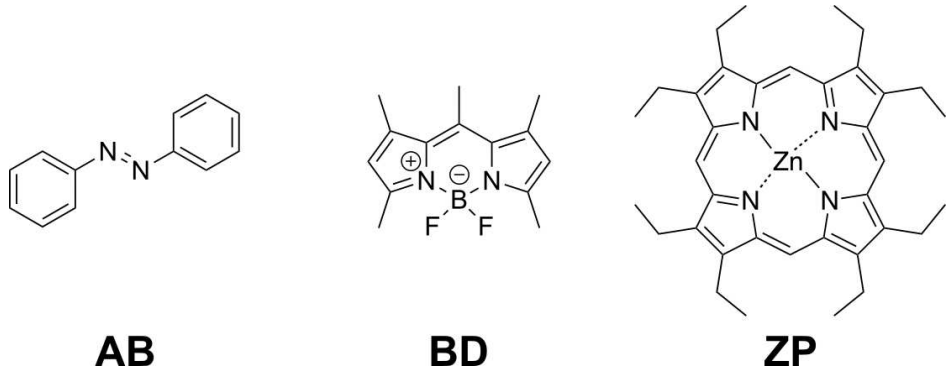

Figure 4.1: Well studied chromophores to test the breadth of LR-TDA/ΔSCF.**AB** is Diphenyldiazene, **BD** is 1,3,5,7,8-Pentamethyl-4,4-difluoro-4-bora-3a,4a-diaza-s-indacene, and **ZP** is 2,3,7,8,12,13,17,18-Octaethyl-21*H*,23*H*-porphine zinc(II).

excited-state spectral features to individual processes or species remains challenging, particularly without reliable theoretical predictions of energies and oscillator strengths for energetically and spin-accessible states below the initial excited state(s).

This work introduces an alternative approach for predicting excited-state absorption spectra by combining the ΔSCF maximum overlap method (MOM)[51] with the linear response Tamm-Dancoff approximation (LR-TDA).[88] We refer to this approach as LR-TDA/ΔSCF. Excited states are self-consistently optimized using MOM, followed by LR-TDA calculations on these configurations to predict excited-state absorption spectra that can be directly compared to raw TAS and DADS data.

Three chromophores (photoswitchable azobenzene (**AB**), emissive pentamethyl-BODIPY (**BD**), and phosphorescent zinc octaethylporphyrin (**ZP**) (Figure 4.1)) with well studied excited-state dynamics are modeled using LR-TDA/ΔSCF method.[301] Theoretical excited-state absorption spectra, derived from both ground- and excited-state geometries, are compared to raw and GLA-fitted TAS data. The effects of orbital relaxation are analyzed by comparing LR-TDA/ΔSCF spectra to LR-TDA expectation value formalism spectra. Key excited-state absorption features are assigned to hole-electron pairs to describe their character. Overall, this method offers a cost-effective, DFT-based approach for predicting excited-state absorption in systems that can be accurately described by a few low-energy excited states.

4.2 Theoretical Methods

4.2.1 Density Functional Theory Optimization and Frequency Calculations

Molecular geometries were optimized in ORCA 6.0[301] using tight SCF convergence criteria, the PBE0[302] or LC-PBE[303] XC-functional, a def2-TZVP basis set,[304] D4 dispersion corrections,[305] and a CPCM solvent model[280] that matched experimental conditions. **AB** and **BD** were optimized in acetonitrile while **ZP** was optimized in chloroform. Subsequent frequency calculations confirmed that the optimized geometries were true local minima, with all positive frequencies.

4.2.2 LR-TDA and LR-TDDFT Calculations on Aufbau Reference Wavefunctions

Linear Response Time-Dependent DFT (LR-TDDFT)[61,66,68,277] and Tamm-Dancoff Approximation (LR-TDA)[88] calculations were carried out on the optimized structures, using the same level of theory as the optimization and frequency calculations. The first 30 excited states of **AB** and **BD** and 60 excited state of **ZP** were calculated using a restricted singlet reference or an unrestricted triplet reference, depending on the molecule and/or the state of interest. Computed excitation energies and oscillator strengths were used to produce stem plots and Gaussian-broadened absorption spectra ($\sigma = 0.4\ eV$) for comparison with experimental ground-state absorption spectra.

4.2.3 Excited-State Absorption Spectra via the Expectation Value Formalism

Predicting ground- or excited-state absorption spectra from first-principles calculations requires, at a minimum, excitation energies and oscillator strengths. Assuming that the excitation energy (ε_{JI}) from excited-state I, with energy E_I, to excited-state J, with energy E_J, is given by

$$\varepsilon_{JI} = E_J - E_I, \tag{4.1}$$

excited-state to excited-state excitation energies can be approximated using either LR-TDDFT or LR-TDA.[287,288] Notably, this approximation neglects orbital and solvent relaxation effects, which can lead to significant energetic shifts relative to experiment. Previous studies have demonstrated that the accuracy of the expectation value formalism is functional-specific and depends on the

fraction of exact exchange.[287,288] For instance, global hybrid functionals with lower exact exchange exhibit poor agreement with experimental data, while 50% exchange is recommended to improve accuracy.[287] Range-separated hybrids, such as CAM-B3LYP,[306] also predict spectra in good agreement with experiment.[287]

To maintain consistency and ensure comparability with the LR-TDA/ΔSCF results presented in a later section, excitation energies and oscillator strengths were calculated using LR-TDA within the expectation value formalism. Excitation energies (ω) were determined by solving the Hermitian eigenvalue problem,

$$\mathbf{A}\vec{X} = \omega\vec{X}, \tag{4.2}$$

where $\mathbf{A}$ is the orbital rotation Hessian matrix, ω are the excitation energies, and $\vec{X}$ is the eigenvector of excitation amplitudes.[61] Excited-state to excited-state oscillator strengths,

$$f_{JI} = \frac{2}{3}\varepsilon_{JI}|\langle\Psi_J|\hat{\mu}|\Psi_I\rangle|^2, \tag{4.3}$$

were obtained as the product of the excitation energy and the squared norm of the transition dipole moment ($\langle\Psi_J|\hat{\mu}|\Psi_I\rangle$).[287] Here, Ψ_I and Ψ_J denote excited-state wavefunctions of the same spin multiplicity, and $\hat{\mu}$ is the dipole moment operator. In LR-TDA, excited-state wavefunctions are expressed as linear combinations of singly excited determinants (Φ_i^a) with excitation amplitudes (C_i^a),

$$\Psi_I = \sum_i^{occ}\sum_a^{vir} C_i^a\Phi_i^a, \tag{4.4}$$

where the excitation amplitudes are normalized (*i.e.*, $\sum_{i,a}(C_i^a)^2 = 1$).[287,307]

To cover the spectral window in the TAS experiments, the 30 lowest-energy singlet excited states were computed using LR-TDA for **AB** and **BD**, while 60 singlet and 60 triplet excited states were computed for **ZP**. Excited-state to excited-state energies and oscillator strengths were used to generate stick plots and Gaussian-broadened absorption spectra ($\sigma = 0.4$ eV). All calculations were carried out using methods implemented in ORCA 6.0.[301]

4.2.4 ΔSCF to Variationally Converge Excited-State Non-Aufbau Wavefunctions

Molecular orbital coefficients in Hartree-Fock (HF) or Kohn-Sham DFT are generally determined in a variational and self-consistent manner.[308] The self-consistent field (SCF) procedure typically results in a minimum-energy Slater determinant that satisfies the time-independent Schrödinger equation:

$$\hat{H}\Psi_k = E_k\Psi_k, \tag{4.5}$$

where $k = 0$ for a given spin state and geometry within the Born-Oppenheimer (BO) approximation. To determine excited states, methods such as LR-TDDFT,[61,66,68,277] LR-TDA,[88] or more computationally demanding wavefunction-based approaches like EOM-CC,[96] ADC,[113,116] CASSCF,[309] and CASPT2[37,290] are typically employed. While one can attempt to convergence to excited-state (non-Aufbau) electron configurations using KS-DFT, standard SCF algorithms generally favor the lowest energy configuration, leading to variational collapse.[51] To address this, non-standard SCF algorithms, collectively known as ΔSCF[51,310] or orbital optimized (OO-)DFT,[55] have been developed to avoid variational collapse while remaining self-consistently solvable.

Among these methods, the maximum overlap method (MOM)[51] in ORCA 6.0[301] provides a way to self-consistently converge excited-state configurations. MOM enforces that the new set of occupied orbitals maximally overlaps with the set of previously occupied orbitals during each iteration of the SCF procedure.[51] From this point forward, MOM and ΔSCF are used synonymously, with the latter being used more frequently.

An excited-state non-Aufbau configuration is typically generated by singly occupying a previously unoccupied orbital and singly un-occupying a previously doubly occupied orbital. For an unrestricted reference configuration, where the orbitals are singly occupied spin up (α) or spin down (β), the non-Aufbau excitation is created by singly occupying an unoccupied α/β-orbital and singly un-occupying a previously occupied α/β-orbital. This non-Aufbau guess configuration is relaxed energetically using ΔSCF, and, ideally, converges to the nearest excited-state solution, rather than the lowest energy ground-state solution.[51]

A simple example of ΔSCF in action is shown in Figure 4.2. Starting from the self-consistently optimized ground-state orbitals (Figure 4.2, left), a non-Aufbau configuration was generated by

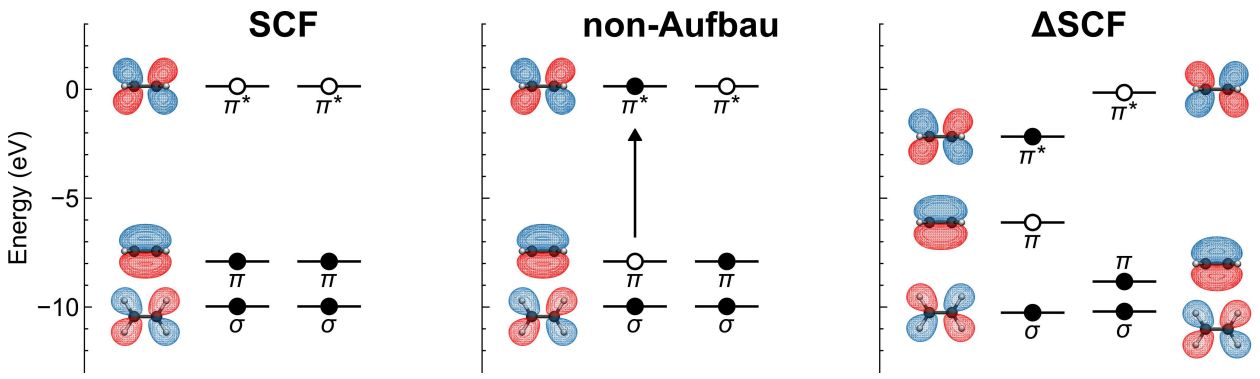

Figure 4.2: ΔSCF applied to the first excited state of ethene. (left) Ground-state SCF molecular orbital (MO) diagram, (middle) non-Aufbau guess for the excited-state configuration without orbital relaxation, and (right) the first singlet ΔSCF excited-state of gas-phase ethene at the PBE0-D4/def2-TZVP level of theory.

promoting an electron from the α-HOMO (π) to the α-LUMO (π^*) of ethene (Figure 4.2, middle). This non-Aufbau configuration was then relaxed using ΔSCF and converged to the nearest energy solution (Figure 4.2, right). The set of ΔSCF-optimized orbitals approximates the lowest-energy $\pi \rightarrow \pi^*$ excited-state of ethene.

Unfortunately, identifying and converging to excited states of interest with ΔSCF can be challenging without prior knowledge of the main orbitals involved in these excitations. A simple yet effective strategy to overcome this limitation is to use the results from LR-TDDFT or LR-TDA calculations to guide the selection of orbitals to excite from and into. By identifying the pair of orbitals with the largest contribution (*i.e.,* the largest C^2) for a given excited state, this pair serves as a reliable starting point for converging the excited state using ΔSCF. If this initial pair fails to converge or results in an undesired excited state, the second or third largest contributing orbital pairs can be used to produce guess configurations for ΔSCF. Once the desired excited state is successfully converged, ΔSCF excitation energies can be approximated as the energy difference between the excited- and ground-state. This strategy was use to converge one or two low-lying singlet excited states with ΔSCF for **AB**, **BD**, and **ZP** in various geometries.

4.2.5 LR-TDA Calculations on Non-Aufbau ΔSCF References (LR-TDA/ΔSCF)

Excited-state absorption spectra were predicted by performing LR-TDA calculations on ΔSCF excited-state configurations. The excited-state indices (e.g., S_1, S_2, etc.) from the ΔSCF calcu-

lations were validated by examining the number of negative eigenvalues obtained with LR-TDA. For example, if the system is in the first excited singlet state (S_1), LR-TDA on the ΔSCF configuration should predict a transition to the ground state with a negative energy corresponding to an approximate emission energy. Similarly, for the second excited state (S_2), two negative energy transitions should be predicted with LR-TDA. After confirming the identity of the excited states, molecular orbitals were analyzed to verify their excited-state character.

As above, Gaussian-broadened (σ = 0.4 eV) excited-state absorption spectra were generated from the energies and oscillator strengths predicted by LR-TDA/ΔSCF. By subtracting the LR-TDA ground-state absorption spectra from various LR-TDA/ΔSCF excited-state spectra, theoretical species-associated difference spectra were obtained. These theoretical difference spectra were be compared to the raw TAS and DADS to better understand the orbitals that contribute to the various features.

4.3 Results and Discussion

4.3.1 Overview

This section presents a detailed evaluation of the LR-TDA/ΔSCF method for predicting excited-state absorption spectra and interpreting TAS spectral features. LR-TDA/ΔSCF results are compared with excited-state absorption predictions obtained from the expectation value formalism. The first subsection examines the photoevolution of a relatively simple organic photoswitch, azobenzene (**AB**). Following excitation to the S_2 state, and its subsequent decay through the S_1/S_0 conical intersection, meta-stable *Z*-**AB** is formed (Figure 4.3). The second investigates a simple two-level system. A BODIPY derivative (**BD**) that fluoresces following excitation to the S_1 state (Figure 4.3) is used to examine subtle changes in excited-state absorption arising from geometric relaxation in the S_1 state. The third explores a multiconfigurational system, where LR-TDA/ΔSCF is expected to perform poorly. Octaethyl zinc porphyrin (**ZP**), which, upon excitation into the Q-bands (*i.e.*, S_1 and S_2), can undergo intersystem crossing to the triplet manifold (Figure 4.3). In this system, both the ground and excited states have multiconfigurational character.

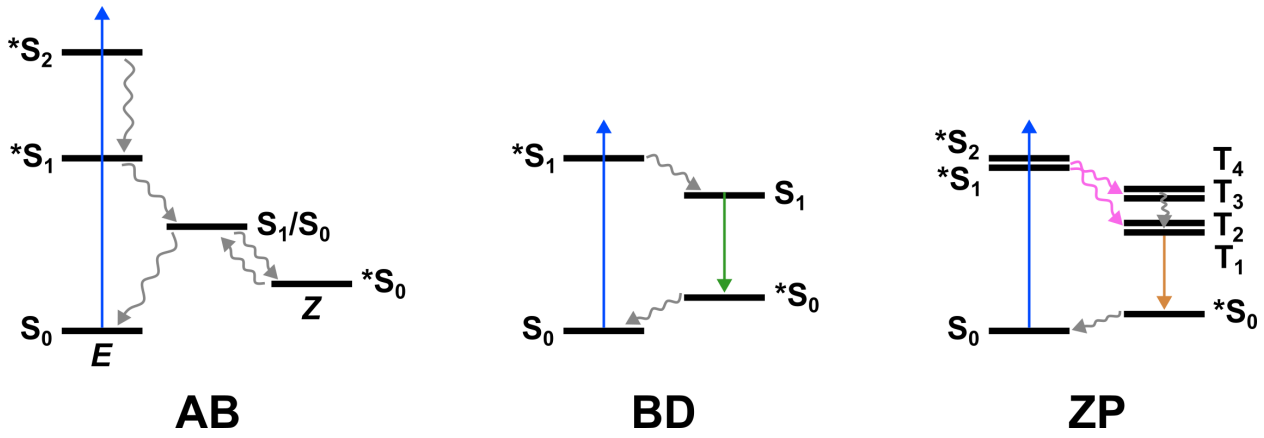

Figure 4.3: Jablonski diagrams illustrating the established photophysics of **AB**, **BD**, and **ZP**. Solid arrows correspond to absorption (blue) and emission, fluorescence (green) and phosphorescence (orange) and squiggly arrows represent non-radiative internal conversion (IC, grey) and intersystem crossing (ISC, pink).

4.3.2 Azobenzene

Azobenzenes, including **AB**, are prototypical photoswitches that undergo E–Z photoisomerization. Their main absorption feature corresponds to excitation to the S_2 state, which involves a $\pi \rightarrow \pi^*$ transition. In contrast, the lower-energy S_1 state involves an $n \rightarrow \pi^*$ transition that is formally symmetry-forbidden, but gains intensity through vibronic coupling. Excitation to S_2 is followed by rapid internal conversion to S_1. Once in the S_1 state, either by direct excitation or through relaxation from S_2, rotation about the azo-bond dihedral relieves geometric strain. Near a dihedral angle of 90°, a conical intersection with the S_0 ground state enables relaxation to either the E reactant or the Z product. Modeling the photophysics of **AB** thus requires consideration of the S_2 and S_1 states, along with the optimized E, Z, and S_1 geometries along the rotational reaction coordinate.

The ground-state ($E(S_0)$) and meta-stable ($Z(S_0)$) geometries of **AB** were optimized as true minima using the PBE0 and LC-PBE functionals (Figure 4.4). The most significant differences between the PBE0- and LC-PBE-optimized structures occur in the Z-isomers (RMSD = 0.189 Å), likely due to variations in the long-range $\pi - \pi$ interactions between the phenyl rings that can be sensitive to the amount of exact exchange.[311] In contrast, the E-isomers primarily differ in their dihedral angles D_{1234} and D_{3456} (RMSD = 0.053 Å). The PBE0 structure has a $D_{1234} = 179.8°$ and $D_{3456} = 179.8°$ while the LC-PBE structure has $D_{1234} = 170.8°$ and $D_{3456} = 170.8°$.

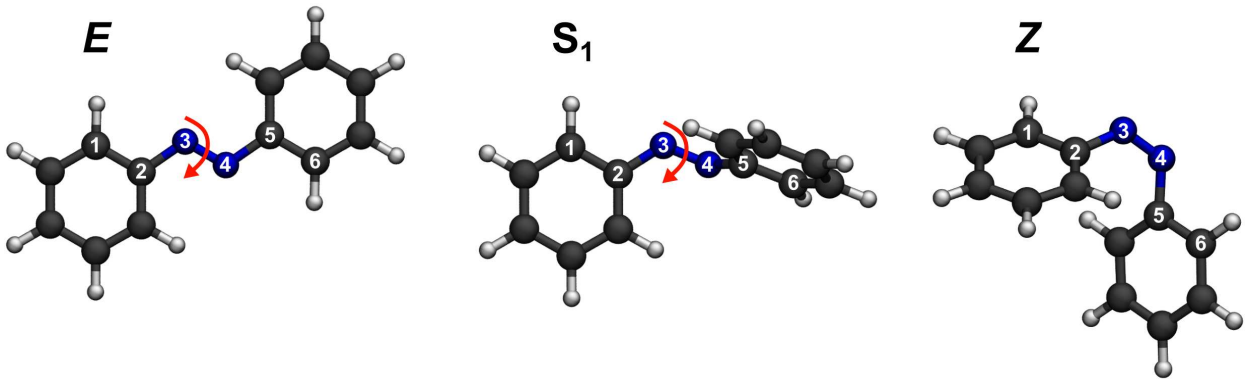

Figure 4.4: Three optimized geometries of **AB**. The ground state *E*-**AB** (*trans*) and meta-stable *Z*-**AB** (*cis*) are both S_0 states. S_1-**AB** represents the lowest-energy geometry on the first excited-state surface, highlighting the rotational photoisomerization reaction coordinate (red arrow). Hydrogen atoms are white, carbon atoms are gray, and nitrogen atoms are blue. PBE0-D4/def2-TZVP/CPCM(MeCN) level of theory.

The LR-TDA approximation reliably describes the absorption spectrum of *E*-**AB**. The excitation energies obtained from LR-TDA are linearly correlated with those from LR-TDDFT (Figure 4.5), though systematically blue-shifted in energy, as expected.[278] However, the LR-TDA and LR-TDDFT oscillator strengths do not exhibit a linear correlation (Figure 4.5). Given that LR-TDA violates the Thomas-Reiche-Kuhn sum rule,[312] which asserts that the integrated oscillator strength of a chromophore equals its number of electrons, this outcome is anticipated. Nevertheless, the overall shape and key features of the Gaussian-broadened ground-state absorption spectrum remain consistent between the two methods, with a 64% overlap between the LR-TDA and LR-TDDFT spectra ($\sigma = 0.4$ eV).

The LR-TDA/PBE0 S_1 and S_2 excitation energies from the ground state geometry closely match the experimental absorption spectrum (Figure 4.6 and Table 4.1). Both PBE0 and LC-

Molecule	**State**	**TDA**/eV	**TDDFT**/eV	**ΔSCF**/eV	**Exp.**/eV
AB	S_1	2.662 (2.986)	2.604 (2.882)	2.143 (2.327)	2.73
AB	S_2	3.837 (4.667)	3.664 (4.496)	3.054 (4.031)	3.87
BD	S_1	3.219 (3.193)	2.944 (2.974)	2.116 (2.615)	2.51
ZP	S_1	2.526 (2.579)	2.462 (2.172)	2.361 (DNC[a])	2.17
ZP	S_2	2.526 (2.579)	2.462 (2.172)	DNC[a] (2.730)	2.33

[a]did not converge.

Table 4.1: Predicted excitations in the main absorption features. $S_0 \rightarrow S_n$ excitation energies in eV from **TDA**, **TDDFT**, and **ΔSCF** at PBE0-D4 (LC-PBE-D4) level of theory. Experimental energies determined from absorption maximum near the various features of interest.

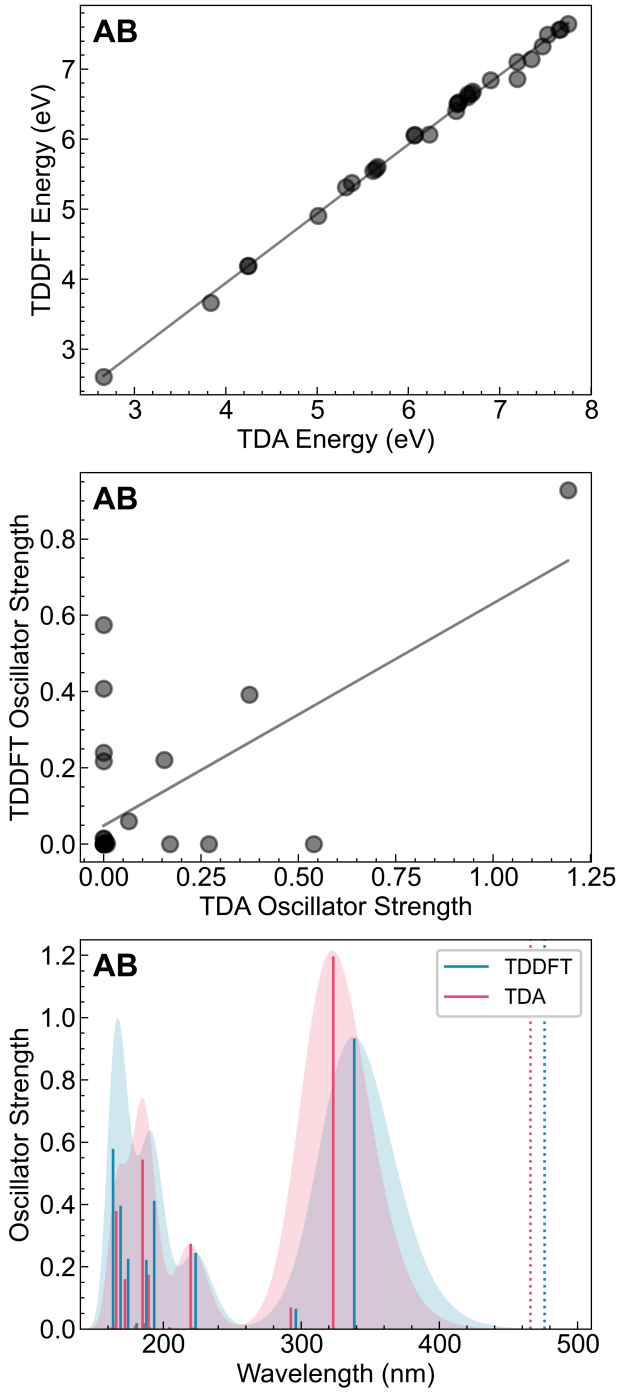

Figure 4.5: Correlations between TDA and TDDFT energies and oscillator strengths for E-**AB**. Best fit lines: (top) $y = 0.9901x - 0.0152$ and $R^2 = 0.9968$, (middle) $y = 0.5830x + 0.0484$ and $R^2 = 0.4333$. (Bottom) Substantial overlap (64%) between spectra despite no correlation between TDA and TDDFT oscillator strengths. S_1 excitations with zero oscillator strength are represented by dotted lines.

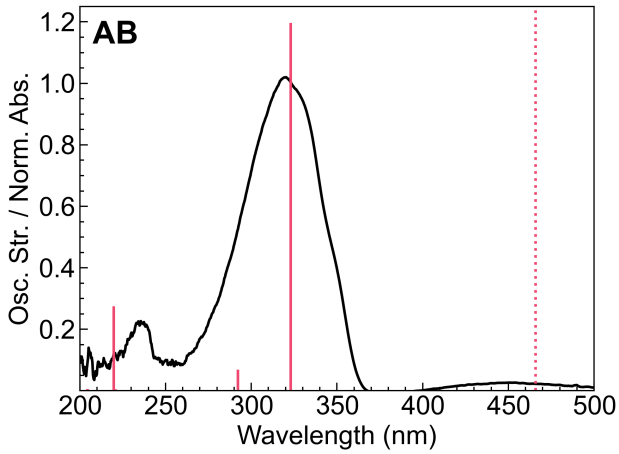

Figure 4.6: Normalized UV-vis absorption of E-**AB** in MeCN (black curve) and LR-TDA/PBE0 excitations (red sticks). The symmetry forbidden first excited state (S_1, $n \rightarrow \pi^*$) energy is plotted as a dotted line.

PBE predict that the S_1 state has an oscillator strength of approximately zero at the ground-state (E) geometry, as this corresponds to an $n \rightarrow \pi^*$ transition, which is symmetry-forbidden. In practice, however, this state becomes accessible through vibronic coupling and solvent interactions that break symmetry, leading to a small but finite oscillator strength.[313] This explains the weak absorption feature observed at 450 nm in the experimental spectrum (Figure 4.6). In contrast, the S_2 excitation corresponds to a $\pi \rightarrow \pi^*$ transition with a large oscillator strength, calculated to be 1.2 with LR-TDA/PBE0 and 1.1 with LR-TDA/LC-PBE. As expected, LR-TDA/LC-PBE systematically predicts excitation energies that are blue-shifted relative to both experiment and LR-TDA/PBE0. Thus, the rest of the analysis focuses on PBE0 and ΔPBE as they provide excitation energies in better agreement with experiment. LC-PBE results that systematically overestimate excitation energies are included in the Supporting Information for comparison.

Approximate excited states are generated by (1) constructing non-Aufbau singly-excited determinants through the exchange of one virtual and one occupied orbital (Figure 4.2 middle) from the S_0-E-AB reference determinant (Figure 4.2 left) and (2) allowing the orbitals to self-consistently relax using ΔSCF (Figure 4.2 right).

Occupied and virtual orbital pairs are selected based on the results of ground-state LR-TDA calculations. For example, LR-TDA predicts that the S_1 excited state of E-**AB** is primarily ($C^2 = 0.98$) characterized by the excitation of an electron from an n-orbital (α-HOMO-1) to a π^*-orbital

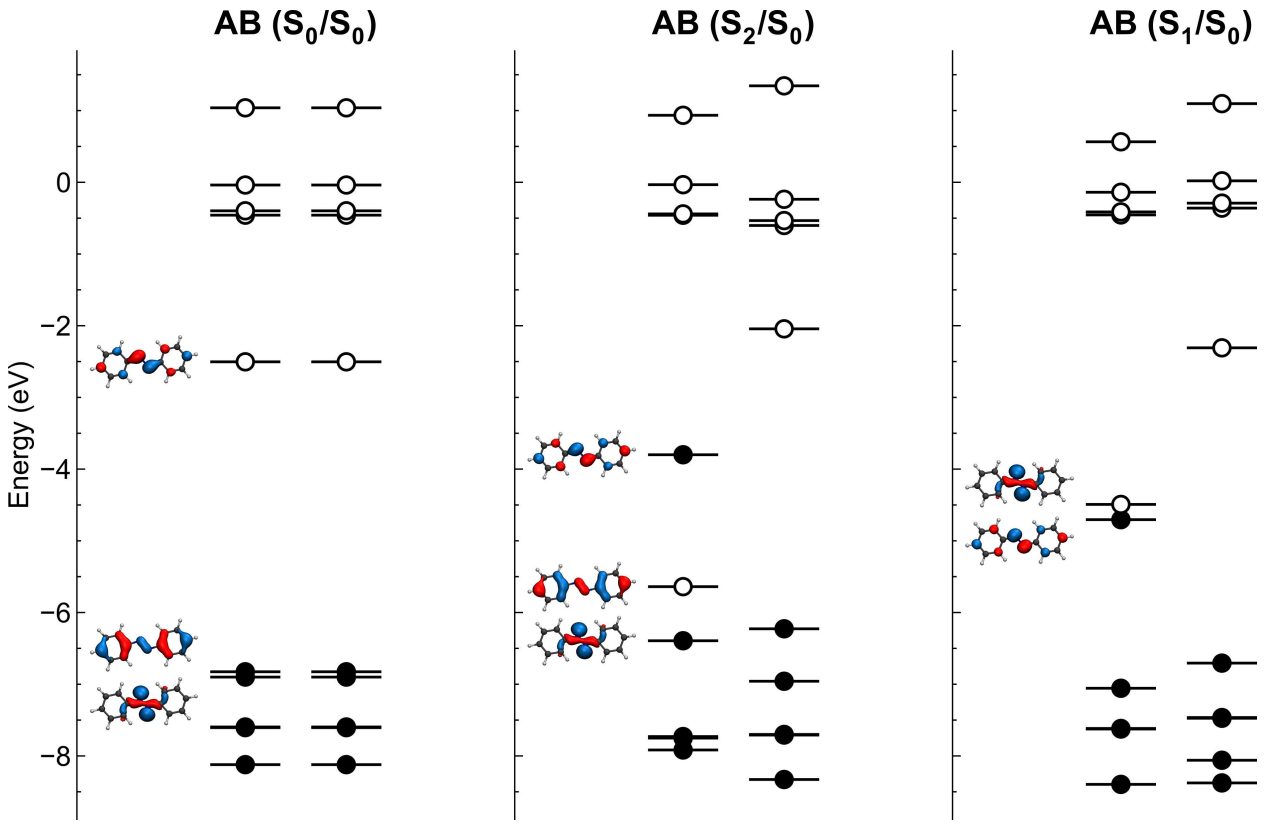

Figure 4.7: α-MO (left) and β-MO (right) diagrams for E-**AB** in the ground state (S_0, left), and first (S_1, middle) and second (S_2, right) excited states. PBE0-D4/def2-TZVP/CPCM(MeCN) and ΔPBE0-D4/def2-TZVP/CPCM(MeCN) levels of theory.

(α-LUMO) (Figure 4.7 left). This non-Aufbau configuration converges to the S_2 state rather than the expected S_1 state with ΔSCF. The state has a depopulated α-π-orbital and a singly occupied α-π^* orbital (Figure 4.7 middle). Energetically, the resulting ΔSCF energy (3.05 eV) is closer to the experimental S_1 energy (2.73 eV) than to the experimental S_2 energy (3.87 eV). However, when attempting to converge to the S_2 state by exciting an electron from the α-π-orbital to the α-π^*-orbital, a lower-energy excited state (2.14 eV) was obtained. This state has a depopulated α-n-orbital and a singly occupied α-π^*-orbital (Figure 4.7 right). These results indicate that the initial "S_1 guess" converged to the true S_2 state, while the "S_2 guess" instead converged to the true S_1 state.

LR-TDA calculations on the S_1 and S_2 excited-state references confirm the state assignments. The lower-energy 2.14 eV ΔSCF excited state has a single *negative* excitation energy of -2.00 eV with $\langle S^2 \rangle = 0.033674$, where $\langle S^2 \rangle$ is the square of the total spin angular momentum. In comparison, the unrestricted open-shell excited-state reference has $\langle S^2 \rangle = 1.025705$, indicating that this transition is a relaxation back to the closed-shell S_0 state. Analysis of the orbitals involved in the transition confirmed that it corresponds to a de-excitation from the α-π^*-orbital to the α-n-orbital. The higher-energy 3.05 eV ΔSCF excited state has two negative excitation energies of -2.88 and -0.73 eV. The -2.88 eV transition corresponds to a de-excitation from the α-π^*-orbital to the α-π-orbital and has $\langle S^2 \rangle = 0.027084$, suggesting relaxation to the closed-shell S_0 state. Meanwhile, the -0.73 eV transition corresponds to a de-excitation from the α-n-orbital to the α-π-orbital, with $\langle S^2 \rangle = 1.012204$.

The S_1 ΔSCF geometry optimization converged to an open-shell singlet ($\langle S^2 \rangle = 1.010254$) with an azo dihedral angle of 109.3°, 16.5° larger than what has been predicted with CASSCF (92.8°).[314] The absence of imaginary frequencies confirmed that the structure corresponds to the S_1 minimum rather than the rotational transition state of the ground state (S_0). A LR-TDA calculation further validated this assignment by predicting a single negative excitation energy of -0.026 eV and $\langle S^2 \rangle =$ 0.048049, confirming de-excitation to the closed-shell S_0 state. The small de-excitation energy suggests that this geometry is near, if not at, the conical intersection. Since LR-TDA relies on the adiabatic approximation, it cannot explicitly converge to a true conical intersection.[315] Notably, the ΔSCF de-excitation energy was even smaller at -0.016 eV, providing additional evidence that this structure corresponds to the conical intersection. A frequency calculation on the S_1 geometry in

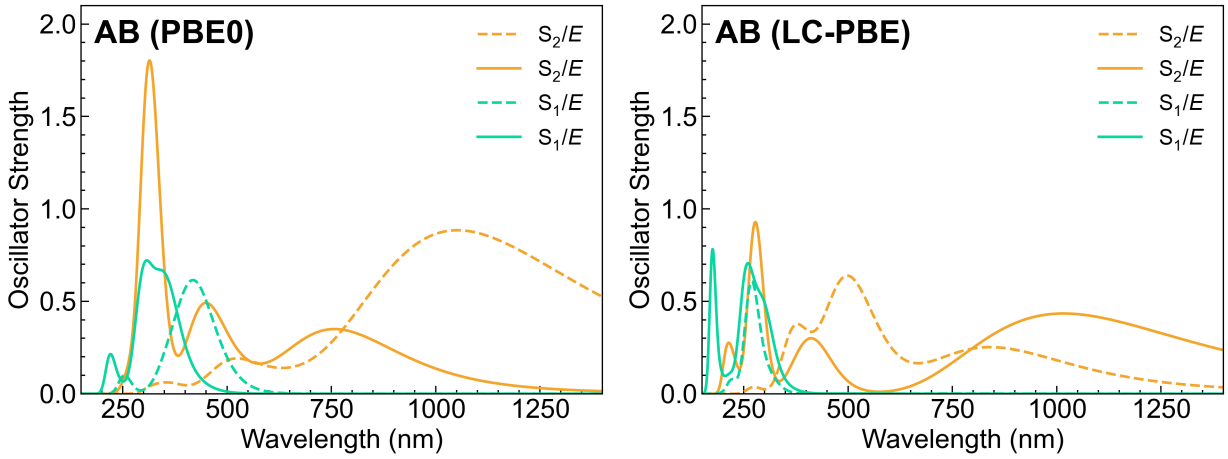

Figure 4.8: Predicted excited-state absorption of **AB**. ΔSCF (solid lines) vs. expectation value formalism (dashed lines) of both the S_1 and S_2. X/Y indicates the X excited-state configuration at the Y geometry.

the closed-shell S_0 state revealed a single imaginary frequency, with the corresponding vibrational mode resembling a characteristic azo bond rotational transition state. Collectively, this strongly supports that the ΔSCF optimization converged to the S_1/S_0 conical intersection.

A comparison of the Gaussian-broadened spectra for the first 30 singlet excited states predicted by LR-TDA/ΔSCF and the expectation value formalism highlights the significance of orbital relaxation (Figure 4.8). Three main absorption features are predicted by both methods, a hybrid and long-range corrected PBE functional. However, they appear at significantly different energies and oscillator strengths. With the PBE0 functional, it is clear that orbital relaxation has a substantial effect, as the ΔSCF S_2 and S_1 excited-state absorption spectra are significantly blue-shifted relative to the expectation value formalism spectra. The newly occupied exited-state α-HOMO is stabilized substantially with respect to the ground state α-LUMO, with only a minor shift in the energies of the unoccupied orbitals. As the α-HOMO energy level decreases, the energetic gap between it and the unoccupied orbitals increases. Interestingly, the magnitude of this blue shift is considerably reduced when using the long-range corrected LC-PBE functional, indicating that the effects of orbital relaxation are less pronounced.

The **AB** TAS data is best fit with four lifetimes, which is generally consistent with previous reports for **AB**.[313,316–318] Typically, the shortest lifetime, 0.2 ps, is assigned to the simultaneous vibrational cooling of the S_2 state and the internal conversion from the S_2 state to the S_1 state. The

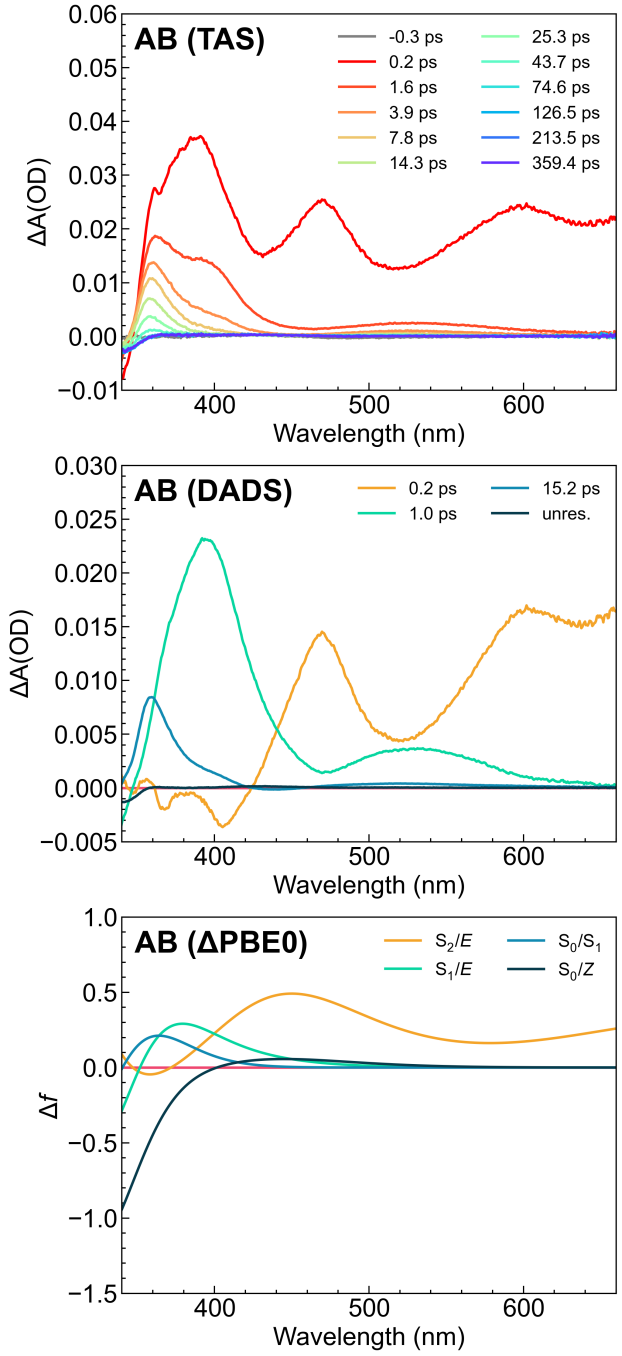

Figure 4.9: Experimental vs. theoretical difference spectra for **AB**. (top) Raw TAS difference spectra at various time delays. (middle) DADS and their respective lifetimes in picoseconds. (bottom) ΔSCF excited-state difference spectra where X/Y indicates the X excited-state configuration at the Y geometry − the ground-state spectrum (S_0/E).

second lifetime, 1.0 ps, is assigned to the vibrational relaxation, through an azo dihedral rotation, to the S_1/S_0 conical intersection, where rapid internal conversion occurs. The third lifetime, 15.2 ps, is assigned to the cooling of the hot-S_0 state to either the *trans-* or *cis*-isomer. The fourth *unresolved* lifetime, *i.e.,* beyond the 5.5 ns TAS window and undetectable by ns-TAS due to low signal, is assigned to the lifetime of the metastable *cis*-isomer.

Theoretical species-associated difference spectra, generated by subtracting the S_0-E-**AB** absorption spectra from various LR-TDA/ΔSCF excited-state absorption spectra, match the respective DADS in both overall shape and energy (Figure 4.9). Specifically, the 0.2 ps DADS aligns with the S_2/E difference spectrum (excited-state absorption/geometry), the 1.0 ps DADS corresponds to the S_1/E difference spectrum, the 15.2 ps DADS matches the S_0/S_1 difference spectrum, and the unresolved DADS is consistent with the S_0/Z difference spectrum.

The LR-TDA/ΔSCF method not only enables the assignment of species to particular lifetimes, but also facilitates the mapping of excited-state spectral features to molecular orbital (MO) transitions, much like what is commonly done in ground-state LR-TDA or LR-TDDFT. The key excited-state transitions from various references are highlighted in Figure 4.10 by their root, *i.e., excited-state number*, and orbital indexes. For E-**AB**, the 1^{st} and 2^{nd} roots (*i.e.,* S_1 and S_2) are involved in $E \rightarrow Z$ photoisomerization. As a result, predicting the excited-state absorption spectra from these states is crucial for interpreting the TAS and DADS spectral features involved in **AB** photoisomerization.

From the S_2 ΔPBE0 reference, two prominent features with significant oscillator strength within or near the TAS spectral window ($\approx$ 340 nm and 660 nm) are the 5^{th} and 9^{th} LR-TDA roots. The 5^{th} root corresponds to a $\pi \rightarrow \pi^*$ transition from a low-energy α-π-orbital to the α-LUMO (the former α-HOMO of S_0-E-**AB**), while the 9^{th} root corresponds to a high-energy $\pi \rightarrow \pi^*$ excitation from the α-HOMO (the former α-LUMO of S_0-E-**AB**) to the α-LUMO+3 orbital. The 9^{th} root is within 20 nm of the experimental absorption feature between 400 and 500 nm, whereas the 5^{th} root is red-shifted by more than 100 nm relative to the experimental feature around 600 nm.

From the S_1 ΔPBE0 reference, the main absorption feature (*i.e.,* the 9^{th} root) is red-shifted relative to the ground-state bleach. Like the 9^{th} root from the S_2 reference, this transition involves a high-energy $\pi \rightarrow \pi^*$ excitation from the α-HOMO to the α-LUMO+3 orbital, and exhibits nearly identical character. However, the transition from the S_1 state has a higher energy than the corre-

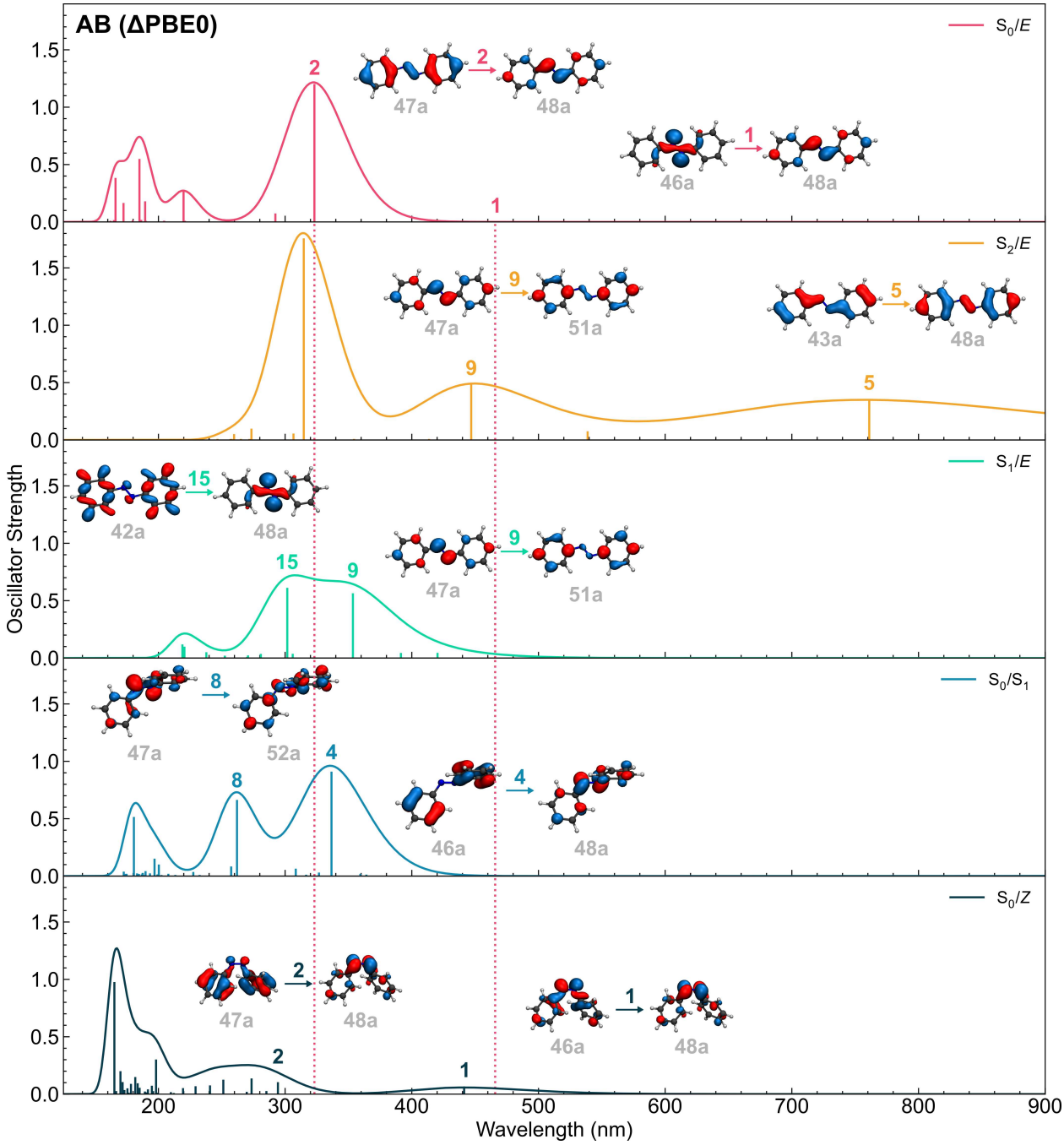

Figure 4.10: Molecular orbital transitions in the ground- and excited-state absorption spectra of **AB**. X/Y, indicates the X excited-state configuration at the Y geometry. Red dotted lines mark the ground-state S_1 and S_2 excitation energies for reference. Select roots, *i.e.*, excited-state indices, are labeled above the transitions. HOMO = $47\alpha/\beta$ and LUMO = $48\alpha/\beta$.

sponding 9^{th} root from the S_2 state due to the distinct non-Aufbau molecular orbital configuration and the subsequent ΔSCF orbital relaxation. When comparing the S_1 and S_2 molecular orbital diagrams (Figure 4.7), it is evident that the α-HOMO of the S_1 state is lower in energy than that of the S_2, while the π^* energies remain essentially consistent. The shift in the α-HOMO energy of the S_1 state to a lower value than in the S_2 state explains the higher excitation energy in the S_1 state. The λ_{max} of the S_1/E difference spectrum is once again within 20 nm of the λ_{max} of the 1 ps lifetime.

Importantly, comparing the λ_{max} of the theoretical difference spectra with the λ_{max} of the DADS reveals a key distinction. Unlike the 9^{th} root from the S_2 state, which is well separated from the ground-state S_2 feature, theory suggests significant spectral overlap between the ground-state S_2 feature and the 9^{th} root from the S_1 state. This overlap leads to a red shift in the position of the feature away from the true λ_{max} in the difference spectra. Therefore, in this case, comparing the difference spectra is likely to yield a closer match to experimental reality than simply considering the excitation energy of the 9^{th} root.

Because the spectral window of the TAS is roughly between 340 nm and 680 nm, features that are blue-shifted to the ground-state bleach remain undetected. However, the 15^{th} root from the S_1 reference is highlighted in Figure 4.10, as it could be resolved in a future study if the spectral window were extended to cover this region. This high-energy feature is particularly noteworthy because it involves a $\sigma(\mathrm{C}) \rightarrow n^*(\mathrm{N})$ transition from the α-HOMO-5 to the α-LUMO orbital, a transition not typically observed in small molecule organic compounds using UV-vis spectroscopy.

The λ_{max} of both the 15.2 ps DADS and theoretical S_0/S_1 (*i.e.,* the S_0 state at the S_1 minimum) difference spectra are approximately 360 nm, indicating that this lifetime likely corresponds to the relaxation of the hot-S_0. Because there is considerable overlap between the 4^{th} root from the S_0/S_1 state and the S_2-E-**AB**, comparing the difference spectra may be more reliable than the excitation energy of the 4^{th} root to the λ_{max} of the 15.2 ps DADS. This transition involves a π to mixed-n^*/π^* transition from the α-HOMO-1 to the α-LUMO. Additionally, the 8^{th} root is blue-shifted and well separated from the ground-state bleach and could likely be observed if the TAS spectral window could be adjusted appropriately. This transition involves a mixed-n/π to mixed-n^*/π^* transition from the α-HOMO to the α-LUMO+4 and its observation could further confirm that the 15.2 ps species is majority hot-S_0 rather than an S_1 excited state.

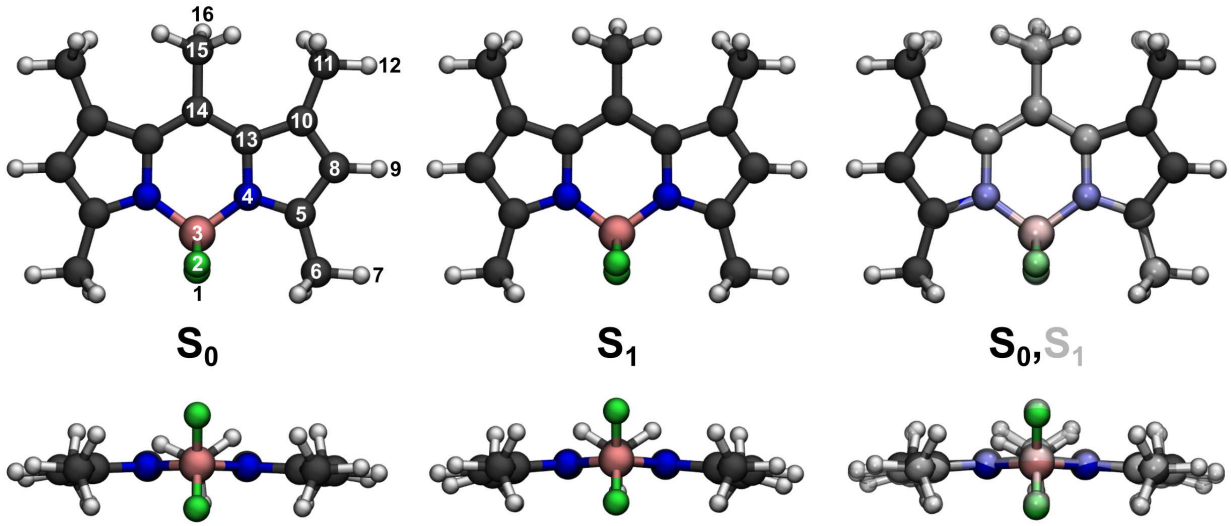

Figure 4.11: Optimized geometries of S_0-**BD** and S_1-**BD** at the PBE0-D4/def2-TZVP/CPCM(MeCN) level of theory. Hydrogen atoms are white, carbon atoms are gray, boron atoms are pink, nitrogen atoms are blue, and fluorine atoms are green.

The long-lived, unresolved, lifetime is most likely due to the thermal reversion from *Z*-**AB** to *E*-**AB**. The S_0/Z difference spectra matches the unresolved DADS well, and similar assignments are available in a plethora of literature.[313,316–318] *Z*-**AB** has only one singlet excited state red-shifted to the ground-state bleach. The 1^{st} root has an excitation energy around 440 nm but exhibits a relatively small oscillator strength due to the poor, yet non-negligible, overlap between the α-HOMO-1 and α-LUMO orbitals. This transition is of mixed-n/π to mixed-n^*/π^* character and has the expected low oscillator strength because of the nearly orthogonal n-component of the orbitals. This detailed mechanistic understanding of the excited-state orbitals validates a complex photophysical mechanism that required years of study and hundreds of experiments to unravel.

4.3.3 BODIPY

The main absorption feature (S_1) of pentamethyl-BODIPY (**BD**, Figure 4.11) and related BODIPYs[223] corresponds to a HOMO–LUMO $\pi \rightarrow \pi^*$ transition. Upon excitation, **BD** exhibits strong green fluorescence with no evidence of phosphorescence. BODIPYs with aromatic *meso*-substituents can undergo intramolecular charge transfer to access the triplet manifold,[319] but this intramolecular charge transfer is absent in **BD** due to its *meso*-methyl substitution. As a result, modeling the photophysics of **BD** requires consideration only of the ground state and first excited

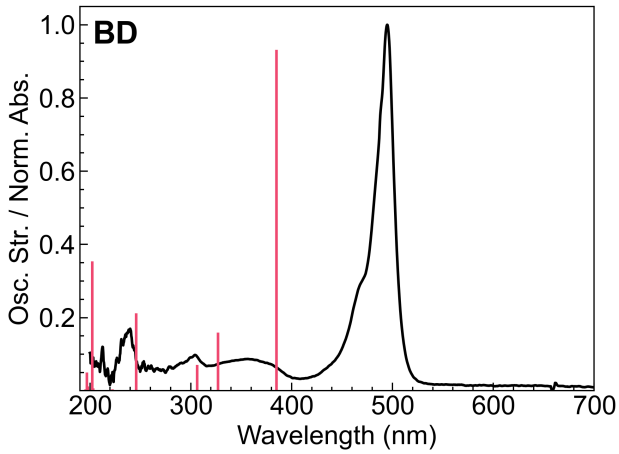

Figure 4.12: Normalized UV-vis absorption of **BD** in MeCN (black curve) and LR-TDA/PBE0-D4/def2-TZVP/CPCM(MeCN) excitations (red sticks).

state, along with their optimized geometries.

The optimized ground-state (S_0) geometries of **BD** showed no significant deviations between the PBE0 and LC-PBE methods (RMSD = 0.077 Å). The ΔSCF first excited-state (S_1) geometries exhibit a pronounced puckering of the BODIPY backbone, causing both the methyl group on C_{14} and the BF_2 unit to shift upward (Figure 4.11). Additionally, the C_{14} methyl group undergoes rotation in the S_1 state, adopting a nearly ideal staggered conformation relative to the BF_2 unit (Figure 4.11).

Similar to **AB**, the excitation energies from LR-TDA and LR-TDDFT exhibit a linear correlation, with LR-TDA systematically blue-shifted relative to LR-TDDFT. While the oscillator strengths are not linearly correlated, the overall shape of the Gaussian-broadened LR-TDA absorption spectrum closely matches that of LR-TDDFT, with an integrated overlap of 52%. The largest discrepancies in excitation energy and oscillator strength between the two methods are observed in the S_1 feature. With the PBE0 functional, LR-TDDFT predicts an excitation energy of 3.219 eV, whereas LR-TDA predicts 2.944 eV. A similar trend is seen with the LC-PBE functional, where LR-TDDFT and LR-TDA yield excitation energies of 3.193 eV and 2.974 eV, respectively. Regardless of the functional or TD-approximation used, all methods predict an S_1 feature that is blue-shifted relative to the experimental λ_{max} at 2.51 eV (Table 4.1, Figure 4.12).

Since **BD** emits from the S_1 excited state, ground- and excited-state absorption spectra were predicted using LR-TDA and LR-TDA/ΔSCF, respectively, from the S_0 and S_1 geometries. The

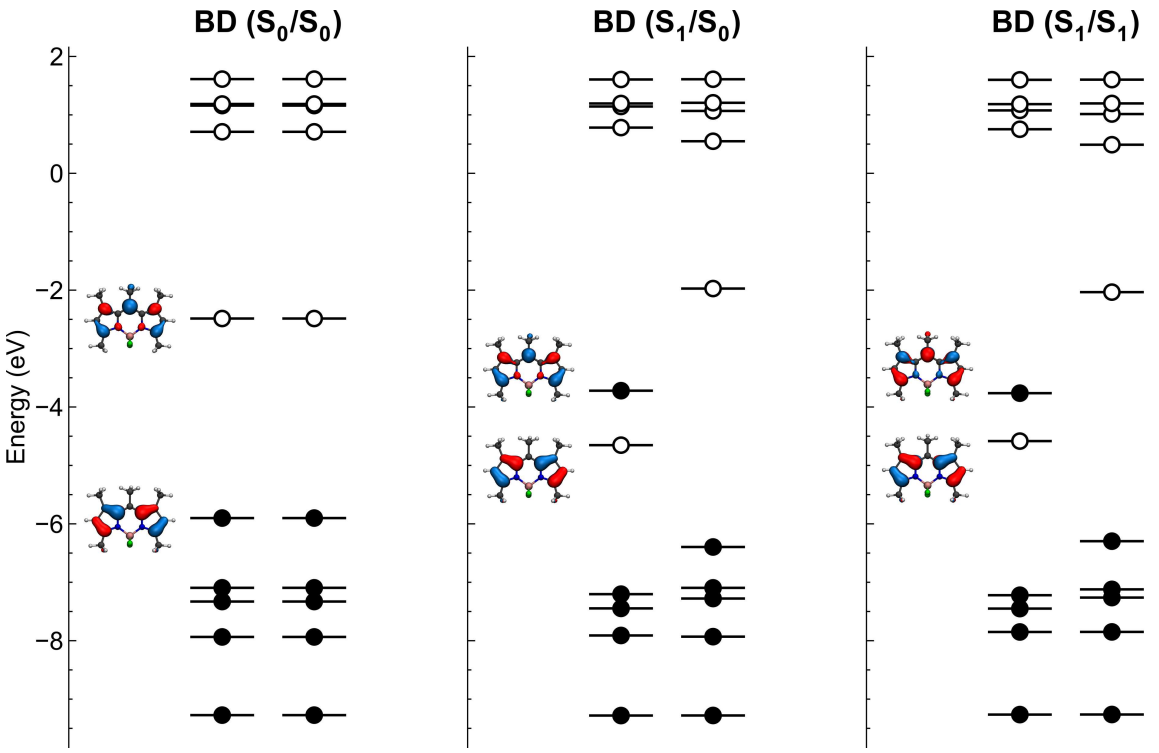

Figure 4.13: α-MO (left) and β-MO (right) diagrams for S_0-**BD** in the ground state (S_0, left) and first excited state (S_1, middle), as well as the optimized S_1-**BD** in the first excited state (S_1, right). PBE0-D4/def2-TZVP/CPCM(MeCN) and ΔPBE0-D4/def2-TZVP/CPCM(MeCN) levels of theory.

S_1 absorption feature from the S_0 state corresponds to a $\pi \rightarrow \pi^*$ transition from the HOMO to the LUMO, with an oscillator strength of 0.9278 with LR-TDA/PBE0 (Figure 4.13). A guess configuration with a singly occupied α-LUMO and a singly occupied β-HOMO was generated and ΔSCF converged to an orbital- and energetically-relaxed S_1 configuration with an α-HOMO and α-LUMO that closely resemble the S_0 LUMO (π^*) and HOMO (π), respectively. The most significant difference is in the α-HOMO and α-LUMO energy levels, followed by the β-HOMO and β-LUMO energy levels. In the α-manifold, the highest occupied π^* orbital is significantly stabilized, while the lowest unoccupied π orbital is destabilized by a comparable amount relative to their S_0 counterparts (Figure 4.13). Additionally, the β-HOMO is partially stabilized, whereas the β-LUMO is slightly destabilized. The energies of orbitals below the α/β-HOMO or above the α/β-LUMO remained largely unperturbed.

LR-TDA on the S_1 ΔSCF reference (1) confirms that this is indeed the S_1 state by predicting a single negative excitation energy and (2) provides its excited-state absorption spectrum. The S_1

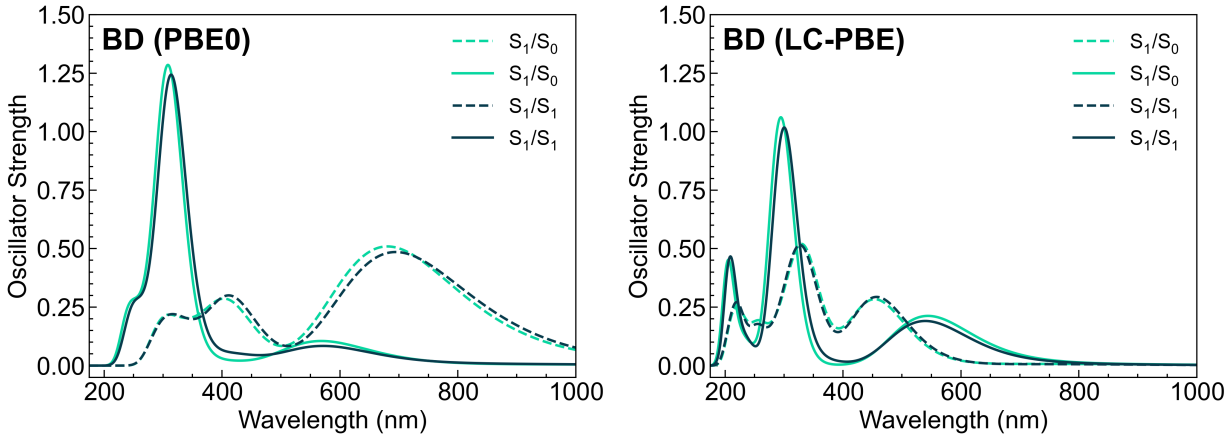

Figure 4.14: Predicted excited-state absorption of **BD**. ΔSCF (solid lines) vs. expectation value formalism (dashed lines) of both the S_1 and S_2. X/Y indicates the X excited-state configuration at the Y geometry.

ΔSCF state exhibits a negative excitation energy of -1.74 eV from the α-HOMO (occupied π^*) to the α-LUMO (unoccupied π) with a $\langle \hat{S}^2 \rangle = 0.060456$. In contrast, the reference open-shell S_1 state has $\langle \hat{S}^2 \rangle = 1.032256$, confirming that de-excitation yields a closed-shell singlet that resembles the S_0 state.

The LR-TDA/ΔSCF S_1 excited-state absorption spectra predicted using the expectation value formalism and ΔSCF with both PBE0 and LC-PBE functionals show similar trends as **AB** (Figure 4.14). The PBE0 functional shows more significant effects of orbital relaxation compared to LC-PBE. Orbital relaxation leads to a blue shift in ΔSCF excitation energies relative to the expectation value formalism predicted with the PBE0 functional. This shift is due to the substantial relaxation of the occupied π^* orbital during the ΔSCF optimization. Since the unoccupied orbitals, apart from the α-LUMO, remain largely unchanged, excitations from the relaxed configuration occur at higher energies than those predicted by the unrelaxed expectation value formalism.

Both methods and functionals predict all three main absorption features, but the effects of orbital relaxation are less pronounced in the LC-PBE excited-state absorption spectra (Figure 4.14). The features from both LR-TDA/ΔSCF and the expectation value formalism align well and are generally consistent. Notably, the first excited-state feature predicted by the expectation value formalism is blue-shifted relative to the LR-TDA/ΔSCF feature, which differs from the PBE0 functional, where the first excited-state feature predicted by the expectation value formalism is significantly red-shifted.

Excited-state absorption spectra from the ΔSCF-optimized S_1 geometry provides insight into the emissive S_1 state. Both ΔPBE0 and ΔLC-PBE show that S_1 geometry optimization has little effect on the S_1/S_1 excited-state absorption spectrum compared to the S_1/S_0 spectrum (Figure 4.14). This suggests that the raw TAS and DADS should show only minor differences in the excited-state absorption spectra.

When **BD** is selectively excited into the S_1 state with a 505 nm pump pulse (Figure 4.15), near its λ_{max}, three species contribute to the process: (1) the S_0 state at the S_0 geometry (S_0/S_0), (2) the S_1 state at the S_0 geometry (S_1/S_0), and (3) the S_1 state at the S_1 geometry (S_1/S_1). The fs- and ns-TAS of **BD** in MeCN is best fit with two distinct lifetimes: a short-lived vibrational relaxation within the S_1 state (15.6 ps) and a long-lived emissive process (5.883 ± 0.529 ns). However, based solely on the TAS data, it is unclear which excited state of the system the absorption features and geometries are associated with. For example, in **BD**, the long-lived component arises from the S_1 minimum geometry rather than the initially excited S_1.

Theoretical difference spectra from the S_1 state at both the S_0 and S_1 geometries provide a way to assign the observed features in the raw TAS data as well as in the short- and long-lived DADS (Figure 4.15). The PBEO S_1 excited-state absorption spectra from the S_0 and S_1 geometries are very similar (Figure 4.14), and consequently, their difference spectra show only minor variations (Figure 4.15). Both geometries are predicted to have two distinct excited-state absorption features not present in the ground-state spectrum. The most prominent appears blue-shifted (around 310 nm) relative to the ground-state bleach, while a weaker red-shifted feature emerges around 560 nm.

The raw TAS data shows the growth of the blue-shifted feature on short time scales, followed by its decay on longer time scales (Figure 4.15). This feature is also observed in both the 15.6 ps and 5.86 ns DADS. In general, the ΔPBE0 features from both the S_0 and S_1 geometries align well with the DADS, though they appear at slightly higher energies, as expected. However, the red-shifted feature with a low oscillator strength, predicted by both ΔPBE0 and ΔLC-PBE, was not observed in either the raw TAS or DADS. This feature comes from the 4^{th} root of the S_1 configuration, corresponding to a $\pi \rightarrow \pi^*$ excitation from the α-HOMO-3 to the α-LUMO (the unoccupied S_0 π-orbital) (Figure 4.16). However, this red-shifted ESA is observed in toluene with greater intensity.[320] This not only supports the computational assignment of this feature but directly shows how orbital level understanding of the ESA makes the LR-TDA/ΔSCF method

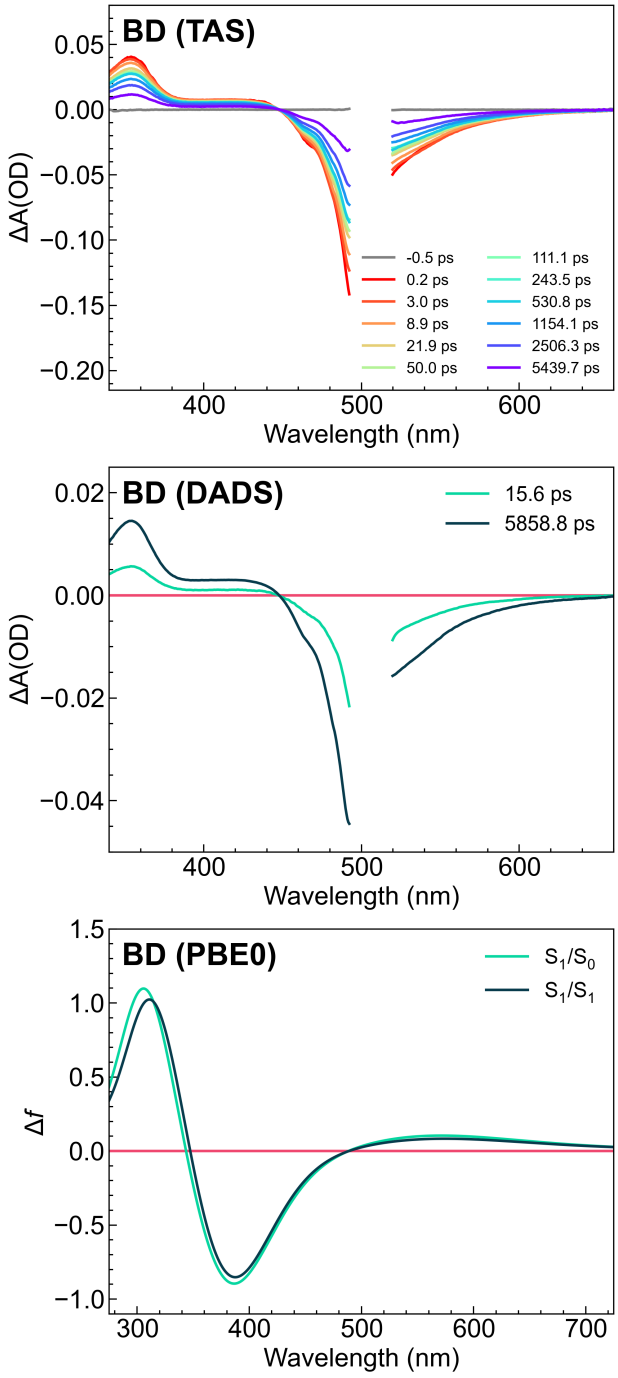

Figure 4.15: Experimental vs. theoretical difference spectra for **BD**. (top) Raw TAS difference spectra at various time delays. (middle) DADS and their respective lifetimes in picoseconds. (bottom) ΔSCF excited-state difference spectra where X/Y indicates the X excited-state configuration at the Y geometry − ground-state spectrum (S_0/S_0).

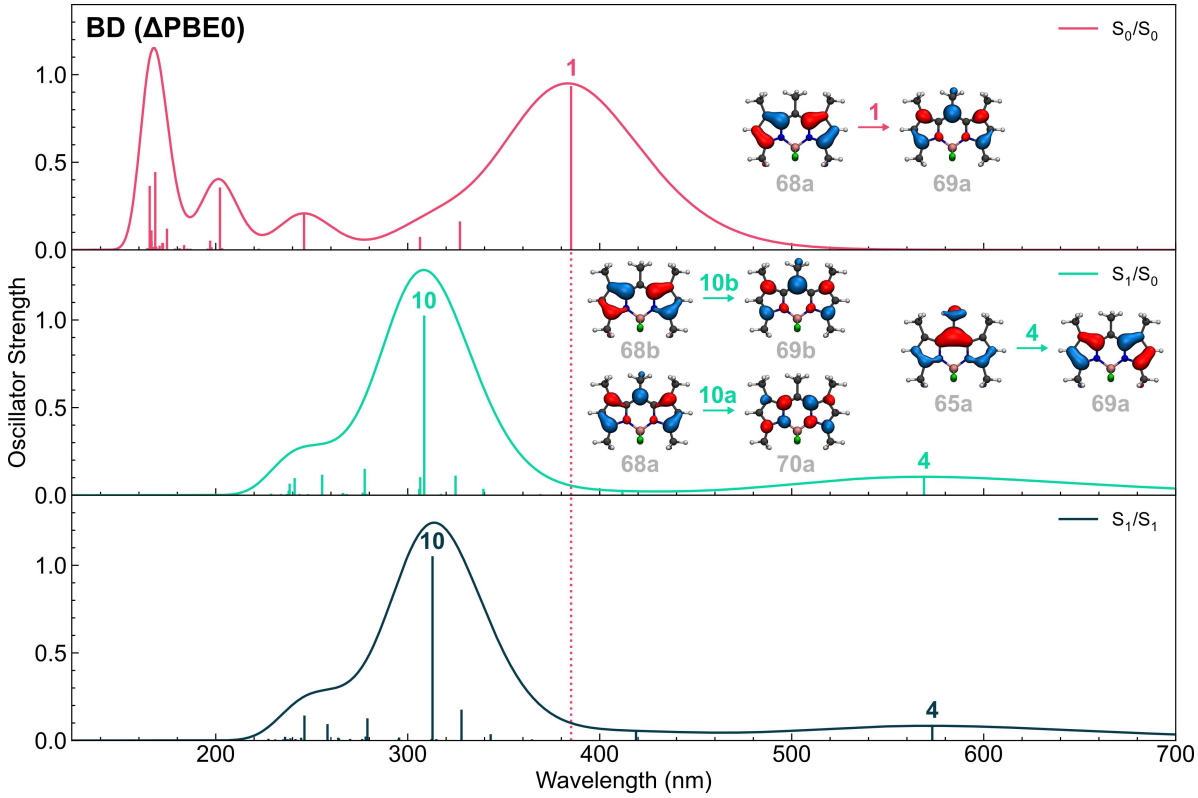

Figure 4.16: Molecular orbital transitions in the ground- and excited-state absorption spectra of **BD**. X/Y indicates the X excited-state configuration at the Y geometry. Red dotted line marks the ground-state S_1 excitation energy for reference. Select roots, *i.e.*, excited-state indices, are labeled above the transitions. HOMO = $68\alpha/\beta$ and LUMO = $69\alpha/\beta$.

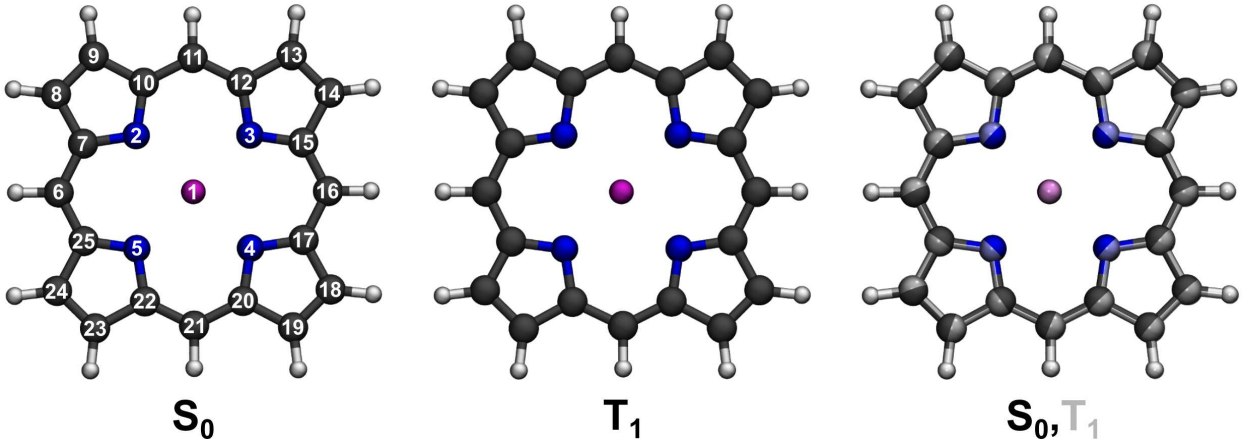

Figure 4.17: Optimized geometries of S_0-**ZP** and T_1-**ZP** at the PBE0-D4/def2-TZVP/CPCM($CHCl_3$) level of theory. Hydrogen atoms are white, carbon atoms are gray, nitrogen atoms are blue, and zinc atoms are magenta.

particularly powerful for understanding TAS data.

The main excited-state absorption feature from the S_1 state corresponds to the 10^{th} root. This excitation primarily involves two pairs of orbitals. The first pair ($C^2 = 0.35$) is a $\pi \rightarrow \pi^*$ transition from the β-HOMO to the β-LUMO at the S_0 geometry. This transition, along with the initial excitation from the α-HOMO to the α-LUMO, effectively approximates a double excitation, or a doubly excited configuration. Alternatively, a double excitation could be optimized using standard ΔSCF by promoting both electrons from the π (HOMO) to the π^* (LUMO). The second orbital pair ($C^2 = 0.31$) is a $\pi \rightarrow \pi^*$ excitation from the α-HOMO (occupied π^*) to the α-LUMO+1 at the S_0 geometry. At the S_1 geometry, the dominant configuration changes, but the orbital shapes and energies remain generally consistent. The excitation of the beta electron has $C^2 = 0.32$, while the excitation of the α-electron has $C^2 = 0.35$. Because these structural changes are minimal, the 10^{th} root at the S_0 and S_1 geometries remains similar in both energy and oscillator strength. This supports assignment of the two lifetimes to $S_1^{\rightarrow} S_1$ and $S_1 \rightarrow S_0$, respectively. Thus, LR-TDA/ΔSCF identifies features that merit further investigation, either through solvatochromism or by modifying the chromophore's structure.

4.3.4 Zinc porphyrin

The orbital symmetry in zinc porphyrins (one of the simplest is **ZP** in Figure 4.17), leads to symmetry-forbidden transitions (S_1 and S_2) between the degenerate HOMO and HOMO-1 $\rightarrow$

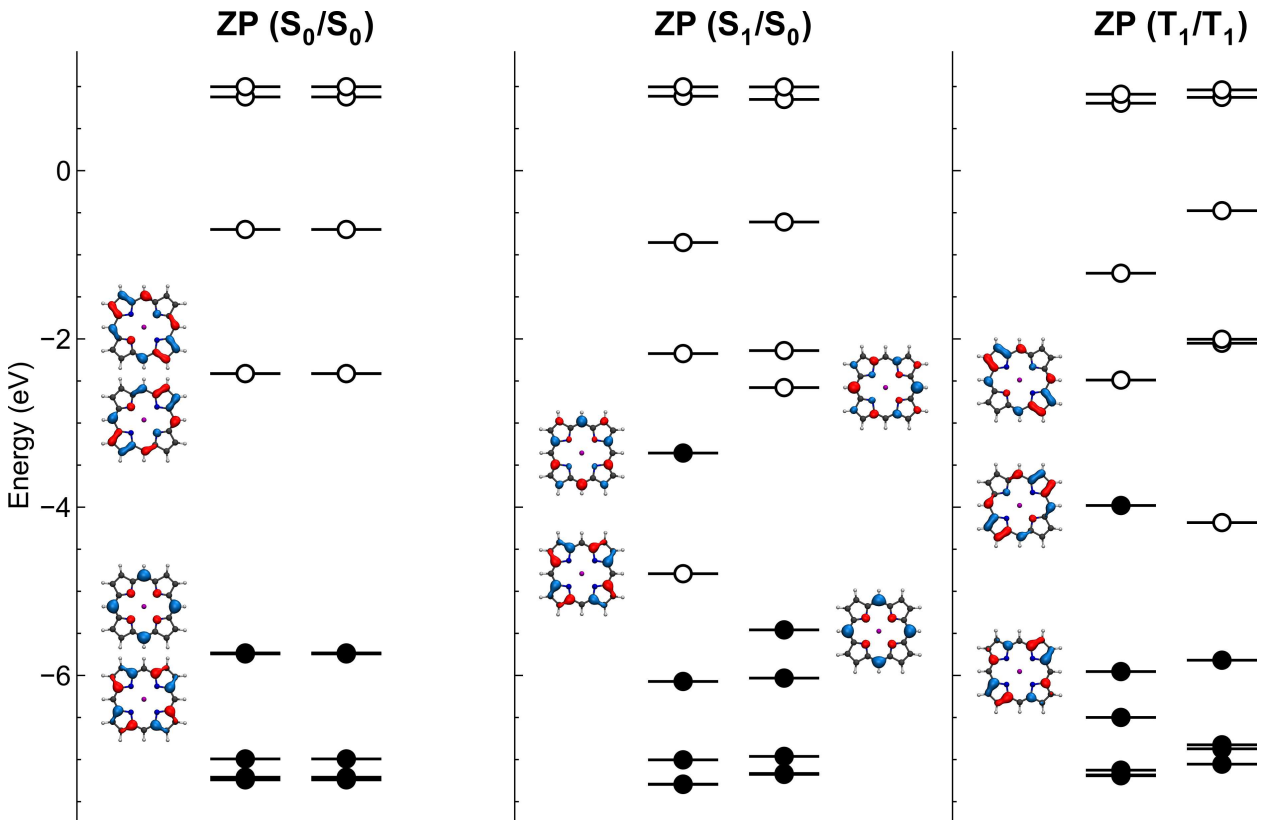

Figure 4.18: α-MO (left) and β-MO (right) diagrams for S_0-**ZP** in the ground state (S_0, left), first singlet excited state (S_1, middle) and optimized first triplet excited state (T_1, right). PBE0-D4/def2-TZVP/CPCM($CHCl_3$) and ΔPBE0-D4/def2-TZVP/CPCM($CHCl_3$) levels of theory.

LUMO and LUMO+1. These "Q-band" excitations gain intensity through vibronic coupling.[321] In addition, zinc porphyrins have a strong $\pi \rightarrow \pi^*$ absorption in the blue, the Soret-bands (*i.e.,* S_5 and S_6). The Q and Soret bands of zinc porphyrins are well described by Gouterman's four-orbital model (Figures 4.18 (left) and 4.22 (top)). When excited into the Q-bands, **ZP** can either relax via fluorescence back to the ground state or phosphorescence[321,322] through the triplet manifold via spin-orbit coupling between the S_1 or S_2 states and the T_4, T_3, T_2, or T_1 states. Therefore, at minimum, the lowest energy triplet state must be included in a model of **ZP** photophysics.

The optimized ground-state (S_0) and first triplet excited-state (T_1) geometries of an unsubstituted zinc porphyrin (**ZP**) (Figure 4.17) are similar when calculated with either PBE0 and LC-PBE, showing minimal deviations (RMSD (S_0) = 0.041 Å and RMSD (T_1) = 0.040 Å) for either geometry. The most significant differences between the S_0 and T_1 geometries appear in the C−C and Zn−N bond lengths. In the T_1 geometry, there is a symmetric expansion around one

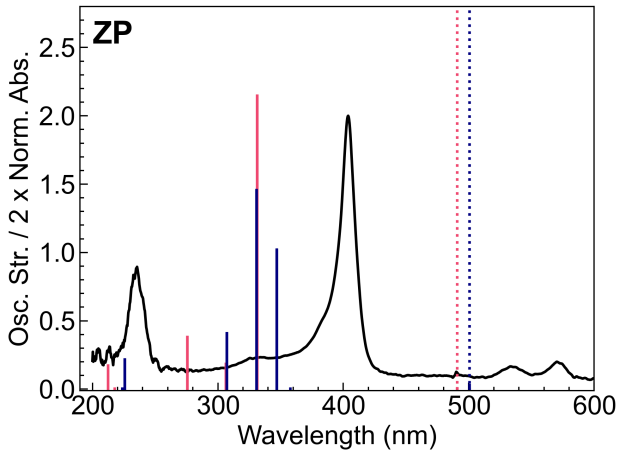

Figure 4.19: Normalized UV-vis absorption of octaethyl-**ZP** in chloroform (black curve) and LR-TDA of unsubsituted-**ZP** (red sticks) and octaethyl-**ZP** (navy sticks). The symmetry-forbidden Q-bands (S_1 and S_2) are marked with dotted lines. PBE0-D4/def2-TZVP/CPCM($CHCl_3$) level of theory.

N−Zn−N diagonal, this leads to elongation of C_{11}−C_{12}, C_{13}−C_{14}, C_{15}−C_{16}, C_{21}−C_{22}, C_{23}−C_{24}, and C_{25}−C_{26} bonds, while the C_{14}−C_{15} and C_{22}−C_{23} bonds contract. Additionally, the Zn−N bonds exhibit elongation (Figure 4.17).

Neither the first nor the second singlet excited states were successfully optimized to local minima using either ΔPBE0 or ΔLC-PBE. In both cases, the resulting structures exhibited one or more imaginary frequencies that could not be eliminated through finite displacements along the imaginary normal modes. Instead, the excited states at the S_0 and T_1 geometries are analyzed to provide insight into the photophysics of **ZP**.

Like **AB** and **BD**, the LR-TDA excitation energies from the S_0 reference state and geometry are linearly correlated with, but systematically blue shifted relative to, LR-TDDFT excitation energies. The oscillator strengths predicted using the PBE0 functional do not exhibit a linear correlation, whereas those predicted with LC-PBE do. The Q-band excitation energies predicted via LR-TDA and LR-TDDFT with PBE0 are in good agreement but remain blue-shifted by approximately 50 nm relative to experiment (Figure 4.19). In contrast, LR-TDA and LR-TDDFT with LC-PBE yield significantly different Q-band excitation energies. Because of this, the LR-TDA approximation with the LC-PBE functional may be unsuitable for describing the Q-band excited states.

The PBE0 LR-TDA S_1 state consists of a mixed $\pi \rightarrow \pi^*$ excitation, primarily involving transitions from the HOMO-1 to the LUMO+1 ($C^2 = 0.50$) and from the HOMO to the LUMO

($C^2 = 0.48$). Similarly, the S_2 state is a mixed $\pi \rightarrow \pi^*$ excitation, with contributions from the HOMO-1 to the LUMO ($C^2 = 0.50$) and the HOMO to the LUMO+1 ($C^2 = 0.48$). For unsubstituted **ZP**, the oscillator strength of these transitions is predicted to be 0.0049. Since vibronic coupling effects are not accounted for in the Gaussian-broadened spectra, the Q-bands remain degenerate at 2.54 eV according to PBE0 and do not exhibit the energy splitting observed experimentally (Figure 4.19). Likewise, for octaethyl-substituted **ZP**, where the ethyl groups are either all eclipsed or all staggered, the Q-bands are predicted to be degenerate at 2.48 eV. Thus, further analysis focuses on the unsubstituted **ZP**.

A non-Aufbau configuration of the S_1 state was optimized at the S_0 geometry by exciting an electron from the α-HOMO-1 to the α-LUMO+1, which represents the dominant $S_0 \rightarrow S_1$ contribution according to LR-TDA. This ΔSCF S_1 excited state has a single LR-TDA negative excitation energy of -2.15 eV and an $\langle S^2 \rangle$ value of 0.0801, indicating a de-excitation from an open-shell excited state ($\langle S^2 \rangle = 1.051073$) to a closed-shell S_0 state. Moreover, the first positive excitation energy is 0.052 eV, which likely corresponds to the excitation to the nearly degenerate S_2 state. Interestingly, the α-LUMO of S_1, as expected, resembles the HOMO-1 of S_0 (Figure 4.18). However, the α-HOMO of S_1 does not resemble either the α-LUMO or α-LUMO+1 of S_0. The β-HOMO of S_1 closely resembles the HOMO of S_0, but the β-LUMO does not. Notably, the α-HOMO and β-LUMO are related by a 90° rotation.

Only one ΔSCF state could be converged at the S_0 geometry. However, the S_1 and S_2 states are degenerate or nearly degenerate, and the expectation value formalism predicts identical excited-state absorption spectra for these states (Figure 4.20) when neglecting vibronic coupling. An alternative guess for the S_1 state was constructed by exciting from the α-HOMO to the α-LUMO. This guess failed to converge within 124 SCF cycles. Similarly, two attempts were made to converge the S_2 excited state: one by exciting from the α-HOMO-1 to the α-LUMO and another from the α-HOMO to the α-LUMO+1. Neither approach achieved convergence within 124 SCF cycles. Convergence issues are primarily attributed to the use of a single-reference method to describe multiconfigurational excitations.

The LR-TDA/ΔSCF S_1 excited-state absorption spectrum of unsubstituted **ZP** is blue-shifted relative to the S_1 and S_2 excited-state absorption spectra predicted using the expectation value formalism with either the PBE0 or LC-PBE (Figure 4.20). Similar to **AB** and **BD**, the effects of

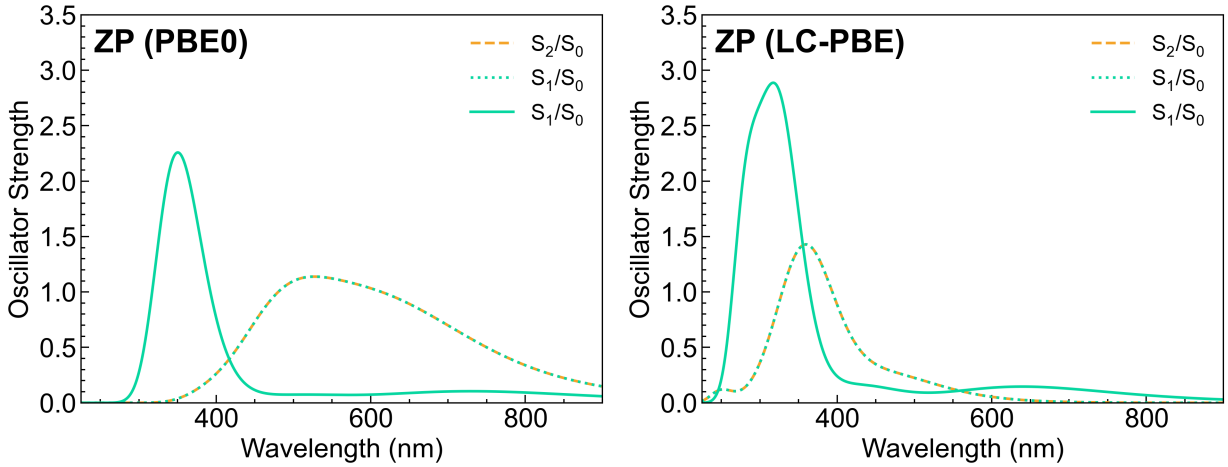

Figure 4.20: Predicted excited-state absorption of unsubstituted **ZP**. ΔSCF (solid lines) vs. expectation value formalism (dashed lines) of both the S_1 and S_2. X/Y indicates the X excited-state configuration at the Y geometry.

orbital relaxation are less pronounced for LC-PBE compared to PBE0. This is evident from the fact that the excitation energies predicted with LC-PBE in the expectation value formalism are in better agreement with the LR-TDA/ΔSCF results.

Selective excitation into the Q-bands of octaethyl-**ZP** in chloroform is best fit with two lifetimes (Figure 4.21). A relatively long-lived 1.1 ns lifetime is attributed to the decay of the convoluted S_1 and S_2 populations into the triplet manifold. Due to slow intersystem crossing from small spin-orbit coupling,[321] the singlet excited states of **ZP** exhibit a significantly longer lifetime compared to the excited singlets of **AB** and **BD**. In turn, the 34.8 ± 2.0 μs lifetime is assigned as the lifetime of the T_1 population. Aside from the absence of vibronic structure, the theoretical excited-state absorption spectra of **ZP** align well with the experimental TAS and DADS spectra (Figure 4.21). Similarly, the theoretical S_1 and T_1 absorption spectra of octaethyl-**ZP** are in good agreement with the experimental TAS and DADS spectra. However, the triplet geometries of octaethyl-**ZP** do not represent true minima, as they exhibit one or more imaginary frequencies corresponding to the motion of the ethyl substituents.

Experimentally, the difference spectra in the region between 400-500 nm show a blue shift over time as the S_1/S_2 population decays and the T_n population grows. In contrast, the theoretical excited-state absorption spectra are nearly aligned in energy but differ in intensity. The blue shift from the excited singlet manifold to the excited triplet manifold, around 400-500 nm, can

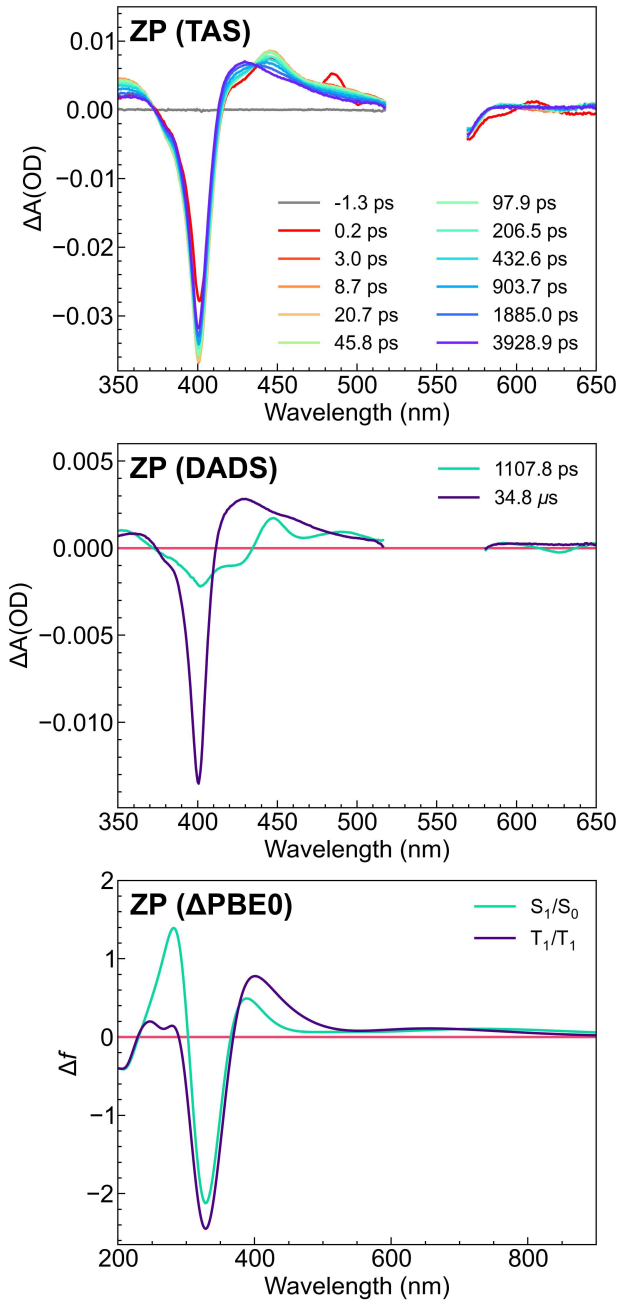

Figure 4.21: Experimental vs. theoretical difference spectra for **ZP**. (top) Raw TAS difference spectra at various time delays. (middle) DADS and their respective lifetimes in picoseconds. (bottom) ΔSCF excited-state difference spectra where X/Y indicates the X excited-state configuration at the Y geometry − ground-state spectrum (S_0/S_0). μs lifetime obtained from ns-TAS.

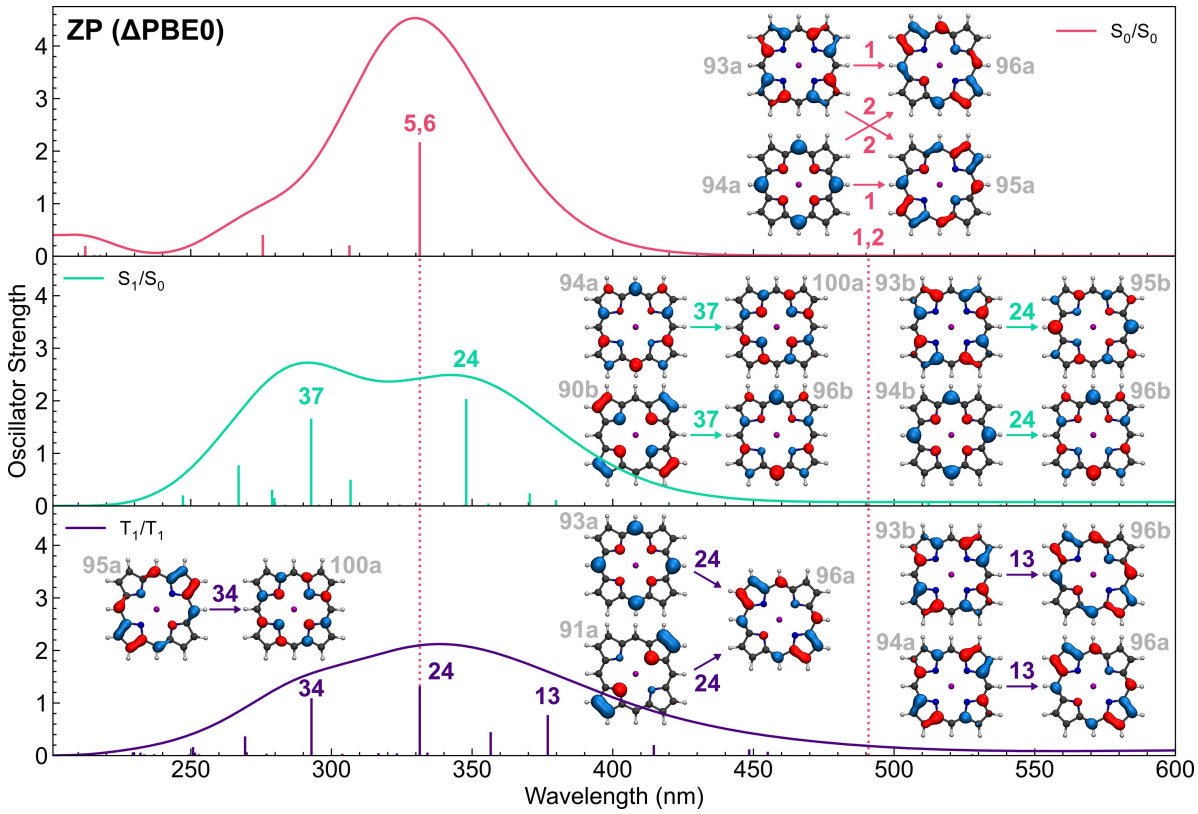

Figure 4.22: Molecular orbital transitions in the ground- and excited-state absorption spectra of **ZP**. X/Y indicates the X excited-state configuration at the Y geometry. The red dotted lines mark the ground-state q-bands and the Soret band. Select roots, *i.e.*, excited-state indices, are labeled above the transitions. HOMO = $94\alpha/\beta$ ($95\alpha/\beta$ for T_1) and LUMO = $95\alpha/\beta$ ($96\alpha/\beta$ for T_1).

be understood by examining the excited-state absorption spectra in more detail (Figure 4.22). Given the known multiconfigurational character of **ZP**, it is not surprising that the molecular orbital transitions (Figure 4.22) involve multiple hole-electron pairs, though they can be generally summarized as $\pi \rightarrow \pi^*$.

Focusing on the 24^{th} root, which corresponds to the approximate λ_{max}, from both the S_1 and T_1 excited-state references, it is observed that the T_1 feature is blue-shifted relative to the S_1 feature. Additionally, the 24^{th} root of the T_1 state aligns closely with the 5^{th} and 6^{th} roots from the S_0 reference, which effectively cancel each other out in the theoretical difference spectra, making this shift impossible to see.

Around 350 nm, TAS reveals an excited-state absorption feature that decays over time (Figure 4.21). This feature persists throughout the 5.5 ns time window, gradually diminishing in intensity,

and is attributed to the decay of the 37^{th} root from the S_1 reference to the lower-intensity 34^{th} root from the T_1 reference.

Surprisingly, LR-TDA/ΔSCF accurately captures the main excited-state absorption features revealed by TAS using a single reference. In fact, ground- and excited-state spectral features can be mapped to molecular orbital transitions (Figure 4.22), providing a basis for evaluating how substitutions and synthetic modifications influence the spectra. If similar accuracy is observed for other transition metal complexes, LR-TDA/ΔSCF would be a powerful approach for investigating the photophysics of new systems lacking extensive TAS data.

4.4 Conclusions

LR-TDA/ΔSCF offers an accurate and efficient approach for predicting excited-state absorption spectra across a wide range of chromophores. Benchmarking against experimental TAS data for **AB**, **BD**, and **ZP** demonstrates its effectiveness in assigning transient spectral features and elucidating excited-state relaxation mechanisms. ΔSCF optimizes excited-state single-reference wavefunctions and geometries, while LR-TDA applied to ΔSCF references reliably predicts excited-state absorption energies and oscillator strengths. Although the expectation value formalism with PBE0 results in significant red-shifting, using a long-range corrected hybrid like LC-PBE improves the agreement between calculated and experimental excitation energies for systems where non-Aufbau configurations are computationally expensive or difficult to converge. The complexity and diversity of the test systems demonstrate that LR-TDA/ΔSCF is a practical, efficient, and interpretable method for analyzing TAS spectral features. The molecular orbital-level understanding of excited-state transitions provided by LR-TDA/ΔSCF offers valuable chemical insights, making it an effective tool for exploring photophysical and photochemical mechanisms, and for guiding the design of chromophores.

Part III

Modeling Charge Transport in Organic Semiconductors

Chapter 5

Real Temperature Model of Dynamic Disorder[†,‡]

5.1 Introduction

Organic semiconductors (OSC) represent a class of modular solid state materials with numerous applications in electronic devices including organic field effect transistors (OFET), organic light emitting diodes (OLED), organic solar cells, chemical sensors, spintronic devices, *etc.*[323–328] In the majority of organic solids, individual molecules are bound via soft van der Waals interactions. These rather weak forces allow the molecules to arrange in a number of nearly energetically equivalent, but electronically different crystalline polymorphs.[329–331] Organic materials can be prepared as single crystals, deposited as thin-films, or even mixed as blends of donor/acceptor molecules for photovoltaic applications. With careful preparations, it is possible to grow crystals of single polymorphs;[332,333] however, most organic materials have defects or impurities that restrict perfect packing arrangements. Often various polymorphs cluster together creating local and large-scale crystalline irregularities. This sort of static disorder is believed to be a primary source of device performance limitations in organic electronic materials.[334] In particular, at the boundaries between the crystallites, charge transport becomes energetically unfavorable because of mismatched orbital overlap between nearest neighbor molecular substituents.[335,336]

[†]Reprinted with permission from Knepp, Z. J.; Fredin, L. A. *J. Phys. Chem. A* **2022**, 126, 3265–3272. Copyright 2022 American Chemical Society.

[‡]Electronic supplementary information is available at https://doi.org/10.1021/acs.jpca.2c02120.

Conduction in organic materials is often seen as either delocalized, band-like transport, or as localized, Marcus hopping transport.[337–340] Both of these regimes rely on good valence orbital overlap between nearest neighbor molecules. In highly ordered materials, intermolecular orbital interactions are maximized allowing carriers to delocalize and drift through the material with minimal resistance, resulting in a band-like transport mechanism. Interestingly, depending on the direction that one measures carrier mobilities, it is likely that a pure organic single crystal will express anisotropic mobilities because of the differences in molecular overlap (and electronic couplings) based on crystalline symmetry[332] and phasing. In low carrier mobility regimes ($\leq 1\ cm^2/Vs$), where the majority of organic semiconductor materials reside, the Marcus hopping model coupled with molecular dynamics or kinetic Monte Carlo can accurately predict intermolecular charge transfer rates.[341,342] Marcus theory assumes a localized charge transport mechanism, where charge carriers probabilistically hop between the frontier orbitals among nearest neighbor molecules, through channels of minimal resistance. To achieve minimal resistance (*i.e.* high conductivity), nearest neighbor monomers must have excellent orbital overlap and large electronic couplings. Marcus theory quantifies the carrier hopping rate as being proportional to the square of the effective charge transfer integral (*i.e.* effective electronic coupling) between two neighboring molecules.

In single crystal organic semiconductors whose mobilities decrease with temperature (e.g., rubrene, pentacene, tetracene, etc.), it has been proposed that conduction may occur via some hybrid form of charge transport that combines hopping and band transport.[337–339,343,344] In particular, these materials display a negative temperature dependence indicative of band-like transport, but the reported experimental mobilities for these crystals are far too small to be entirely band-like.[332] One way to describe materials that shift between delocalized band and localized hopping transport is via transient localization theory (TLT).[343,345–349] The theory suggests that intermolecular oscillations cause a temporary localization of the charge carrier wavefunction over some finite length and on timescales less than a typical molecular vibration. These charge carrier localization events can be understood as the direct consequence of temperature dependent lattice vibrations. Specifically, a perfectly ordered molecular crystal with no intermolecular vibrations would have charge carriers that delocalize across many molecules within the lattice.[339,350,351] However, in real organic materials, temperature induced lattice fluctuations or crystalline vibrations (*i.e.* phonons) disrupt this perfectly delocalized network. When following the path of a particular phonon, at

some finite displacement amplitude, on short timescales (*i.e.* << the length of a molecular vibration), the electrons rearrange into a configuration that minimizes the energy of the system for the new set of nuclear coordinates. Therefore, phonons may temporarily change (either increase or decrease) the electronic coupling between nearest neighbor molecules, inducing ultra-fast localization events. In the case of disrupting favorable coupling, it is not until the nuclei oscillate back (*i.e.* on timescales $1/\omega$), or return to their equilibrium positions, that the favorable electronic couplings are reestablished. Therefore, the diffusive nature of charge carriers could be heavily influenced by propagating phonons within a given molecular crystal, or any van der Waals solid.

Importantly, as temperature increases so do the amplitudes of the phonons, especially the intermolecular modes. Therefore, increasing the temperature is expected to induce more significant dynamic disorder that can further disrupt favorable electronic interactions leading to even smaller charge carrier mobilities. In particular, low energy phonons ($\leq kT$) are excited into higher energy vibrational quantum states at finite temperature. Thus low energy phonons oscillate with larger amplitudes than the higher energy phonons at the same thermal energy. Because of this, the lowest energy phonons are generally blamed for interrupting favorable packing arrangements, and in-turn, decreasing the effective electronic couplings between molecules in highly ordered organic materials.

In a recent study attempting to reveal which phonons lead to the largest mobility disruptions, a single phonon was termed the "killer-phonon" for several high mobility single crystal organic semiconductors.[352] The phonon identified is a sliding motion, where monomers with large effective electronic couplings slide past one another in a way that is electronically unfavorable. This motion was theoretically predicted to significantly reduce the effective electronic couplings between the monomers and is therefore expected to reduce the mobility through a transient localization process. Importantly, both the magnitude of the vibrational amplitudes and the effects of the vibration on the monomer overlap(s) are critical in quantifying the resulting decrease in carrier mobility. Thus in order to predict what normal modes disrupt (or enhance) conduction in an ordered organic materials, it is necessary to calculate experimentally relevant phonon amplitudes and test a wide range of thermally excitable phonons whose motions change the molecular overlap and electronic couplings the most.

In this study, low frequency phonons that cause considerable effective hole coupling fluctuations (HOMO-HOMO couplings) at room temperature (300 K) are quantified for a set of single

crystal organic semiconductors (Figure 5.1). Here, we do not assume that the off-diagonal (intermolecular) electron-phonon couplings scale with some linear coupling constant, but rather solve for the self-consistent electron configurations, at the predetermined semi-classical phonon extrema. We selected a few single crystal organic semiconductors, which are commonly referenced in the literature for their large charge carrier mobilities[353,354] and focus on their highest mobility conduction pathways. First, a model that predicts the expected amplitudes of oscillation at a finite temperature, given the quantum ground state amplitudes, is developed. With periodic DFT, the harmonic oscillations (*i.e.* displacement matrices) of the ground state normal modes are calculated. Then, the thermally expected displacements of each atom/molecule are calculated as a scalar multiple of the quantum ground state amplitudes according to their maximum classical displacements. The electronic couplings between monomers in the high mobility directions are then calculated directly in extracted dimers from expanded unit-cells at the equilibrium configurations, and at the temperature-depended maximum displacements for each of the phonons $\leq kT$ (Figure 5.1). The effect of these displacements on the transport are estimated as the effective electronic couplings (J_{eff}, eqn. 5.7), since this quantifies the orbital interaction energies, which are correlated to both band and hopping transport. Finally, we attempt to determine if particularly detrimental phonons (like the long-axis sliding "killer phonon") can be limited by bulky short-axis phenyl substituents (*i.e.*, rubrene; 9,10-diphenylanthracene; 2,6-diphenylanthracene).

5.2 Methods

At low temperatures, Boltzmann statistics predict that individual organic molecules primarily exist in the ground state (both electronic and vibrational). As temperature (or light) is introduced into the system, molecules can be excited into higher energy quantum vibrational states, with some finite probability. The energy levels (E_n) of a vibrational quantum harmonic oscillator (QHO) are quantized solutions to the time-independent Schrodinger equation that linearly depend on the frequency of the vibration (eqn. 5.1).

$$E_n = h\nu(n + \frac{1}{2}) \tag{5.1}$$

In small molecule organic crystals, low energy intermolecular vibrations can be excited into higher energy quantum states, even at low temperatures. Thus, it is necessary to correlate both temperature and frequency to predict experimentally representative amplitudes of oscillation in molecular crystals. The canonical partition function for a quantum harmonic oscillator (Z_i, eqn. 5.2), where $\theta_i \equiv \frac{h\nu_i}{k_B}$, provides said coupling of temperature (T) and frequency ν). Here, k_B represents the Boltzmann constant and θ_i the i^{th} vibrational temperature in Kelvin.

$$Z_i = \sum_{n=0}^{\infty} e^{\frac{-E_n}{k_B T}} = \sum_{n=0}^{\infty} e^{\frac{-\theta_i(n+\frac{1}{2})}{T}} = \frac{e^{-\theta_i/2T}}{1-e^{-\theta_i/T}} \tag{5.2}$$

Assuming that each vibrational mode in an organic crystal is an uncoupled, non-interacting, single harmonic oscillator allows us to form a probability distribution function (P_i, eqn. 5.3) of the quantized vibrational states of each oscillation.

$$P_i = \frac{e^{-\theta_i(n+\frac{1}{2})/T}}{Z_i} = (e^{-\theta_i/T})^n(1-e^{-\theta_i/T}) \tag{5.3}$$

These are unique distributions for each of the computed normal modes from the complete set of normal modes $\{\theta\} \equiv \sum_{i=1}^{3N} \theta_i$, where N is the number of atoms in the unit cell. Uncoupled oscillators are a fine assumption here, since it is possible to represent any type of molecular or crystalline vibration through weighted linear combinations of individual normal modes. From the probability distribution (eqn. 5.3), the expected excited state quantum number (*i.e.* the Bose occupation number, $\langle n \rangle$) can be determined (eqn. 5.4) for each crystalline vibrational mode given a finite temperature (T) and vibrational temperature (θ_i).

$$\langle n(\theta_i, T) \rangle = \sum_{n=0}^{\infty} nP_i = \frac{1}{e^{\theta_i/T}-1} \tag{5.4}$$

Since harmonic amplitudes of oscillation are correlated to the populated excited state (eqn. 5.5), the expected amplitude of each oscillation can be predicted as a function of the expected vibrational excited state at some finite temperature (eqn. E.1). A_n is the amplitude of i^{th} vibration in the n^{th} quantum state, where A_0 is the maximal classical displacement of the ground state of each mode.

$$A_n = A_0\sqrt{(2n+1)} \tag{5.5}$$

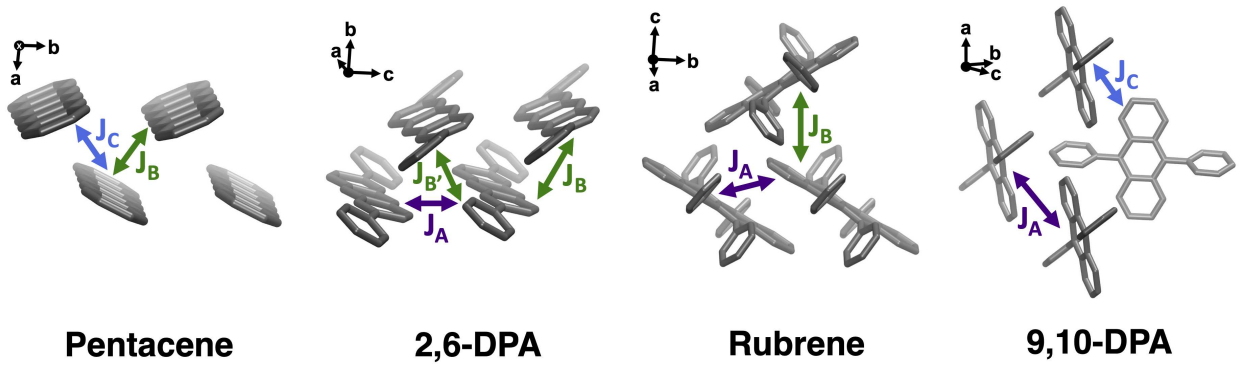

Figure 5.1: High mobility, non-equivalent dimers within the equilibrium crystalline structures

$$\langle A_n \rangle = A_0 \sqrt{(2\langle n(\theta_i, T)\rangle + 1)} = A_0 \sqrt{(\frac{2}{e^{\theta_i/T} - 1} + 1)} \tag{5.6}$$

Here we use periodic density functional theory (DFT), to determine the Γ-point vibrational frequencies (eigenvalues) and normal modes (eigenvectors) through diagonalizing the mass-weighted dynamical matrix at equilibrium crystalline geometries.[355–358] We derive the temperature dependent expected amplitudes (*i.e.* expected atomic displacements, eqn. E.1) for the complete set of normal modes calculated with CRYSTAL17 at the B3LYP/pob-TZVP-rev2 level of theory.[359–363] In this study, rounded values of expected excitation numbers were used to retain harmonic oscillator quantization. Because of the harmonic assumption, normal modes are defined to be symmetric in either displacement direction. Crucially though, this mode-induced symmetric oscillation is not linearly correlated with electron rearrangements, making it critical to study the effect of both the positive and negative displacements on the molecular orbital overlap to be able to assign each phonon as being helpful or harmful. Choosing room-temperature for this study, as a test case, we attempt to reveal which modes fluctuate the effective electronic couplings the most, on average.

5.3 Results and Discussion

First, the model was tested for its predictive capabilities with respect to experimentally representative, temperature dependent atomic displacements. We choose a set of well-studied experimental crystals that differ by length and axial substitutions (Figure 5.1). The model predicted long-axis sliding motions whose amplitudes were generally consistent with some of the previously reported x-ray diffraction studies (Table 5.1).[364] For example, we determined an expected long-axis displace-

Table 5.1: The predicted sliding motion magnitudes via eqn. E.1

Molecule	Δd(Å)[+ or –]
Pentacene	0.18
Rubrene	0.10
9,10-DPA	0.14
2,6-DPA	0.12

ment amplitude of 0.10 Å for rubrene. In a room temperature diffraction experiment, a standard deviation of 0.08 Å was measured. In addition, the model predicted amplitudes of 0.09 – 0.15 Å that are on par with many common organic single crystals,[364,365] confirming the applicability of the model for room temperature electron-phonon coupling analyses.

With the well established DIPRO (dimer projection) method, fluctuations in effective transfer integrals (J_{eff}) were quantified as a function of the expected oscillator amplitudes.[341,366,367] The effective charge transfer integral (eqn. 5.7) includes the effects of site energy fluctuations (eqns. A.5 & A.6), electronic coupling between monomers (eqn. A.3), and the overlap of between the carrier orbitals (HOMOs or LUMOs) (eqn. A.4). Here, the Hamiltonian (H) is used to compute the couplings between two discrete monomers ϕ_1 and ϕ_2. Each phonon induces electronic rearrangements that produce, potentially, in-equivalent site energies among the monomers of the lattice, so we quantify the effect of each mode on the effective transfer integrals between the largest equilibrium J_{eff} dimers (shown in Figure 5.1). The integrals were calculated with the CATNIP code,[368] for monomers and dimers extracted from periodically optimized (and normal mode perturbed) expanded unit cell lattices. The single point energy calculations (B3LYP/def2-TZVP)[359–362,369,370] were performed in Gaussian 16.[371]

$$J_{eff} = \frac{J - S(\epsilon_1 + \epsilon_2)/2}{1 - S^2} \tag{5.7}$$

$$\epsilon_1 = \langle \phi_1 | H | \phi_1 \rangle \tag{5.8}$$

$$\epsilon_2 = \langle \phi_2 | H | \phi_2 \rangle \tag{5.9}$$

$$J = \langle \phi_1 | H | \phi_2 \rangle \tag{5.10}$$

$$S = \langle \phi_1 | \phi_2 \rangle \tag{5.11}$$

Hole J_{eff} fluctuations were evaluated for the modes whose frequencies were below k_BT to save on computational cost, since this method requires $[2*(modes)*(unique\ dimers+unique\ monomers)]$ number of calculations and because high frequency vibrations are generally statistically restricted to their zero-point vibrational level (eqn. 5.4).

For all of the organic crystals (with the exception of 9,10-DPA), several modes were predicted to induce large J_{eff} fluctuations (deviations from the vertical line in Figure 5.2). While each crystal was predicted to have a long-axis sliding phonon (*"killer phonon"*), large J_{eff} fluctuations were only realized in pentacene and the long-axis phenyl substituted 2,6-DPA (Figure 5.3). This result was initially surprising, since sliding motions tend to be the lowest (or second lowest) energy phonon in many single crystal organic semiconductors.[352] Therefore, these oscillations should persist with significantly large amplitudes at room temperature (eqn. E.1). While this is true for the approximate displacement distances, it is important to consider how the unique dimers (*e.g.* J_b dimer of pentacene) move as a function of the mode itself. Since the monomers in the high-mobility dimers of pentacene and 2,6-DPA slide past one another (asymmetrically), this causes a significant change in J_{eff} in both directions of the oscillation. For rubrene and 9,10-DPA, the high mobility dimer instead moves together symmetrically (Figure 5.3) and thus the sliding motion does not significantly change the effective charge transfer integral. Therefore, if monomer pairs in the high mobility direction(s) can be symmetrically restricted to oscillate in the same direction, the detrimental effect of these low energy phonons will be reduced. Additionally, rubrene has been predicted to have not one, but two low energy sliding motions (modes 4 and 5, Figure 5.4). In both of these phonons, the high mobility dimer moves symmetrically - as a pair. It is, in fact, the low mobility (small J_{eff}) dimer whose monomers slide asymmetrically. Because of this, the favorable $\pi-\pi$ interactions in the high mobility dimer pathway are only marginally perturbed, leaving large effective electronic couplings.

Accurately mapping electron-phonon couplings is critical for ensuring realistic physical interpretations of transport in these complex materials. Of the asymmetric motions that cause significant J_{eff} fluctuations, the two directions of the harmonic motion (denoted as $+/-$ displacements) need not be electronically equivalent. For instance, temperature dependent displacements of the asymmetric sliding motion in pentacene (Figure 5.5) over a temperature range from 100 K to 900 K clearly show that the overlap (S_{ab}) between the HOMOs of the monomers become misaligned to

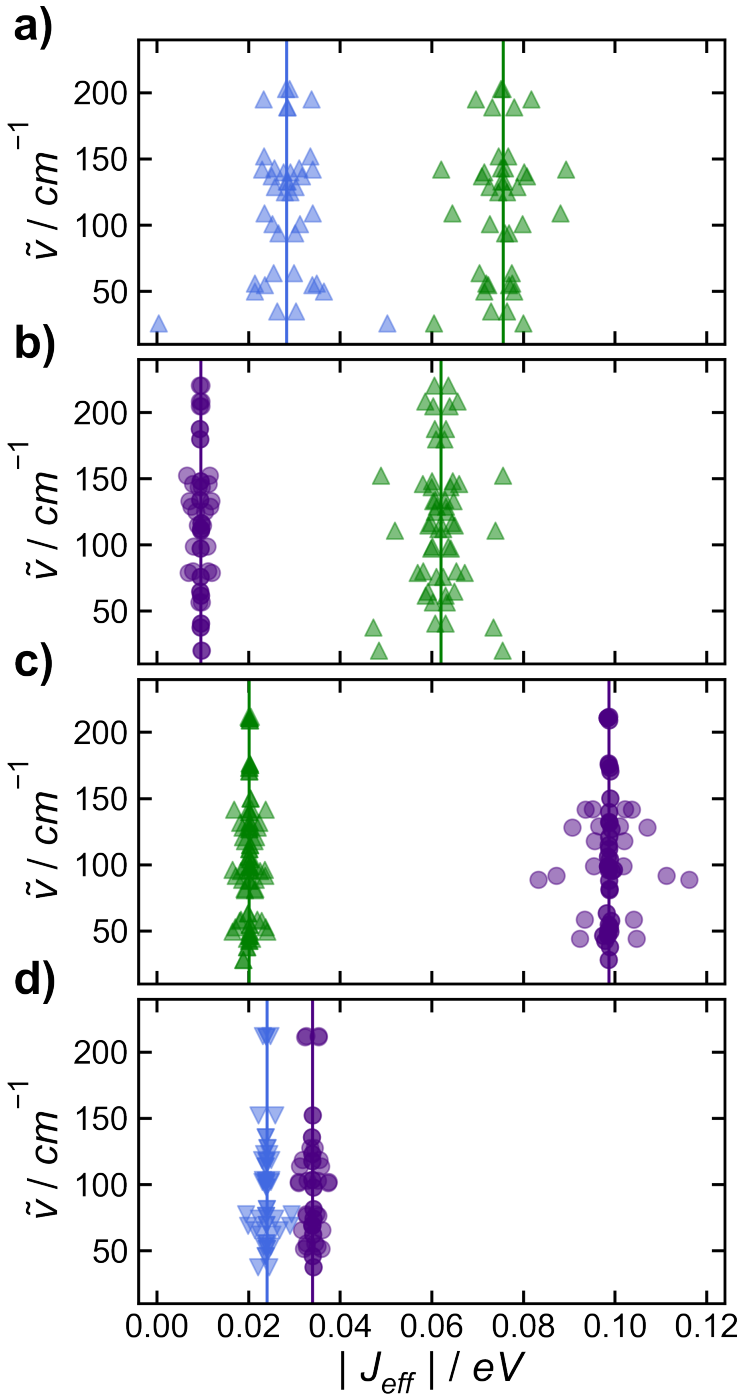

Figure 5.2: Normal mode induced J_{eff} fluctuations of (a) pentacene, (b) 2,6-DPA, (c) rubrene, and (d) 9,10-DPA. Symmetric motion about the normal mode (*i.e.* positive and negative displacements) are plotted on the same axis. Indigo ($\circ$) represents the J_A direction. Green (Δ) represents the J_B direction. Blue (∇) represents the J_C direction.

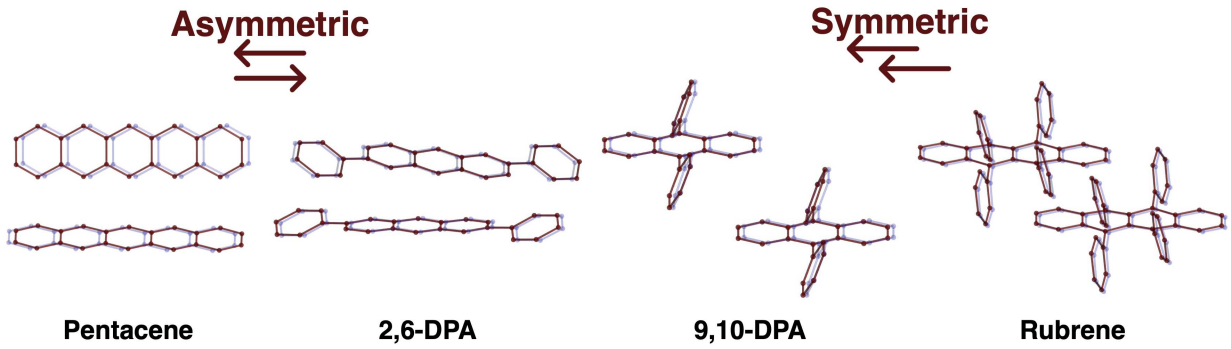

Figure 5.3: Sliding motion effect on dimers in the high mobility direction for each single crystal. Red atoms are positive displacements and blue are the negative. All displacements are scaled using eqn. E.1

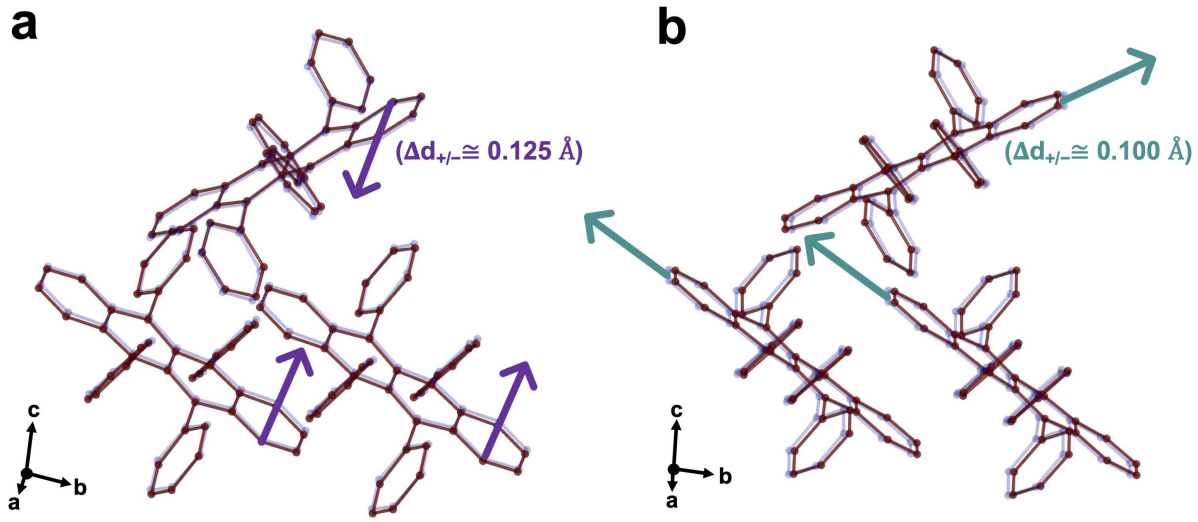

Figure 5.4: Displacements for the two lowest frequency (non-translational) phonons in rubrene. a) Short axis slide: The high mobility dimer move as a pair. b) Long axis slide: High mobility dimer move as a pair. The amplitudes represent displacements from the equilibrium structure, not the distance between the negative and positive coordinates.

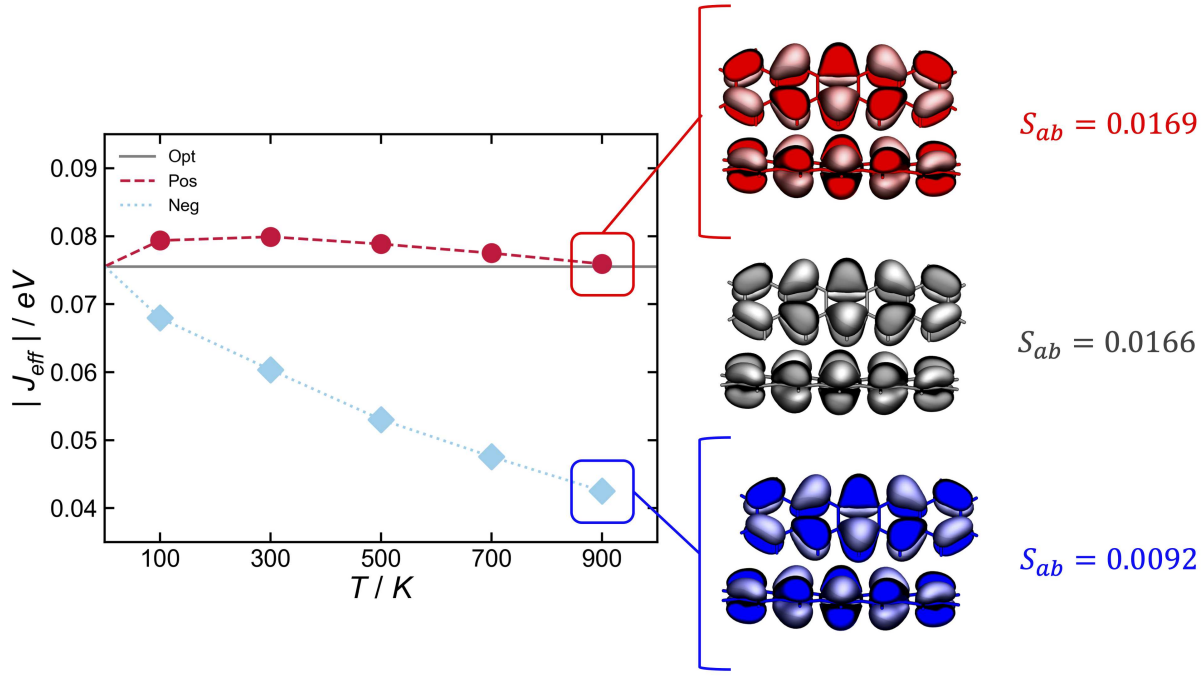

Figure 5.5: The effective charge transfer integral of the asymmetric sliding motion in pentacene as a function of temperature (or displacement distance). The red-circles(blue-diamonds) are displacements in the positive(negative) direction.

a greater extent in the negative (blue) direction than the positive (red) direction. This leads to changes in the electronic couplings that are both non-linear and non-symmetric. Thus the model presented here, provides significant improvement in predicting electron-phonon couplings over the commonly used linear Peierls type coupling constant approximation.

In addition, the detrimental (− displacement) electronic effect of the long axis asymmetric slide in pentacene is not linearly dependent on the magnitude of the vibration in this direction. Specifically, the phonon displacement in each direction is 77 % higher at 900 K than 300 K but the J_{eff} is only 33 % lower in the negative direction. Interestingly, while the phonons explored here are detrimental for conduction at higher temperatures, it would be interesting to apply this method to find phonons where a change in temperature provides overall enhancement of the conduction in molecular crystals.

Within the short axis-substituted molecules (*i.e.* rubrene and 9,10-DPA), two types of phonons are predicted to dominate their dynamic disorder. See-saw like motion (Figure 5.6), phenyl rotations, or some combination of the two, cause the largest fluctuations in the effective charge transfer

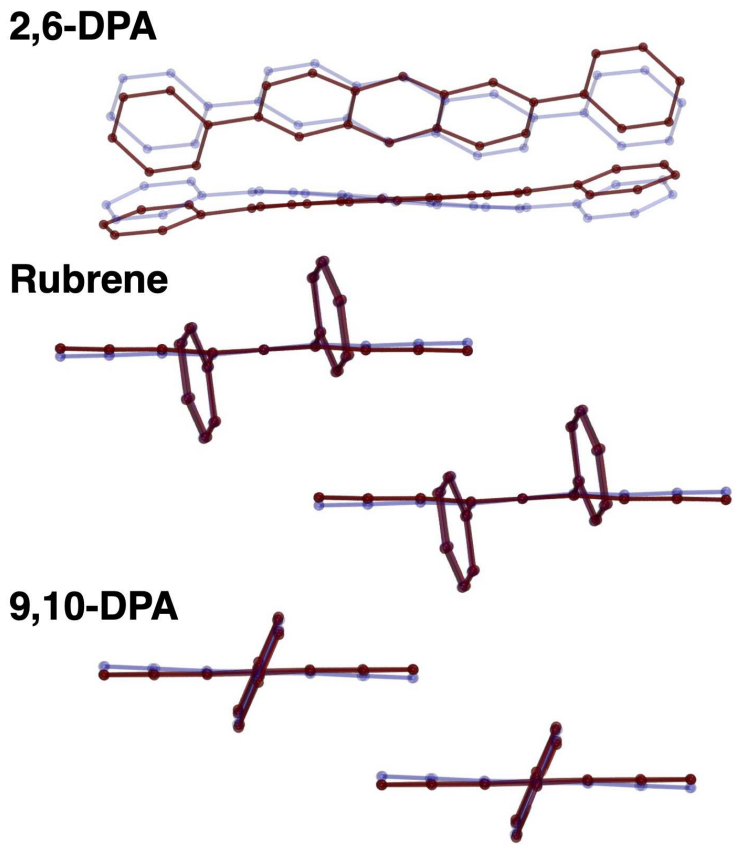

Figure 5.6: Lowest energy seesaw modes in the single crystals. Red atoms are negative displacements and shadowed blue are the positive. All displacements are scaled using eqn. E.1

integrals. Curiously, seesaw motions represent the three most disruptive phonons in 9,10-DPA, the top two in rubrene (where one is mixed with a phenyl rotation), and the second most disruptive in 2,6-DPA (Table 5.2). Therefore, modes of these symmetries may hinder device performance in materials of similar packing and molecular structures as those in this study. Unlike the long-axis slide, these types of phonons have been given little or no attention in the literature.

By normalizing phonon induced electronic couplings (ΔJ_{eff}) of each mode to the crystal, how much each phonon varies from the equilibrium structure can be quantified as a percent fluctuation. The $\Delta J_{eff}/J_{eff}^{gs}$ (Table 5.2) allows for direct comparison across a set of similar molecular crystals. Unsurprisingly, due to unideal packing for high mobility transport, small % fluctuations were predicted in 9,10-DPA. Because of the limited overlap between molecules, lower $\Delta J_{eff}/J_{eff}^{gs}$ values were predicted, since the integrals are strongly distance dependent. Interestingly, the tightly packed rubrene crystal displayed the second lowest percent fluctuations of the set. This can be attributed

Table 5.2: Summary of the vibrationally induced J_{eff} fluctuations in each single crystal. The most disruptive modes are ranked in order of reduction of J_{eff} in the highest mobility dimer.

Molecule	*Rank*	cm^{-1}	Motion	$\Delta J_{eff}^{min}(eV)$	$\Delta J_{eff}^{min}/J_{eff}^{gs}(\%)$
Pentacene	I	26	l-axis slide	-0.0152	-20.1
	II	142	libration	-0.0135	-17.9
	III	109	central-trans.	-0.0111	-14.7
Rubrene	I	89	see-saw	-0.0154	-15.6
	II	92	see-saw + phenyl rot.	-0.0115	-11.7
	III	128	phenyl rot.	-0.0080	-8.13
9,10-DPA	I	78	see-saw	-0.0030	-10.4
	II	66	see-saw + phenyl rot.	-0.0025	-8.7
	III	69	see-saw + phenyl rot.	-0.0021	-7.4
2,6-DPA	I	38	l-axis slide	-0.0149	-24.0
	II	20	see-saw	-0.0136	-21.9
	III	152	libration	-0.0132	-21.3

to the fact that the monomers in the high-mobility direction move symmetrically with one-another (Figure 5.3 and 5.4), so that large vibrational displacements lead to small ΔJ_{eff} *vide supra*.

If aligned with high mobility dimers the "killer phonon", an asymmetric slide, does cause the largest percent fluctuations in charge transfer integrals. However, short axis substitutions that result in good packing arrangements, like orthorhombic rubrene, seem to reduce the detrimental nature of this sliding phonon, by changing the orientation of the high mobility dimers with respect to the slide. Interestingly, long-axis substitutions, like those in 2,6-DPA, don't seem to provide the same benefit. In 2,6-DPA, the long-axis sliding mode shows the most significant J_{eff} fluctuations, followed by a see-saw motion, and a long-axis libration. Because this crystal displays similar detrimental modes to pentacene, and shares a similar packing arrangement, it seems that the long-axis phenyl substitutions on 2,6-DPA do not limit the detrimental effect of long-axis slide.

Surprisingly, short-axis phenyl rotations, which we initially hypothesized would cause only minor J_{eff} fluctuations, because of the HOMO localization on the acene-centers, produced the most disorder in both rubrene and 9,10-DPA. These types of modes induced J_{eff} fluctuations $\leq 11.7\%$, which is less than the asymmetric long axis slide J_{eff} fluctuations in pentacene (20.1%) and 2,6-DPA (24.0%). These results are consistent with the strongly coupled Peierls phonons previously identified by Girlando *et. at.* within a rubrene single crystal.[372] Interestingly, the effect of long axis phenyl rotations in 2,6-DPA were much less significant than short axis phenyl rotations. Indeed,

of the four phonons in 2,6-DPA that resemble phenyl rotations, the induced disorder was predicted to be between 1.7 and 4.7 %, not significantly contributing to the total dynamic disorder. Based on these results, the severity of J_{eff} fluctuations could be ranked with asymmetric sliding motions being the most detrimental, followed by see-saw and long-axis librations in a close tie for second, and short-axis phenyl rotations in third (at least for those materials with short axis phenyl substituents).

5.4 Conclusion

The temperature dependent model presented here coupled with the dimer projection method provides a powerful tool to study phonon induced dynamic disorder in crystalline organic semiconductor materials. Periodic frequency calculations predicted that the long-axis sliding phonon persist in all of the crystals studied here. Critically, large J_{eff} fluctuations induced by this mode were only realized in pentacene and the long-axis substituted 2,6-DPA, where the monomers of the high mobility dimer of these crystals move asymmetrically with respect to each-other. Thus, this motion interrupts favorable $\pi - \pi$ interactions and is predicted to decrease charge carrier mobilities according to Marcus or band transport theory. The high mobility dimer of the short axis substituted crystals (9,10-DPA and rubrene) moves as a single unit (*i.e.* the monomers move symmetrically) in the sliding phonon causing only minor deviations to the charge transfer integrals. This indicates that one could limit the detrimental effect of the "killer phonon" through short axis substitutions. A temperature dependent displacement study revealed the limitations of the constant non-local electron-phonon coupling approximation through unveiling an asymmetric and non-linear electronic coupling relationship.

This test set of molecules revealed other phonons that might contribute to the over-all dynamic disorder in these materials. In particular, a seesaw-like motion was revealed to induce large J_{eff} fluctuations in all of the phenyl substituted molecules. Additionally, phenyl rotations surprisingly contributed to some modest deviations in the overlap integrals of the short axis substituted molecules. Importantly, this model also makes it possible to reveal beneficial phonons that may increase charge carrier mobilities, especially in the Marcus hopping regime. These types of insights could enable improved device performances through molecular design or crystal engineering to limit detrimental and encourage beneficial phonons.

Chapter 6

Anisotropic Carrier Mobility with Boltzmann Transport Theory[†]

6.1 Introduction

Organic semiconductors (OSCs) are a promising class of materials for cutting edge electronic applications including light emitting diodes (OLED), field effect transistors (OFET), photovoltaics (OPV), and chemical sensors.[323–327] Their reasonable cost, processability, flexibility, and their synthetic and electronic tunability makes them an attractive alternative to traditional inorganic semiconductors. One drawback of organic semiconductors is that the molecules comprising the crystalline lattice are weakly bound to one another through soft van der Waals interactions.[337,351] These weak interactions lead to charge carrier anisotropy, packing defects or crystalline irregularities, and phonon induced transient charge carrier localization.[332,337,339,343,343–349,373,374] Combinations of these effects significantly limit the maximum charge carrier mobilities of OSCs to generally less than 10 $cm^2V^{-1}s^{-1}$.[354]

Because of the complicated interplay of electronic structure and crystalline symmetry, predicting anisotropic conductivities and charge carrier mobilities in crystalline organic semiconductors is rather difficult and computationally expensive.[338,339,346,375–377] It is common to assume that the charge carrier dynamics are dominated by a completely localized monomer-to-monomer hopping

[†]Reprinted with permission from Z. J. Knepp, G. B. Masso, L. A. Fredin, J. Chem. Phys. **158**, 064704 (2023). Copyright 2023, American Institute of Physics.

mechanism.[341,342,374] In the Marcus formalism of small polaron theory, charge carriers hop between the frontier orbitals (HOMO to HOMO for holes, LUMO to LUMO for electrons) of nearest neighbor monomers in a lattice. Hopping rates, W_i, are usually predicted with the Marcus-Hush equation (Eq. 6.1)

$$W_i = \frac{V_i^2}{\hbar}\left(\frac{\pi}{\lambda k_B T}\right)^{1/2} \exp(-\frac{\lambda}{4k_B T}) \tag{6.1}$$

where V_i is the effective electronic coupling between the nearest neighbor monomers of the bulk lattice, λ is the total reorganization energy, which is commonly approximated as the intramolecular portion only as the intermolecular reorganization energy is often assumed to be negligible, T is the temperature, and $\hbar$ is the reduced Planck's constant.[374] The expression assumes that the free energy difference (ΔG) to exchange a charge carrier between two nearest neighbor monomers is zero. Additional details regarding how the parameters V_i and λ are computed with density functional theory are presented in Appendix A.

In assuming that charge carriers probabilistically hop through various channels in materials with some directional preference, mobility anisotropy (Eq. 6.2) can be described by a Marcus hopping rate by assuming Einstein carrier diffusion.[374]

$$\mu(\theta) = \frac{e}{k_B T} D(\theta) \approx \frac{e}{k_B T}\frac{1}{2n}\sum_i r_i^2 W_i P_i F_i(\theta) \tag{6.2}$$

Here, e is the fundamental charge of the carrier, n is the number of spacial dimensions, r_i is the hopping distance between the mass-weighted centers of two monomers that make up the i^{th} dimer, P_i is the probability ($P_i \equiv W_i / \sum_i W_i$) to hop in the i^{th} direction, and $F_i(\theta)$ is an approximate decay function (usually cos^2) away from the mass centered vectors between two monomers.

Critically, this model assumes that isolated monomers and their corresponding dimer couplings correctly capture the behavior of the crystalline bulk. These assumptions are problematic for highly ordered organic crystals such as pentacene and rubrene whose charge carriers dynamically delocalize across many molecules of the lattice (∼17 in pentacene and ∼14 in rubrene).[378,379] In such materials, the Marcus hopping assumption underestimates charge carrier mobilities by enforcing maximal localization. Additionally, hopping models become invalid when the electronic couplings are greater than half of the reorganization energy ($V_i > \lambda/2$).[380] In this limit, the hopping

activation energy approaches zero and therefore the small polaron does not exist. Thus, individual monomer localized states are a bad representation of the carrier in high mobility materials, making the Marcus hopping mobilities strictly undefined. This would be the case for organic crystals that are conductive enough to be relevant for semiconductor applications, in fact tetracene, pentacene, hexacene, and rubrene already surpass this limit.

In an attempt to approximate the charge transport dynamics of more delocalized materials, affordable computational models beyond the Marcus hopping approximation are required. Band theory based models, like the constant relaxation time Boltzmann Transport Equation (BTE), provide a completely delocalized carrier picture. BTE may better describe the carriers in high mobility organic crystals where carriers delocalize across multiple molecules. Band theory mobilities depend on the band velocity of a carrier until it is scattered. For organic crystals the mean free path of charge carriers is significantly smaller ($\sim$ 1.0 Å) than typical lattice vector magnitudes or the intermolecular distances, and thus the Mott-Ioffe-Regel (MIR) limit is violated.[380,381] At this limit, band theory breaks down and the predicted BTE conductivities are probably not representative of the true carrier dynamics.

In recent years, more robust and physically relevant models, such as the transient localization theory, have been developed to describe charge transport in high mobility organic semiconductor materials that are between the limits of $V_i > \lambda/2$ and MIR.[343,377–379] These models predict mobilities that agree exceptionally well with what is observed experimentally. For screening purposes, though, these models are rather computationally demanding and are probably less practical because of this. As an alternative to Marcus hopping mobilities for screening organic semiconductors, this contribution benchmarks BTE as an initial screening tool for predicting the mobility trends of new organic semiconductor materials. Even though the MIR limit is surpassed in these materials, we show that BTE ($\tau = 10\ fs$) predicts the mobilities of a set of unsubstituted and substituted oligoacene single crystals (Figure 6.1) in agreement with experiment and to those predicted by some higher level methods providing an efficient way to benchmark new transport theories.

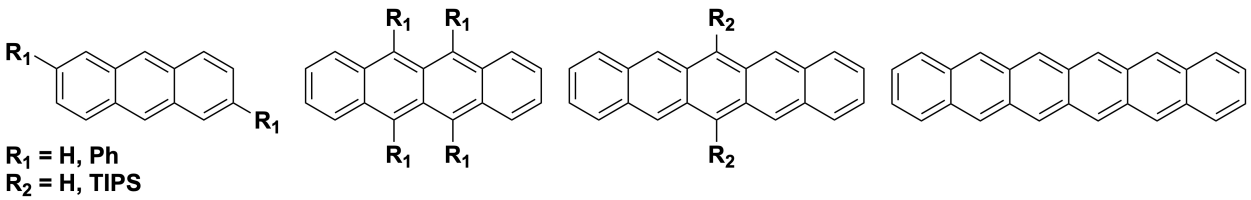

Figure 6.1: Monomers of the test set of high mobility single crystals. From left to right these include: (**left**) anthracene (ANT, R_1 = H) and 2,6-diphenylanthracene(DPA, R_1 = Ph), (**left-center**) tetracene (TET, R_1 = H) and rubrene (RUB, R_1 = Ph), (**right-center**) pentacene (PEN, R_2 = H) and TIPS-pentacene (TIPS, R_2 = TIPS), (**right**) hexacene (HEX).

6.2 Theoretical Methodology

Since the mobility of charge carriers in conductive or semiconductive materials is approximately proportional to the electrical conductivity divided by the charge carrier concentration, it is possible to predict mobilities from the semiclassical BTE conductivity.[382–384] The BTE predicts the electrical conductivity (σ) through various paths of a lattice from a periodic density functional theory (DFT) band structure (Eq. C.2)

$$\sigma_\alpha(\mathcal{F},T) = e^2 \int dE(-\frac{\partial f(E,\mathcal{F},T)}{\partial E})\Xi_\alpha(E) \tag{6.3}$$

where Ξ is the k-point ($\mathbf{K}$) dependent transport distribution function describing the α direction through the crystal. f is the Fermi-Dirac distribution which depends on the energy (E), the Fermi-level ($\mathcal{F}$) or chemical potential, and the temperature (T). Here, the transport distribution function (Ξ, Eq. C.5)

$$\Xi_\alpha(E) = \tau \sum_{\boldsymbol{K}} \frac{1}{N_{\boldsymbol{K}}} \sum_{i,j} v_{i,\alpha}(\boldsymbol{K}) v_{j,\alpha}(\boldsymbol{K}). \tag{6.4}$$

is defined in terms of the mean charge carrier scattering time (τ) and the band velocities ($v_{i,\alpha}$), which are the band energy derivatives along reciprocal space vectors that map to the Cartesian directions of a lattice (*i.e.* α = x, y, or z). Only calculating conductivities along Cartesian directions rather than any reciprocal space vector is a limitation of the current CRYSTAL17 implementation. Finally, the Fermi-level BTE conductivities (Eq. C.2) divided by carrier concentration (number of carriers ($N_{\mathcal{F},T}$ at the Fermi-level) per volume ($\mathbf{V}$)) provides a direct way to calculate the anisotropic

hole mobilities (Eq. 6.5) with periodic DFT.

$$\boldsymbol{\mu}_{\alpha}(E,\mathcal{F},T) = \frac{\sigma_{\alpha}(\mathcal{F},T)\mathbf{V}}{eN_{\mathcal{F},T}(E)}. \tag{6.5}$$

Within the CRYSTAL17 code the electrical conductivities are calculated with the constant relaxation time (τ) BTE.[357,358] This approximation assumes that charge carrier scattering events, which are expected to be induced predominantly by lattice phonons in softly bound organic crystals, can be represented by an averaged, directionally invariant, constant scattering time.[382] Directly computing approximate electron-phonon scattering rates ($1/\tau$) is significantly more computationally demanding.[383] To limit the computational cost of the present model, we further assume that charge carrier relaxation times are approximately equivalent among the selected set of crystals. One study approximated τ at 300 K to be $\sim 2\ fs$ in naphthalene.[381,385] It is common to affordably approximate τ with a deformation potential model.[386,387] This approximation includes the effects from acoustic phonon scattering but it ignores optical phonon effects. Using the deformation potential model at the B3LYP/6-311++G(d,p) level of theory,[387] Kobayashi *et .al.* predict τ to be 43 and 19 fs for pentacene and rubrene, respectively.[387] As a middle ground, we set τ to be 10 fs in all the crystals, allowing for easy scaling.

In this study, the BTE was used to predict directional mobilities in a set of high-mobility single crystals including four unsubstituted acenes (anthracene, tetracene, pentacene, and hexacene) and three substituted acenes with various axial substitutions (2,6-diphenylanthracene, rubene, and TIPS-pentacene) (Figure 6.1). First, the various crystal structures were independently optimized with several density functionals. The DFT optimized geometries are important since the electronic structure and the resulting transport properties are highly sensitive to the geometry of the system.[337,351,366,388] In particular, to reproduce or understand experimental anisotropic observations, it is crucial that the optimized structures be close to that of the experimental geometries, symmetries, and lattice parameters, so that the predicted electronic structure and charge transport properties are physically relevant. Here, atom only optimizations with B3LYP/pob-TZVP-rev2 and full (*i.e.,* atoms plus lattice vectors) geometry optimizations with B3LYP/pob-TZVP-rev2, PBE-D3/pob-TZVP-rev2, PBE0-D3/pob-TZVP-rev2, PBEsol0-3c/sol-def2-mSVP, and HSEsol-3c/sol-def2-mSVP were performed.[359–362,369,370,389–391] Grimme's D3 corrected density functionals were

included to correct for the weak but important intermolecular dispersion in all but the fully optimized B3LYP structures.[392] Additionally, solid-state composite functionals (3c) that combine small basis sets, geometrical counterpoise corrections, and dispersion corrections (two and three body dispersion) were tested because of their computational affordably and good solid-state electronic descriptions.[391,392] For all of the optimizations, the DIIS convergence accelerator was used. An anisotropic k-mesh was defined separately for each crystal such that each real space primitive lattice vector times its corresponding SHRINK factor was greater than 30 Å. The anisotropic k-mesh was quadrupled for all of the BTE computations to increase the accuracy of the electronic structure for the band velocities. The tolerance on change in total energy (TOLDEE) was set to 10^{-8} for all calculations. Truncation criteria for the bi-electronic integrals were set with the keyword TOLINTEG to 8 8 8 8 16. Periodic vibrational frequency calculations were conducted to assure that the optimized structures were true local minima. The BTE mobilities were then compared with Cartesian-axis projected Marcus-Hush-Goddard mobilities to reveal the similarities and differences between the models for each crystal by closely inspecting the mobilities and their trends.

6.3 Results

6.3.1 Relevant Geometric Structure

The mean absolute relative error (MARE, Eq. 6.6) in the primitive cell volume (V) shows how each crystalline optimization procedure compares with the experimental lattice volumes (Figure 6.2, Table 6.1). Mean relative errors (MREs) are included in Table 6.1 to portray the sign errors across the set. It is clear that the solid-state functionals (HSEsol and PBEsol0) deviate the least from the experimental lattice volumes, with MARE of 2.51 and 3.65%, respectively.

$$MARE = \frac{100\%}{n} \sum_{i=1}^{n} \frac{|\mathbf{V}_i^{DFT} - \mathbf{V}_i^{EXP}|}{\mathbf{V}_i^{EXP}} \tag{6.6}$$

B3LYP full optimizations (nuclear coordinates and crystalline lattice vectors) resulted in consistent volume expansions (MRE = +13.77), while the dispersion corrected (D3) PBE (MRE = −9.55)

Table 6.1: Density functional specific mean absolute and (relative) errors in the lattice volumes and band gaps for each computational method. MARE (Mean Absolute Relative Error), MRE (Mean Relative Error), and ME (Mean Error).

Method	Vol. (MARE(%))	Vol. (MRE(%))	Band gap (MAE(eV))	Band gap (ME(eV))
B3LYP (atom only)	—	—	0.30	–0.30
B3LYP	13.77	+13.77	0.18	–0.11
PBE-D3	9.55	–9.55	1.46	–1.46
PBE0-D3	10.91	–10.91	0.36	–0.36
PBEsol0-3c	3.65	+3.65	0.21	+0.003
HSEsol-3c	2.51	+2.38	0.61	–0.61

and PBE0 (MRE = −10.91) functionals resulted in geometries whose unit cells were consistently contracted. The B3LYP expansions were expected since functionals without dispersion corrections are known to underestimate the intermolecular London-dispersion attractive forces.[392] The opposite seems to be true when only dispersion corrections are applied there is an overestimation of intermolecular attractions, as in PBE and PBE0. Over contraction may be due to DFT neglecting temperature dependent lattice expansion effects.[393] These compacted unit-cells likely overestimate conductivity making them unsuitable for experimental comparison. HSEsol-3c (MRE = +2.38) and PBEsol0-3c (MRE = +3.65) only slightly overestimate the volumes. Thus overall, the solid-state composite functionals (3c) provide the most experimentally relevant optimized unit cells.

6.3.2 Capturing Experimental Electronic Structure

Since the transport properties are directly derived from the DFT band structure, a correct electronic structure is required. Predicted indirect optical band gaps provide a good assessment of the overall electronic structure for each computational method. Here, experimental solution phase optical band gaps of anthracene, tetracene, pentacene, rubrene, and TIPS-pentacene were used for comparison to avoid inconsistencies in reported solid-state band gaps due to variations in preparation.[394,395] Larger mean absolute errors (MAEs, Eq. 6.7) of the band gaps (BG) indicate that a method provides unrepresentative electronic structure.

$$MAE = \frac{1}{n}\sum |BG_i^{DFT} - BG_i^{EXP}| \tag{6.7}$$

Of all the functionals tested, the fully optimized B3LYP ($MAE = 0.18\ eV$) and PBEsol0-3c

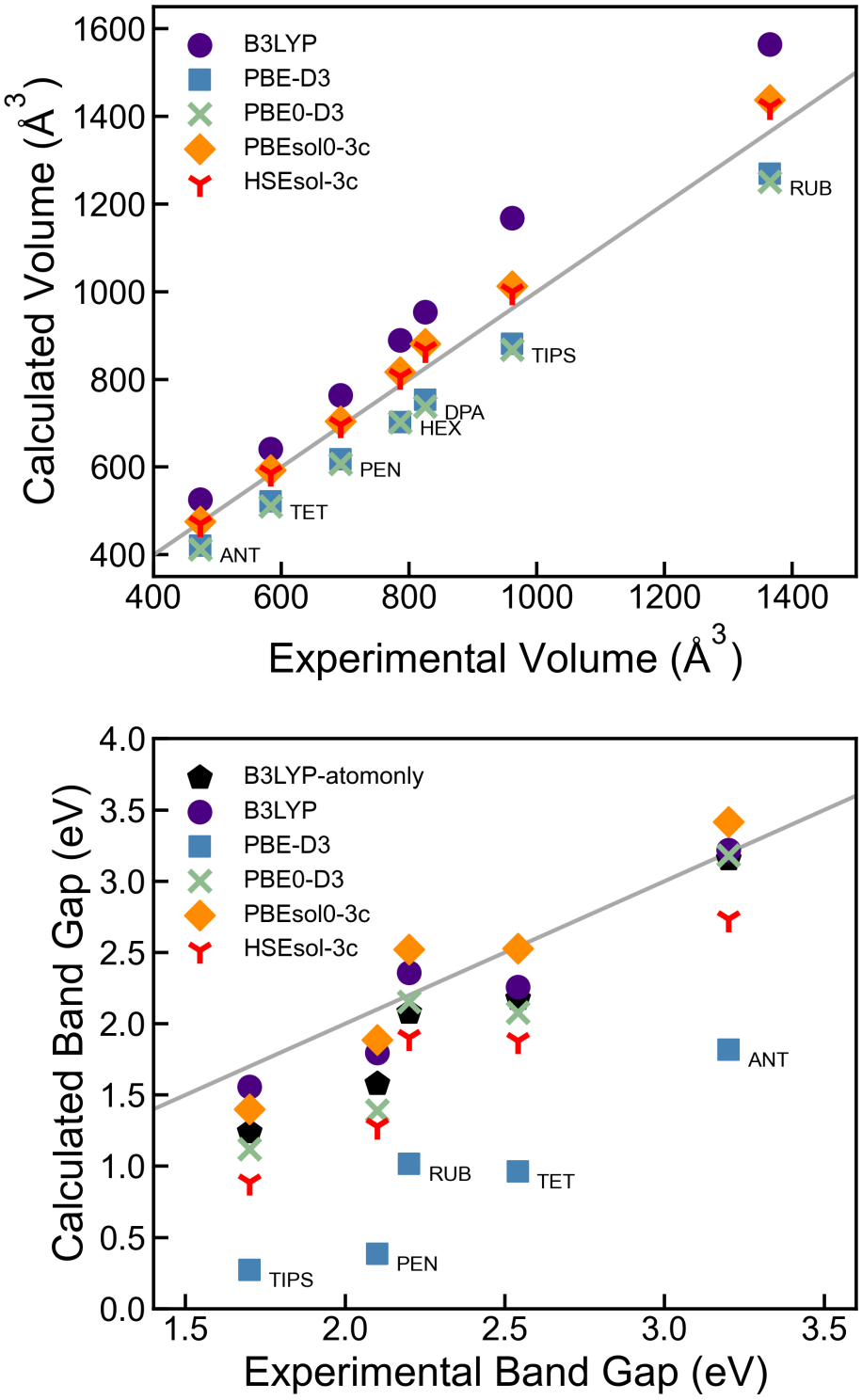

Figure 6.2: Calculated vs. experimental unit cell volumes and solution phase optical band gaps. The optical band gaps included were anthracene, tetracene, pentacene, rubrene, and TIPS-pentacene.

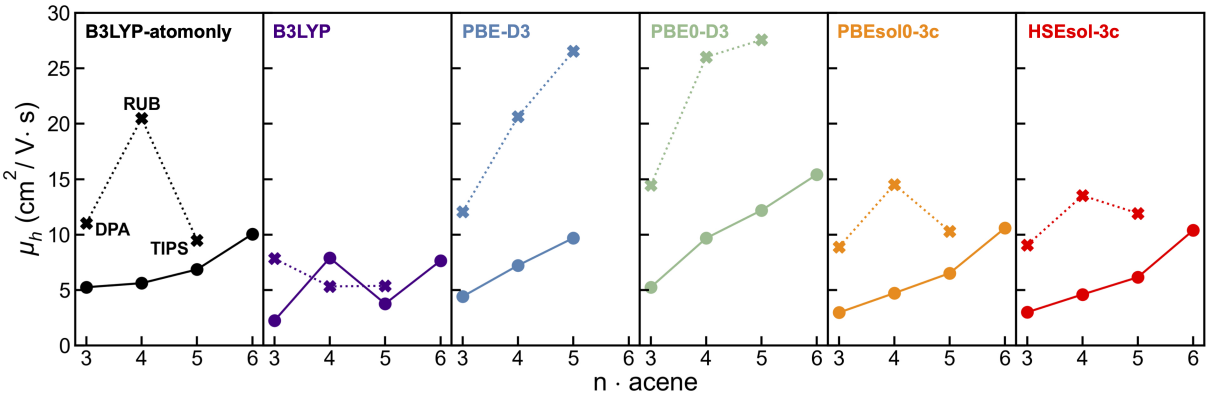

Figure 6.3: Largest Fermi-level hole mobilities of any Cartesian direction for the different methods. Solid circles and lines are unsubstituted acenes and bold x's with dotted lines are the substituted acenes.

($MAE = 0.21\ eV$) resulted in the smallest mean absolute errors in the band gap. The PBE-D3 ($MAE = 1.46\ eV$) and HSEsol0-3c ($MAE = 0.61\ eV$) functionals consistently underestimated the band gap for all of the crystals in the test set. While the fully optimized B3LYP has the smallest band gap MAE, its large geometric MARE makes it a poor method overall. Thus, fully optimized PBEsol0-3c provides the most experimentally relevant geometric and electronic structure of all the DFT methods tested.

6.3.3 Anisotropic Charge Carrier Mobility with BTE

Previously reported theoretical hole mobilities for the unsubstituted acene series suggest that the maximum charge carrier mobilities should increase as a function of acene backbone lengthening both for Marcus models[396] and fragment orbital-based surface hopping (FOB-SH).[378] After determining a computational method that provides both good geometric and electronic structure, the mobility-lengthening trend indicates a functional that provides representative BTE mobilities. The largest Fermi-level hole mobilities of any Cartesian direction (*i.e.,* of the diagonal matrix elements of the conductivity tensor) for each method mentioned above (Figure 6.3) compare reasonably well with those by Deng *et. al.*[396]

The B3LYP atom only, PBEsol0-3c, and HSEsol-3c functionals all predict rubrene to have the highest hole mobility followed by either hexacene, TIPS-pentacene, or DPA. All of the density functionals tested, except for the B3LYP full optimizations (purple), correctly describe the increasing

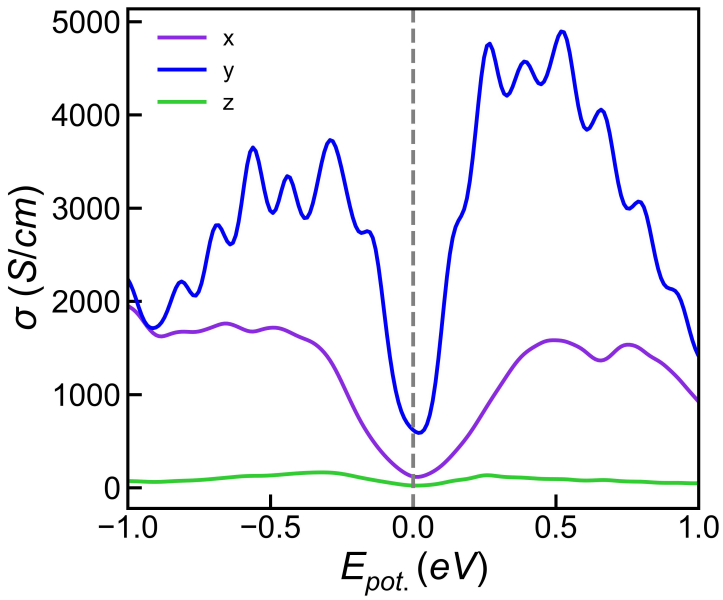

Figure 6.4: PBE-D3 BTE predicted hexacene anisotropic conductivity (x = purple, y = blue, z = green). The grey dotted line is the SCF Fermi-level.

mobility as a function of the lengthening of the unsubstituted acene backbone. Unsurprisingly, the expansion and contraction of unit cells are correlated with either the decrease or increase, respectively, in the magnitude of the calculated mobilities.

Unit cell contraction effects became particularly problematic and obvious for the non-hybrid PBE-D3, whose structural compaction suggested that hexacene would behave like a semi-metal, with non-zero conductivity through the band gap (Figure 6.4). This unphysical prediction suggests that non-hybrid density functionals should be avoided for small band gap materials. The fully optimized B3LYP unsubstituted acene BTE mobilities are the only method we tested that did not have the acene lengthening trend. However, the mobilities do match reported maximum hole mobilities from a deformation potential model at the LDA level of theory, which predicts mobilities of 42.2, 92.5, and 55.6 $cm^2V^{-1}s^{-1}$ for anthracene, tetracene, and pentacene, respectively.[386] Since neither LDA nor B3LYP include dispersion corrections to account for known intermolecular interactions, it is likely that this trend is unrepresentative.

The PBEsol0-3c largest Fermi-level hole mobilities of the three Cartesian directions for pentacene ($\mu_x = 6.525\ cm^2V^{-1}s^{-1}$) and rubrene ($\mu_y = 14.524\ cm^2V^{-1}s^{-1}$) compare reasonably well with those reported by Kobayashi et. al.[387] They report the largest unit cell vector mobilities

Table 6.2: Anisotropic Fermi-level hole mobilities computed at the PBEsol0-3c/sol-def2-mSVP level of theory in the Cartesian directions x, y, and z.

Crystal	$\mu_x^{BTE}(cm^2/Vs)$	$\mu_y^{BTE}(cm^2/Vs)$	$\mu_z^{BTE}(cm^2/Vs)$
anthracene	2.802	2.974	2.176
tetracene	4.728	2.430	0.669
pentacene	6.525	2.687	0.454
hexacene	3.508	10.602	0.867
2,6-diphenylanthracene	0.324	8.883	4.413
rubrene	0.354	14.524	5.161
TIPS-pentacene	10.306	4.872	0.004

to be 58 $cm^2V^{-1}s^{-1}$ and 51 $cm^2V^{-1}s^{-1}$ for pentacene and rubrene, respectively. If we scale our $\tau = 10\ fs$ to match their deformation potential model derived τ ($\tau_{PEN} = 43\ fs$, $\tau_{RUB} = 19\ fs$) then this implementation of BTE predicts mobilities that are on the same order of magnitude and ordering, 28.058 $cm^2V^{-1}s^{-1}$ and 27.596 $cm^2V^{-1}s^{-1}$, respectively. They are also consistent with maximum 2D hole mobilities along the herringbone plane predicted with FOB-SH by Giannini *et. al.*[378] The FOB-SH mobilities for naphthalene, anthracene, and pentacene (2.1, 3.5, and 9.6 $cm^2V^{-1}s^{-1}$, respectively)[378] are a similar magnitude to the PBEsol0-3c BTE mobilities (Table 6.2). Additionally, FOB-SH predicts rubrene to have a higher maximum 2D mobility than pentacene, in line with BTE.

Since the PBEsol0-3c functional resulted in the combination of small errors in the geometries and band gaps and the correct directional mobility trends of the unsubstituted acenes, we chose to study its optimized crystal structures more closely. The PBEsol0-3c Cartesian directional conductivities (Figure 6.5) show a range of variation across the test set. In particular, the y-direction in rubrene or anthracene and the x-direction in tetracene or pentacene are predicted to be significantly more conductive than the other directions in those crystals. The largest Fermi-level hole mobilities (grey-dashed line, computed with Eq. 6.5, Table 6.2) highlight the varying anisotropy among the crystals, even those who have similar herringbone structures.

The directionally dependent mobility ratios provide a quantitative metric of conduction/mobility anisotropy, where ratios close to one indicate isotropic carrier diffusion, and ratios much larger than one indicate anisotropic carrier diffusion. Of the group, anthracene ($\mu_y/\mu_x = 1.061$, $\mu_y/\mu_z = 1.367$) is predicted to be the most isotropic of the unsubstituted acenes, according to the Cartesian directions measured. Both tetracene ($\mu_x/\mu_y = 1.946$, $\mu_x/\mu_z = 7.067$) and pentacene ($\mu_x/\mu_y = 2.428$,

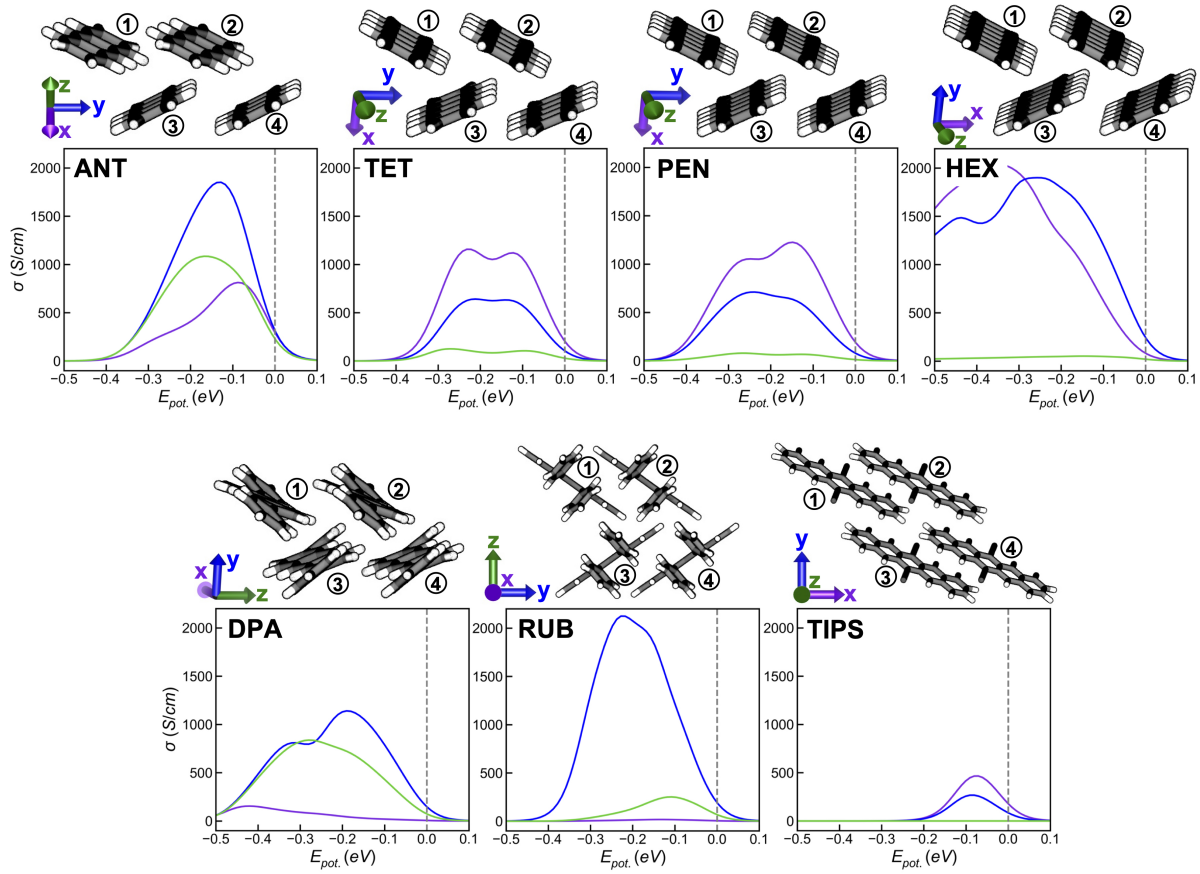

Figure 6.5: PBEsol0-3c/sol-def2-mSVP hole conductivity in the x (purple), y (blue), and z (green) directions of the crystal lattices, labeled with their standard crystal abbreviations. The grey dotted line marks the SCF Fermi-level and molecule numbers show the nearest neighbor dimers used for projections in Table 6.4.

$\mu_x/\mu_z = 14.37$) share similar preferential anisotropic transport in the x-direction of the lattice, while hexacene ($\mu_y/\mu_x = 3.022$, $\mu_y/\mu_z = 12.23$) prefers conducting in the y-direction. However, it is important to note that the y-direction of hexacene is symmetrically equivalent to the x-direction in tetracene and pentacene, making these results directly comparable. For the substituted acenes, 2,6-diphenylanthracene ($\mu_y/\mu_z = 2.013$, $\mu_y/\mu_x = 27.417$) and rubrene ($\mu_y/\mu_z = 2.814$, $\mu_y/\mu_x = 41.03$) prefer conducting in the y-direction, while TIPS-pentacene prefers conducting in the x-direction ($\mu_x/\mu_y = 2.115$, $\mu_x/\mu_z = 2576.5$). Of the set of crystals, TIPS-pentacene and rubrene show the most anisotropic charge transport.

6.3.4 Comparison of BTE and Marcus-Hush-Goddard Mobilities

The BTE band derivatives can be interpreted as an average velocity of a charge carrier (*i.e.* hole) in some i^{th} band (*i.e.* highest valence band) along a direction (α) in the absence of any external forces. In any materials at finite temperature, phonons are expected to disrupt (or scatter) charge carriers and therefore govern their average lifetime(s) (which BTE defines as constant τ). In contrast, Marcus theory predicts hopping rates that depend on treating each carrier hop as a separate event with some finite probability of occurring. The Marcus-Hush-Goddard mobility then comes from a random walk of uncorrelated hopping events between neighboring molecules in a material, or diffusion of the carrier.

Conceptually BTE assumes complete delocalization, while Marcus hopping assumes complete localization of the carrier. Both theories calculate a maximum carrier mobility that is reduced through scattering or geometric reorganization, respectively. One might expect that as charge carrier lifetimes decrease (*i.e.* the constant scattering limit) or as the hopping rates increase (*i.e.* at a constant measurable velocity) the mobilities predicted by the two models would converge. However, because both models breakdown at their respective limits ($V_i > \lambda/2$ and MIR, *vide supra*), the error in the predicted mobilities may be very large. As the mobility trends of the selected materials have been well described by Marcus rates previously, we use these mobilities to compare our BTE mobilities against. We keep the geometry consistent in both models to make the comparison as appropriate as possible.

First, the hopping rates for each unique dimer pair of a crystal are calculated according to the effective electronic couplings (Table 6.4, computed via Gaussian16 and CATNIP) and the isolated

Table 6.3: Effective electronic couplings (V) of projected dimer (numbered in Figure 6.5) at the PBE0-D3/def2-TZVP level of theory.

Crystal	$\|V_{12}\|(eV)$	$\|V_{13}\|(eV)$	$\|V_{23}\|(eV)$	$\|V_{34}\|(eV)$	$\|V_{15}\|(eV)$	$\|V_{26}\|(eV)$	$\|V_{37}\|(eV)$	$\|V_{48}\|(eV)$
anthracene	0.0389	0.0286	0.0286	0.0389	0.0004	0.0004	0.0004	0.0004
tetracene	0.0074	0.0119	0.0702	0.0119	0.0015	0.0015	0.0005	0.0005
pentacene	0.0148	0.0288	0.0725	0.0017	0.0011	0.0011	0.0005	0.0005
hexacene	0.0493	0.0755	0.1001	0.0482	0.0005	0.0005	0.0005	0.0005
2,6-DPA[1]	0.0082	0.0562	0.0562	0.0082	0.0061	0.0061	0.0061	0.0061
rubrene	0.0699	0.0170	0.0170	0.0699	0.0025	0.0025	0.0025	0.0025
TIPS-pentacene	0.0169	0.0137	$\|V_{14}\| = 0.0007$	0.0169	0.0001	0.0001	0.0001	0.0001

Table 6.4: Unique directional nearest neighbor hopping rates at the PBE0-D3/def2-TZVP level of theory.

Crystal	$W_{avg(12,34)}(THz)$	$W_{13}(THz)$	$W_{23}(THz)$	$W_{ortho}(THz)$
anthracene	15.350	8.342	8.342	0.002
tetracene	1.685	2.033	71.004	0.031
pentacene	4.035	15.419	97.988	0.019
hexacene	54.852	131.577	231.610	0.006
2,6-diphenylanthracene	0.510	23.726	23.726	0.280
rubrene	44.255	2.625	2.624	0.054
TIPS-pentacene	3.054	2.071	$W_{14} = 0.005$	0.000

monomer reorganization energy (Appendix A).[368,371]

Within the Goddard extension of the Marcus-Hush transport model, mobilities are predicted along particular conduction channels via weighted sums of dimer couplings.[374] The unique dimer hopping rates, W_i, decay according to a cos^2 function away from the vector between the centers of mass of each monomer, *i.e.,* the dimer-center-of-mass (d-COM) vector. Because the d-COM directions are defined by the original dimer orientations, the unique d-COM vectors are normalized and projected along the Cartesian directions (details in Appendix B). Importantly, the Cartesian projected mobilities, are normalized so that only unique conduction channels are combined and all nearest neighbor dimer pairs are included.

The Marcus-Hush-Goddard mobilities (Table 6.5) show similar trends to the BTE predicted mobilities (Table 6.2) but have magnitudes that are significantly smaller. In addition, the relative directional magnitudes of a particular crystal seem to be highly effected by the bulk effects included in BTE. This is especially true in the directions that do not align with the high mobility channels of the organic crystals, where BTE predicts significantly higher mobilities than Marcus-Hush-Goddard along these directions, more in line with measured anisotropic mobilities.[332] For all of

Table 6.5: Cartesian projected and normalized Marcus-Hush-Goddard hole mobilities at the PBE0-D3/def2-TZVP level of theory with T = 300K.

Crystal	$\mu_x^M(cm^2/Vs)$	$\mu_y^M(cm^2/Vs)$	$\mu_z^M(cm^2/Vs)$
anthracene	0.0056	0.6122	0.1451
tetracene	1.8850	1.1842	0.0000
pentacene	2.3107	1.4996	0.0000
hexacene	3.6215	4.9251	0.0000
2,6-diphenylanthracene	0.0012	0.6552	0.4629
rubrene	0.0000	4.0435	0.0297
TIPS-pentacene	0.2871	0.1004	0.0000

the materials considered, with the exception of anthracene, the predicted ordering of the Cartesian carrier mobilities match between both models (Tables 6.2 and 6.5). The anthracene ordering mismatch can be attributed, at least partially, to both how similar its directional conductivity magnitudes are at the Fermi-level and that the directional ordering changes just below the Fermi-level with $\mu_z < \mu_x$ (Figure 6.5, grey dotted line). Of course, the Marcus dimer projection model doesn't include the band curvature at the Fermi-level as it assumes only localized charges, and thus doesn't capture this band-like unique phenomenon. For all of the other crystals, reordering of the largest conductivity doesn't occur near the Fermi-level, if at all.

The similarities between BTE and Marcus-Hush-Goddard are captured by plotting the largest Fermi-level Cartesian mobility of each crystal on the same axis (Figure 6.6). The primary difference between the Marcus and BTE substituted vs. unsubstituted results arises from the hole induced reorganization energy (Figure 6.7). In the Marcus model, a hole is localized on a single molecule as it probabilistically hops through the lattice via channels of minimal resistance. In many cases, addition of a localized hole can significantly change the energy and geometry of the isolated monomers. This is captured in the Marcus reorganization energies (λ), and leads to large reductions in the predicted hopping rates. Two trends are observed in the monomer reorganization energy results: 1) reorganization energy tends to decreases as the length of the n-acene backbone increases, 2) all of the substituted acenes, when compared with their unsubstituted counterparts of the same acene backbone length, are predicted to have substantially larger reorganization energies. So, as molecules of the crystal become less rigid, either with more substitution (*i.e.,* from di- to tetra-phenyl substitutions in 2,6-diphenylanthracene and rubrene) or with more substituent flexibility (*i.e.,* from phenyls to TIPS), the difference in their reorganization energy is expected to increase.

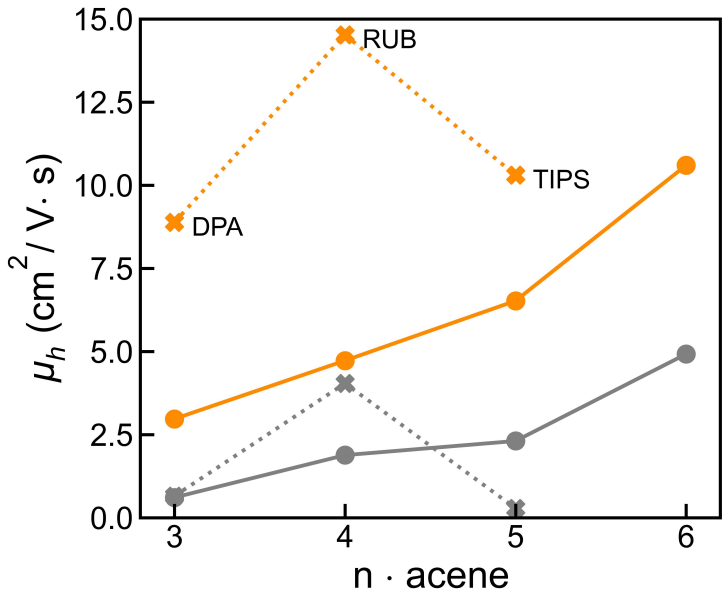

Figure 6.6: Largest mobilities of any Cartesian direction, PBE0-D3/def2-TZVP Marcus-Hush (grey) and PBEsol0-3c BTE (orange). Solid circles and lines are unsubstituted acenes and bold x's with dotted lines are the substituted acenes.

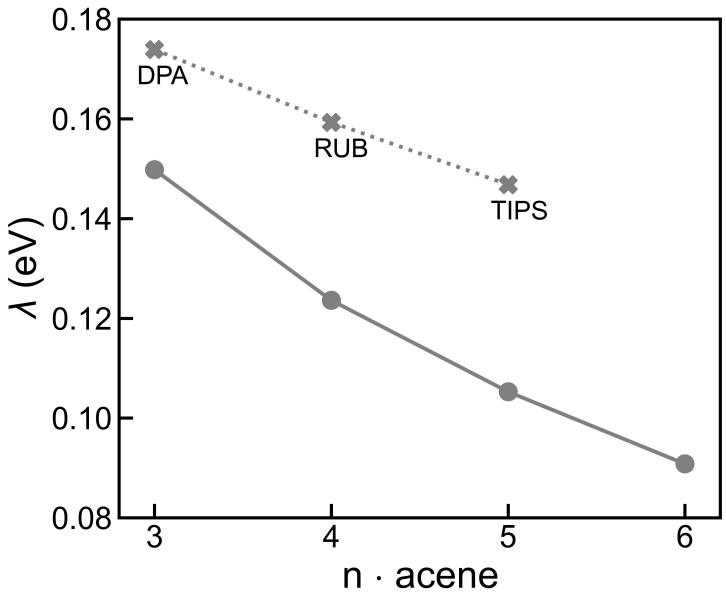

Figure 6.7: Marcus reorganization energies at the PBE0-D3/def2-TZVP level of theory. Solid circles and lines are unsubstituted acenes and bold x's with dotted lines are the substituted acenes.

Thus, structural rigidity and hole delocalization length should both increase the mobility of organic single crystals.

The periodicity of the BTE model allows for the delocalization of the hole, across the whole unit cell. Thus, constant-relaxation-time BTE assumes that the reorganization energy is approximately zero because of this charge spreading. Since the charge carrier is completely delocalized, movement of the charge leads to less geometric reorganization as it propagates. This, of course, may be an oversimplification of true the charge transport mechanism in organic crystals where phonon-induced transient localization events may introduce some significant reorganization.[343]

The predicted mobilities from the two models might then be expected to converge for longer acenes, as the Marcus reorganization energy steeply decreases as a function of acene backbone length. Surprisingly, this was not observed, and the gap between the BTE and Marcus mobilities of the unsubstituted acenes increased as a function of backbone lengthening (Figure 6.6). This directly shows that a different constant relaxation time cannot align the two theories quantitatively. Again, this means that the implementations of these two theories do not converge at the fast scattering rate (small τ).

6.3.5 Computational Costs

Predicting mobilities with both BTE and Marcus require multiple DFT energy calculations. Thus computational efficiency should be measured in total CPU-hr cost (post optimization) to calculate the Cartesian mobilities with either model (Figure 6.8). BTE conductivities require a dense k-point grid SCF calculation (denser than the optimization grid) and a finite temperature (300K) Cartesian conductivity calculation. Marcus effective electronic couplings are derived from single point energy calculations of all of the unique monomers and dimers (the number depends on the crystalline symmetry). Marcus reorganization energies are estimated by four additional charge localization calculations (2 optimizations + 2 single point energies) (see Appendix A). Figure 6.8 shows the cost of the best computational methodology for each model, the BTE/PBEsol0-3c/def2-mSVP (orange) cost is significantly lower than Marcus/PBE0-D3/def2-TZVP (grey). However these are of different basis set sizes, which might over estimate the advantage of the BTE method. So in addition, the cost of BTE/PBE0-D3/pob-TZVP-rev2 (green) is included. These results clearly show the benefit of using the modified double-ζ basis over the triple-ζ, and the cost difference between the BTE and

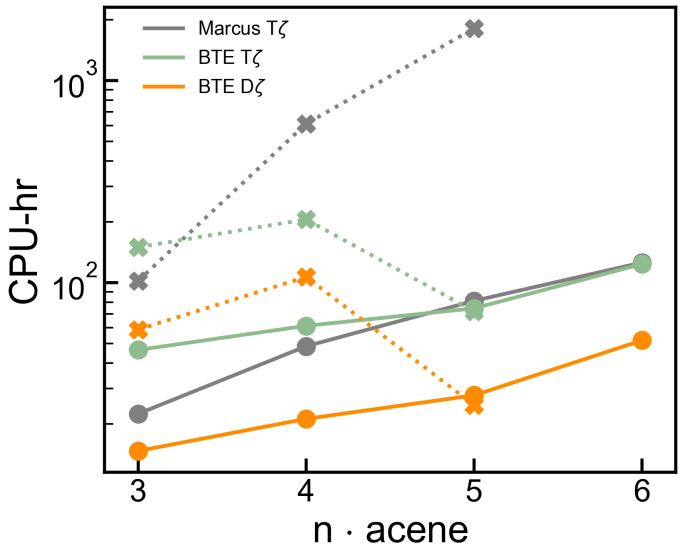

Figure 6.8: Computational cost (in CPU-hrs) of DFT calculations to calculate mobilities, PBE0-D3/def2-TZVP Marcus-Hush (grey), PBEsol0-3c/def2-mSVP BTE (orange), and PBE0-D3/pob-TZVP-rev2 (green). Solid circles and lines are unsubstituted acenes and bold x's with dotted lines are the substituted acenes.

Marcus models for each crystal. On average, the BTE triple-ζ basis costs 2.65 ±0.38 times that of the modified double-ζ basis at a comparable level of theory. Marcus mobilities, on the other hand, cost 4.59 ±8.42 times the average BTE cost. The large standard deviation in the cost of each method arises primarily from the highly substituted rubrene and TIPS-pentacene crystals. In these crystals, the cost to calculate the reorganization energy is substantially larger than the other crystals. In fact, it cost 13.3 and 48.5 times the average cost of the other crystals, respectively. This result is expected because configurational flexibility is correlated with computational cost. Therefore, for large and highly flexible systems, the BTE model is even more computationally efficient than the Marcus model.

6.4 Conclusion

The BTE model presented here provides an efficient and effective way to compute relative anisotropic conductivities and charge carrier mobilities of high-mobility organic semiconductor materials. The BTE model when coupled with an affordable composite functional (PBEsol0-3c) correctly predicted experimental geometries, band gaps, and the theoretically consistent increasing mobilities across

the n-acenes. In addition, the overall anisotropic mobility trends of the dimer Marcus mobilities were reproduced with BTE. The magnitude of the predicted mobilities of the substituted acenes with both models are significantly different due to the larger reorganization energies in Marcus theory. BTE consistently provides quantitative and qualitative ordering of mobilities within and between various acene crystals with less computational cost and numerical manipulation providing a efficient screening method for large sets of crystals.

Chapter 7

Finite Displacement Boltzmann Transport Theory[†]

Crystalline organic semiconductors are modular materials with numerous applications including OLEDs, OFETs, OSCs, and sensors.[323–327] In organic materials, molecules pack together in various polymorphs primarily through non-covalent van der Waals forces.[331,336,337,351] Because of this, their solid structures are highly susceptible to both static and dynamic disorder. While examples of the former include packing defects and broken symmetries, dynamic disorder arises from stochastic combinations of lattice phonons, *i.e.,* the normal vibrational modes of the crystal. This disorder transiently alters the inter- and intra-molecular interactions between or within the molecules of the crystal.[337–340,373]

Combinations of experimental and theoretical evidence suggest that dynamic disorder largely limits the charge carrier mobilities of organic semiconductors by reducing intermolecular electronic couplings and by inducing charge carrier localization from several molecules (≈ 10) down to single monomers.[332,343–348,352,364,365,378,379,397] This effect leads to a necessary shift in the description of the transport mechanism from delocalized band-like to localized hopping and back depending on the time-varying phonon populations. While band and hopping models are able to provide reasonable approximations for electron-phonon coupling in organic semiconductor materials individually,[146,329,366,383,388,396] neither can completely describe the transport mechanism.[347,349,375,376]

[†]Reprinted with permission from Z. J. Knepp, L. A. Fredin, Physical Review B **109**, 094307 (2024). Copyright 2024 by the American Physical Society.

Because disorder induced localization limits electrical conduction in these materials, hopping models are often used to predict trends in mobility. Constant relaxation time Boltzmann transport theory has been shown to predict accurate mobility trends of organic crystals with substantially less computational effort than hopping-based models.[146] While the limitations of hopping and band-based models are well understood, they continue to be used to screen and understand trends in related sets of crystals because they are widely available, are based on fundamental physics, and provide insight in terms of chemical intuition.

Some models have included dynamic disorder by examining the effect of some normal modes on coupling in a crystal.[329,366,383,388,396] Of all the possible vibrational modes for a given material, the low frequency regime results in the largest structural distortions on average since these populate vibrational excited states beyond the zero point energy level. Such large displacement intermolecular motions induce large electronic structure rearrangements. The low frequency regime has been studied using combinations of transmission electron microscopy (TEM), molecular dynamics (MD), and density functional theory (DFT) on various crystalline organic semiconductors.[332,364,365] Low frequency modes dominate the electron-phonon scattering rates limiting the charge-carrier mobility.[383] In particular, the lowest frequency mode of typical herringbone organic crystals, a long axis asymmetric sliding motion, significantly reduces intermolecular electronic coupling and leads to frequent transient localization events.[352,364]

Theoretical studies investigating the dynamic disorder of various organic crystals often neglect the majority of the high frequency regime ($> 207\ cm^{-1}$) because these modes are not expected to significantly reduce charge carrier mobility.[352,364,367,388,398,399] Because the high frequency modes are generally restricted to the ground vibrational state ($n = 0$) at room temperature, according to the Bose-Einstein occupation number, they result in root mean square displacements (RMSD) up to two orders of magnitude less than the low frequency regime. However, inclusion of the full frequency range leads to more accurate mobilities,[400,401] and shows that many modes contribute to dynamic disorder.[400,402] This is because electronic structure reorganization is not necessarily correlated with atomic displacement amplitudes.

In this study, the dynamic disorder of tetracene, a prototypical organic semiconductor crystal, is investigated to reveal the effects that each of its 180 Γ-point normal modes have on the anisotropic charge carrier mobility. This is accomplished using a novel quantum-harmonic-oscillator-based

finite displacement Boltzmann transport theory model (Δ-BTE). Finite displacement amplitudes are derived from the uncertainty in the position of each atom, which differs from the classical analog where displacements were set at the edge of the harmonic well.[388] A substantial benefit of Δ-BTE is that it does not require dimer extraction and electronic coupling evaluations, and thus serves as a high throughput method for screening the normal-mode-induced mobility effects from band structure renormalization for a wide range of materials, including both inorganic (*e.g.* oxides, perovskites, MOFs) and organic (*e.g.* organic single crystals, COFs, interfaces).

7.1 Computational Methodologies

The PBEsol0-3c solid-state composite density functional method was used to fully optimize the lattice parameters and nuclear coordinates of the tetracene (TETCEN) crystal structure[403] with the CRYSTAL17 code.[357,358] PBEsol0-3c combines a small atom-centered def2-mSVP basis set with geometric counterpoise corrections and Grimme's D3 dispersion corrections to accurately and affordably predict the geometric and electronic structure of many materials, including weakly bound organic semiconductor crystals.[146,391,392] For all calculations, the DIIS convergence accelerator was used. For the optimization, an anisotropic 4x5x3 k-point mesh was generated via the SHRINK factor such that the real space primitive lattice vectors multiplied by these were $>$ 30 Å. For the Boltzmann transport theory (BTE) calculations, the k-point mesh was quadrupled to increase the accuracy and to minimize the error of band derivatives. The SCF convergence threshold on total energy (TOLDEE) was set to 10^{-8} $Hartree$ for the optimization and 10^{-10} $Hartree$ for the frequency calculation. Tolerances for coulomb and exchange sums (TOLINTEG) were set to 8 8 8 8 16 for all calculations.

7.2 Results and Discussion

The density functional theory (DFT) optimized tetracene crystal structure closely matches the room temperature TETCEN crystal structure with comparable lattice parameters and a primitive-cell volume that is only 1.73% larger than experiment (Table 7.1).[403] A Γ-point frequency calculation on the optimized structure produced only positive real eigenvalues, indicating a minimum. A bandgap of 2.54 eV was predicted, which matches the experimental optical gap of 2.54 eV.[395] Due to a band

Table 7.1: Unit cell lattice vectors and angles of the PBEsol0-3c optimized and the experimental triclinic TETCEN unit cell.[403]

	a (Å)	b (Å)	c (Å)	α (°)	β (°)	γ (°)	V (Å^3)
TETCEN	7.90	6.03	13.53	100.30	113.20	86.30	582.85
PBEsol0-3c	7.99	6.03	13.57	100.75	112.68	86.24	592.96

Table 7.2: BTE-derived conductivity tensor matrix elements at the computed Fermi level of the PBEsol0-3c structure. Here, the carrier concentration is $\rho \equiv N_{\mathcal{F},T}/V$. The constant relaxation time τ is set to 2 fs.

	σ_{xx} (S/cm)	σ_{xy}	σ_{xz}	σ_{yy}	σ_{yz}	σ_{zz}	σ_1	σ_2	σ_3	ρ (cm^{-3})
PBEsol0-3c	43.5	-20.9	0.0	22.4	0.2	6.2	56.4	9.5	6.2	$2.9{\cdot}10^{20}$

crossing between the Γ-point and [−110] direction, the total theoretical bandwidth is the sum of the widths of the valence band edge (VB) and the VB-1 band. The predicted valence bandwidth of 0.35 eV is comparable to previous DFT and experimental values of 0.39 eV[404] and $0.35-0.7$ eV,[405] respectively. The broad experimental range may be the result of vibrational effects or could be from the convolution of the bulk band structure with that of a reconstructed surface.[404,405]

The fact that the geometric and the electronic structure of tetracene are well represented by the PBEsol0-3c composite density functional confirms its usefulness for predicting charge transport properties. The conductivity tensor[146] matrix elements in a Cartesian basis **x**,**y**,**z** within the constant relaxation time approximation of the Boltzmann transport equation (BTE, Appendix C)[357,358,382–384] can be derived from the optimized structure. By default, CRYSTAL17 aligns the **x** vector parallel to the optimized **a** lattice vector, then sets **y** 90° away and closest to the **b** axis, and then sets **z** orthogonal to **x** and **y**.[357,358] Because the BTE off-diagonal conductivity matrix elements are non-zero for tetracene, the tensor is diagonalized (Appendix D) to determine the principal axis eigenvectors and their corresponding eigenvalues (Table 7.2).

According to BTE, tetracene preferentially conducts along the $\mathbf{e}_1$ direction (Fig. 7.1) at 56.4 S/cm when a constant relaxation time of 2 fs is assumed.[381,385] The angle between $\mathbf{e}_1$ and the **a** lattice vector ($\theta_{\mathbf{e}_1,a} = 148.4°$) agrees well with the experimental angle of 141.3°.[332] Substantially smaller conductivities are predicted in the $\mathbf{e}_2$ (9.5 S/cm) and $\mathbf{e}_3$ (6.2 S/cm) directions. In the $\mathbf{e}_1$ direction, the mobility is 1.2 cm^2/Vs (Table 7.3) when using the intrinsic carrier concentration from the number of carriers at the Fermi level divided by the primitive cell volume, which agrees

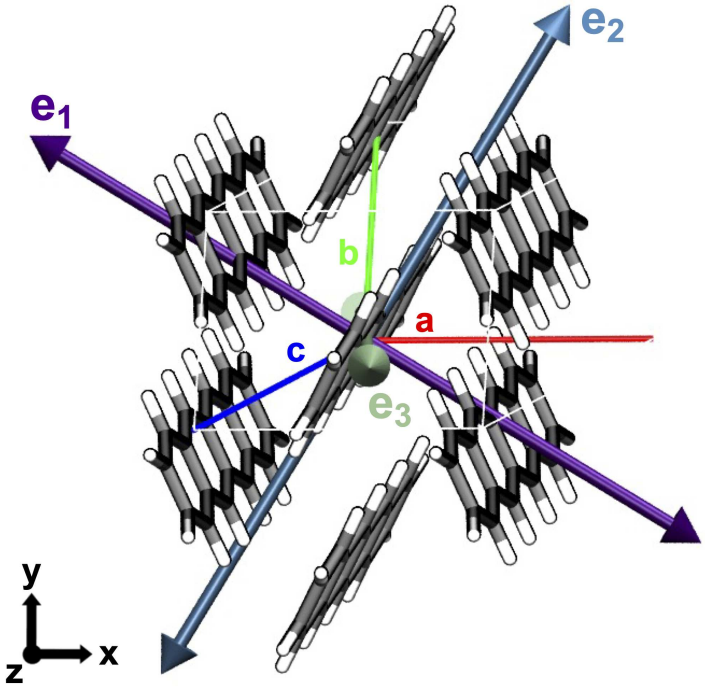

Figure 7.1: Principal axis eigenvectors ($\mathbf{e_1}, \mathbf{e_2}, \mathbf{e_3}$) and the primitive lattice vectors ($\mathbf{a}, \mathbf{b}, \mathbf{c}$) of the fully optimized PBEsol0-3c tetracene crystal structure.

Table 7.3: BTE and experimental charge carrier mobilities along the principal directions of the crystal.

	μ_1 (cm^2/Vs)	μ_2 (cm^2/Vs)	μ_3 (cm^2/Vs)	μ_1/μ_2	$\theta_{\mathbf{e}_1,a}$(deg)
experiment	$\mu_H = 0.8$[332], 2.4[406]	$\mu_L = 0.4$[332]	——	$\mu_H/\mu_L \approx$ 1.5-2.0[332]	≈ 141.3[332]
PBEsol0-3c	1.2	0.2	0.1	6.0	148.4

well with experimental reports of 0.8 and 2.4 cm^2/Vs.[332,406]

Projecting the principal axes mobilities in the high mobility plane (**ab**) produces a curve (Fig. 7.2) that agrees with experimental results for crystalline tetracene.[332] BTE predicts an anisotropy ratio between the high and low mobilities (μ_H/μ_L) of 6 in the high mobility plane, which is on the same order of magnitude as the experimental value of $\mu_H/\mu_L = 1.5 - 2$. Previous theoretical ratios predicted larger anisotropy ratios, > 10,[374,407] indicating an improvement in the description of the electronic structure with PBEsol0-3c.

Δ-BTE quantifies the vibration-induced mobility change by calculating conductivity and carrier concentration at the Fermi level of the optimized and finite displaced structures. The temperature-dependent finite displacement amplitudes of each normal mode were determined from the DFT-

Table 7.4: Widths of the frontier bands in meV, including the highest filled valence band (VB) and one band above (VB+1) and below (VB−1). 0 K and 300 K bandwidths are averaged over all the normal modes in both the negative and positive displacement directions.

	VB−1 (meV)	VB (meV)	VB+1 (meV)
PBEsol0-3c (opt)	161.1	188.1	270.5
PBEsol0-3c (0 K)	160.5	186.6	269.6
PBEsol0-3c (300 K)	160.4	186.2	269.3

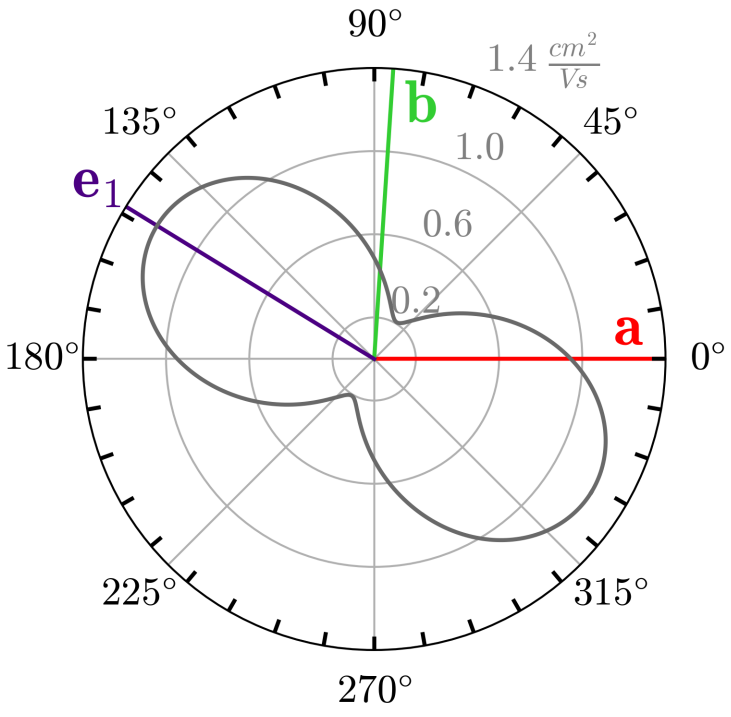

Figure 7.2: Theoretically derived polar mobility curve in the **ab** plane of tetracene. The radial component corresponds to the counter-clockwise degrees away from the a-axis.

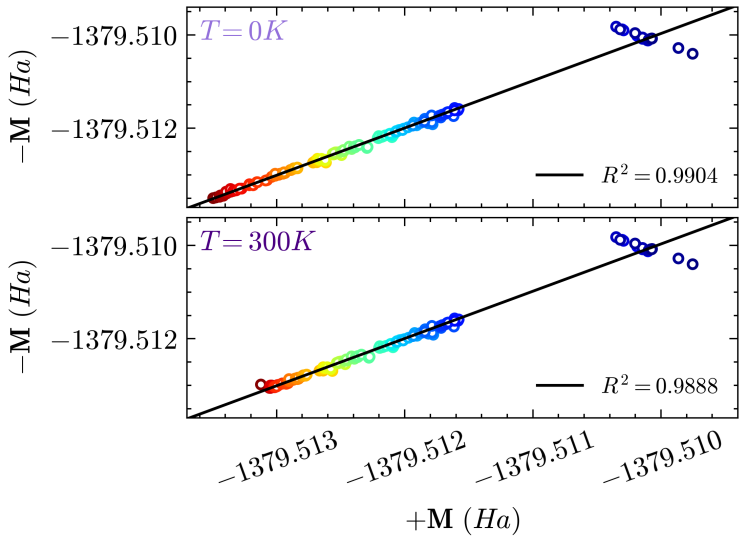

Figure 7.3: Anharmonicity in the SCF displacement energies at 0 and 300 K due to the harmonic structural displacement of $+\mathbf{M}$ (x-axis) and $-\mathbf{M}$ (y-axis). The black line corresponds to the best fit line between the positive and negative displacement energies.

derived uncertainty in the positions (Appendix E.1). The approximation of finite displacements provides a way to correct for vibrational energy without relying on the electronic structure being linearly correlated to the vibration. Overall, the majority of the normal modes are harmonic in energy, with $R^2(0\ K) = 0.9940$ and $R^2(300\ K) = 0.9888$. A few of the high frequency modes that do not significantly change the mobility are marginally anharmonic in energy (Fig. 7.3), even though their displacement amplitudes are harmonic.

The ground state DFT bandwidth of 349 meV, approximated by the sum of the VB-1 and VB bandwidths because these bands cross, is within the $350 - 700$ meV range of experimentally measured bandwidths.[405] As expected, the vibrationally perturbed (colored and grey) VB and VB-1 bands are significantly different in both energy and shape than the bands of the optimized structure (Fig. 7.4). Isolated normal modes and the averages over all the modes result in the narrowing of each band including the VB-1, VB, and VB+1 (Table 7.4). This is consistent with a band velocity reduction and a decrease in the charge carrier mobility. Additionally, a sub-meV reduction in the bandwidths is observed as a function of increasing the temperature from 0 to 300 K. Focusing in on normal mode # 4 (yellow), it is easy to see the effect of bandwidth narrowing as a function of populating higher vibrational excited states at 300 K when compared to the zero-point vibrational energy at 0 K. However, substantially larger bandwidth narrowing effects have been observed both

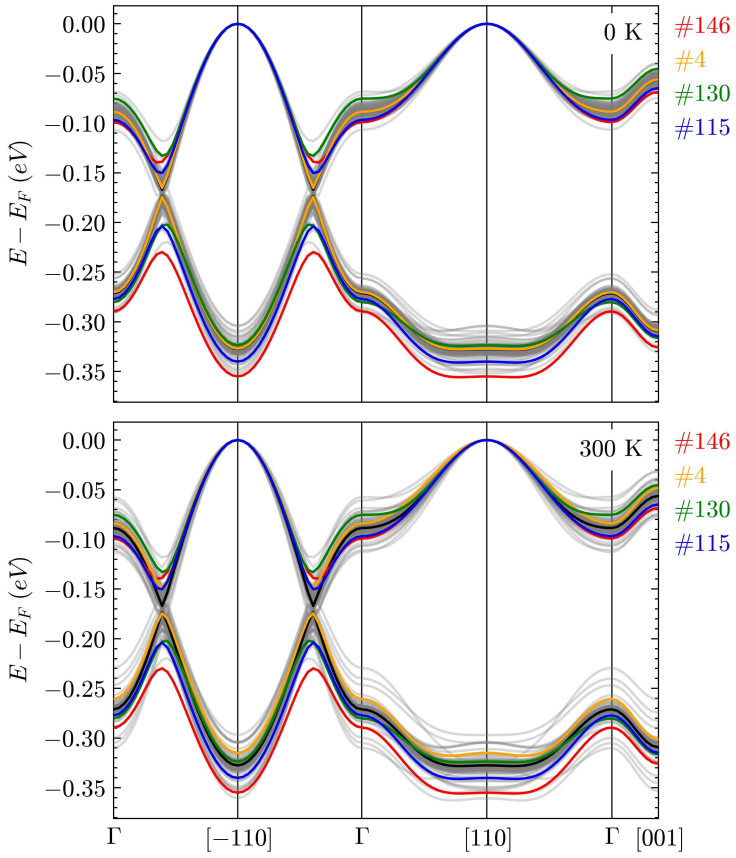

Figure 7.4: Fully optimized (black) and the 0 K (top) and 300 K (bottom) finite displaced (grey and colored) VB and VB−1 bands centered around the ground state Fermi-level. Particularly problematic modes (#) are highlighted in red, orange, green, and blue.

experimentally and theoretically for oligoacene crystals from a combination of polaron formation and thermal lattice expansion, which Δ-BTE doesn't capture explicitly.[407–411]

Normal mode induced mobility changes happen primarily in the $\mathbf{e}_1$ direction and very little in the $\mathbf{e}_2$ and $\mathbf{e}_3$ directions (Fig. 7.5). For each normal mode, the conductivity tensors were calculated and diagonalized at each of the normal mode-perturbed Fermi levels. Calculated mobilities at 0 K and 300 K (Fig. 7.6) show large changes across a wide range of frequencies. The percent change in mobility is reported as it results in the cancellation of τ, eliminating the constant relaxation time. This, however, does not eliminate the effects from electron-phonon scattering.

Interestingly, even though the majority of the modes are harmonic in energy, in either displacement direction, their resulting mobilities are not. This mobility anharmonicity is observed over the full frequency range at both 0 K and 300 K. In fact, for particular modes in either the $+\mathbf{M}$ or

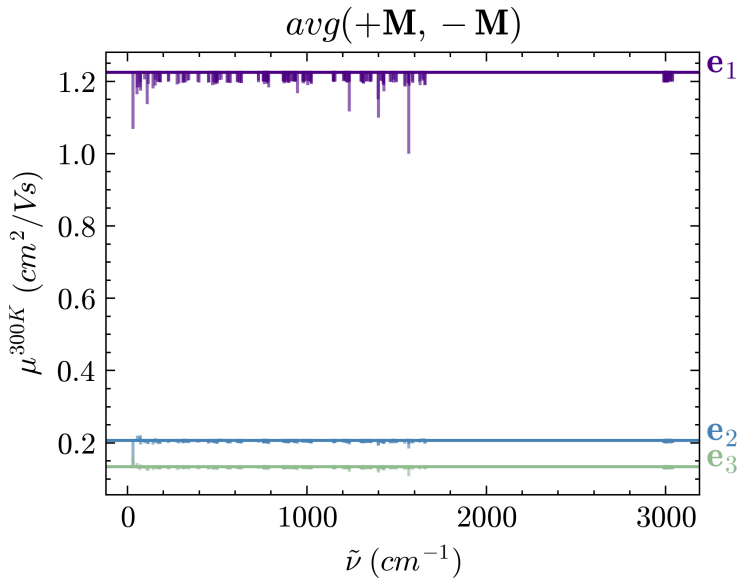

Figure 7.5: Normal mode induced mobility changes along the three principal directions $(\mathbf{e_1}, \mathbf{e_2}, \mathbf{e_3})$ averaged over the $+\mathbf{M}$ and $-\mathbf{M}$ finite displacements at 300 K.

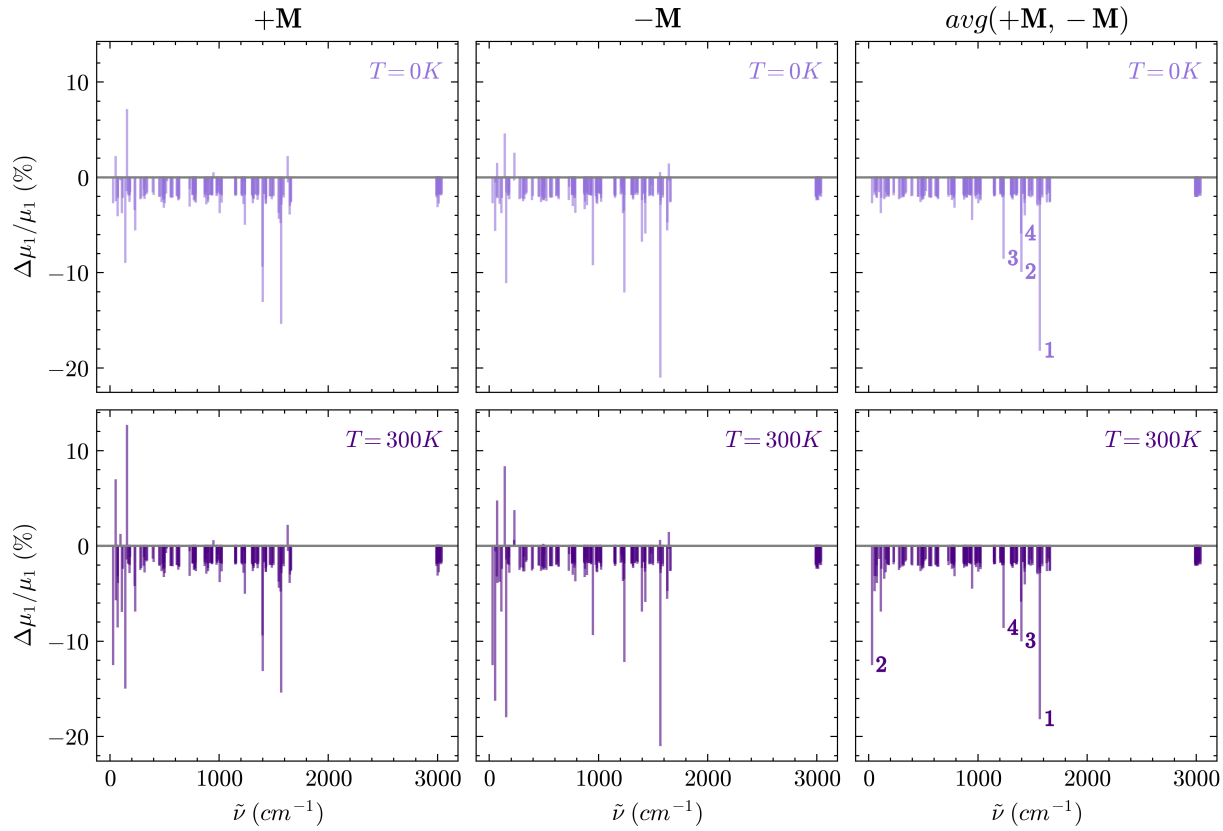

Figure 7.6: Normal mode induced mobility changes along the principal direction (e_1) at 0 K (light purple, top) and 300 K (dark purple, bottom). $\Delta\mu/\mu$ is expressed as a percentage, to allow for easy visualization along a single set of axes.

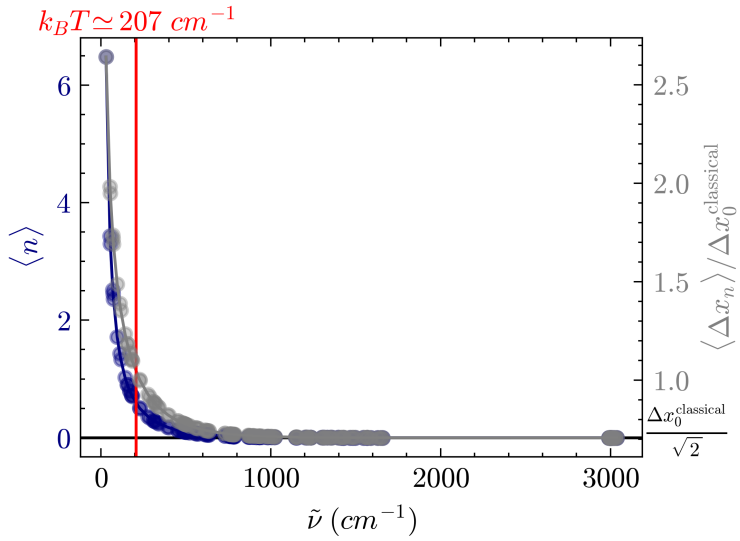

Figure 7.7: Expected vibrational quantum number ($\langle n \rangle$, dark blue) and the uncertainty (Δx_n) in the position at 300 K (gray) as a fraction of the zero point energy level maximum classical displacement amplitude ($\Delta x_0^{\text{classical}}$) for each normal mode.

–**M** direction, mobilities infrequently increased in magnitude, suggesting that those modes could be beneficial for charge transport. However, because each mode oscillates in both directions, the average mobility (Fig. 7.6 right) revealed that *all* Γ*-point normal modes are detrimental to the charge transport of tetracene* along the $\mathbf{e}_1$ direction.

Mobility differences between 0 K and 300 K occur within the low frequency regime ($< 207\ cm^{-1}$) because low frequency modes populate vibrational excited states, *i.e.*, $n > 0$, at 300 K (Fig. 7.7). Differences in the average mobility changes (Fig. 7.8) up to 10% were found for the lowest frequency normal mode at 300 K. As frequencies increase beyond 207 cm^{-1}, the differences between the two temperatures become negligible as the zero-point vibrational energy level is populated at all temperatures.

By inspecting the average mobility changes mode-by-mode, four normal modes were identified to reduce the mobility significantly (Fig. 7.6 and 7.9). Of the four, the 2^{nd} most detrimental mode is the previously identified intermolecular asymmetric sliding motion.[352] Interestingly, particular high frequency modes (modes 146, 130, and 115) lead to the 1^{st}, 3^{rd}, and 4^{th} largest mobility reductions, up to 18.1 %. Even though their average structural displacements are considerably small, on the order of 0.005 - 0.012 Å (Table 7.5 and Fig. 7.9), their detrimental impact on mobility is not (Table 7.5). Even though the effects of inelastic electron scattering from phonons likely limit the

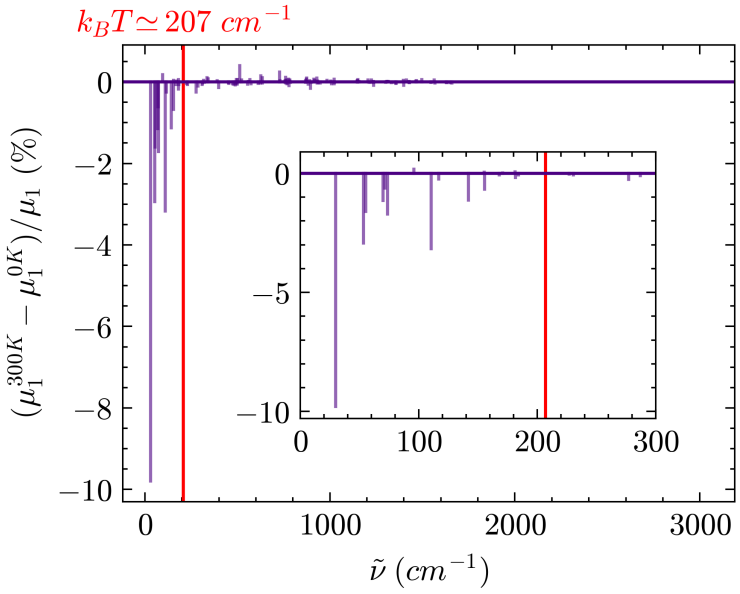

Figure 7.8: Differences in the mobility between 300 K and 0 K as a percent of mobility along the primary axis in the optimized structure (μ_1). The red vertical line marks room temperature (300 K).

Table 7.5: Four most detrimental modes identified by finite displacement BTE at 300 K. RMSD were calculated on four molecule clusters extracted from the unit-cells.

Temperature (K)	Rank	Mode (#)	RMSD (Å)	cm^{-1}	$\Delta\mu_1$ (cm^2/Vs)	$\Delta\mu_1/\mu_1$ (%)	Description
0	**1**	146	0.005	1568	-0.22	-18.1	ring breathing / C-C-H bending
	2	130	0.005	1398	-0.12	-9.8	ring breathing / C-C-H bending
	3	115	0.012	1236	-0.10	-8.4	C-C-H bending
	4	129	0.005	1397	-0.07	-5.8	C-C-H bending
300	**1**	146	0.005	1568	-0.22	-18.1	ring breathing / C-C-H bending
	2	4	0.132	30	-0.15	-12.4	long-axis asymmetric slide
	3	130	0.005	1398	-0.12	-9.9	ring breathing / C-C-H bending
	4	115	0.012	1236	-0.10	-8.5	C-C-H bending

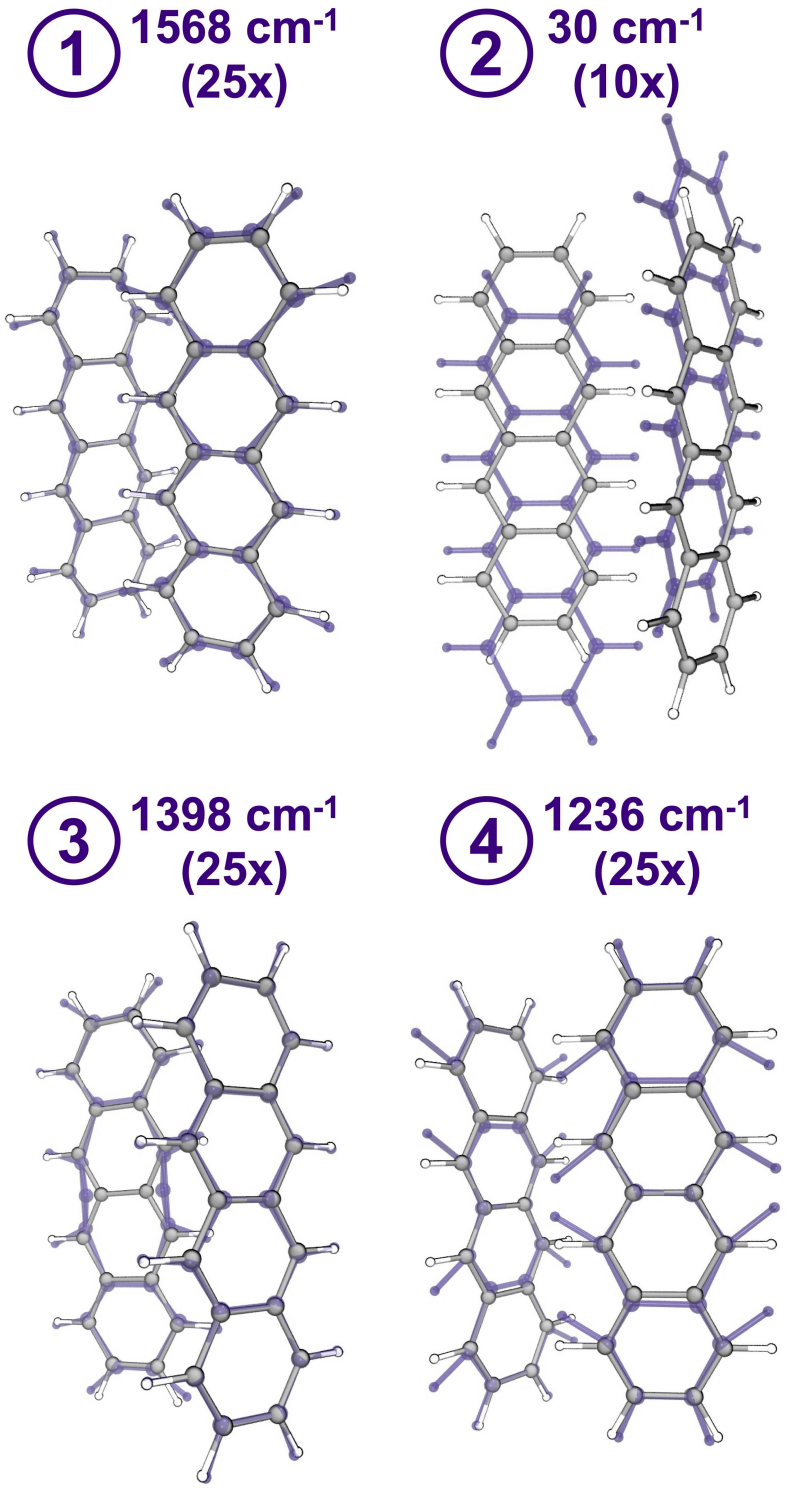

Figure 7.9: Dimers depicting the four most detrimental modes. Grey/white show the optimized structures and the finite displaced structure of each mode is shown as a multiple (10x or 25x) of the maximum classical displacement (dark purple).The optimized structures are in grey and white.

maximum mobility of tetracene significantly more than the band structure changes considered here, it is still rather surprising that such small displacements lead to such large mobility changes. These findings are in contrast to previous assumptions that only large displacements have a large effect of the electronic structure. However, this parallels very recent insights that high frequency modes contribute to dynamic disorder found using an electronic coupling based approach.[402]

To rationalize why these particular high frequency modes are so problematic, the valence band projected density matrices are plotted as isosurfaces (Fig. 7.10). The **most** detrimental mode (mode 146, 1568 cm^{-1}) is characteristic of ring breathing and C-C-H in-plane bending. When compared to the fully optimized projected valence band, the motion (RMSD = 0.005 Å) results in a transiently localized polaron-like band density. Interestingly, as a function of the vibration, the density seemingly "hops" between the tetracene monomers along the principal $\mathbf{e}_1$ direction. To the best of our knowledge, this is the first report of a *switch* in the charge transport mechanism between band and hopping by combining finite displacements with BTE. Until now, calculating such processes has required a higher level fragment orbital-based surface hopping methods.[378]

Similar polaronic behavior is observed for the 3^{rd} (1398 cm^{-1}, ring breathing / C-C-H bending, RMSD = 0.005 Å) and 4^{th} (1236 cm^{-1}, C-C-H bending, RMSD = 0.012 Å) modes, although to a lesser extent (Fig. 7.10). The intermolecular asymmetric sliding phonon (30 cm^{-1}, RMSD = 0.132 Å), however, does not appear to be polaronic. Instead, the asymmetric sliding motion leads to unfavorable orbital overlap and electronic coupling along the vibration as reported previously.[352,388] Interestingly according to BTE, it appears that the sliding phonon is detrimental in both directions of the oscillation, which differs from our results when evaluating pentacene with a Marcus dimer projection method.[388]

7.3 Conclusion

Δ-BTE is an efficient method for evaluating the dynamic disorder of molecular crystals with finite temperature and zero-point energy effects. It correctly predicts both the mobility magnitudes and the preferential transport direction of tetracene after conductivity tensor diagonalization. Δ-BTE is relatively cheap so the full frequency range can be explored. This allows high-frequency modes that result in significant mobility reductions, even with minuscule structural changes, to be identified

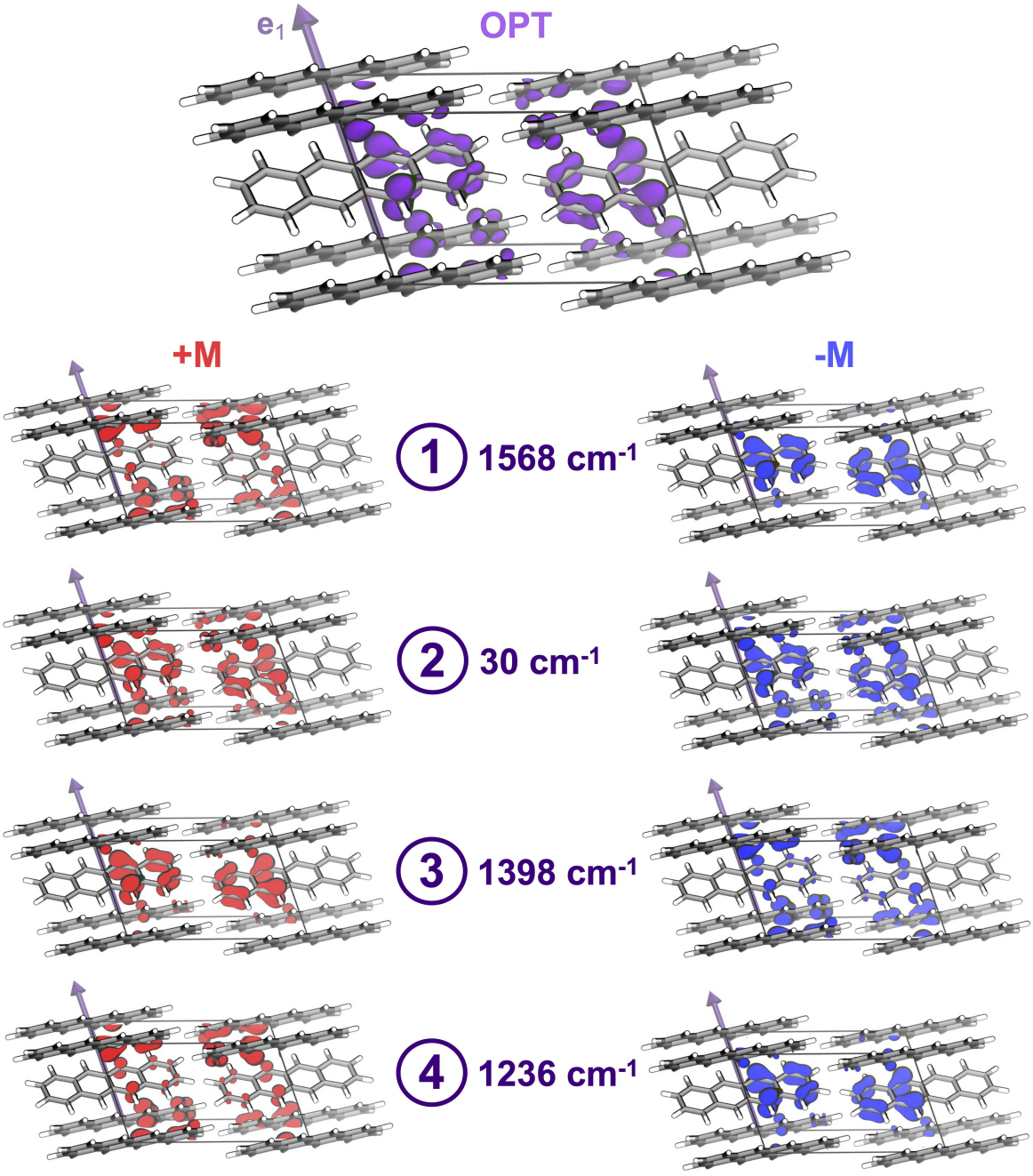

Figure 7.10: Effect of finite displacement on the valence band (VB) projected density. The optimized VB is plotted in purple, while density resulting from finite $+\mathbf{M}$ (red) and $-\mathbf{M}$ (blue) finite displacement are shown for the four worst modes. The VB projected density matrices are plotted as an isosurface with an isovalue of 0.03.

for the first time. Surprisingly, three of tetracene's four most detrimental modes are high-frequency ring-breathing modes that appear to be polaronic. This means that neglecting the high-frequency regime when evaluating vibrational effects in molecular semiconductors misses an important part of the transport picture at finite temperatures.

Appendix A

Marcus Reorganization Energies and Electronic Couplings

It is common that intra-molecular reorganization energies λ_{intra} are computed using a four point method which utilizes the adiabatic potential energy surfaces of a single isolated monomer from the crystal structure.[374]

$$\begin{aligned}\lambda_{intra} = \langle\phi^0_{opt}|H^+|\phi^0_{opt}\rangle - \langle\phi^0_{opt}|H^0|\phi^0_{opt}\rangle + \\ \langle\phi^+_{opt}|H^0|\phi^+_{opt}\rangle - \langle\phi^+_{opt}|H^+|\phi^+_{opt}\rangle\end{aligned} \tag{A.1}$$

The states ϕ^0_{opt} and ϕ^+_{opt} correspond to the optimized Cartesian coordinates of an isolated monomer in the neutral and charged states, respectively; H^0 and H^+ represent the Kohn-Sham Hamiltonian's for the neutral and charge electronic states. In general, according to Eq. 6.1, charge hopping rates are maximized when the reorganization energy is minimized.

The effective electronic couplings (V_{ab} or V_i) can be computed with density function theory (DFT) through projecting the isolated monomer orbitals onto the coupled dimer orbitals (DIPRO).[341,366,368]

$$V_{ab} = \frac{J_{ab} - S_{ab}(\epsilon_a + \epsilon_b)/2}{1 - S^2_{ab}} \tag{A.2}$$

Effective, here, means that in addition to the charge transfer integral (J_{ab}) one also takes into consideration the orbital overlap (S_{ab}) between the monomers and site energy fluctuations (ϵ_a and

ϵ_b) among the unique monomers within a given dimer.

$$J_{ab} = \langle \phi_a | H | \phi_b \rangle \tag{A.3}$$

$$S_{ab} = \langle \phi_a | \phi_b \rangle \tag{A.4}$$

$$\epsilon_a = \langle \phi_a | H | \phi_a \rangle \tag{A.5}$$

$$\epsilon_b = \langle \phi_b | H | \phi_b \rangle \tag{A.6}$$

In our calculations, we make use of the CATNIP code to compute the quantities mentioned above.[368]

Appendix B

Renormalization of Marcus Couplings Along Cartesian Directions

For direct comparison between BTE and Marcus mobilities, the unique d-COM vectors are decomposed into their three orthogonal Cartesian components such that the sums of the square projections are normalized.

$$\cos^2(\theta_{ix}) + \cos^2(\theta_{iy}) + \cos^2(\theta_{iz}) = 1 \tag{B.1}$$

Here, $\theta_{i\alpha}$ is the angle between d-COM vector i and a Cartesian vector α. The product of the cos^2 projection and the initial d-COM vector magnitude may be interpreted as an adjusted hopping length in a particular Cartesian direction.

$$r_{i\alpha}^2 = (r_i \cos(\theta_{i\alpha}))^2 \tag{B.2}$$

In this assumption, the charge carriers are still expected to hop between the monomers centers of mass in each dimer, on average, so the distance traveled in particular Cartesian directions depends on the projection of this hop or the $r \cdot cos^2$ components. Then, the hopping probabilities are weighted according to the unique dimer hopping rates

$$P_i = \frac{W_i}{\sum_i W_i}. \tag{B.3}$$

Before computing the weights, the non-unique conduction channel directions such as r_{12} and r_{34} were combined in a weighted average of the hopping rates in the d-COM direction.

$$W_{ij,kl,...} = \frac{W_{ij}^2}{W_{ij} + W_{kl} + ...} + \frac{W_{kl}^2}{W_{ij} + W_{kl} + ...} + ... \tag{B.4}$$

In doing this, the actual weighting in the projection (Eq. B.5) is limited to the unique conducting directions. After weighting, the Cartesian projected mobilities are represented by the product of the hopping probability, hopping weight, and corrected hopping distance squared.

$$\mu_\alpha = \frac{e}{k_B T} D_\alpha \approx \frac{e}{k_B T} \frac{1}{2} \sum_i (r_i \cos(\theta_{i\alpha}))^2 W_i P_i \tag{B.5}$$

The sum over the i indices results in an estimate for the Einstein diffusion coefficient D_α in each Cartesian direction. This model is identical to the 2D Goddard equation with a single cos^2 function.[374]

In the diffusion coefficient sums, hopping rates between the nearest neighbor dimer pairs of an isolated herringbone slice ($\{W_{avg(12,34)}, W_{13}, W_{23}\}$) and an end-on-end dimer (W_{ortho}) are included. The planar and orthogonal dimers were required to accurately predict mobilities in all the projected Cartesian directions as some Cartesian directions are not well aligned with the high conductivity herringbone slice. All drift mobilities (Eq. B.5) were computed at 300 K to match the temperature set in BTE.

Appendix C

Charge Carrier Mobilities with Boltzmann Transport Theory

Anisotropic charge carrier mobilities ($\mu_{\alpha\beta}$, Eqn. C.1) can be extracted from periodic density functional theory derived electrical conductivities (σ, Eqn. C.2) and charge carrier concentrations within the constant relaxation time Boltzmann transport theory approximation.

$$\mu_{\alpha\beta} = \frac{\sigma_{\alpha\beta} V}{e N_{\mathcal{F},T}} \tag{C.1}$$

$$\sigma_{\alpha\beta}\left(\mathcal{F},T\right) = e^2 \int dE \left(-\frac{\partial f_0\left(E,T\right)}{\partial E}\right) \Xi_{\alpha\beta}\left(E\right) \tag{C.2}$$

Here, $\mu_{\alpha\beta}$ is the charge carrier mobility (Eqn. C.1) matrix element in the $\alpha\beta$ direction of the cell. $\mathcal{F}$ is the approximate Fermi level from the highest energy k-point at the top of the valence bands, E is the energy, V is the volume of the primitive unit-cell, and e is the fundamental charge of the carrier. $N_{\mathcal{F},T}$ is the DFT derived number of charge carriers at a particular energy,

$$N_{F,T} = \frac{n}{N_{\mathbf{k}}} \sum_{\mathbf{k}} \sum_{i} \frac{1}{\exp\left(\frac{E-\mathcal{F}}{k_B T}\right)+1} \Theta(E - E_i(\mathbf{k})) \tag{C.3}$$

where n is the number of electrons per state, $N_{\mathbf{k}}$ is the number of k-points, and $\Theta(E - E_i(\mathbf{k}))$ is the theta function. The conductivity $\sigma_{\alpha\beta}$ is a symmetric 2^{nd}-rank 3x3 tensor with nine unique

coefficients, (Eqn. C.4),

$$[\sigma] = \begin{bmatrix} \sigma_{\alpha\alpha} & \sigma_{\alpha\beta} & \sigma_{\alpha\gamma} \\ \sigma_{\beta\alpha} & \sigma_{\beta\beta} & \sigma_{\beta\gamma} \\ \sigma_{\gamma\alpha} & \sigma_{\gamma\beta} & \sigma_{\gamma\gamma} \end{bmatrix}. \tag{C.4}$$

In BTE, σ is derived from the integral over the energy of the product of the negative partial derivative of the Fermi Dirac distribution with respect to energy ($\partial f_0/\partial E$). The transport distribution function (χ, Eqn. C.5) is the product of the band velocities ($v_{i,\alpha}(\boldsymbol{K}) = \partial E_i(\boldsymbol{K})/\partial k_\alpha$) indexed over each band combination, i and j.

$$\Xi_{\alpha\beta}(E) = \tau \sum_{\boldsymbol{K}} \frac{1}{N_{\boldsymbol{K}} V} \sum_{i,j} v_{i,\alpha}(\boldsymbol{K})\, v_{j,\beta}(\boldsymbol{K}) \tag{C.5}$$

In the constant relaxation time approximation, Ξ includes a time τ that approximates the mean charge carrier lifetime. Through the paper, τ is assumed to be 2 fs to match what has been predicted for similar organic materials.[381,385]

Appendix D

Determining the Principal Transport Axes from BTE Calculations

For isotropic conductors, Ohm's law is defined as $\mathbf{J} = \sigma\mathbf{E}$, where σ is the conductivity, $\mathbf{E}$ is the direction of the applied electric field, and $\mathbf{J}$ is the current from the applied field. As the current is not necessarily parallel to the applied field, the anisotropic form of Ohm's law is

$$J_\alpha = \sigma_{\alpha\beta} E_\beta. \tag{D.1}$$

With this, the electrical current can be determined from an applied field with a set of arbitrary defined Cartesian basis vectors, x, y, and z. The current density vector depends on all of the electric field components simultaneously

$$j_x = \sigma_{xx}E_x + \sigma_{xy}E_y + \sigma_{xz}E_z \tag{D.2}$$

$$j_y = \sigma_{yx}E_x + \sigma_{yy}E_y + \sigma_{yz}E_z \tag{D.3}$$

$$j_z = \sigma_{zx}E_x + \sigma_{zy}E_y + \sigma_{zz}E_z \ . \tag{D.4}$$

This makes the electrical conductivity a 2^{nd}-rank 3x3 tensor with the number of coefficients depending on the symmetry of the crystal. For higher symmetry crystals, the off-diagonal terms may vanish and the diagonal terms can even become equivalent.

With the symmetric 2^{nd}-rank 3x3 conductivity tensor, *i.e.*, $\sigma_{\alpha\beta} = \sigma_{\beta\alpha}$, it is possible to transform

the arbitrary basis vectors into a set of principal axes, to simplify the current vectors to

$$j_1 = \sigma_{11} E_1 \tag{D.5}$$

$$j_2 = \sigma_{22} E_2 \tag{D.6}$$

$$j_3 = \sigma_{33} E_3, \tag{D.7}$$

where $\sigma_{11}, \sigma_{22}, \sigma_{33} \equiv \sigma_1, \sigma_2, \sigma_3$. To do this, the tensor is diagonalized to satisfy the secular equation,$|\sigma - \lambda \mathbf{I}| = 0$. The resulting eigenvalues, or principal values, that satisfy the equation are labeled in the text as σ_1, σ_2, and σ_3.

Appendix E

Finite Normal Mode Displacements of Unit Cells

In periodic crystalline systems, the temperature-dependent dynamic structural disorder can be simply and efficiently described by a the normal mode basis at the Γ-point of a particular crystal. The inclusion of phonon dispersion beyond, *i.e.*, beyond the Γ-point, is important but the cost of evaluating such effects often prohibits it in practice.[412] Recent evaluation of the full Brillouin zone shows that Γ-point analyses can underestimate the effect of dynamic disorder.[400] At the Γ-point of a crystal, the total number of normal modes is determined by the number of spatial dimensions multiplied by the number of atoms in the primitive/unit/super cell, minus the three zero energy translational modes ($3N - 3$). Each normal mode, represented by i, has a quantized energy (eigenvalue, $\hbar\omega_i$) and an eigenvector (a displacement matrix, $+/-\mathbf{M}$) that describes how each atom of the cell moves as a function of time. In this study, the harmonic approximation was used to displace the atoms in either ($+\mathbf{M}$) or negative ($-\mathbf{M}$) directions. In either direction, the energies are assumed to be equivalent for small displacement amplitudes. The matrix elements of the Hessian (*i.e.* the second derivatives of the energy) were determined numerically with the analytical gradients. Frequencies were determined by diagonalizing the mass-weighted Hessian. The resulting eigenvectors are the normal modes.[357,358]

The displacement amplitudes of each normal modes are determined from the uncertainty in the

positions from the operator $\Delta\hat{x}_n$. The displacements are correlated to temperature according to

$$\begin{aligned}\Delta\hat{x}_n &= \Delta\hat{x}_0\sqrt{(2n+1)} \\ &= \sqrt{\left(\frac{\hbar}{2m\omega}\right)\left(\frac{2}{e^{\hbar\omega/k_BT}-1}+1\right)}.\end{aligned} \tag{E.1}$$

In this expression, $\Delta\hat{x}_0$ is the uncertainty in the positions at the zero-point energy level, n is the Bose-Einstein occupation number, T is the temperature, ω is the normal mode frequency, m is the reduced mass of the normal mode, $\hbar$ is the reduced Planck's constant, and k_B is Boltzmann's constant. The conductivity and mobility changes for each normal mode can be evaluated at the extrema of the uncertainty displacements at any finite temperature. In the limit where $n = 0$ the displacements are equivalent to quantum mechanical zero-point energy asymptote.

Bibliography

[1] Szabo, A.; Ostlund, N. *Modern Quantum Chemistry: Introduction to Advanced Electronic Structure Theory*; Dover Books on Chemistry; Dover Publications, 2012.

[2] Sherrill, C. D. An Introduction to Hartree-Fock Molecular Orbital Theory. 2000; `https://vergil.chemistry.gatech.edu/static/content/hf-intro.pdf`.

[3] Koopmans, T. *Physica* **1934**, *1*, 104–113.

[4] Kohn, W.; Sham, L. J. *Phys. Rev.* **1965**, *140*, A1133–A1138.

[5] Hohenberg, P.; Kohn, W. *Phys. Rev.* **1964**, *136*, B864–B871.

[6] Levy, M. *Proc. Natl. Acad. Sci. U.S.A.* **1979**, *76*, 6062–6065.

[7] Cramer, C. J. *Essentials of computational chemistry: theories and models*, 2nd ed.; Wiley: Chichester, West Sussex, England ; Hoboken, NJ, 2004.

[8] Yu, H. S.; Li, S. L.; Truhlar, D. G. *The Journal of Chemical Physics* **2016**, *145*, 130901.

[9] Teale, A. M. et al. *Physical Chemistry Chemical Physics* **2022**, *24*, 28700–28781.

[10] Perdew, J. P.; Burke, K.; Ernzerhof, M. *Phys. Rev. Lett.* **1997**, *78*, 1396–1396.

[11] Cremer, D. *Molecular Physics* **2001**, *99*, 1899–1940.

[12] Tao, J.; Perdew, J. P.; Staroverov, V. N.; Scuseria, G. E. *Physical Review Letters* **2003**, *91*, 146401.

[13] Tsuneda, T.; Hirao, K. **2014**, *4*, 375–390.

[14] Lin, Y.-S.; Li, G.-D.; Mao, S.-P.; Chai, J.-D. *Journal of Chemical Theory and Computation* **2013**, *9*, 263–272.

[15] Grimme, S.; Neese, F. *The Journal of Chemical Physics* **2007**, *127*, 154116.

[16] Grimme, S.; Antony, J.; Schwabe, T.; Mück-Lichtenfeld, C. *Org. Biomol. Chem.* **2007**, *5*, 741–758.

[17] Møller, C.; Plesset, M. S. *Phys. Rev.* **1934**, *46*, 618–622.

[18] Pople, J. A.; Binkley, J. S.; Seeger, R. *Int. J. Quantum Chem.* **2009**, *10*, 1–19.

[19] Pople, J. A.; Seeger, R.; Krishnan, R. *Int. J. Quantum Chem.* **2009**, *12*, 149–163.

[20] Head-Gordon, M.; Pople, J. A.; Frisch, M. J. *Chemical Physics Letters* **1988**, *153*, 503–506.

[21] Krishnan, R.; Pople, J. A. *Int J of Quantum Chemistry* **1978**, *14*, 91–100.

[22] Leininger, M. L.; Allen, W. D.; Schaefer, H. F.; Sherrill, C. D. *The Journal of Chemical Physics* **2000**, *112*, 9213–9222.

[23] Ross, I. G. *Trans. Faraday Soc.* **1952**, *48*, 973.

[24] Shavitt, I. *Molecular Physics* **1998**, *94*, 3–17.

[25] Čížek, J. *The Journal of Chemical Physics* **1966**, *45*, 4256–4266.

[26] Sinanoğlu, O. *The Journal of Chemical Physics* **1962**, *36*, 706–717.

[27] Monkhorst, H. J. *Int. J. Quantum Chem.* **2009**, *12*, 421–432.

[28] Purvis, G. D.; Bartlett, R. J. *The Journal of Chemical Physics* **1982**, *76*, 1910–1918.

[29] Bartlett, R. J.; Musiał, M. *Rev. Mod. Phys.* **2007**, *79*, 291–352.

[30] Dutta, A.; Sherrill, C. D. *The Journal of Chemical Physics* **2003**, *118*, 1610–1619.

[31] Hegarty, D.; Robb, M. A. *Molecular Physics* **1979**, *38*, 1795–1812.

[32] Eade, R. H.; Robb, M. A. *Chemical Physics Letters* **1981**, *83*, 362–368.

[33] Siegbahn, P. E. *Chemical Physics Letters* **1984**, *109*, 417–423.

[34] Klene, M.; Robb, M. A.; Frisch, M. J.; Celani, P. *The Journal of Chemical Physics* **2000**, *113*, 5653–5665.

[35] Olsen, J.; Roos, B. O.; Jo/rgensen, P.; Jensen, H. J. A. *The Journal of Chemical Physics* **1988**, *89*, 2185–2192.

[36] Klene, M.; Robb, M. A.; Blancafort, L.; Frisch, M. J. *The Journal of Chemical Physics* **2003**, *119*, 713–728.

[37] Andersson, K.; Malmqvist, P. A.; Roos, B. O.; Sadlej, A. J.; Wolinski, K. *J. Phys. Chem.* **1990**, *94*, 5483–5488.

[38] Andersson, K.; Roos, B. O. *Int J of Quantum Chemistry* **1993**, *45*, 591–607.

[39] Lischka, H.; Nachtigallová, D.; Aquino, A. J.; Szalay, P. G.; Plasser, F.; MacHado, F. B.; Barbatti, M. *Chemical Reviews* **2018**, *118*, 7293–7361.

[40] Chen, Z.; Zhang, D.; Jin, Y.; Yang, Y.; Su, N. Q.; Yang, W. *The Journal of Physical Chemistry Letters* **2017**, *8*, 4479–4485.

[41] Marian, C. M.; Heil, A.; Kleinschmidt, M. *WIREs Computational Molecular Science* **2019**, *9*, e1394.

[42] Grimme, S. *The Journal of Chemical Physics* **2003**, *118*, 9095–9102.

[43] Grimme, S.; Goerigk, L.; Fink, R. F. *WIREs Computational Molecular Science* **2012**, *2*, 886–906.

[44] Jung, Y.; Lochan, R. C.; Dutoi, A. D.; Head-Gordon, M. *The Journal of Chemical Physics* **2004**, *121*, 9793–9802.

[45] Phillipson, P.; Mulliken, R. *The Journal of Chemical Physics* **1958**, *28*, 1248–1249.

[46] Basch, H.; McKoy, V. *The Journal of Chemical Physics* **1970**, *53*, 1628–1637.

[47] Bagus, P.; Bennett, B. *International Journal of Quantum Chemistry* **1975**, *9*, 143–148.

[48] Shea, J. A. R.; Neuscamman, E. *The Journal of Chemical Physics* **2018**, *149*, 081101.

[49] Ye, H.-Z.; Van Voorhis, T. *Journal of Chemical Theory and Computation* **2019**, *15*, 2954–2965.

[50] Hait, D.; Head-Gordon, M. *Journal of Chemical Theory and Computation* **2020**, *16*, 1699–1710.

[51] Gilbert, A. T. B.; Besley, N. A.; Gill, P. M. W. *The Journal of Physical Chemistry A* **2008**, *112*, 13164–13171.

[52] Yamaguchi, K.; Jensen, F.; Dorigo, A.; Houk, K. *Chemical Physics Letters* **1988**, *149*, 537–542.

[53] Kowalczyk, T.; Tsuchimochi, T.; Chen, P.-T.; Top, L.; Van Voorhis, T. *The Journal of Chemical Physics* **2013**, *138*, 164101.

[54] Besley, N. A.; Asmuruf, F. A. *Physical Chemistry Chemical Physics* **2010**, *12*, 12024–12039.

[55] Hait, D.; Head-Gordon, M. *The Journal of Physical Chemistry Letters* **2021**, *12*, 4517–4529.

[56] Cederbaum, L. S. *Physical Review A* **1987**, *35*, 622–631.

[57] Coriani, S.; Koch, H. *Journal of Chemical Physics* **2015**, *143*.

[58] Vidal, M. L.; Feng, X.; Epifanovsky, E.; Krylov, A. I.; Coriani, S. *Journal of Chemical Theory and Computation* **2019**, *15*, 3117–3133.

[59] Mester, D.; Kállay, M. *Journal of Chemical Theory and Computation* **2023**, *19*, 1310–1321.

[60] Dreuw, A.; Head-Gordon, M. *Chemical Reviews* **2005**, *105*, 4009–4037.

[61] Casida, M. E. *Recent Advances in Computational Chemistry*; WORLD SCIENTIFIC, 1995; Vol. 1; pp 155–192.

[62] Casida, M. E. *Journal of Molecular Structure: THEOCHEM* **2009**, *914*, 3–18.

[63] Casida, M.; Huix-Rotllant, M. *Annu. Rev. Phys. Chem.* **2012**, *63*, 287–323.

[64] Hättig, C. *Advances in Quantum Chemistry* **2005**, *50*, 37–60.

[65] Head-Gordon, M.; Rico, R. J.; Oumi, M.; Lee, T. J. *Chemical Physics Letters* **1994**, *219*, 21–29.

[66] Runge, E.; Gross, E. K. U. *Phys. Rev. Lett.* **1984**, *52*, 997–1000.

[67] Ekardt, W. *Phys. Rev. B* **1985**, *31*, 6360–6370.

[68] Petersilka, M.; Gossmann, U. J.; Gross, E. K. U. *Phys. Rev. Lett.* **1996**, *76*, 1212–1215.

[69] Ullrich, C. *Time-Dependent Density-Functional Theory: Concepts and Applications*; Oxford Graduate Texts; OUP Oxford, 2011.

[70] Lacombe, L.; Maitra, N. T. *npj Computational Materials* **2023**, *9*, 124.

[71] Loos, P.-F.; Scemama, A.; Boggio-Pasqua, M.; Jacquemin, D. *Journal of Chemical Theory and Computation* **2020**, *16*, 3720–3736.

[72] Loos, P.-F.; Jacquemin, D. *The Journal of Physical Chemistry A* **2021**, *125*, 10174–10188.

[73] Mester, D.; Kállay, M. *Journal of Chemical Theory and Computation* **2022**, *18*, 1646–1662.

[74] Kozma, B.; Tajti, A.; Demoulin, B.; Izsák, R.; Nooijen, M.; Szalay, P. G. *Journal of Chemical Theory and Computation* **2020**, *16*, 4213–4225.

[75] Van Dijk, J.; Casanova-Páez, M.; Goerigk, L. *ACS Physical Chemistry Au* **2022**, *2*, 407–416.

[76] Tureček, F. *The Journal of Physical Chemistry A* **2015**, *119*, 10101–10111.

[77] Peach, M. J. G.; Williamson, M. J.; Tozer, D. J. *Journal of Chemical Theory and Computation* **2011**, *7*, 3578–3585.

[78] Frisch, M. J. et al. **2016**, Gaussian 16, Gaussian, Inc., Wallingford CT.

[79] Sun, J.; Remsing, R. C.; Zhang, Y.; Sun, Z.; Ruzsinszky, A.; Peng, H.; Yang, Z.; Paul, A.; Waghmare, U.; Wu, X.; Klein, M. L.; Perdew, J. P. *Nature Chem* **2016**, *8*, 831–836.

[80] Brémond, ; Pérez-Jiménez, J.; Sancho-García, J. C.; Adamo, C. *The Journal of Chemical Physics* **2019**, *150*, 201102.

[81] Furness, J. W.; Kaplan, A. D.; Ning, J.; Perdew, J. P.; Sun, J. *J. Phys. Chem. Lett.* **2020**, *11*, 8208–8215.

[82] Mester, D.; Kállay, M. *J. Chem. Theory Comput.* **2021**, *17*, 927–942.

[83] Casanova-Páez, M.; Goerigk, L. *J. Chem. Theory Comput.* **2021**, *17*, 5165–5186.

[84] Schwabe, T.; Goerigk, L. *Journal of Chemical Theory and Computation* **2017**, *13*, 4307–4323.

[85] Mester, D.; Kállay, M. *Journal of Chemical Theory and Computation* **2021**, *17*, 4211–4224.

[86] Casanova-Páez, M.; Dardis, M. B.; Goerigk, L. *Journal of Chemical Theory and Computation* **2019**, *15*, 4735–4744.

[87] Parker, S. M.; Rappoport, D.; Furche, F. *Journal of Chemical Theory and Computation* **2018**, *14*, 807–819.

[88] Hirata, S.; Head-Gordon, M. *Chemical Physics Letters* **1999**, *314*, 291–299.

[89] Kalai, C.; Toulouse, J. *The Journal of Chemical Physics* **2018**, *148*, 164105.

[90] Shao, Y.; Head-Gordon, M.; Krylov, A. I. *The Journal of Chemical Physics* **2003**, *118*, 4807–4818.

[91] Zhang, X.; Herbert, J. M. *The Journal of Chemical Physics* **2015**, *143*, 234107.

[92] Casanova, D.; Krylov, A. I. *Physical Chemistry Chemical Physics* **2020**, *22*, 4326–4342.

[93] Cordova, F.; Doriol, L. J.; Ipatov, A.; Casida, M. E.; Filippi, C.; Vela, A. *Journal of Chemical Physics* **2007**, *127*.

[94] Horbatenko, Y.; Sadiq, S.; Lee, S.; Filatov, M.; Choi, C. H. *Journal of Chemical Theory and Computation* **2021**, *17*, 848–859.

[95] Li, X.; Govind, N.; Isborn, C.; DePrince, A. E.; Lopata, K. *Chemical Reviews* **2020**, *120*, 9951–9993.

[96] Geertsen, J.; Rittby, M.; Bartlett, R. J. *Chemical Physics Letters* **1989**, *164*, 57–62.

[97] Sekino, H.; Bartlett, R. J. *Int. J. Quantum Chem.* **1984**, *26*, 255–265.

[98] Stanton, J. F.; Bartlett, R. J. *The Journal of Chemical Physics* **1993**, *98*, 7029–7039.

[99] Damour, Y.; Scemama, A.; Jacquemin, D.; Kossoski, F.; Loos, P.-F. *Journal of Chemical Theory and Computation* **2024**, *20*, 4129–4145.

[100] Bartlett, R. J. *WIREs Computational Molecular Science* **2012**, *2*, 126–138.

[101] Sarkar, R.; Boggio-Pasqua, M.; Loos, P.-F.; Jacquemin, D. *Journal of Chemical Theory and Computation* **2021**, *17*, 1117–1132.

[102] Nooijen, M.; Bartlett, R. J. *The Journal of Chemical Physics* **1997**, *106*, 6441–6448.

[103] Berraud-Pache, R.; Neese, F.; Bistoni, G.; Izsák, R. *Journal of Chemical Theory and Computation* **2020**, *16*, 564–575.

[104] Christiansen, O.; Koch, H.; Jørgensen, P. *Chemical Physics Letters* **1995**, *243*, 409–418.

[105] Tajti, A.; Kozma, B.; Szalay, P. G. *Journal of Chemical Theory and Computation* **2021**, *17*, 439–449.

[106] Loos, P.-F.; Comin, M.; Blase, X.; Jacquemin, D. *Journal of Chemical Theory and Computation* **2021**, *17*, 3666–3686.

[107] Watts, J. D. In *Radiation Induced Molecular Phenomena in Nucleic Acids*; Leszczynski, J., Shukla, M. K., Leszczynski, J., Eds.; Springer Netherlands: Dordrecht, 2008; Vol. 5; pp 65–92, Series Title: Challenges and Advances In Computational Chemistry and Physics.

[108] Kánnár, D.; Szalay, P. G. *J. Chem. Theory Comput.* **2014**, *10*, 3757–3765.

[109] Christiansen, O.; Koch, H.; Jo/rgensen, P. *The Journal of Chemical Physics* **1996**, *105*, 1451–1459.

[110] Schirmer, J. *Phys. Rev. A* **1982**, *26*, 2395–2416.

[111] Von Niessen, W.; Schirmer, J.; Cederbaum, L. *Computer Physics Reports* **1984**, *1*, 57–125.

[112] Dreuw, A.; Wormit, M. *WIREs Comput Mol Sci* **2015**, *5*, 82–95.

[113] Dreuw, A.; Papapostolou, A.; Dempwolff, A. L. *J. Phys. Chem. A* **2023**, *127*, 6635–6646.

[114] Starcke, J. H.; Wormit, M.; Schirmer, J.; Dreuw, A. *Chemical Physics* **2006**, *329*, 39–49, Electron Correlation and Multimode Dynamics in Molecules.

[115] Schirmer, J. *Phys. Rev. A* **1991**, *43*, 4647–4659.

[116] Mertins, F.; Schirmer, J. *Phys. Rev. A* **1996**, *53*, 2140–2152.

[117] Mertins, F.; Schirmer, J.; Tarantelli, A. *Phys. Rev. A* **1996**, *53*, 2153–2168.

[118] Shaalan Alag, A.; Jelenfi, D. P.; Tajti, A.; Szalay, P. G. *Journal of Chemical Theory and Computation* **2022**, *18*, 6794–6801.

[119] Goerigk, L.; Hansen, A.; Bauer, C.; Ehrlich, S.; Najibi, A.; Grimme, S. *Phys. Chem. Chem. Phys.* **2017**, *19*, 32184–32215.

[120] Schreiber, M.; Silva-Junior, M. R.; Sauer, S.; Thiel, W. *The Journal of chemical physics* **2008**, *128*.

[121] Liang, J.; Feng, X.; Hait, D.; Head-Gordon, M. *Journal of Chemical Theory and Computation* **2022**, *18*, 3460–3473.

[122] Leang, S. S.; Zahariev, F.; Gordon, M. S. *The Journal of Chemical Physics* **2012**, *136*, 104101.

[123] Fransson, T.; Brumboiu, I. E.; Vidal, M. L.; Norman, P.; Coriani, S.; Dreuw, A. *Journal of Chemical Theory and Computation* **2021**, *17*, 1618–1637.

[124] Silva-Junior, M. R.; Schreiber, M.; Sauer, S. P. A.; Thiel, W. *The Journal of Chemical Physics* **2010**, *133*, 174318.

[125] Dallos, M.; Lischka, H. *Theoretical Chemistry Accounts: Theory, Computation, and Modeling (Theoretica Chimica Acta)* **2004**, *112*, 16–26.

[126] Caricato, M.; Trucks, G. W.; Frisch, M. J. *The Journal of Chemical Physics* **2009**, *131*, 174104.

[127] Silva-Junior, M. R.; Schreiber, M.; Sauer, S.; Thiel, W. *The Journal of chemical physics* **2010**, *133*.

[128] Silva-Junior, M. R.; Sauer, S. P.; Schreiber, M.; Thiel, W. *Molecular Physics* **2010**, *108*, 453–465.

[129] Kannar, D.; Tajti, A.; Szalay, P. G. *Journal of Chemical Theory and Computation* **2017**, *13*, 202–209.

[130] Reisler, H.; Krylov, A. I. *International Reviews in Physical Chemistry* **2009**, *28*, 267–308.

[131] Loos, P.-F.; Jacquemin, D. *ChemPhotoChem* **2019**, *3*, 684–696.

[132] Mewes, S. A.; Plasser, F.; Krylov, A.; Dreuw, A. *Journal of Chemical Theory and Computation* **2018**, *14*, 710–725.

[133] Izsák, R. *Wiley Interdisciplinary Reviews: Computational Molecular Science* **2020**, *10*, e1445.

[134] Sarkar, R.; Loos, P.-F.; Boggio-Pasqua, M.; Jacquemin, D. *Journal of Chemical Theory and Computation* **2022**, *18*, 2418–2436, PMID: 35333060.

[135] Véril, M.; Scemama, A.; Caffarel, M.; Lipparini, F.; Boggio-Pasqua, M.; Jacquemin, D.; Loos, P.-F. *Wiley Interdisciplinary Reviews: Computational Molecular Science* **2021**, *11*, e1517.

[136] Loos, P.-F.; Scemama, A.; Jacquemin, D. *The Journal of Physical Chemistry Letters* **2020**, *11*, 2374–2383.

[137] Li, J.; Yu, J.; Chen, Z.; Yang, W. *The Journal of Physical Chemistry A* **2023**, *127*, 7811–7822.

[138] Antony, J.; Grimme, S. *Phys. Chem. Chem. Phys.* **2006**, *8*, 5287–5293.

[139] Martin, S. M.; Repa, G. M.; Hamburger, R. C.; Pointer, C. A.; Ward, K.; Pham, T. N.; Martin, M. I.; Rosenthal, J.; Fredin, L. A.; Young, E. R. *Physical Chemistry Chemical Physics* **2023**,

[140] Martin, S. M.; Oldacre, A. N.; Pointer, C. A.; Huang, T.; Repa, G. M.; Fredin, L. A.; Young, E. R. *Dalton Transactions* **2021**, *50*, 7265–7276.

[141] Wehrmann, C. M.; Imran, M.; Pointer, C.; Fredin, L. A.; Young, E. R.; Chen, M. S. *Chemical Science* **2020**, *11*, 10212–10219.

[142] Hamburger, R. C.; Huang, T.; Martin, S. M.; Pointer, C. A.; Fredin, L. A.; Young, E. R. *Physical Chemistry Chemical Physics* **2023**,

[143] Martin, S. M.; Knepp, Z. J.; Thongchai, I. A.; Englehart, K.; Sorto, K.; Jaffer, A.; Fredin, L. A.; Young, E. R. *New Journal of Chemistry* **2023**,

[144] Ninis, O.; El kharrim, A.; Agda, F.; Nebbach, D.; Kaya, S.; Abarkan, M.; Bouachrine, M. *Journal of Molecular Structure* **2023**, *1284*, 135332.

[145] Mizera, A.; Dubis, A. T.; Łapiński, A. *Polymer* **2022**, *255*, 125127.

[146] Knepp, Z. J.; Masso, G. B.; Fredin, L. A. *The Journal of Chemical Physics* **2023**, *158*, 064704.

[147] Spielvogel, E. H.; Stevenson, B. G.; Stringer, M. J.; Hu, Y.; Fredin, L. A.; Swierk, J. R. *Journal of Organic Chemistry* **2022**, *87*, 223–230.

[148] Stevenson, B. G.; Gironda, C.; Talbott, E.; Prascsak, A.; Burnett, N. L.; Kompanijec, V.; Nakhamiyayev, R.; Fredin, L. A.; Swierk, J. R. *The Journal of Organic Chemistry* **2023**,

[149] Stevenson, B. G.; Prascsak, A. V.; Lee, A. A.; Talbott, E. D.; Fredin, L. A.; Swierk, J. R. *Chemical Communications* **2023**,

[150] He, Q.; Yu, B.; Li, Z.; Zhao, Y. *ENERGY & ENVIRONMENTAL MATERIALS 2*, 264–279.

[151] Wu, X.; Kang, F.; Duan, W.; Li, J. *Progress in Natural Science: Materials International* **2019**, *29*, 247–255, Special Issue of Computational Materials.

[152] Alkhatib, Q.; Helal, W.; Afaneh, A. T. *New Journal of Chemistry* **2022**, *46*, 7682–7694.

[153] Hancock, A. C.; Goerigk, L. *RSC Advances* **2023**, *13*, 35964–35984.

[154] Helal, W. *The Journal of Physical Chemistry A* **2022**, *127*, 131–141.

[155] Casanova-Páez, M.; Goerigk, L. *The Journal of Chemical Physics* **2020**, *153*, 064106.

[156] Goerigk, L.; Grimme, S. *Journal of Chemical Physics* **2010**, *132*.

[157] Laurent, A. D.; Jacquemin, D. *International Journal of Quantum Chemistry* **2013**, *113*, 2019–2039.

[158] Postils, V.; Ruiperez, F.; Casanova, D. *Journal of Chemical Theory and Computation* **2021**, *17*, 5825–5838.

[159] Yanai, T.; Tew, D. P.; Handy, N. C. *Chemical Physics Letters* **2004**, *393*, 51–57.

[160] Fehér, P. P.; Madarász, Á.; Stirling, A. *Chemistry-Methods* **2023**, *3*, e202200069.

[161] Shao, Y.; Mei, Y.; Sundholm, D.; Kaila, V. R. *Journal of chemical theory and computation* **2019**, *16*, 587–600.

[162] Jacquemin, D. *Journal of Chemical Theory and Computation* **2016**, *12*, 3993–4003.

[163] Goerigk, L.; Grimme, S. *Journal of Chemical Theory and Computation* **2011**, *7*, 3272–3277.

[164] Martin, J. M.; Santra, G. *Israel Journal of Chemistry* **2020**, *60*, 787–804.

[165] Chan, B.; Radom, L. *Journal of Chemical Theory and Computation* **2011**, *7*, 2852–2863.

[166] Wang, J.; Durbeej, B. *Journal of Computational Chemistry* **2020**, *41*, 1718–1729.

[167] Bremond, E.; Savarese, M.; Adamo, C.; Jacquemin, D. *Journal of chemical theory and computation* **2018**, *14*, 3715–3727.

[168] Kruse, H.; Grimme, S. *The Journal of Chemical Physics* **2012**, *136*, 154101.

[169] Kaur, J.; Ospadov, E.; Staroverov, V. N. *Journal of Chemical Theory and Computation* **2019**, *15*, 4956–4964, PMID: 31386366.

[170] Friede, M.; Ehlert, S.; Grimme, S.; Mewes, J.-M. *Journal of Chemical Theory and Computation* **2023**, *19*, 8097–8107.

[171] Kozma, B.; Berraud-Pache, R.; Tajti, A.; Szalay, P. G. *Molecular Physics* **2020**, *118*, e1776903.

[172] Grimme, S.; Parac, M. *ChemPhysChem* **2003**, *4*, 292–295.

[173] Parac, M.; Grimme, S. *Chemical Physics* **2003**, *292*, 11–21.

[174] Guido, C. A.; Cortona, P.; Mennucci, B.; Adamo, C. *Journal of Chemical Theory and Computation* **2013**, *9*, 3118–3126.

[175] Le Bahers, T.; Adamo, C.; Ciofini, I. *Journal of Chemical Theory and Computation* **2011**, *7*, 2498–2506.

[176] Hennefarth, M. R.; Hermes, M. R.; Truhlar, D. G.; Gagliardi, L. *Journal of Chemical Theory and Computation* **2023**, *19*, 3172–3183.

[177] Staroverov, V. N.; Davidson, E. R. *Chemical Physics Letters* **2000**, *330*, 161–168.

[178] Herbert, J. M.; Mandai, A. *Time-Dependent Density Functional Theory*, 1st ed.; Jenny Stanford Publishing: New York, 2022; pp 361–404.

[179] Li, Z.; Liu, W. *Journal of Chemical Theory and Computation* **2016**, *12*, 2517–2527.

[180] Li, Z.; Liu, W. *Journal of Chemical Theory and Computation* **2016**, *12*, 238–260.

[181] Yang, C.-H.; Hsu, C.-P. *The Journal of Chemical Physics* **2006**, *124*, 244507.

[182] Widmark, P.-O. *European Summerschool in Quantum Chemistry*; University of Lund, 2009.

[183] Izsák, R.; Ivanov, A. V.; Blunt, N. S.; Holzmann, N.; Neese, F. *J. Chem. Theory Comput.* **2023**, *19*, 2703–2720.

[184] Neogrády, P.; Urban, M. *International Journal of Quantum Chemistry* **1995**, *55*, 187–203.

[185] JR., R. A. D.; Head-Gordon, M. *Molecular Physics* **2007**, *105*, 1073–1083.

[186] Lochan, R. C.; Jung, Y.; Head-Gordon, M. *The Journal of Physical Chemistry A* **2005**, *109*, 7598–7605.

[187] Lawson Daku, L. M.; Aquilante, F.; Robinson, T. W.; Hauser, A. *Journal of Chemical Theory and Computation* **2012**, *8*, 4216–4231.

[188] Feldt, M.; Phung, Q. M. *European Journal of Inorganic Chemistry* **2022**, *2022*, e202200014.

[189] Schmidt, M. W.; Gordon, M. S. *Annual Review of Physical Chemistry* **1998**, *49*, 233–266.

[190] Veryazov, V.; Malmqvist, P. ; Roos, B. O. *International Journal of Quantum Chemistry* **2011**, *111*, 3329–3338.

[191] Stein, C. J.; Reiher, M. *Journal of Chemical Theory and Computation* **2016**, *12*, 1760–1771.

[192] Freitag, L.; Knecht, S.; Keller, S. F.; Delcey, M. G.; Aquilante, F.; Bondo Pedersen, T.; Lindh, R.; Reiher, M.; González, L. *Physical Chemistry Chemical Physics* **2015**, *17*, 14383–14392.

[193] Bokareva, O. S.; Baig, O.; Al-Marri, M. J.; Kühn, O.; González, L. *Physical Chemistry Chemical Physics* **2020**, *22*, 27605–27616.

[194] Drosou, M.; Mitsopoulou, C. A.; Pantazis, D. A. *Journal of Chemical Theory and Computation* **2022**, *18*, 3538–3548.

[195] Villaume, S.; Strich, A.; Daniel, C.; Perera, S. A.; Bartlett, R. J. *Physical Chemistry Chemical Physics* **2007**, *9*, 6115.

[196] Weaver, M. N.; Yang, Y.; Merz, K. M. *The Journal of Physical Chemistry A* **2009**, *113*, 10081–10088.

[197] Pierloot, K. *Molecular Physics* **2003**, *101*, 2083–2094.

[198] Pierloot, K.; Vancoillie, S. *The Journal of Chemical Physics* **2006**, *125*, 124303.

[199] Ashley, D. C.; Jakubikova, E. *Coordination Chemistry Reviews* **2017**, *337*, 97–111.

[200] Escudero, D.; González, L. *Journal of Chemical Theory and Computation* **2012**, *8*, 203–213.

[201] Malmqvist, P. ; Pierloot, K.; Shahi, A. R. M.; Cramer, C. J.; Gagliardi, L. *The Journal of Chemical Physics* **2008**, *128*, 204109.

[202] Phung, Q. M.; Wouters, S.; Pierloot, K. *Journal of Chemical Theory and Computation* **2016**, *12*, 4352–4361.

[203] Marti, K. H.; Ondík, I. M.; Moritz, G.; Reiher, M. *The Journal of Chemical Physics* **2008**, *128*, 014104.

[204] Sang, S.; Unruh, T.; Demeshko, S.; Domenianni, L. I.; Van Leest, N. P.; Marquetand, P.; Schneck, F.; Würtele, C.; De Zwart, F. J.; De Bruin, B.; González, L.; Vöhringer, P.; Schneider, S. *Chemistry – A European Journal* **2021**, *27*, 16978–16989.

[205] Van Leest, N. P.; De Bruin, B. *Inorganic Chemistry* **2021**, *60*, 8380–8387.

[206] Neese, F. *Coordination Chemistry Reviews* **2009**, *253*, 526–563.

[207] Harvey, J. N. *Annual Reports Section "C" (Physical Chemistry)* **2006**, *102*, 203.

[208] Sen, A.; Ghosh, S. *The Journal of Physical Chemistry C* **2024**, *0*, null.

[209] Harvey, J. N. *Principles and Applications of Density Functional Theory in Inorganic Chemistry I*; Springer Berlin Heidelberg: Berlin, Heidelberg, 2004; Vol. 112; pp 151–184, Series Title: Structure and Bonding.

[210] Bowman, D. N.; Jakubikova, E. *Inorganic Chemistry* **2012**, *51*, 6011–6019.

[211] Mai, S.; Plasser, F.; Dorn, J.; Fumanal, M.; Daniel, C.; González, L. *Coordination Chemistry Reviews* **2018**, *361*, 74–97.

[212] Piteša, T.; Polonius, S.; González, L.; Mai, S. *Journal of Chemical Theory and Computation* **2024**,

[213] Sirohiwal, A.; Berraud-Pache, R.; Neese, F.; Izsák, R.; Pantazis, D. A. *The Journal of Physical Chemistry B* **2020**, *124*, 8761–8771.

[214] Alkhatib, Q.; Helal, W.; Marashdeh, A. *RSC Advances* **2022**, *12*, 1704–1717.

[215] Hernández-Castillo, D.; Eder, I.; González, L. *Coordination Chemistry Reviews* **2024**, *510*, 215819.

[216] Latouche, C.; Skouteris, D.; Palazzetti, F.; Barone, V. *Journal of Chemical Theory and Computation* **2015**, *11*, 3281–3289.

[217] Arroyo, I. J.; Hu, R.; Merino, G.; Tang, B. Z.; Peña-Cabrera, E. *The Journal of Organic Chemistry* **2009**, *74*, 5719–5722.

[218] Knysh, I.; Lipparini, F.; Blondel, A.; Duchemin, I.; Blase, X.; Loos, P.-F.; Jacquemin, D. *Journal of Chemical Theory and Computation* **2024**, *20*, 8152–8174.

[219] Momeni, M. R.; Brown, A. *Journal of Chemical Theory and Computation* **2015**, *11*, 2619–2632.

[220] Feldt, M.; Brown, A. *Journal of Computational Chemistry* **2021**, *42*, 144–155.

[221] Sandoval, J. S.; McCamant, D. W. *The Journal of Physical Chemistry A* **2023**, *127*, 8238–8251.

[222] Chibani, S.; Le Guennic, B.; Charaf-Eddin, A.; Laurent, A. D.; Jacquemin, D. *Chemical Science* **2013**, *4*, 1950.

[223] Helal, W.; Alkhatib, Q.; Gharaibeh, M. *Computational and Theoretical Chemistry* **2022**, *1207*, 113531.

[224] Le Guennic, B.; Jacquemin, D. *Accounts of Chemical Research* **2015**, *48*, 530–537.

[225] Subotnik, J. E.; Jain, A.; Landry, B.; Petit, A.; Ouyang, W.; Bellonzi, N. *Annual Review of Physical Chemistry* **2016**, *67*, 387–417.

[226] Ben-Nun, M.; Quenneville, J.; Martínez, T. J. *The Journal of Physical Chemistry A* **2000**, *104*, 5161–5175.

[227] Zhao, R.; You, P.; Meng, S. *Physical Review Letters* **2023**, *130*, 166401.

[228] Abedi, A.; Maitra, N. T.; Gross, E. K. U. *Physical Review Letters* **2010**, *105*, 123002.

[229] Curchod, B. F. E.; Martínez, T. J. *Chemical Reviews* **2018**, *118*, 3305–3336.

[230] Nelson, T. R.; White, A. J.; Bjorgaard, J. A.; Sifain, A. E.; Zhang, Y.; Nebgen, B.; Fernandez-Alberti, S.; Mozyrsky, D.; Roitberg, A. E.; Tretiak, S. *Chemical Reviews* **2020**, *120*, 2215–2287.

[231] Hammes-Schiffer, S. *The Journal of Chemical Physics* **2021**, *155*, 030901.

[232] Li, J.; Reiser, P.; Boswell, B. R.; Eberhard, A.; Burns, N. Z.; Friederich, P.; Lopez, S. A. *Chemical Science* **2021**, *12*, 5302–5314.

[233] Bandara, H. M.; Burdette, S. C. *Chemical Society Reviews* **2012**, *41*, 1809–1825.

[234] Benkhaya, S.; M'rabet, S.; El Harfi, A. *Heliyon* **2020**, *6*, e03271.

[235] Alsantali, R. I.; Raja, Q. A.; Alzahrani, A. Y.; Sadiq, A.; Naeem, N.; Mughal, E. U.; Al-Rooqi, M. M.; El Guesmi, N.; Moussa, Z.; Ahmed, S. A. *Dyes and Pigments* **2022**, *199*, 110050.

[236] Asano, T.; Okada, T. *The Journal of Organic Chemistry* **1984**, *49*, 4387–4391.

[237] Martin, S. M.; Knepp, Z. J.; Thongchai, I. A.; Englehart, K.; Sorto, K.; Jaffer, A.; Fredin, L. A.; Young, E. R. *New Journal of Chemistry* **2023**, *47*, 11882–11889.

[238] Thongchai, I.-A.; Knepp, Z. J.; Fertal, D. R.; Flynn, H.; Young, E. R.; Fredin, L. A. *The Journal of Physical Chemistry A* **2024**, *128*, 785–791.

[239] Martin, S. M.; Hamburger, R. C.; Huang, T.; Fredin, L. A.; Young, E. R. *Physical Chemistry Chemical Physics* **2024**, *26*, 10804–10813.

[240] Lentes, P.; Fruhwirt, P.; Freimuth, H.; Moormann, W.; Kruse, F.; Gescheidt, G.; Herges, R. *Journal of Organic Chemistry* **2021**, *86*, 4355–4360.

[241] Sekkat, Z.; Wood, J.; Knoll, W. **1995**, 17226–17234.

[242] Wachtveitl, J.; Nägele, T.; Puell, B.; Zinth, W.; Krüger, M.; Rudolph-Böhner, S.; Oesterhelt, D.; Moroder, L. *Journal of Photochemistry and Photobiology A: Chemistry* **1997**, *105*, 283–288.

[243] Cembran, A.; Bernardi, F.; Garavelli, M.; Gagliardi, L.; Orlandi, G. *Journal of the American Chemical Society* **2004**, *126*, 3234–3243.

[244] Crespi, S.; Simeth, N. A.; König, B. *Nature Reviews Chemistry* **2019**, *3*, 133–146.

[245] Aleotti, F.; Nenov, A.; Salvigni, L.; Bonfanti, M.; El-Tahawy, M. M.; Giunchi, A.; Gentile, M.; Spallacci, C.; Ventimiglia, A.; Cirillo, G.; Montali, L.; Scurti, S.; Garavelli, M.; Conti, I. *Journal of Physical Chemistry A* **2020**, *124*, 9513–9523.

[246] Calbo, J.; Weston, C. E.; White, A. J.; Rzepa, H. S.; Contreras-García, J.; Fuchter, M. J. *Journal of the American Chemical Society* **2017**, *139*, 1261–1274.

[247] Velema, W. A.; Szymanski, W.; Feringa, B. L. *Journal of the American Chemical Society* **2014**, *136*, 2178–2191.

[248] Broichhagen, J.; Frank, J. A.; Trauner, D. *Accounts of Chemical Research* **2015**, *48*, 1947–1960.

[249] Lerch, M. M.; Hansen, M. J.; van Dam, G. M.; Szymanski, W.; Feringa, B. L. *Angewandte Chemie - International Edition* **2016**, *55*, 10978–10999.

[250] Hüll, K.; Morstein, J.; Trauner, D. *Chemical Reviews* **2018**, *118*, 10710–10747.

[251] Fuchter, M. J. *Journal of Medicinal Chemistry* **2020**, *63*, 11436–11447.

[252] Yang, Y.; Huang, S.; Ma, Y.; Yi, J.; Jiang, Y.; Chang, X.; Li, Q. *ACS Applied Materials and Interfaces* **2022**, *14*, 35623–35634.

[253] Zhang, B.; Feng, Y.; Feng, W. *Nano-Micro Letters*; Springer Nature Singapore, 2022; Vol. 14; pp 1–37.

[254] Kwaria, D.; McGehee, K.; Liu, S.; Kikkawa, Y.; Ito, S.; Norikane, Y. *ACS Applied Optical Materials* **2023**, *1*, 633–639.

[255] Gelebart, A. H.; Jan Mulder, D.; Varga, M.; Konya, A.; Vantomme, G.; Meijer, E. W.; Selinger, R. L. B.; Broer, D. J. *Nature* **2017**, *546*, 632–636.

[256] Ren, H.; Qiu, X.-P.; Shi, Y.; Yang, P.; Winnik, F. M. *Macromolecules* **2019**, *52*, 2939–2948.

[257] Ren, H.; Yang, P.; Yu, H. *Molecules* **2022**, *27*, 3977.

[258] Mukherjee, A.; Seyfried, M. D.; Ravoo, B. J. *Angew Chem Int Ed* **2023**, *62*, e202304437.

[259] Garcia-Amorós, J.; Díaz-Lobo, M.; Nonell, S.; Velasco, D. *Angew Chem Int Ed* **2012**, *51*, 12820–12823.

[260] Lednev, I. K.; Ye, T.-q.; Hester, R. E.; Moore, J. N. **1996**, *3654*, 13338–13341.

[261] Chang, C. W.; Lu, Y. C.; Wang, T. T.; Diau, E. W. G. *Journal of the American Chemical Society* **2004**, *126*, 10109–10118.

[262] Ciminelli, C.; Granucci, G.; Persico, M. *Chemistry - A European Journal* **2004**, *10*, 2327–2341.

[263] Crecca, C. R.; Roitberg, A. E. *Journal of Physical Chemistry A* **2006**, *110*, 8188–8203.

[264] Conti, I.; Garavelli, M.; Orlandi, G. *Journal of the American Chemical Society* **2008**, *130*, 5216–5230.

[265] Böckmann, M.; Doltsinis, N. L.; Marx, D. *Journal of Physical Chemistry A* **2010**, *114*, 745–754.

[266] Pederzoli, M.; Pittner, J.; Barbatti, M.; Lischka, H. *Journal of Physical Chemistry A* **2011**, *115*, 11136–11143.

[267] Quick, M.; Dobryakov, A. L.; Gerecke, M.; Richter, C.; Berndt, F.; Ioffe, I. N.; Granovsky, A. A.; Mahrwald, R.; Ernsting, N. P.; Kovalenko, S. A. *Journal of Physical Chemistry B* **2014**, *118*, 8756–8771.

[268] Tan, E. M.; Amirjalayer, S.; Smolarek, S.; Vdovin, A.; Zerbetto, F.; Buma, W. J. *Nature Communications* **2015**, *6*, 5860.

[269] Reimann, M.; Teichmann, E.; Hecht, S.; Kaupp, M. *Journal of Physical Chemistry Letters* **2022**, *13*, 10882–10888.

[270] Hamburger, R.; Rumble, C.; Young, E. R. *JoVE* **2024**, e65519.

[271] Hamburger, R. C.; Huang, T.; Martin, S. M.; Pointer, C. A.; Fredin, L. A.; Young, E. R. *Physical Chemistry Chemical Physics* **2023**, 15302–15313.

[272] Maurer, R. J.; Reuter, K. *The Journal of Chemical Physics* **2011**, *135*, 224303.

[273] Siampiringue, N.; Guyot, G.; Monti, S.; Bortolus, P. *Journal of Photochemistry* **1987**, *37*, 185–188.

[274] Haynie, D. T. *Biological Thermodynamics*, 2nd ed.; Cambridge University Press, 2008.

[275] Ishikawa, T.; Noro, T.; Shoda, T. *Journal of Chemical Physics* **2001**, *115*, 7503–7512.

[276] Iriepa, C. G., Marazzi, M., Eds. *Theoretical and Computational Photochemistry: Fundamentals, Methods, Applications and Synergy with Experimental Approaches*; Elsevier: Amsterdam, Netherlands ; Cambridge, MA, United States, 2023; OCLC: on1356958776.

[277] Gross, E.; Kohn, W. *Advances in Quantum Chemistry*; Elsevier, 1990; Vol. 21; pp 255–291.

[278] Laurent, A. D.; Jacquemin, D. *Int. J. Quantum Chem* **2013**, *113*, 2019–2039.

[279] Huix-Rotllant, M.; Ferré, N.; Barbatti, M. In *Quantum Chemistry and Dynamics of Excited States*, 1st ed.; González, L., Lindh, R., Eds.; Wiley, 2020; pp 13–46.

[280] Garcia-Ratés, M.; Neese, F. *J Comput Chem* **2020**, *41*, 922–939.

[281] Marenich, A. V.; Cramer, C. J.; Truhlar, D. G. *J. Phys. Chem. B* **2009**, *113*, 6378–6396.

[282] Bursch, M.; Mewes, J.; Hansen, A.; Grimme, S. *Angew Chem Int Ed* **2022**, *61*, e202205735.

[283] Kucharski, S. A.; Włoch, M.; Musiał, M.; Bartlett, R. J. *The Journal of Chemical Physics* **2001**, *115*, 8263–8266.

[284] Maitra, N. T.; Zhang, F.; Cave, R. J.; Burke, K. *The Journal of Chemical Physics* **2004**, *120*, 5932–5937.

[285] Zhang, C.; Ye, C.; Yao, J.; Wu, L.-Z. *National Science Review* **2024**, *11*, nwae244.

[286] Wang, J.; Durbeej, B. *J Comput Chem* **2020**, *41*, 1718–1729.

[287] Sheng, X.; Zhu, H.; Yin, K.; Chen, J.; Wang, J.; Wang, C.; Shao, J.; Chen, F. *J. Phys. Chem. C* **2020**, *124*, 4693–4700.

[288] Zhu, H.; Wang, J.; Wang, F.; Feng, E.; Sheng, X. *Chemical Physics Letters* **2021**, *785*, 139150.

[289] Sałek, P.; Vahtras, O.; Helgaker, T.; Ågren, H. *The Journal of Chemical Physics* **2002**, *117*, 9630–9645.

[290] Andersson, K.; Malmqvist, P.-; Roos, B. O. *The Journal of Chemical Physics* **1992**, *96*, 1218–1226.

[291] Cronstrand, P.; Christiansen, O.; Norman, P.; Ågren, H. *Phys. Chem. Chem. Phys.* **2000**, *2*, 5357–5363.

[292] Cronstrand, P.; Christiansen, O.; Norman, P.; Ågren, H. *Phys. Chem. Chem. Phys.* **2001**, *3*, 2567–2575.

[293] Conti, I.; Cerullo, G.; Nenov, A.; Garavelli, M. *J. Am. Chem. Soc.* **2020**, *142*, 16117–16139.

[294] Kochman, M. A.; Durbeej, B.; Kubas, A. *J. Phys. Chem. A* **2021**, *125*, 8635–8648.

[295] Fischer, S. A.; Cramer, C. J.; Govind, N. *J. Chem. Theory Comput.* **2015**, *11*, 4294–4303.

[296] Mosquera, M. A.; Chen, L. X.; Ratner, M. A.; Schatz, G. C. *The Journal of Chemical Physics* **2016**, *144*, 204105.

[297] Mosquera, M. A.; Jackson, N. E.; Fauvell, T. J.; Kelley, M. S.; Chen, L. X.; Schatz, G. C.; Ratner, M. A. *J. Am. Chem. Soc.* **2017**, *139*, 3728–3735.

[298] Hamburger, R.; Rumble, C.; Young, E. R. *JoVE* **2024**, 65519.

[299] Woodhouse, J. et al. *Nat Commun* **2020**, *11*, 741.

[300] Sakizadeh, J. D.; Weiss, R.; Scholes, G. D.; Kudisch, B. *Annual Review of Physical Chemistry* **2025**,

[301] Neese, F. *WIREs Comput Mol Sci* **2022**, *12*, e1606.

[302] Adamo, C.; Barone, V. *The Journal of Chemical Physics* **1999**, *110*, 6158–6170.

[303] Iikura, H.; Tsuneda, T.; Yanai, T.; Hirao, K. *The Journal of Chemical Physics* **2001**, *115*, 3540–3544.

[304] Weigend, F.; Ahlrichs, R. *Phys. Chem. Chem. Phys.* **2005**, *7*, 3297.

[305] Caldeweyher, E.; Ehlert, S.; Hansen, A.; Neugebauer, H.; Spicher, S.; Bannwarth, C.; Grimme, S. *The Journal of Chemical Physics* **2019**, *150*, 154122.

[306] Yanai, T.; Tew, D. P.; Handy, N. C. *Chemical Physics Letters* **2004**, *393*, 51–57.

[307] Lu, T. *The Journal of Chemical Physics* **2024**, *161*, 082503.

[308] Szabo, A.; Ostlund, N. S. *Modern quantum chemistry: introduction to advanced electronic structure theory*; Dover Publications: Mineola, N.Y, 1996.

[309] Roos, B. O.; Taylor, P. R.; Sigbahn, P. E. *Chemical Physics* **1980**, *48*, 157–173.

[310] Corzo, H. H.; Abou Taka, A.; Pribram-Jones, A.; Hratchian, H. P. *J Comput Chem* **2022**, *43*, 382–390.

[311] Waller, M. P.; Robertazzi, A.; Platts, J. A.; Hibbs, D. E.; Williams, P. A. *J Comput Chem* **2006**, *27*, 491–504.

[312] Zheng, L.; Polizzi, N. F.; Dave, A. R.; Migliore, A.; Beratan, D. N. *J. Phys. Chem. A* **2016**, *120*, 1933–1943.

[313] Chang, C.-W.; Lu, Y.-C.; Wang, T.-T.; Diau, E. W.-G. *J. Am. Chem. Soc.* **2004**, *126*, 10109–10118.

[314] Casellas, J.; Bearpark, M. J.; Reguero, M. *ChemPhysChem* **2016**, *17*, 3068–3079.

[315] Taylor, J. T.; Tozer, D. J.; Curchod, B. F. E. *The Journal of Chemical Physics* **2023**, *159*, 214115.

[316] Lednev, I. K.; Ye, T.-Q.; Hester, R. E.; Moore, J. N. *J. Phys. Chem.* **1996**, *100*, 13338–13341.

[317] Bandara, H. M. D.; Burdette, S. C. *Chem. Soc. Rev.* **2012**, *41*, 1809–1825.

[318] Quick, M.; Dobryakov, A. L.; Gerecke, M.; Richter, C.; Berndt, F.; Ioffe, I. N.; Granovsky, A. A.; Mahrwald, R.; Ernsting, N. P.; Kovalenko, S. A. *J. Phys. Chem. B* **2014**, *118*, 8756–8771.

[319] Imran, M.; Kurganskii, I.; Taddei, M.; Butera, V.; Zhao, J.; Fedin, M. V.; Di Donato, M.; Mazzone, G. *ChemPhotoChem* **2024**, *8*, e202300320.

[320] Strahan, J.; Popere, B. C.; Khomein, P.; Pointer, C. A.; Martin, S. M.; Oldacre, A. N.; Thayumanavan, S.; Young, E. R. *Dalton Trans.* **2019**, *48*, 8488–8501.

[321] Liu, X.; Yeow, E. K. L.; Velate, S.; Steer, R. P. *Phys. Chem. Chem. Phys.* **2006**, *8*, 1298.

[322] Gray, V.; Dreos, A.; Erhart, P.; Albinsson, B.; Moth-Poulsen, K.; Abrahamsson, M. *Phys. Chem. Chem. Phys.* **2017**, *19*, 10931–10939.

[323] Jiang, L.; Dong, H.; Hu, W. *J. Mater. Chem.* **2010**, *20*, 4994–5007.

[324] Liu, K.; Ouyang, B.; Guo, X.; Guo, Y.; Liu, Y. *npj Flex. Electron.* **2022**, *6*, 1.

[325] Bauri, J.; Choudhary, R. B.; Mandal, G. *J. Mater. Sci.* **2021**, *56*, 18837–18866.

[326] Chen, L. X. *ACS Energy Lett.* **2019**, *4*, 2537–2539.

[327] Imran, M.; Chen, M. S. *ACS Appl. Mater. Interfaces* **2022**, *14*, 1817–1825.

[328] Zhang, Y.; Guo, L.; Zhu, X.; Sun, X. *Front. Chem.* **2020**, *8*, 589207.

[329] Troisi, A.; Orlandi, G. *J. Phys. Chem. B* **2005**, *109*, 1849–1856.

[330] Jurchescu, O. D.; Mourey, D. A.; Subramanian, S.; Parkin, S. R.; Vogel, B. M.; Anthony, J. E.; Jackson, T. N.; Gundlach, D. J. *Phys. Rev. B* **2009**, *80*, 21–23.

[331] Diao, Y.; Lenn, K. M.; Lee, W. Y.; Blood-Forsythe, M. A.; Xu, J.; Mao, Y.; Kim, Y.; Reinspach, J. A.; Park, S.; Aspuru-Guzik, A.; Xue, G.; Clancy, P.; Bao, Z.; Mannsfeld, S. C. *J. Am. Chem. Soc.* **2014**, *136*, 17046–17057.

[332] Bittle, E. G.; Biacchi, A. J.; Fredin, L. A.; Herzing, A. A.; Allison, T. C.; Hight Walker, A. R.; Gundlach, D. J. *Commun. Phys.* **2019**, *2*, 29.

[333] Cruz-Cabeza, A. J.; Feeder, N.; Davey, R. J. *Commun. Chem.* **2020**, *3*, 10–13.

[334] Vehoff, T.; Chung, Y. S.; Johnston, K.; Troisi, A.; Yoon, D. Y.; Andrienko, D. *J. Phys. Chem. C* **2010**, *114*, 10592–10597.

[335] Cataldo, S.; Pignataro, B. *Materials* **2013**, *6*, 1159–1190.

[336] Patel, B. B.; Diao, Y. *Nanotechnology* **2018**, *29*, 044004.

[337] Coropceanu, V.; Cornil, J.; da Silva Filho, D. A.; Olivier, Y.; Silbey, R.; Brédas, J. L. *Chem. Rev.* **2007**, *107*, 926–952.

[338] Ortmann, F.; Bechstedt, F.; Hannewald, K. *Phys. Status Solidi B* **2011**, *248*, 511–525.

[339] Troisi, A. *Chem. Soc. Rev.* **2011**, *40*, 2347–2358.

[340] Coropceanu, V.; Li, Y.; Yi, Y.; Zhu, L.; Brédas, J. L. *MRS Bull.* **2013**, *38*, 57–64.

[341] Baumeier, B.; Kirkpatrick, J.; Andrienko, D. *Phys. Chem. Chem. Phys.* **2010**, *12*, 11103–11113.

[342] Ji, L. F.; Fan, J. X.; Qin, G. Y.; Zhang, N. X.; Lin, P. P.; Ren, A. M. *J. Phys. Chem. C* **2018**, *122*, 21226–21238.

[343] Fratini, S.; Mayou, D.; Ciuchi, S. *Adv. Funct. Mater.* **2016**, *26*, 2292–2315.

[344] Li, W.; Ren, J.; Shuai, Z. *Nat. Commun.* **2021**, *12*, 4260.

[345] Fratini, S.; Ciuchi, S.; Mayou, D.; De Laissardière, G. T.; Troisi, A. *Nat. Mater.* **2017**, *16*, 998–1002.

[346] Nematiaram, T.; Ciuchi, S.; Xie, X.; Fratini, S.; Troisi, A. *J. Phys. Chem. C* **2019**, *123*, 6989–6997.

[347] Landi, A. *J. Phys. Chem. C* **2019**, *123*, 18804–18812.

[348] Fratini, S.; Nikolka, M.; Salleo, A.; Schweicher, G.; Sirringhaus, H. *Nat. Mater.* **2020**, *19*, 491–502.

[349] Fratini, S.; Ciuchi, S. *Phys. Rev. Res.* **2020**, *2*, 013001.

[350] Troisi, A.; Orlandi, G. *Phys. Rev. Lett.* **2006**, *96*, 086601.

[351] Troisi, A.; Orlandi, G. *J. Phys. Chem. A* **2006**, *110*, 4065–4070.

[352] Schweicher, G. et al. *Adv. Mater.* **2019**, *31*, 1902407.

[353] Liu, J.; Dong, H.; Wang, Z.; Ji, D.; Cheng, C.; Geng, H.; Zhang, H.; Zhen, Y.; Jiang, L.; Fu, H.; Bo, Z.; Chen, W.; Shuai, Z.; Hu, W. *Chem. Commun.* **2015**, *51*, 11777–11779.

[354] Hu, P.; He, X.; Jiang, H. *InfoMat* **2021**, *3*, 613–630.

[355] Pascale, F.; Zicovich-Wilson, C. M.; Lo´pezlo´, F.; Gejo, L.; Civalleri, B.; Orlando, R.; Dovesi, R. *J. Comput. Chem.* **2004**, *25*, 888–897.

[356] Zicovich-Wilson, C. M.; Pascale, F.; Roetti, C.; Saunders, V. R.; Orlando, R.; Dovesi, R. *J. Comput. Chem.* **2004**, *25*, 1873–1881.

[357] Dovesi, R.; Erba, A.; Orlando, R.; Zicovich-Wilson, C. M.; Civalleri, B.; Maschio, L.; Rérat, M.; Casassa, S.; Baima, J.; Salustro, S.; Kirtman, B. *Wiley Interdiscip. Rev.: Comput. Mol. Sci.* **2018**, *8*, e1360.

[358] Dovesi, R. et al. *J. Chem. Phys.* **2020**, *152*, 204111.

[359] Becke, A. D. *J. Chem. Phys.* **1993**, *98*, 5648–5652.

[360] Lee, C.; eitao Yang; Parr, R. G. *Phys. Rev. B* **1988**, *37*, 785.

[361] Wilk A N, L.; Nusair, D. M. *Can. J. Phys.* **1980**, *58*, 1200–1211.

[362] Stephens, P. J.; Devlin, F. J.; Chabalowski, C. F.; Frisch, M. J. *J. Phys. Chem.* **1994**, *98*, 11623 – 11627.

[363] Vilela Oliveira, D.; Laun, J.; Peintinger, M. F.; Bredow, T. *J. Comput. Chem.* **2019**, *40*, 2364–2376.

[364] Illig, S.; Eggeman, A. S.; Troisi, A.; Jiang, L.; Warwick, C.; Nikolka, M.; Schweicher, G.; Yeates, S. G.; Henri Geerts, Y.; Anthony, J. E.; Sirringhaus, H. *Nat. Commun.* **2016**, *7*, 10736.

[365] Eggeman, A. S.; Illig, S.; Troisi, A.; Sirringhaus, H.; Midgley, P. A. *Nat. Mater.* **2013**, *12*, 1045–1049.

[366] Valeev, E. F.; Coropceanu, V.; Da Silva Filho, D. A.; Salman, S.; Brédas, J. L. *J. Am. Chem. Soc.* **2006**, *128*, 9882–9886.

[367] Otaki, T.; Terashige, T.; Tsurumi, J.; Miyamoto, T.; Kida, N.; Watanabe, S.; Okamoto, T.; Takeya, J.; Okamoto, H. *Phys. Rev. B* **2020**, *102*, 245201.

[368] Brown, J. S. *CATNIP*, Version 1.9. `https://github.com/JoshuaSBrown/QC_Tools`, 2018.

[369] Weigend, F.; Ahlrichs, R. *Phys. Chem. Chem. Phys.* **2005**, *7*, 3297–3305.

[370] Weigend, F. *Phys. Chem. Chem. Phys.* **2006**, *8*, 1057–1065.

[371] Frisch, M. J. et al. *Gaussian 16* Revision C.01. Gaussian Inc. Wallingford CT, 2016.

[372] Girlando, A.; Grisanti, L.; Masino, M.; Bilotti, I.; Brillante, A.; Della Valle, R. G.; Venuti, E. *Phys. Rev. B* **2010**, *82*, 035208.

[373] Yu, X.; Kalihari, V.; Frisbie, C. D.; Oh, N. K.; Rogers, J. A. *Appl. Phys. Lett.* **2007**, *90*.

[374] Wen, S.-h.; Li, A.; Song, J.; Deng, W.-q.; Han, K.-l.; Goddard, W. A. *J. Phys. Chem. B* **2009**, *113*, 8813–8819.

[375] Landi, A.; Borrelli, R.; Capobianco, A.; Velardo, A.; Peluso, A. *J. Chem. Theory Comput.* **2018**, *14*, 1594–1601.

[376] Jiang, Y.; Geng, H.; Li, W.; Shuai, Z. *J. Chem. Theory Comput.* **2019**, *15*, 1477–1491.

[377] Giannini, S.; Carof, A.; Ellis, M.; Yang, H.; Ziogos, O. G.; Ghosh, S.; Blumberger, J. *Nat. Commun.* **2019**, *10*, 1–12.

[378] Giannini, S.; Ziogos, O. G.; Carof, A.; Ellis, M.; Blumberger, J. *Advanced Theory and Simulations* **2020**, *3*, 1–11.

[379] Giannini, S.; Blumberger, J. *Acc. Chem. Res.* **2022**, *55*, 819–830.

[380] Oberhofer, H.; Reuter, K.; Blumberger, J. *Chemical Reviews* **2017**, *117*, 10319–10357.

[381] Schilcher, M. J.; Robinson, P. J.; Abramovitch, D. J.; Tan, L. Z.; Rappe, A. M.; Reichman, D. R.; Egger, D. A. *ACS Energy Letters* **2021**, *6*, 2162–2173.

[382] Sansone, G.; Ferretti, A.; Maschio, L. *J. Chem. Phys.* **2017**, *147*, 0–6.

[383] Lee, N. E.; Zhou, J. J.; Agapito, L. A.; Bernardi, M. *Physical Review B* **2018**, *97*, 1–8.

[384] Linnera, J.; Sansone, G.; Maschio, L.; Karttunen, A. J. *J. Phys. Chem. C* **2018**, *122*, 15180–15189.

[385] Cheng, Y. C.; Silbey, R. J.; Da Silva Filho, D. A.; Calbert, J. P.; Cornil, J.; Brédas, J. L. *Journal of Chemical Physics* **2003**, *118*, 3764–3774.

[386] Xi, J.; Long, M.; Tang, L.; Wang, D.; Shuai, Z. *Nanoscale* **2012**, *4*, 4348–4369.

[387] Kobayashi, H.; Kobayashi, N.; Hosoi, S.; Koshitani, N. *The journal of chemical Physics* **2013**, *014707*, 2–9.

[388] Knepp, Z. J.; Fredin, L. A. *J. Phys. Chem. A* **2022**, *126*, 3265–3272.

[389] Perdew, J. P.; Burke, K.; Ernzerhof, M. *Physical Review Letters* **1996**, *77*, 3865–3868.

[390] Adamo, C.; Barone, V. *J. Chem. Phys.* **1999**, *110*, 6158–6170.

[391] Doná, L.; Brandenburg, J. G.; Civalleri, B. *J. Chem. Phys.* **2019**, *151*.

[392] Grimme, S.; Antony, J.; Ehrlich, S.; Krieg, H. *J. Chem. Phys.* **2010**, *132*.

[393] Van Der Lee, A.; Polentarutti, M.; Roche, G. H.; Dautel, O. J.; Wantz, G.; Castet, F.; Muccioli, L. *J. Phys. Chem. Lett.* **2022**, *13*, 406–411.

[394] Griffith, O. L.; Anthony, J. E.; Jones, A. G.; Lichtenberger, D. L. *J. Am. Chem. Soc.* **2010**, *132*, 580–586.

[395] Costa, J. C.; Taveira, R. J.; Lima, C. F.; Mendes, A.; Santos, L. M. *Opt. Mater.* **2016**, *58*, 51–60.

[396] Deng, W. Q.; Goddard, W. A. *J. Phys. Chem. B* **2004**, *108*, 8614–8621.

[397] Girlando, A.; Grisanti, L.; Masino, M.; Bilotti, I.; Brillante, A.; Della Valle, R. G.; Venuti, E. *Phys. Rev. B* **2010**, *82*.

[398] Banks, P. A.; Dyer, A. M.; Whalley, A. C.; Ruggiero, M. T. *Chemical Communications* **2022**, *58*, 12803–12806.

[399] Banks, P. A.; D'Avino, G.; Schweicher, G.; Armstrong, J.; Ruzié, C.; Chung, J. W.; Park, J. I.; Sawabe, C.; Okamoto, T.; Takeya, J.; Sirringhaus, H.; Ruggiero, M. T. *Advanced Functional Materials* **2023**,

[400] Vong, D.; Nematiaram, T.; Dettmann, M. A.; Murrey, T. L.; Cavalcante, L. S. R.; Gurses, S. M.; Radhakrishnan, D.; Daemen, L. L.; Anthony, J. E.; Koski, K. J.; Kronawitter, C. X.; Troisi, A.; Moulé, A. J. *The Journal of Physical Chemistry Letters* **2022**, *13*, 5530–5537.

[401] Harrelson, T. F. et al. *Mater. Horiz.* **2019**, *6*, 182–191.

[402] Dettmann, M. A.; Cavalcante, L. S. R.; Magdaleno, C. A.; Moulé, A. J. *Advanced Functional Materials* **2023**, *33*, 2213370.

[403] Campbell, R. B.; Robertson, J. M.; Trotter, J. *Acta Crystallographica* **1962**, *15*, 289–290.

[404] Morisaki, H.; Koretsune, T.; Hotta, C.; Takeya, J.; Kimura, T.; Wakabayashi, Y. *Nature Communications* **2014**, *5*, 5400.

[405] Vollmer, A.; Ovsyannikov, R.; Gorgoi, M.; Krause, S.; Oehzelt, M.; Lindblad, A.; Mårtensson, N.; Svensson, S.; Karlsson, P.; Lundvuist, M.; Schmeiler, T.; Pflaum, J.; Koch, N. *Journal of Electron Spectroscopy and Related Phenomena* **2012**, *185*, 55–60.

[406] Reese, C.; Chung, W. J.; Ling, M. M.; Roberts, M.; Bao, Z. *Applied Physics Letters* **2006**, *89*.

[407] Hannewald, K.; Stojanović, V. M.; Bobbert, P. A. *Journal of Physics Condensed Matter* **2004**, *16*, 2023–2032.

[408] Koch, N.; Vollmer, A.; Salzmann, I.; Nickel, B.; Weiss, H.; Rabe, J. P. *Physical Review Letters* **2006**, *96*, 10–13.

[409] Hatch, R. C.; Huber, D. L.; Höchst, H. *Physical Review Letters* **2010**, *104*, 2–5.

[410] Li, Y.; Coropceanu, V.; Brédas, J. L. *Journal of Physical Chemistry Letters* **2012**, *3*, 3325–3329.

[411] Graf, L.; Kusber, A.; Büchner, B.; Knupfer, M. *Physical Review B* **2022**, *106*, 1–6.

[412] Tu, Z.; Yi, Y.; Coropceanu, V.; Brédas, J.-L. *The Journal of Physical Chemistry C* **2018**, *122*, 44–49.

Zachary J. Knepp

CONTACT INFORMATION

Address: Alfred, NY
Email: knepp@alfred.edu
Google Scholar: Zachary J. Knepp
LinkedIn: zacharyjknepp

EXPERIENCE

Incoming Assistant Professor; Alfred, NY — Summer 2025
Department of Chemistry; Alfred University

Instructor of Record; Bethlehem, PA — Spring 2025
Department of Chemistry; Lehigh University

Comat Medic; Danville, PA — 2015 – 2020
Pennsylvania Army National Guard

EDUCATION

Lehigh University; Bethlehem, PA — 2025
Ph.D. in Chemistry
Thesis: "Modeling Excited States and Charge Transport with Density Functional Theory"
Advisor: Lisa Fredin

Lock Haven University; Lock Haven, PA — 2020
B.S. in Chemistry and Biology, Mathematics minor, *summa cum laude*
Advisors: Kyle Root and Kevin Range

United States Army; Fort Sill, OK and JBSA-Sam Houston, TX — 2015
Basic combat and 68W training

AWARDS AND FELLOWSHIPS

Department of Energy Travel Award; Lehigh University — Winter 2025
CAS Dean's Research Fellowship; Lehigh University — Spring 2024
Summer Opportunity Award for Research; Lock Haven University — Summer 2018/19
Rose Witt Kleinman Memorial Scholarship; Lock Haven University — 2018

TECHNICAL SKILLS

Software Languages: Python, Bash, LaTeX, Mathematica
Simulation: Gaussian, ORCA, NWChem, MOLCAS, CRYSTAL, VASP, LAMMPS
Visualization: VMD, Gaussview, IQmol, WebMO, VESTA, Inkscape, Blender
Spectroscopy Techniques: UV-Vis, Fluorescence, Ultrafast Transient Absorption

PUBLICATIONS

Undergraduate mentees are underlined

Knepp, Z. J.; Fertal, D. R.; Masso, G. B.; Hamburger, R. C.; Guzman, C. A.; Young, E. R.; Fredin, L. A. Predicting Excited-State Absorption Spectra from Non-Aufbau Configurations. *Submitted.*

Leach, K.; **Knepp, Z. J.**; Sutton, M.; Falls, T.; Bobb, S. C.; McKeefery, C.; Smith, K.; Root, K. T. Characterization of a Highly Stable Solvent-Tolerant SGNH Superfamily Lipase from Sphaerobacter thermophilus. *Under Revision at Biochemistry.*

11. **Knepp, Z. J.**; Repa, G. M.; Fredin, L. A. Excited-State Methods for Molecular Systems: Performance, Pitfalls, and Practical Guidance. *Accepted at Chem. Phys. Rev.*
10. Chen, A. H.; **Knepp, Z. J.**; Guzman, C. A.; Young, E. R.; Fredin, L. A. Intramolecular Subtleties in Indole Azo Dyes Revealed by Multidimensional Potential Energy Surfaces. *Phys. Chem. Chem. Phys.*, **2025**, 27, 6430-6437.
9. Yan, M.; Bowman, Z.; **Knepp, Z. J.**; Peterson, A.; Fredin, L. A.; Morris, A. J. Reaction Type Dependent Behavior of Redox-Hopping in MOFs–Does Charge Transport Have a Preferred Direction? *J. Phys. Chem. Lett.* **2024**, *15*, 11919–11926.
8. **Knepp, Z. J.**; Hamburger, R. C.; Thongchai, I. A.; Englehart, K.; Sorto, K.; Jaffer, A.; Young, E. R.; Fredin, L. A. Pinning Down Small Populations of Photoinduced Intermediates Using Transient Absorption Spectroscopy and Time-Dependent Density Functional Theory Difference Spectra to Provide Mechanistic Insight into Controlling Pyridine Azo Dynamics with Protons. *J. Phys. Chem. Lett.* **2024**, *15*, 9593–9600.

7. Repa, G. M.; **Knepp, Z. J.**; Fredin, L. A. A-site doping to alter oxygen vacancy diffusion in $SrTiO_3$. *ACS Omega* **2024**, *24*, 26719–26723.

6. **Knepp, Z. J.**; Fredin, L. A. Finite-displacement Boltzmann transport theory reveals the detrimental effects of high-frequency normal modes on mobility. *Phys. Rev. B* **2024**, *109*, 094307.

5. Thongchai, I. A.; **Knepp, Z. J.**; Fertal, D. R.; Flynn, H.; Young, E. R.; Fredin, L. A. Acid Violet 3: A base activated water-soluble photoswitch. *J. Phys. Chem. A* **2024**, *128*, 785–791.

4. Martin, S. M.; **Knepp, Z. J.**; Thongchai, I. A.; Englehart, K.; Sorto, K.; Jaffer, A.; Fredin, L. A.; Young, E. R. The doorstop proton: acid-controlled photoisomerization in pyridine-based azo dyes. *New J. Chem.* **2023**, *47*, 11882–11889. *Selected for NJC Outstanding Paper, 2023.*

3. **Knepp, Z. J.**; Masso, G. B.; Fredin, L. A. Efficiently predicting directional carrier mobilities in organic materials with the Boltzmann transport equation. *J. Chem. Phys.* **2023**, *158*, 064704.

2. **Knepp, Z. J.**; Fredin, L. A. Real temperature model of dynamic disorder in molecular crystals. *J. Phys. Chem. A* **2022**, *126*, 3265–3272.

1. **Knepp, Z. J.**; Ghaner, A.; Root, K. T. Purification and refolding protocol for cold-active recombinant esterase AaSGNH1 from Aphanizomenon flos-aquae expressed as insoluble inclusion bodies. *Prep. Biochem. Biotech.* **2021**, *52*, 394–403.

Selected Talks and Posters

13. **Knepp, Z. J.**; Masso, G. B.; Fertal D. R.; Young, E. R.; Fredin, L. A. Predicting Excited-State Absorption Spectra from Ground- and Excited-State References, **2025**, Poster presented at the 2025 Inter-American Photochemical Society Conference, Miramar Beach, FL.

12. **Knepp, Z. J.**; Fredin, L. A. Investigating dynamic disorder in organic semiconductors with Boltzmann transport theory, **2024**, Poster presented at the 2024 American Conference on Theoretical Chemistry, Chapel Hill, NC.

11. **Knepp, Z. J.**; Fredin, L. A. Investigating the vibrational disorder of tetracene using a new finite-displacement Boltzmann transport theory, **2024**, Talk presented at the 2024 American Chemical Society Middle Atlantic Regional Meeting, State College, PA.

10. **Knepp, Z. J.**; Young, E. R.; Fredin, L. A. Investigating the Photoisomerization Mechanisms of Heteroaryl Azo Dyes with Theory and Experiment, **2023**, Poster present at the Photochemistry GRC, Lewiston, ME.

9. **Knepp, Z. J.**; Fredin, L. A. Computational Pump-Probe Spectra for Free with LR-TDDFT, **2023**, Poster presented at TDDFT School and Workshop, Newark NJ.

8. Howzen, A.; Repa, G. M.; **Knepp, Z. J.**; Pimputkar, S.; Strandwitz, N. C.; Fredin, L. A. Data driven interface design, **2023**, Poster presented at the Institute for Data, Intelligent Systems, and Computation, Bethlehem PA.

7. **Knepp, Z. J.**; Fredin, L. A. Modeling Dynamic Disorder in Organic Materials, **2022**, Poster presented at the Mid-Atlantic Regional ACS Meeting, Ewing, NJ.

Teaching and Mentoring

Physical Chemistry Lab (CHM 343) Instructor — **Lehigh University**
TAs: Andrea Dorsa & Domenica Fertal — Spring 2025
– Set up and instructed physical chemistry lab with 17 students

Photochemistry Undergraduate Research Experience Mentor — **Lehigh University**
Advisors: Lisa Fredin and Elizabeth Young — Summer 2021 – Current
– Mentored 12 undergraduates
– Taught essentials of data processing with Python and graphical design
– Aided students in the interpretation of spectroscopic and computational chemistry results
– Taught photochemistry, quantum mechanics, and DFT to freshman and sophomore students
– Provided feedback on writing, presentations, and projects through weekly check-ins
– Designed step-by-step tutorials for complicated computational methods and data work-ups
– Guided 2 undergraduate projects from concept to publication

MoleCVUE Co-facilitator at ACS MARM 2024 — **Penn State University**

2024 Chair: Heidi Hendrickson Summer 2024
– Co-facilitator of "Hands-on Computational Activities for the Chemistry Classroom"

Molecular Structure, Bonding, & Dynamics Guest Lecturer **Lehigh University**
Instructor: Lisa Fredin Spring 2023, Spring 2024
– Gave 3 lectures on topics including: particle-in-a-box, superposition, and uncertainty, multi-electron atoms, the variation theorem, and HF theory

Quantum Chemistry Workshop Teaching Assistant **Lehigh University**
Instructor: Lisa Fredin Summers 2021 – 2024
– Lead hands-on facilitator
– Assisted students with executing Linux commands and scripting, command-line text editors including Vim, Emacs, and Nano, and running calculations on high performance computers
– Helped students run molecular calculations on HPCs with Gaussian and Gaussview software
– Aided students in constructing unit cells of simple periodic solids
– Advised students on how to run DFT jobs in Quantum Espresso and VASP

Physical Chemistry Lab (CHM 343) Teaching Assistant **Lehigh University**
Instructor: Elizabeth Young Spring 2022
– Set up and co-instructed physical chemistry labs to $\sim$ 34 students
– Graded lab reports and provided editorial suggestions and comments
– Assisted in the development of Mathematica-based data-processing scripts for lab experiments

General Chemistry Lab (CHM 030) Teaching Assistant **Lehigh University**
Instructors: Hannah Cronk, Daniel Prendergast, and Cynthia Velgus Fall 2020, Spring 2021
– Assisted in the set up of experiments and solution preparation
– Taught pre-labs to $\sim$ 18 students for 2 sections and graded $\sim$ 36 lab reports, weekly
– Supervised experimental setup and execution
– Held office hours every two weeks to assist students with lab reports

Mathematics Tutor **Lock Haven University**
Supervisor: Jacinth Maynard Fall 2019, Spring 2020
– Provided drop-in tutoring for students in algebra, calculus I, and calculus II

Tactical Combat Casualty Care Course Instructor **Fort Pickett**
Supervisor: Erica Smith 2018
– Co-instructed a 40-hour TCCC Combat Lifesaver course to non-medical military personnel

Students Mentored

Nagoya Institute of Technology Graduate Students
Shota Asayama: Master's Exchange Student Fall 2024

Lehigh University Graduate Students
Isabelle Herlinger: Chemistry PhD '28 Spring 2024 – Spring 2025

Lehigh University Undergraduate Students
Nabeel Rifai: IDEAS Major '27 Summer 2024
Matthew Reeves: Chemistry Major '27 Summer 2024
Vanessa Elias: Chemistry Major '27 Summer 2024
Sabine Dalais: Engineering Major '27 Summer 2024
Hao-Ran (Allen) Chen: Physics Major '25 Summer 2022 – Spring 2025
Rachel Joh: Chemistry Major '25 Summer 2022 – Spring 2023
Jake Haber: Chemistry Major '25 Summer 2022 – Spring 2023
Gabe Masso: Chemistry Major '24 Spring 2022 – Summer 2024
Ing-Angsara Thongchai: Chemistry Major '24 Summer 2021 – Spring 2024
Keyri Sorto: Chemical Engineering Major '24 Summer 2021 – Spring 2022
Athina Jaffer: IDEAS Major '23 Summer 2021 – Spring 2022
Kiera Englehart: Chemistry Major '22 Summer 2021 – Spring 2022

Research Experience

Predicting excited-state absorption spectra with ΔSCF **Lehigh University**
Advisor: Lisa Fredin 2023 – 2025
– Tested the limits of LR-TDA-DFT and ΔSCF to predict excited-state absorption spectra

Modeling vibrational disorder in organic semiconductors **Lehigh University**
Advisor: Lisa Fredin 2021 – 2024
– Developed models that pair periodic-DFT with Marcus and/or BTE to investigate the effects of crystalline vibrations on charge transport in organic semiconductors.

Sterically hindered indole-based azo dyes **Lehigh University**
Advisors: Lisa Fredin and Elizabeth Young 2022 – 2025
– Explored how steric R-groups at the indole C2 site impact the photophysical properties of indole-based azo dyes with DFT, TD-DFT, and UV-vis spectrscopy.

Desymmetrized cyclopentannulated acenes **Lehigh University**
Advisor: Lisa Fredin 2023 – 2024
– Investigated the ability of desymmetrized cyclopentannulated acenes to conduct charge and undergo singlet fission with DFT and TD-DFT.

Base-activated water-soluble photoswitch **Lehigh University**
Advisors: Lisa Fredin and Elizabeth Young 2022 – 2024
– Investigated the photoisomerizability of Acid Violet 3 (AV3) in three protonation states using a combination of UV-vis spectroscopy and TD-DFT.

Limiting photoisomerization of azo dyes with protons **Lehigh University**
Advisors: Lisa Fredin and Elizabeth Young 2021 – 2024
– Explored the photoisomerization and reversion mechanisms of protonated pyridine-based azo dyes with DFT, TD-DFT, UV-vis spectrscopy, and fs-TAS spectroscopy.

Molecular dynamics of M37 lipase **Lock Haven University**
Advisor: Kevin Range 2020
– Executed molecular dynamics (MD) simulations of M37 lipase in solution (water) and in a bilayer using AMBER force fields and software.

Charaterizing extremophilic esterase enzymes **Lock Haven University**
Advisor: Kyle Root 2018-2019
– Purified and characterized a thermophilic lipase native to *Sphaerobacter thermophilus* and a psychrophilic esterase native to *Aphanizomenon flos-aquae*.

Service and Outreach

STEM Outreach Volunteer at Pre-K Daycares **Bethlehem, PA**
Supervisor: Elizabeth Young Fall 2022 – Summer 2023
– Prepared and conducted age-appropriate science experiments with $\sim$ 20 pre-K children 6 times

Pennsylvania Army National Guard Combat Medic (68W) **Danville, PA**
Supervisors: Terry Cropf and Jason Kling October 2015 - May 2020
– Administered (emergency) medical treatments

Workshops and Events

Inclusive Excellence in Teaching and Learning Workshop **Bethlehem, PA**
Sponsor: Office of Diversity, Inclusion, and Equity at Lehigh University Winter 2024

Teacher Development Series **Bethlehem, PA**
Sponsor: Center for Innovation in Teaching and Learning at Lehigh University Fall 2024

TDDFT School and Workshop: Excited States and Dynamics **Newark, NJ**
Sponsor: Rutgers University - Newark Summer 2023

Solid State Materials Chemistry and Data Science Hackathon **Bethlehem, PA**
Sponsors: NSF, University of Utah, and Lehigh University Winter 2023

Additional Activities

Chemistry Club VP: Fall 2021 – Spring 2022 **Lehigh University**
Chemistry Club VP: Fall 2020 – Spring 2021 **Lock Haven University**